4-30-2021

Modified biochar adsorbents for aqueous contaminant remediation

Herath Mudiyanselage Nimeshika Amali Herath
aherath91@gmail.com

Modified biochar adsorbents for aqueous contaminant remediation

By

Herath Mudiyanselage Nimeshika Amali Herath

Approved by:

Todd E. Mlsna (Major Professor)
David O.Wipf
Debra Ann Mlsna
Amanda Patrick
Janice E. Chambers
Joseph P. Emerson (Graduate Coordinator)
Rick Travis (Dean, College of Arts & Sciences)

A Dissertation
Submitted to the Faculty of
Mississippi State University
in Partial Fulfillment of the Requirements
for the Degree of Doctor of Philosophy
in Chemistry
in the Department of Chemistry

Mississippi State, Mississippi

April 2021

Name: Herath Mudiyanselage Nimeshika Amali Herath

Date of Degree: April 30, 2021

Institution: Mississippi State University

Major Field: Chemistry

Major Professor: Todd E. Mlsna

Title of Study: Modified biochar adsorbents for aqueous contaminant remediation

Pages in Study: 205

Candidate for Degree of Doctor of Philosophy

Continuous population growth and rapid industrial advancement and development have paved the way for ever increasing environmental pollution. At present, water pollution is a serious global issue that threatens environmental sustainability. The contamination of aquatic bodies with potentially toxic organic and inorganic substances are the result of world-wide anthropogenic activities. These pollutants can have detrimental health consequences on humans and ecosystems. Over the past decades, techniques such as chemical precipitation, ion-exchange, adsorption, membrane filtration, and electrocoagulation–flocculation have been developed and employed for the treatment of drinking and wastewater. Among the currently available techniques, pollutant removal by adsorption is most promising due to its cost-effectiveness, simplicity in operation, environmental friendliness, and abundance of adsorbents. This study emphasized the utilization of biochar (BC), after appropriate surface modification, for the removal of potentially toxic contaminants.

In the first study, a base activated biochar was synthesized by treating the biochar with potassium hydroxide (KOH) at 700 °C in a muffle furnace for 1 h. The resulting high surface area biochar (KOHBC) was used for the removal of Cr(VI), Pb(II) and Cd(II). In the second study, a biochar-supported polyaniline hybrid was synthesized for aqueous chromium and nitrate

adsorption. Introduction of amine and imine groups to the biochar facilitated the removal of these contaminants. In the final study, a composite containing Fe-Ti oxide/biochar (Fe_2TiO_5/BC) was synthesized for sorptive removal of metal cations, oxy anions, inorganics, and organic contaminants from aqueous solutions. Additionally, this composite was used as a photocatalyst towards aqueous methylene blue (MB) degradation. The surface chemistry and composition of these adsorbents were examined by PZC SEM, TEM, XPS, FTIR, TGA, elemental analysis, and surface area measurements.

DEDICATION

I would like to dedicate this dissertation

To my loving father Prof. Ajith Herath and mother Mrs. Thilaka Herath

for their support and encouragement

ACKNOWLEDGEMENTS

First and foremost, I would like to express my sincere gratitude to my advisor Dr. Todd Mlsna whose guidance, motivation, patience and continued support enabled me to complete this dissertation successfully.

I would also like to thank all my committee members, Dr. David O. Wipf, Dr. Deb Mlsna, Dr. Amanda Patrick, and Dr. Janice Chambers for their constructive comments and suggestions given throughout my study program. I big thanks goes to Dr. Charles U. Pittman Jr. whose ideas and scientific insights inspired me to raise my standards a notch higher every time. In addition, I would like to thank my teaching lab coordinator, Dr. Laura Smith, for her support in my teaching career.

Furthermore, my special thanks to wonderful undergraduate researchers who have devoted so much of their time for assisting me with the execution of many experiments. I really appreciate their hard work and effort towards the success. I would particularly like to thank all my co-researchers for their support in numerous ways towards the successful completion of my Ph.D. program. I would like to extend my thanks to Dr. Rooban at image center for helping me with SEM and TEM analysis. I am also grateful to all my dear friends who have immensely supported me along the way while I am being away from my family.

Last, but by no means least, I am grateful to my parents for their endless love, constant care, and who have encouraged me through moral and emotional support in various aspects of my life.

TABLE OF CONTENTS

LIST OF TABLES

LIST OF FIGURES

LIST OF SCHEMES

CHAPTER I

INTRODUCTION

Current projections indicate that the world population is poised to grow from 7. 7 billion in early 2021 to over 9. 8 billion by mid-2050.[1] Along with this growth is the ever-rising demand for improved standards of living. The combination of a growing population and improved standard of living is having a detrimental impact on earth's ecosystems. Technological advancements are needed to combat the expanding textile, pharmaceutical and agricultural sectors as they have the potential to massively contribute unfavorable changes in the four earth spheres -the atmosphere, hydrosphere, biosphere and lithosphere.

1.1 Contamination of hydrosphere

Water is quite ununiformly distributed in the hydrosphere. The ocean contains 97% of all terrestrial water but high salt content makes it of little direct use to humans. The remaining 3% of fresh water is primarily contained in ice sheets and glaciers (75%) and groundwater (14%) below 750 m and is essentially inaccessible.[2] This fresh water is largely consumed in industrial processes and exhausted as wastewater which then flows into canals, rivers and eventually to lakes and seas. The wastewater contains dissolved inorganic and organic matter which can deplete water quality and make it toxic for the environment and humans.

1.2 Sources of water pollutants

Anthropogenic activities are primarily responsible for water pollution,[3] even though natural phenomenon, such as forest fires, which leave toxic runoff in their wake,[4] volcano eruptions,[5] and many geological processes[6] also contribute to deteriorate water quality. One of the most impactful sources of water contamination is the chemical industry. Abundant untreated industrial wastes entering water bodies include textile dyes,[7] potentially toxic metals and metal ions,[8] detergents,[9] and pharmaceutical products.[10] Fertilizers, pesticides, fungicides, herbicides and insecticides are widely applied chemicals in agriculture[11] to enhance the crop yield and to meet current demands. Run off and leaching through the soil is widespread and these substances make their way into aquatic environments where they can cause a serious health threats to humans and other organisms.[12] Human and veterinary pharmaceutical products and their metabolites[13] are emerging pollutants as they could accelerate resistance of bacterial pathogens to antibiotics.[14]

Microplastics (MP) are another class of emerging pollutant reported in a wide range of aquatic environments including drinking water, freshwater sources, marine and subtidal sediments. MP could enter aquatic environments through various routes such as micro-beads found in a wide range of consumer products, microfibers from fabrics (polyester, polyester-cotton blend and acrylic) and plastic products.[15] It has been estimated that 92% of the five trillion plastic particles on the ocean surface are microplastics.[16] Many of the synthetic polymers being used in daily life contain a wide range of heavy metals such as Cd, Pb, As, Sb, Cu, Cr, and Zn as additives. Therefore, once MPs are released, some of their load of such potentially toxic metals will bioaccumulate through the food chain. The increased surface area and hydrophobicity of MP causes high affinity to a broad range of persistent organic pollutants and heavy metals. Even though there is a lack of research-supported evidence for the potential risk of MP to humans, some studies

show that MP can cause cytotoxicity, hypersensitivity, and unwanted immune responses in humans.[17]

1.3 Pollution abatement

Many of the toxic organic and inorganic contaminants in water show high resistance to microbial or chemical degradation and consequently concentrate and persist for a long time after being released to the environment.[18] Exposure to these water contaminants has been implicated in numerous detrimental health effects for humans including reproductive problems, neurotoxicity, cancer, immune system suppression, cardiovascular disease, and metabolic diseases.[19,20] Therefore, measures have to be implemented to remove these harmful substances before discharging industrial effluents into aquatic systems. Removal techniques of these water contaminants are broadly classified into non-destructive and destructive methods (Fig. 1.1) Filtration by electrocoagulation,[21] adsorption,[22] ion exchange,[23] reverse osmosis,[24] and electrodialysis[25] belong to the first category in which the pollutant is not destroyed, but instead it is transferred into another medium. Advanced oxidation processes (AOP)[26] belong to the second category which involve complete destruction of the pollutant into CO_2, H_2O, and simple inorganic ions. AOP on pollutants is accomplished by means of either chemical oxidation[26] electro oxidation,[27] or photocatalytic oxidation.[28] In AOP, the pollutant is destroyed by non-selective potent oxidant hydroxyl radical ($HO^{\bullet}$), superoxide radical anion ($O_2^{\bullet -}$), or singlet oxygen ($^1O_2$) generated in any one of the above methods.

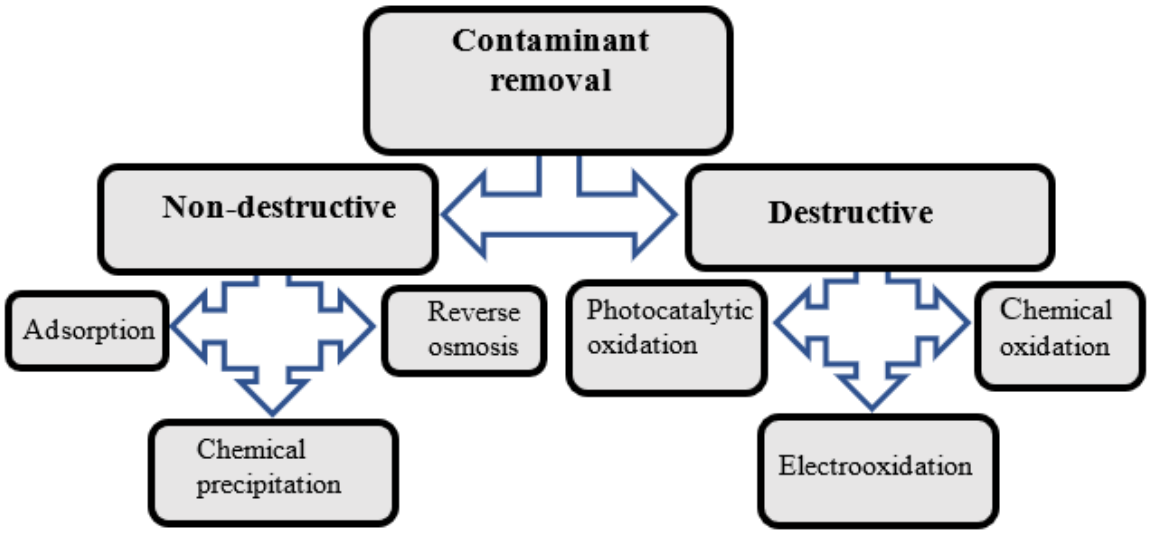

Figure 1.1 Different contaminant removal techniques

1.4 Adsorption mechanism of pollutant removal

Among many available methods for treating polluted water, adsorption technique dates back to several centuries. Egyptians were the first to use adsorption phenomena to treat odorous putrefactive wounds and intestines using charcoal. Scheele in 1894 and Fontana[29] in 1777, experimentally studied for the first time, adsorption of gasses by charcoal and clay. Adsorption has long been practiced as a purification and separation technique on the industrial scale. Adsorption is a surface phenomenon by which an equilibrium is established when the adsorbent surface is in contact with an adsorbate (contaminant) molecule at a specified temperature. Adsorption processes may be either physisorption, due to Van der Waals forces of attraction between the adsorbate entities and adsorbent, or chemisorption from the forming of chemical

bonds with the surface of the adsorbent. Chemisorption is stronger compared to the weak reversible physisorption.[30]

The removal of both organic and inorganic pollutants by adsorption is promising and widely applied on the industrial scale. The adsorption of pollutants onto activated carbon (AC) is often an efficient process and therefore very common. AC has favorable qualities such as simplicity of preparation, environmental friendliness, high efficiency. and abundance of feedstocks.[30] Uptake of heavy metals, Cr(VI), Ni(II), Cd(II), Pb(II), and Zn(II) by AC, prepared by peanut shell,[31] Cucumis melo peel,[32] neem leaf powder,[33] olive stone,[34] and coconut shell[35] has been widely studied. Several studies revealed that AC is a very effective adsorbate for treating textile dye,[36] pesticides,[37] and pharmaceuticals.

Although AC is very popular, commercial grade AC is expensive, hence other naturally occurring adsorbates like clays have received much attention in the scientific community. Clay minerals are hydrous aluminosilicates with a fine particle size. Bentonite and montmorillonite clays exhibit strong affinity to cationic dye molecules and oxyanions and therefore, are promising economic candidates for the removal of industrial dyes and heavy metals.[38,39] Clay contains exchangeable cations held to the surface which facilitates the sorption of metal ions in water.[38] Clay minerals can be modified or activated by acid or base treatment to enhance sorption properties. It has been found that acid-modified clay resulted higher rate of dye adsorption.[40] Kaolinites clay[41] is another option for organic dye removal but it has low cation exchange capacity. Most of the clays for pollutant remediation studies claimed that removal of Cu(II), Cd(II), Pb(II), Cr(VI), and As(V)is due to ion-exchange or adsorption mechanisms.[38]

1.5 Biomass

Biomass rich in carbon are ubiquitous in nature and there are a range of promising feedstock candidates for producing adsorbent materials that can be used to resolve issues with pollution, global warming, and the energy crisis. At present, synthesized carbon materials including crystalline carbon nanotubes/nanofibers,[42, 43] and graphene[44] are widely used to address the pollution issues listed above. The synthetic methods employed to produce the above materials are expensive. Techniques such as chemical vapor deposition,[45] arc discharge and electrochemical treatments[46] have been employed to produce such adsorbents. Some methods also involve organic solvents. Many published processes are not environmentally or economically sustainable in large-scale production.

The utilization of biomass rich in carbon from naturally abundant resources is economically viable and environmental friendly for making a wide range of functionalized carbon materials.[47] Biomass from plants and animals has received increased interest and attention over the past decade as abundant renewable feedstocks. Plant organs such as fruits, seeds, tubers and agricultural wastes from the straw of grain crops such as maize, wheat, barley and rice shell are common abundant feedstocks.[48] The major constituents of plant biomass are lignocellulose and starch while polysaccharides and proteins are the major constituents in biomass from animal origin. (Fig 1.2).

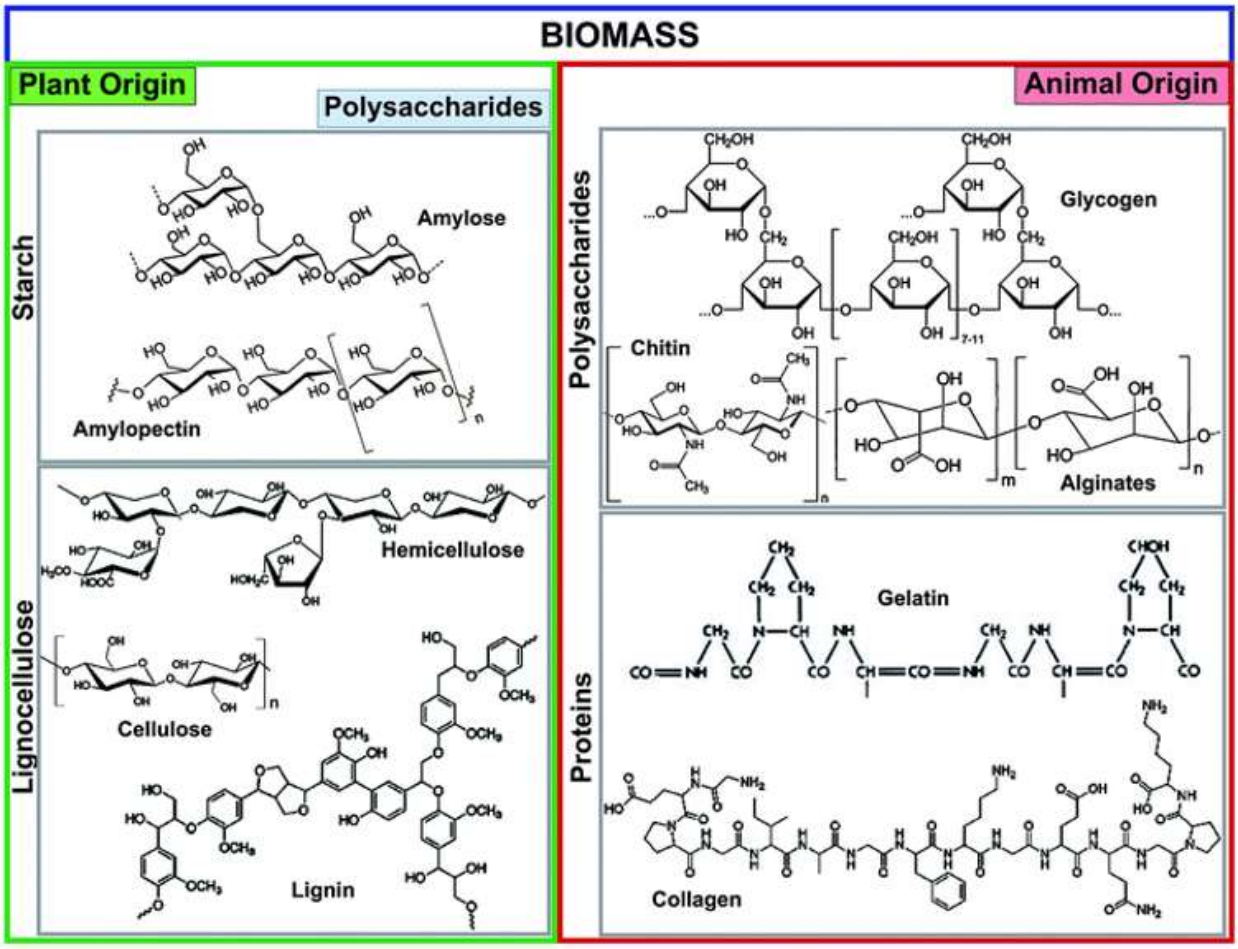

Figure 1.2 Biomass feedstocks derived from plants and animals

Mian, M. M.; Liu, G., Recent progress in biochar-supported photocatalysts: synthesis, role of biochar, and applications. *RSC Advances* **2018,** *8* (26), 14237-14248. Published by The Royal Society of Chemistry.

1.6 Biochar

Biochar (BC) is a porous, highly aromatic and carbon rich solid residual produced from the pyrolysis of lignocellulosic biomass in an oxygen free, or limited oxygen, environment. High surface area, low cost of production, wide feedstock availability, environmental stability, plentiful surface functionality options and recyclability are features of BC.[50,51] Therefore, BC has numerous applications in environmental remediation,[52] carbon sequestration,[53,54] soil fertility

improvement,[55] and energy storage.[56,57] The physical and chemical properties of BC play a vital role in the efficiency of removal of a pollutant. Those properties depend on the type of feedstock and pyrolysis process parameters including pyrolysis temperature, heating rate and residence time.[58] Specific surface area, porosity and surface functional groups of a BC also depend on the origin of the feedstock.[59]

1.6.1 Biochar production techniques

In the production of BC, three methods are currently employed namely (i) pyrolysis, (ii) gasification, and (iii) hydrothermal carbonization.[58,60] Each method uses different conditions for the conversion of feedstock into bioproduct with different characteristic properties.

1.6.2 Chemistry of pyrolysis process

During pyrolysis of biomass, starch, cellulose and lignin undergo thermal decomposition followed by various chemical reactions. The mechanism of this reaction could be characterized by depolymerization, dehydration, decarboxylation intramolecular rearrangement, intramolecular condensation, and aromatization to produce BC or low molar mass bio-oil and syngas[58,60] Free-radical reactions are the major pathway in the production of BC and other products. Free radicals are generated by homolytic bond cleavage of β-O-4 lignin linkage, which can abstract protons of weak C-H or O-H bonds in other species present in the medium. The reaction mechanisms involved in pyrolysis are summarized in Fig. 1.3 and Fig. 1.4.

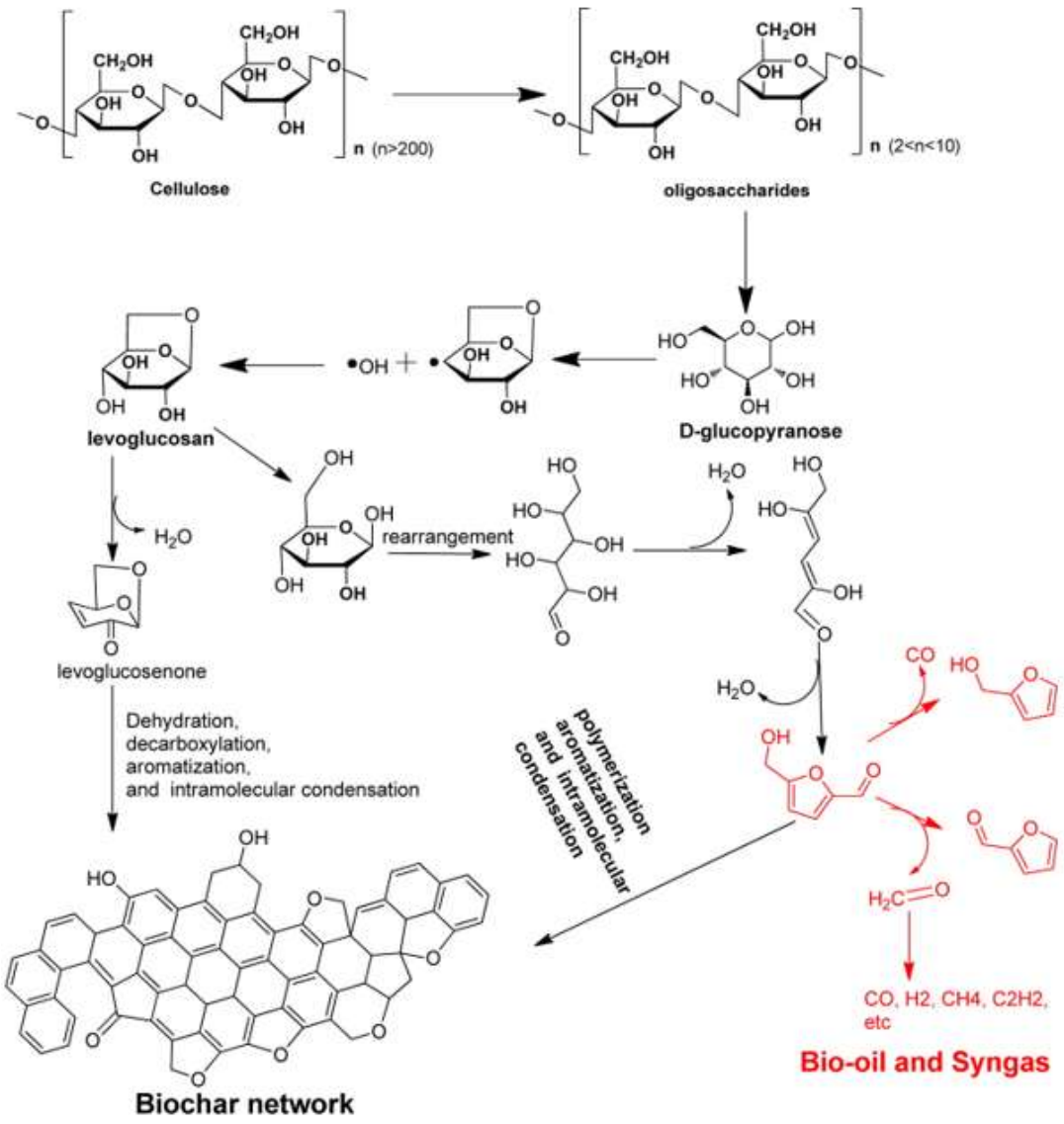

Figure 1.3 Chemical pathway of production of biochar

Reprinted with permission from Liu, W.-J.; Jiang, H.; Yu, H.-Q., Development of biochar-based functional materials: toward a sustainable platform carbon material. *Chemical Reviews* **2015,** *115* (22), 12251-12285. Copyright © 2015 American Chemical Society.

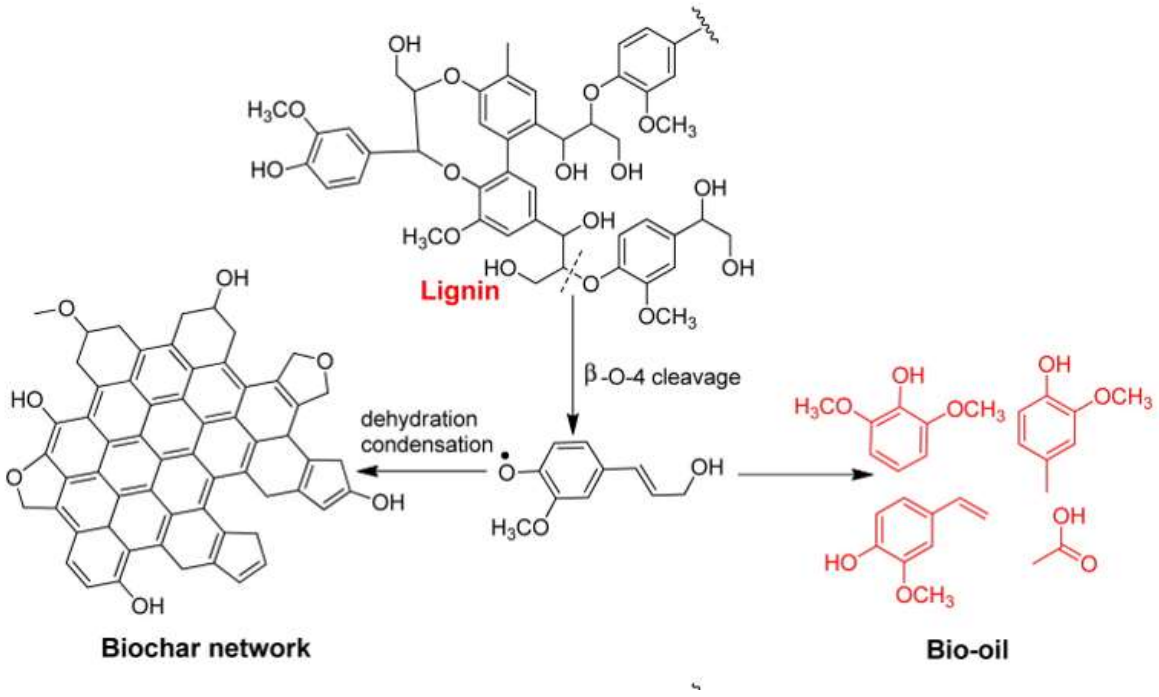

Figure 1.4 Chemical pathway of production of biochar from lignin

Reprinted with permission from Liu, W.-J.; Jiang, H.; Yu, H.-Q., Development of biochar-based functional materials: toward a sustainable platform carbon material. *Chemical Reviews* **2015,** *115* (22), 12251-12285. Copyright © 2015 American Chemical Society.

1.6.3 Composition of biochar

The BC skeleton is composed of C, H and O and often contains surface organic functional groups including aliphatic and aromatic hydroxyl, carboxyl, carbonyl, amido, ester, and phenolic-OH groups. BC oxygen functional groups decrease with increasing pyrolysis temperature, while percent C increases [59]. The proportionality of C, H and O in the final BC depends on the nature of the feedstock[61] and pyrolysis temperature. In addition to organic functionalities, Si-rich biomass is likely to form more compact monomeric and polymeric Si structures under different pyrolysis temperatures. The presence of other inorganic species including HCO_3^{2-}, CO_3^{2-}, metallic oxides and hydroxides have also been reported in biochar. N and P in biomass, undergo for a series of thermal

reactions during pyrolysis and eventually transform into NO_X, NH_4^+, NO_3^-, and PO_4^{3-}. Most BC contains trace level of sulfur, chlorine, alkali, and alkaline-earth metals.

1.6.4 Surface modification techniques of BC

1.6.4.1 Acid/alkaline/H_2O_2 treatment

Physical or chemical surface modification can greatly alter BC surface properties for increase in adsorption of pollutants. Physical treatment includes the activation of carbonized material with steam, CO_2, and air.[62] Steam activation is common and accomplished by forcing steam through the pores of BC at around 800 ºC in an oxygen-free environment after feedstock pyrolysis. Activation with steam or carbon dioxide selectively remove the more reactive carbon from BC as CO_2, or CO. The escape of these gaseous products develop microporosity and increase surface area and aromaticity of BC.[63]

BC chemical treatment can include base or acid activation and result in different changes in the BC structure. In the alkaline treatment, BC is activated by KOH, K_2CO_3, NaOH, and Na_2CO_3 at 400ºC-1000 ºC under inert gas (Ar/N_2) flow in a furnace.[64,53] Alkaline treatment with KOH and K_2CO_3 is more effective in changing surface properties than NaOH or Na_2CO_3. In addition to the evolution of gaseous products, intercalation of metallic K formed in the activation process can expand the carbon lattice. This results in increased porosity, enhanced surface area, surface basicity and more oxygenated functional groups at the BC surface.[53] BC activation with steam, CO_2, and K_2CO_3 using microwave heating at high temperature is another approach to improve the porosity of the material.[65,66]

Acid activation of BC is usually carried out by HNO_3, HCl, H_2SO_4 or H_3PO_4.[67,68] H_3PO_4 being weak and non-corrosive compared to other acids, is particularly attractive in activation of BC. Eliminating C with H_3PO_4 results in high porosity and oxidation of C results in new functional

groups such as -OH, -COOH, and P-containing functional groups including -P=O, -P=OOH, and -P-O-P- at the surface and inside the pores.[69] These functional groups are strong binding sites for many organic and inorganic pollutants.

Oxidation by concentrated HNO_3, a strong oxidizing agent, at ~800°C results in removal of carbon and hydrogen and an increase in oxygen and nitrogen substituted (-C-NO_2, -C-O-NO_2, -C=O, -C-OH, -CO_2H) aromatic rings. Removal of C followed by destruction of pore walls, slightly increase pore volumes and pore sizes of BC. The total surface acidity of BC increases as acid functional groups increases upon acid treatment. During strong acid treatment, the conversion of micro- and mesopores to macropores is favoured.[70]

HCl treatment of BC increases the number of acidic oxygen functional groups and single-bonded oxygen functional groups such as phenols, ethers, and lactones.[70] HCl can wash away metallic impurities thereby decreasing the ash content and at the same time increasing micropore surface area. Further, HCl modification generates adsorbed chloride ions in the micropores as chemisorption sites for several metal pollutants.[71]Activation of BC with H_2O_2 increases the number of carboxylic, lactone, and hydroxyl group at the surface.[72] As an oxidizing agent, H_2O_2 can decompose the aromatic carbons of BC resulting in the formation of aliphatic carboxylic acids, CO_2, H_2 and H_2O. Release of these gaseous products lead to the increased porosity and surface area of BC.[72,73]

1.6.4.2 Metal/metal oxide impregnation

Metal, metal oxide, and metal hydroxide functionalized BC have been reported as promising candidates for removal of inorganic and organic pollutants. Large surface area, high porosity and surface functionalities of BC facilitate efficient metal impregnation. Generally metal oxide and metal hydroxide functionalized BC have a point of zero charge ≥ 10 suggesting that at

near neutral pH, the surface is positively charged[74] and has strong affinity for negatively charged pollutants. Metal-impregnated BC is usually prepared by two methods (i) loading metal salts by wet-impregnation of biomass followed by pyrolysis and (ii) homogeneous metal impregnation on BC using a solution of metal salts. In the first method, metal salt pre-loaded biomass is subjected to a high temperature thermal treatment and dehydration followed by decomposition of the metal salt, leaving the metal oxide on BC surface. MgO,[74] MnO,[75] NiO,[76] and Fe_3O_4/γ-Fe_2O_3[77,78] impregnated BC have been prepared using metal salts of $MgCl_2$. $6H_2O$, $MnCl_2$. $4H_2O$, $Ni(NO_3)_2$, and $FeCl_3$ for the removal of PO_4^{3-}, NO_3^-, AsO_4^{3-}. Ni-impregnation of BC was found to catalyze the cracking process and reactions of volatile compounds in the lignocellulosic matrix to increase the char yields.[76] In recent years, semiconductor metal oxide-BC composites have received increased attention because of their potential ability to mineralize toxic organic contaminants. Heterogeneous photocatalysts such as TiO_2, ZnO, and Fe_2O_3, doped with BC have been used for the degradation of organic pollutants into CO_2, H_2O and simple inorganic products.[49,79]

1.6.4.3 Organic functionalized-BC

Grafting of different organic reactive moieties onto the biochar surface can significantly improve BC sorption properties. Chitosan and chitin are abundant natural biopolymers available at low cost for the preparation of structurally stable environmentally friendly BC composites. The chitosan functional groups, $-NH_3^+$, -OH, $-CH_2COOH$, and $-CONH_2$ effectively and strongly interact with toxic metal ions and organic pollutants through coordinate, electrostatic, ion exchange and H-bonding. Chitosan/chitin-BC composites exhibit high sorption performances in the removal of Cd(II), Cr(VI), Pb(II) and pharmaceuticals from water.[80,81,82] Chitosan-modified BC are attractive candidates with high sorption capacity for herbicides and as a soil amendment.[83] C_3N_4-BC composites prepared by incorporating melamine on to BC followed by thermal treatment

at 300 ºC have shown both adsorption and photocatalytic activity on cationic, anionic and non-ionic organic contaminants.[84]

1.6.4.4 BC Characterization techniques

BC provides reactive surface sites for adsorption and catalytic degradation of pollutants and interactions with inorganic and organic pollutants are characterized using a range of analytical techniques. Various chemical, microscopic, and spectroscopic characterization techniques are available to elucidate the structural properties of BC and sorption mechanism between BC and pollutants. Surface morphology and elemental analysis of all materials are generally carried out by transmission electron microscopy (TEM) and scanning electron microscopy (SEM) facilitated with energy dispersive X-ray spectroscopy (EDX).[85] BET (Brunauer, Emmett, and Teller) surface area, pore volume, and pore size distribution of BC and modified BC are determined using a N_2 adsorption isotherm (at 77 K).[86]

The BC surface is composed of many chemical functional groups such as aliphatic, aromatic, hydroxyl, carboxyl, carbonyl, and amido groups which are the reactive sites that interact with pollutants. The surface functional groups and their interaction with pollutants are identified and monitored by Fourier transform infrared spectroscopy (FTIR),[87] X-ray photoelectron spectroscopy (XPS),[88] NMR spectroscopy also helps to identify surface functional groups, such as carboxyl, carbonyl, phenolic –OH, and ester groups.[89] Although X-ray diffraction (XRD) BC patterns are not well-defined, metal/metal oxide in BC composites and adsorbed toxic metals or metalloids on BC can be identified using XRD.[90] Boehm titration is frequently applied to characterize the acidic and basic functional groups on BC.[91] In this method, the BC is consecutively equilibrated in solutions of $NaHCO_3$, Na_2CO_3, and NaOH. The extract from each solution is

titrated with strong acid or base. Thermogravimetric analysis (TG) is widely employed to provide useful information on thermal stability of BC, biomass, and modified BC. [92]

1.7 Dissertation objectives

The overarching objective of this work was to develop cost-effective surface modification methods for Douglas Fir biochar for achieving high removal of selected potentially toxic metal ions and organic contaminants. The three chemical modification methods employed to prepare engineered biochar were (i) KOH treatment (ii) chemical oxidative polymerization of aniline on BC and (iii) Fe_2TiO_5 impregnation on BC. Each surface modified biochar was characterized and investigated for potential ability to remove Cr(VI), Cd(II), Pb(II), nitrate, fluoride, and methylene blue under various experimental conditions. Plausible sorption mechanisms were suggested.

1.8 References

1. Boretti, A.; Rosa, L., Reassessing the projections of the world water development report. *NPJ Clean Water* **2019,** *2* (1), 1-6.

2. Igor, S., World fresh water resources. *Water in crisis: a guide to the world's. Oxford University Press, Inc, Oxford* **1993**.

3. Häder, D.-P.; Banaszak, A. T.; Villafañe, V. E.; Narvarte, M. A.; González, R. A.; Helbling, E. W., Anthropogenic pollution of aquatic ecosystems: Emerging problems with global implications. *Science of the Total Environment* **2020,** *713*, 136586.

4. Larsen, I. J.; MacDonald, L. H.; Brown, E.; Rough, D.; Welsh, M. J.; Pietraszek, J. H.; Libohova, Z.; de Dios Benavides-Solorio, J.; Schaffrath, K., Causes of post-fire runoff and erosion: Water repellency, cover, or soil sealing? *Soil Science Society of America Journal* **2009,** *73* (4), 1393-1407.

5. Stewart, C.; Johnston, D.; Leonard, G.; Horwell, C.; Thordarson, T.; Cronin, S., Contamination of water supplies by volcanic ashfall: a literature review and simple impact modelling. *Journal of Volcanology and Geothermal Research* **2006,** *158* (3-4), 296-306.

6. Masuda, H., Arsenic cycling in the Earth's crust and hydrosphere: interaction between naturally occurring arsenic and human activities. *Progress in Earth and Planetary Science* **2018,** *5* (1), 1-11.

7. Yaseen, D.; Scholz, M., Textile dye wastewater characteristics and constituents of synthetic effluents: a critical review. *International Journal of Environmental Science and Technology* **2019,** *16* (2), 1193-1226.

8. Adamo, P.; Agrelli, D.; Zampella, M., Chemical speciation to assess bioavailability, bioaccessibility and geochemical forms of potentially toxic metals (PTMs) in polluted soils. In *Environmental Geochemistry*, Elsevier: 2018; pp 153-194.

9. Goel, G.; Kaur, S., A study on chemical contamination of water due to household laundry detergents. *Journal of Human Ecology* **2012,** *38* (1), 65-69.

10. Küster, A.; Adler, N., Pharmaceuticals in the environment: Scientific evidence of risks and its regulation. *Philosophical Transactions of the Royal Society B: Biological Sciences* **2014,** *369* (1656), 20130587.

11. Hassaan, M. A.; El Nemr, A., Pesticides pollution: Classifications, human health impact, extraction and treatment techniques. *The Egyptian Journal of Aquatic Research* **2020**.

12. Fawell, J.; Nieuwenhuijsen, M. J., Contaminants in drinking water, environmental pollution and health. *British Medical Bulletin* **2003,** *68* (1), 199-208.

13. Jaffrézic, A.; Jardé, E.; Soulier, A.; Carrera, L.; Marengue, E.; Cailleau, A.; Le Bot, B., Veterinary pharmaceutical contamination in mixed land use watersheds: from agricultural headwater to water monitoring watershed. *Science of the Total Environment* **2017,** *609*, 992-1000.

14. Serwecińska, L., Antimicrobials and Antibiotic-Resistant Bacteria: A Risk to the Environment and to Public Health. *Water* **2020,** *12* (12), 3313.

15. Koelmans, A. A.; Nor, N. H. M.; Hermsen, E.; Kooi, M.; Mintenig, S. M.; De France, J., Microplastics in freshwaters and drinking water: Critical review and assessment of data quality. *Water Research* **2019,** *155*, 410-422.

16. Coyle, R.; Hardiman, G.; O'Driscoll, K., Microplastics in the marine environment: A review of their sources, distribution processes, uptake and exchange in ecosystems. *Case Studies in Chemical and Environmental Engineering* **2020,** *2*, 100010.

17. Campanale, C.; Massarelli, C.; Savino, I.; Locaputo, V.; Uricchio, V. F., A detailed review study on potential effects of microplastics and additives of concern on human health. *International Journal of Environmental Research and Public Health* **2020,** *17* (4), 1212.

18. Jaishankar, M.; Tseten, T.; Anbalagan, N.; Mathew, B. B.; Beeregowda, K. N., Toxicity, mechanism and health effects of some heavy metals. *Interdisciplinary Toxicology* **2014,** *7* (2), 60-72.

19. Nicolopoulou-Stamati, P.; Maipas, S.; Kotampasi, C.; Stamatis, P.; Hens, L., Chemical pesticides and human health: the urgent need for a new concept in agriculture. *Frontiers in Public Health* **2016,** *4*, 148.

20. Lellis, B.; Fávaro-Polonio, C. Z.; Pamphile, J. A.; Polonio, J. C., Effects of textile dyes on health and the environment and bioremediation potential of living organisms. *Biotechnology Research and Innovation* **2019,** *3* (2), 275-290.

21. Gong, C.; Huang, H.; Qian, Y.; Zhang, Z.; Wu, H., Integrated electrocoagulation and membrane filtration for PAH removal from realistic industrial wastewater: effectiveness and mechanisms. *RSC Advances* **2017,** *7* (83), 52366-52374.

22. Singh, N.; Nagpal, G.; Agrawal, S., Water purification by using adsorbents: a review. *Environmental Technology & Innovation* **2018,** *11*, 187-240.

23. Levchuk, I.; Màrquez, J. J. R.; Sillanpää, M., Removal of natural organic matter (NOM) from water by ion exchange–a review. *Chemosphere* **2018,** *192*, 90-104.

24. Malaeb, L.; Ayoub, G. M., Reverse osmosis technology for water treatment: State of the art review. *Desalination* **2011,** *267* (1), 1-8.

25. Akhter, M.; Habib, G.; Qamar, S. U., Application of electrodialysis in waste water treatment and impact of fouling on process performance. *J Membr Sci Technol* **2018,** *8* (2), 1-8.

26. Deng, Y.; Zhao, R., Advanced oxidation processes (AOPs) in wastewater treatment. *Current Pollution Reports* **2015,** *1* (3), 167-176.

27. Särkkä, H.; Bhatnagar, A.; Sillanpää, M., Recent developments of electro-oxidation in water treatment—A review. *Journal of Electroanalytical Chemistry* **2015,** *754*, 46-56.

28. Prihod'ko, R. V.; Soboleva, N. M., Photocatalysis: oxidative processes in water treatment. *Journal of Chemistry* **2013,** *2013*.

29. Fontana, F., Encyclopedia of surface and colloid science. *Mem. Mat Soc Ital Sci* **1777,** *679*.

30. Jeirani, Z.; Niu, C. H.; Soltan, J., Adsorption of emerging pollutants on activated carbon. *Reviews in Chemical Engineering* **2017,** *33* (5), 491-522.

31. Liu, X.; Xu, X.; Dong, X.; Park, J., Competitive adsorption of heavy metal ions from aqueous solutions onto activated carbon and agricultural waste materials. *Polish Journal of Environmental Studies* **2020,** *29* (1), 749-761.

32. Manjuladevi, M.; Anitha, R.; Manonmani, S., Kinetic study on adsorption of Cr (VI), Ni (II), Cd (II) and Pb (II) ions from aqueous solutions using activated carbon prepared from Cucumis melo peel. *Applied Water Science* **2018,** *8* (1), 1-8.

33. Patel, H., Batch and continuous fixed bed adsorption of heavy metals removal using activated charcoal from neem (Azadirachta indica) leaf powder. *Scientific Reports* **2020,** *10* (1), 1-12.

34. Bohli, T.; Ouederni, A.; Fiol, N.; Villaescusa, I., Evaluation of an activated carbon from olive stones used as an adsorbent for heavy metal removal from aqueous phases. *Comptes Rendus Chimie* **2015,** *18* (1), 88-99.

35. Aziz, H. A.; Adlan, M. N.; Hui, C. S.; Zahari, M.; Hameed, B., Removal of Ni, Cd, Pb, Zn and colour from aqueous solution using potential low cost adsorbent. **2005**.

36. Martins, A.; Nunes, N., Adsorption of a textile dye on commercial activated carbon: a simple experiment to explore the role of surface chemistry and ionic strength. *Journal of Chemical Education* **2015,** *92* (1), 143-147.

37. Martın-Gullón, I.; Font, R., Dynamic pesticide removal with activated carbon fibers. *Water Research* **2001,** *35* (2), 516-520.

38. Uddin, M. K., A review on the adsorption of heavy metals by clay minerals, with special focus on the past decade. *Chemical Engineering Journal* **2017,** *308*, 438-462.

39. Kausar, A.; Iqbal, M.; Javed, A.; Aftab, K.; Bhatti, H. N.; Nouren, S., Dyes adsorption using clay and modified clay: a review. *Journal of Molecular Liquids* **2018,** *256*, 395-407.

40. Adeyemo, A. A.; Adeoye, I. O.; Bello, O. S., Adsorption of dyes using different types of clay: a review. *Applied Water Science* **2017,** *7* (2), 543-568.

41. Chargui, H.; Hajjaji, W.; Wouters, J.; Yans, J.; Jamoussi, F., Direct Orange 34 dye fixation by modified kaolin. *Clay Minerals* **2018,** *53* (2), 271-287.

42. Patel, A.; Loufakis, D.; Flouda, P.; George, I.; Shelton, C.; Harris, J.; Oka, S.; Lutkenhaus, J. L., Carbon Nanotube/Reduced Graphene Oxide/Aramid Nanofiber Structural Supercapacitors. *ACS Applied Energy Materials* **2020,** *3* (12), 11763-11771.

43. Shen, Y.; Fang, Q.; Chen, B., Environmental applications of three-dimensional graphene-based macrostructures: adsorption, transformation, and detection. *Environmental Science & Technology* **2015,** *49* (1), 67-84.

44. Lin, C.-C.; Lin, Y.-W., Synthesis of carbon nanotube/graphene composites by one-step chemical vapor deposition for electrodes of electrochemical capacitors. *Journal of Nanomaterials* **2015,** *2015*.

45. Bardi, N.; Giannakopoulou, T.; Vavouliotis, A.; Trapalis, C., Electrodeposited Films of Graphene, Carbon Nanotubes, and Their Mixtures for Supercapacitor Applications. *ACS Applied Nano Materials* **2020,** *3* (10), 10003-10013.

46. Zhou, C.-H.; Xia, X.; Lin, C.-X.; Tong, D.-S.; Beltramini, J., Catalytic conversion of lignocellulosic biomass to fine chemicals and fuels. *Chemical Society Reviews* **2011,** *40* (11), 5588-5617.

47. Welker, C. M.; Balasubramanian, V. K.; Petti, C.; Rai, K. M.; DeBolt, S.; Mendu, V., Engineering plant biomass lignin content and composition for biofuels and bioproducts. *Energies* **2015,** *8* (8), 7654-7676.

48. Marriott, P. E.; Gómez, L. D.; McQueen-Mason, S. J., Unlocking the potential of lignocellulosic biomass through plant science. *New Phytologist* **2016,** *209* (4), 1366-1381.

49. Mian, M. M.; Liu, G., Recent progress in biochar-supported photocatalysts: synthesis, role of biochar, and applications. *RSC Advances* **2018,** *8* (26), 14237-14248.

50. Enaime, G.; Bacaoui, A.; Yaacoubi, A.; Lübken, M., Biochar for wastewater treatment—conversion technologies and applications. *Applied Sciences* **2020,** *10* (10), 3492.

51. Nartey, O. D.; Zhao, B., Biochar preparation, characterization, and adsorptive capacity and its effect on bioavailability of contaminants: an overview. *Advances in Materials Science and Engineering* **2014,** *2014*.

52. Lu, L.; Yu, W.; Wang, Y.; Zhang, K.; Zhu, X.; Zhang, Y.; Wu, Y.; Ullah, H.; Xiao, X.; Chen, B., Application of biochar-based materials in environmental remediation: from multi-level structures to specific devices. *Biochar* **2020,** *2* (1), 1-31.

53. Liu, W.-J.; Jiang, H.; Yu, H.-Q., Development of biochar-based functional materials: toward a sustainable platform carbon material. *Chemical Reviews* **2015,** *115* (22), 12251-12285.

54. Sharma, S., Biochar for carbon sequestration: Bioengineering for sustainable environment. In *Omics Technologies and Bio-Engineering*, Elsevier: 2018; pp 365-385.

55. Ding, Y.; Liu, Y.; Liu, S.; Li, Z.; Tan, X.; Huang, X.; Zeng, G.; Zhou, L.; Zheng, B., Biochar to improve soil fertility. A review. *Agronomy for Sustainable Development* **2016,** *36* (2), 1-18.

56. Cheng, B.-H.; Zeng, R. J.; Jiang, H., Recent developments of post-modification of biochar for electrochemical energy storage. *Bioresource Technology* **2017,** *246*, 224-233.

57. Liu, W.-J.; Jiang, H.; Yu, H.-Q., Emerging applications of biochar-based materials for energy storage and conversion. *Energy & Environmental Science* **2019,** *12* (6), 1751-1779.

58. Zhang, Z.; Zhu, Z.; Shen, B.; Liu, L., Insights into biochar and hydrochar production and applications: a review. *Energy* **2019,** *171*, 581-598.

59. Choudhary, T. K.; Khan, K. S.; Hussain, Q.; Ahmad, M.; Ashfaq, M., Feedstock-induced changes in composition and stability of biochar derived from different agricultural wastes. *Arabian Journal of Geosciences* **2019,** *12* (19), 1-13.

60. Gholizadeh, M.; Hu, X.; Liu, Q., Progress of using biochar as a catalyst in thermal conversion of biomass. *Reviews in Chemical Engineering* **2019,** *1*.

61. Zhang, G.; Guo, X.; Zhu, Y.; Han, Z.; He, Q.; Zhang, F., Effect of biochar on the presence of nutrients and ryegrass growth in the soil from an abandoned indigenous coking site: the potential role of biochar in the revegetation of contaminated site. *Science of the Total Environment* **2017,** *601*, 469-477.

62. Pastor-Villegas, J.; Durán-Valle, C., Pore structure of activated carbons prepared by carbon dioxide and steam activation at different temperatures from extracted rockrose. *Carbon* **2002,** *40* (3), 397-402.

63. Azargohar, R.; Dalai, A., Steam and KOH activation of biochar: Experimental and modeling studies. *Microporous and Mesoporous Materials* **2008,** *110* (2-3), 413-421.

64. Armandi, M.; Bonelli, B.; Geobaldo, F.; Garrone, E., Nanoporous carbon materials obtained by sucrose carbonization in the presence of KOH. *Microporous and Mesoporous Materials* **2010,** *132* (3), 414-420.

65. Yang, K.; Peng, J.; Srinivasakannan, C.; Zhang, L.; Xia, H.; Duan, X., Preparation of high surface area activated carbon from coconut shells using microwave heating. *Bioresource Technology* **2010,** *101* (15), 6163-6169.

66. Wallace, C. A.; Afzal, M. T.; Saha, G. C., Effect of feedstock and microwave pyrolysis temperature on physio-chemical and nano-scale mechanical properties of biochar. *Bioresources and Bioprocessing* **2019,** *6* (1), 1-11.

67. Liou, T.-H.; Wu, S.-J., Characteristics of microporous/mesoporous carbons prepared from rice husk under base-and acid-treated conditions. *Journal of Hazardous Materials* **2009,** *171* (1-3), 693-703.

68. Wang, Z.; Li, J.; Zhang, G.; Zhi, Y.; Yang, D.; Lai, X.; Ren, T., Characterization of acid-aged biochar and its ammonium adsorption in an aqueous solution. *Materials* **2020,** *13* (10), 2270.

69. Sajjadi, B.; Zubatiuk, T.; Leszczynska, D.; Leszczynski, J.; Chen, W. Y., Chemical activation of biochar for energy and environmental applications: a comprehensive review. *Reviews in Chemical Engineering* **2019,** *35* (7), 777-815.

70. Gokce, Y.; Aktas, Z., Nitric acid modification of activated carbon produced from waste tea and adsorption of methylene blue and phenol. *Applied Surface Science* **2014,** *313*, 352-359.

71. Wang, T.; Wu, J.; Zhang, Y.; Liu, J.; Sui, Z.; Zhang, H.; Chen, W.-Y.; Norris, P.; Pan, W.-P., Increasing the chlorine active sites in the micropores of biochar for improved mercury adsorption. *Fuel* **2018,** *229*, 60-67.

72. Cibati, A.; Foereid, B.; Bissessur, A.; Hapca, S., Assessment of Miscanthus× giganteus derived biochar as copper and zinc adsorbent: study of the effect of pyrolysis temperature, pH and hydrogen peroxide modification. *Journal of Cleaner Production* **2017,** *162*, 1285-1296.

73. Xue, Y.; Gao, B.; Yao, Y.; Inyang, M.; Zhang, M.; Zimmerman, A. R.; Ro, K. S., Hydrogen peroxide modification enhances the ability of biochar (hydrochar) produced from hydrothermal carbonization of peanut hull to remove aqueous heavy metals: batch and column tests. *Chemical Engineering Journal* **2012,** *200*, 673-680.

74. Zhang, M.; Gao, B.; Yao, Y.; Xue, Y.; Inyang, M., Synthesis of porous MgO-biochar nanocomposites for removal of phosphate and nitrate from aqueous solutions. *Chemical Engineering Journal* **2012,** *210*, 26-32.

75. Wang, S.; Gao, B.; Li, Y.; Mosa, A.; Zimmerman, A. R.; Ma, L. Q.; Harris, W. G.; Migliaccio, K. W., Manganese oxide-modified biochars: preparation, characterization, and sorption of arsenate and lead. *Bioresource Technology* **2015,** *181*, 13-17.

76. Shen, Y.; Areeprasert, C.; Prabowo, B.; Takahashi, F.; Yoshikawa, K., Metal nickel nanoparticles in situ generated in rice husk char for catalytic reformation of tar and syngas from biomass pyrolytic gasification. *RSC Advances* **2014,** *4* (77), 40651-40664.

77. Reguyal, F.; Sarmah, A. K.; Gao, W., Synthesis of magnetic biochar from pine sawdust via oxidative hydrolysis of FeCl2 for the removal sulfamethoxazole from aqueous solution. *Journal of Hazardous Materials* **2017,** *321*, 868-878.

78. Yang, J.; Zhao, Y.; Ma, S.; Zhu, B.; Zhang, J.; Zheng, C., Mercury removal by magnetic biochar derived from simultaneous activation and magnetization of sawdust. *Environmental Science & Technology* **2016,** *50* (21), 12040-12047.

79. Mian, M. M.; Liu, G.; Yousaf, B.; Fu, B.; Ahmed, R.; Abbas, Q.; Munir, M. A. M.; Ruijia, L., One-step synthesis of N-doped metal/biochar composite using NH_3-ambiance pyrolysis for efficient degradation and mineralization of Methylene Blue. *Journal of Environmental Sciences* **2019,** *78*, 29-41.

80. Ahmed, M.; Hameed, B.; Hummadi, E., Review on recent progress in chitosan/chitin-carbonaceous material composites for the adsorption of water pollutants. *Carbohydrate Polymers* **2020**, 116690.

81. Liu, J.; Zhou, B.; Zhang, H.; Ma, J.; Mu, B.; Zhang, W., A novel Biochar modified by Chitosan-Fe/S for tetracycline adsorption and studies on site energy distribution. *Bioresource Technology* **2019,** *294*, 122152.

82. Zhang, L.; Tang, S.; He, F.; Liu, Y.; Mao, W.; Guan, Y., Highly efficient and selective capture of heavy metals by poly (acrylic acid) grafted chitosan and biochar composite for wastewater treatment. *Chemical Engineering Journal* **2019,** *378*, 122215.

83. Yavari, S.; Abualqumboz, M.; Sapari, N.; Hata-Suhaimi, H.-A.; Nik-Fuaad, N.-Z., Sorption of imazapic and imazapyr herbicides on chitosan-modified biochars. *International Journal of Environmental Science and Technology* **2020**, 1-10.

84. Pi, L.; Jiang, R.; Zhou, W.; Zhu, H.; Xiao, W.; Wang, D.; Mao, X., g-C_3N_4 modified biochar as an adsorptive and photocatalytic material for decontamination of aqueous organic pollutants. *Applied Surface Science* **2015,** *358*, 231-239.

85. Memon, J. R.; Memon, S. Q.; Bhanger, M.; Memon, G. Z.; El-Turki, A.; Allen, G. C., Characterization of banana peel by scanning electron microscopy and FT-IR spectroscopy and its use for cadmium removal. *Colloids and Surfaces B: Biointerfaces* **2008,** *66* (2), 260-265.

86. Naderi, M., Surface Area: Brunauer–Emmett–Teller (BET). In *Progress in filtration and separation*, Elsevier: 2015; pp 585-608.

87. Uchimiya, M.; Hiradate, S.; Antal Jr, M. J., Dissolved phosphorus speciation of flash carbonization, slow pyrolysis, and fast pyrolysis biochars. *ACS Sustainable Chemistry & Engineering* **2015,** *3* (7), 1642-1649.

88. Biino, G. G.; Gröning, P., Cleavage mechanism and surface chemical characterization of phengitic muscovite and muscovite as constrained by X-ray photoelectron spectroscopy. *Physics and Chemistry of Minerals* **1998,** *25* (2), 168-181.

89. Wong, J.; Webber, J.; Ogbonnaya, U., Characteristics of biochar porosity by NMR and study of ammonium ion adsorption. *Journal of Analytical and Applied Pyrolysis* **2019,** *143*, 104687.

90. Sharma, R.; Bisen, D.; Shukla, U.; Sharma, B., X-ray diffraction: a powerful method of characterizing nanomaterials. *Recent Research in Science and Technology* **2012,** *4* (8).

91. Boehm, H., Some aspects of the surface chemistry of carbon blacks and other carbons. *Carbon* **1994,** *32* (5), 759-769.

92. Yi, Q.; Qi, F.; Cheng, G.; Zhang, Y.; Xiao, B.; Hu, Z.; Liu, S.; Cai, H.; Xu, S., Thermogravimetric analysis of co-combustion of biomass and biochar. *Journal of Thermal Analysis and Calorimetry* **2013,** *112* (3), 1475-1479.

CHAPTER II

KOH-ACTIVATED HIGH SURFACE AREA DOUGLAS FIR BIOCHAR FOR ADSORBING AQUEOUS CHROMIUM(VI), LEAD(II) AND CADMIUM(II)

(Published in *Chemosphere* **2020**, 269, 128409)

2.1 Abstract

Biochar has become a popular research topic in sustainable chemistry for use both in agriculture and pollution abatement. To enhance aqueous Cr(VI), Pb(II) and Cd(II) removal efficiency, high surface area (535 m^2/g) byproduct Douglas fir biochar (DFBC) from commercial syn-gas production obtained by fast pyrolysis (900-1000 °C, 1-10 s), was subjected to a KOH activation. KOH-activated biochar (KOHBC) underwent a remarkable surface area increase to 1049 m^2/g and a three-fold increase in pore volume (BET analysis). Batch sorption studies on KOHBC verses pH revealed that the highest chromium, lead and cadmium removal capacities occurred at pH 2.0, 5.0 and 6.0, respectively. KOHBC exhibited much higher adsorption capacities than unactivated DFBC. Heavy metal loadings onto KOHBC were characterized by scanning electron microscopy, transmission electron microscopy and X-ray photoelectron spectroscopy. Sorption of Cr(VI), Pb(II) and Cd(II) all followed pseudo-second order kinetics and the Langmuir absorption model. The highest Langmuir adsorption capacities at the respective pH's of maximum adsorption were 140.0 $mg\,g^{-1}$ Pb(II), 127.2 $mg\,g^{-1}$ Cr(VI) and 29.0 $mg\,g^{-1}$ Cd(II). Metal ions spiked into natural and laboratory waste water systems exhibited high sorption capacities. Desorption

studies carried out using 0.1M HCl revealed that Pb(II) adsorption onto the KOHBC surface is reversible. Portions of Cd(II) and Cr(VI) adsorbed strongly onto KOHBC were unable to be desorbed by 0.1M HCl and 0.1M NaOH.

2.2 Introduction

Anthropogenic and natural water contamination represents a major environmental issue worldwide. Hazardous heavy metals and toxic organic products can cause adverse effects for human health and aquatic life. Toxic Cr(VI), As (III), Pb(II), Cd(II), Sb(V), Cu(II) at persistent low aqueous concentrations are detrimental.[1,2] Understanding surface adsorption chemistry is vital to develop contaminated water treatment technology which is an objective of this work.

Chromium, a common industrial waste from chrome plating, dyes and pigment manufacturing, leather and wood preservation, and the production of textiles pose serious health problems.[3] Chromium can exist as Cr(VI) or Cr(III) in the environment. Cr(VI) is more mobile and soluble in water than Cr(III). Cr(VI) is a known carcinogen and negatively affects the human respiratory system and kidnys.[4] The US Environment Protection Agency mandates that the maximum levels of chromium safely allowed in drinking water must not exceed 0.1ppm.[5]

Pb(II) and Cd(II) are widely distributed in the environment from both natural and anthropogenic activities such as mining, smelting, industrial processes, and water pipes, paints, fertilizers and pesticides.[6] Lead poisoning causes neurodegenerative, reproductive, cardiovascular, immunological and renal issues in humans.[7] Prolonged exposure to Cd(II) can cause cadmium-mediated oxidative stress, nephrotoxicity, reproductive toxicity, osteo toxicity and tumors.[8,9] Non-biodegradable heavy metals bioaccumulate through the food chain causing further amplification

of toxicity.[10,11] Therefore, implementing efficient remediation techniques is important for safe water production. Reverse osmosis and ion–exchange are not cost effective, while sedimentation, coagulation, and flocculation result in large quantities of metal oxy hydroxide sludges to be disposed of.[12,13] Heavy metals have been adsorbed by peat moss, peat moss-derived biochar,[14] graphene,[15] functionalized graphene oxide[16,17] or activated carbon.[18,19,20] However, activated carbon production is still expensive on a large scale. Peat has a characteristically low surface area and graphene is expensive. A promising, more economically sustainable alternative byproduct, biochar has emerged.[21]

Biochar, the product of biomass pyrolysis in a low or oxygen-free environment, has soil conditioning and carbon sequestration potential and adsorption capabilities.[21] It's surface functions (carboxylic acids, phenolic hydroxyls, lactones, quinone, carbonyls, ethers and condensed aromatic rings) provide adsorption sites for metals.[21] Biochar can also contain tiny silica, calcium carbonate, calcite, and sylvite mineral particles to aid in metal sorption through electrostatic reactions and ion exchange.[21] These generate negative surface charges at pH 7. However, ash components of biochar (Ca, Mg, Na and K hydroxides /oxides/ carbonates) are basic and protonate at pH 7, lowering metal ion adsorption. Biochar surface modifications by acid or base treatments have enhanced adsorptive properties.[22]

The feedstock type and pyrolysis temperature predominantly determine the biochar structure and pore surface functionality which mediate the efficient sorption of heavy metals or organic pollutants.[23] High temperature pyrolysis increases surface area and porosity. The acidic and basic properties of biochar are associated with phenolic hydroxyl, carboxylic and heterocyclic nitrogen bases in the organic phase (in addition to mineral phases). XPS and Boehm titration

analysis have confirmed a significant removal of surface oxygenated biochar functional groups at pyrolysis temperatures > 700 K. This lowers surface acidity and increases basic groups associated with ash. Higher pyrolysis temperatures generate lower O/C and H/C mass ratios, higher degrees of aromaticity and lower biochar polarity in contrast to biochar obtained at lower temperature.[24,25] Biochar modified by acid functions can improve heavy metal uptakes to comparable or better than those of commercial activated carbon.[26]

Biochar oxidation using H_2SO_4/HNO_3, $H_2SO_4/KMnO_4$, H_2SO_4/H_2O_2 and $(NH_4)_2S_2O_8$ increases the amount of acidic functional groups based on the type of oxidizing reagent and the treatment time.[26,27] XPS and FTIR analysis confirmed substantial increases in the amount of C=C, C=O, COOH and phenolic-OH groups on biochar surfaces after acid modification,[28] but decreases in surface area and pore volume have been a frequent drawback from oxidations.[26,29] Activation with KOH, K_2CO_3 NaOH or Na_2CO_3 remarkably improved pore size, surface area and surface basicity compared to that of heat-only treatments.[30] Alkaline treatment enlarges micropores to mesopores through carbon loss, providing channels for adsorbate transport and greater sorption capacities.[30]

A unique advantage of Douglas fir biochar is its low cost. This biochar is a byproduct of bio-syn gas production which supports the cost of its production. It is produced in large amounts by feeding 'green wet' wood into an updraft gasifier where rapid pyrolysis (~ 900-1000 °C for 1-10 s), causes both a steam explosion and a pyrolytic decomposition to char plus syn-gas formation to occur. This leads to a unique biochar morphology having a low material density, high surface area and large pore volumes. This morphology allows rapid liquid penetration which leads to faster adsorption kinetics and contributes to adsorption capacities. The commercial biochar we used in

this study has a higher surface area, (typically 500-700 m^2/g from this process) than many reported biochars. After KOH treatment, the resulting KOHBC surface area was significantly increased (~1049 m^2/g). The present work reports higher surface area, higher metal adsorption capacity and faster uptake kinetics (< 2 h) versus the KOH-activated biochar reported in the current literature.

DFBC and its KOH-activated form (KOHBC) were tested in different aqueous model systems to remove Cr(VI), Cd(II) and Pb(II). Common, natural water, matrix chemicals were added to our target analytes to represent real contaminated water. Real world water sample testing is important to give a clear view of material efficacy in environmental remediation. KOHBC was used to adsorb both toxic anionic metalloids and cations from aqueous phase.

2.3 Materials and methods

All chemicals used in this study were analytical grade from Sigma Aldrich and were used as received. All aqueous solutions were prepared with deionized water obtained from a Millipore-Q water system. pH values were measured using a Hanna HI 2211 pH meter.

2.3.1 Preparation of Douglas Fir biochar (DFBC) and its activation by KOH

Douglas fir green wood chips (3 inches) were introduced into an air-fed updraft gasifier with a 1- 10 s residence time at 900-1000 ^{0}C. The large biochar particles (~2 cm) produced were rinsed thoroughly several times with deionized water to remove impurities, fine particulates adhering to their surface and water soluble organic residues before drying at room temperature for 24 h. Dried particles were ground, sieved to obtain the DFBC particle sizes between 0.1-0.5 mm and stored in a closed container for further application. This DFBC has been used and characterized previously by our group as an adsorbent.[31,32,33] Potassium hydroxide, KOH (4.00 g) was dissolved

in distilled water (20 mL) and added into DFBC (1.00 g). This mixture was stirred for 1 h at room temperature and further heated in a muffle furnace at 700 ^{0}C for 1 h under N_2 at a heating rate of 10 ^{0}C min. The resulting activated biochar was cooled to room temperature under N_2, then washed with 0.1 M HCl and finally washed several times with distilled water to a neutral pH before oven drying at 80 ^{0}C for 24 h. The activated biochar was designated KOHBC.

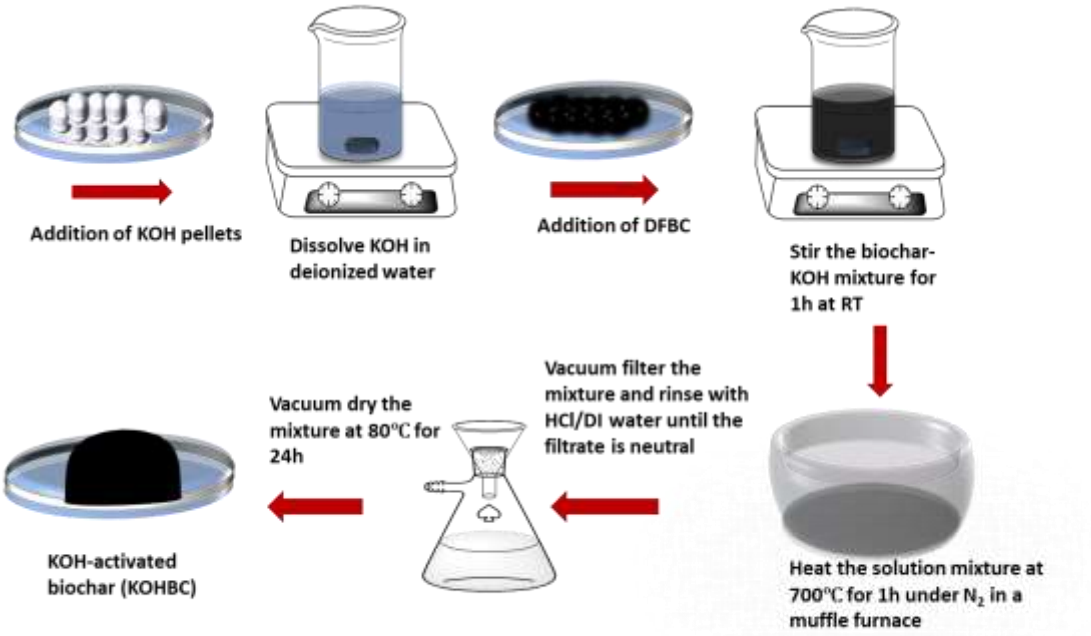

Scheme 2.1 Synthesis of KOH-activated biochar (KOHBC)

2.3.2 Characterization techniques

Biochar surface characterization was carried out by The Brunauer-Emmet-Teller (BET) surface area measurements, Scanning electron microscopy analysis (SEM), Transmission electron microscopy (TEM) and energy dispersive x-ray spectroscopy (EDS), Elemental analysis (ES),

Thermogravimetric analysis (TGA), X-ray photoelectron spectroscopy (XPS), and point of zero charge (PZC) determination. Procedures and instrumentation for characterization in detail are reported in supporting information.

2.3.3 Batch adsorption studies

Equilibrium adsorption studies of Pb(II), Cd(II), and Cr(VI) on DFBC and KOHBC were carried out to investigate the effect of solution pH, contact time and adsorbate concentration. Stock solutions of 1000 mg L^{-1} Cr (V1), Pb(II), and Cd(II) were prepared using $K_2Cr_2O_7$, $Pb(NO_3)_2$, and $Cd(NO_3)_2$ in deionized water. The desired concentrations in the range between 25 to 1000 mg L^{-1} were prepared by subsequent stock solution dilutions. The effect of pH on adsorption was studied in three replicates at pH values from 2 to 10 using 25.0 mL solutions containing 100 mg L^{-1} of each metal. The pH values were adjusted with aqueous 0.1M HCl and 0.1M NaOH. Effect of contact time on biochar adsorption was monitored by varying the equilibrium time for each analyte. Adsorption studies were carried out using 0.025 g of biochar with 25.00 mL of each adsorbate at different concentrations. All sample mixtures were sealed in plastic vials and shaken for 24 h to reach the equilibrium. After equilibration, the solutions were filtered (Whatman filter paper No.1) and the cadmium and lead concentrations remaining in each filtrate were measured by atomic absorption spectroscopy (AAS) (Shimadzu AA-7000). The residual Cr concentration was determined by double beam UV-Vis spectrophotometer at 350 nm. Standard errors were calculated using standard deviations for three replicates. The amount of adsorbate adsorbed per unit mass of biochar at equilibrium, Q_e (mg g^{-1}) was obtained from $Q_e = \frac{(C_i - C_e)V}{W}$ and used for adsorption isotherm analysis. Here C_i and C_e denote the initial and equilibrium concentration of

adsorbate in mg L^{-1}, V is the volume of adsorbate solution in mL and W is the weight of biochar in g.

Three adsorption and desorption cycles after adsorption of Cr(VI), Pb(II) and Cd(II) on to both KOHBC and DFBC were carried out. Initial adsorbate concentrations for Cr(VI), Pb(II) and Cd(II) were 100 mg L^{-1} at pH 2, 5 and 6 respectively. DFBC and KOHBC (0.20 g of each) were separately added to 200 mL of each adsorbate solution in a plastic bottle at 25 °C. They were shaken 1 h until reaching equilibrium. After sorption experiments were carried out, the residual biochar was washed several times with deionized water. Then desorption experiments were carried out using 0.1M HCl for Pb(II), Cd(II) and 0.1 M NaOH for Cr(VI) as stripping solvents.

2.3.4 Sorption analysis for Cr(VI), Pb(II) and Cd(II) spiked into natural and waste water samples

Removal of Cr(VI), Pb(II) and Cd(II) by DFBC and KOHBC was determined from authentic natural environment water samples and chemical laboratory waste water samples. Sanderson lake (Starkville, MS) water samples (pH 8.8) were filtered through Whatman filter paper (No. 1) to remove solid debris prior to the analysis. Cr(VI), Pb(II) 100 ppm of each and Cd(II) 20 ppm were spiked into these samples (25 mL) at room temperature. Experiments were conducted at the initial lake water pH of 8.8 and also at selected pH values of 2 for Cr(VI), 5 for Pb(II) and 6 for Cd(II). DFBC or KOHBC (25 mg) were individually equilibrated with water samples (25 mL) in plastic vials (50 mL) at a shaking speed of 200 rpm for Cr(VI) 2h, Pb(II) and Cd(II) 1 h. Samples were filtered and the residual aqueous metal ion concentrations were measured by UV-Vis spectrometer for Cr(VI) and atomic absorption spectroscopy (AAS) for Pb(II) and Cd(II). Competitive sorption studies were carried out by spiking nitrate, fluoride, phosphate,

chromate, cadmium and lead (1ppm of each in the final solution) into lake water samples adjusted to the above mentioned pH for Cr(VI), Pb(II) and Cd(II). These experiments were repeated with waste water containing traces of heavy metals and inorganics, collected from Mississippi State chemical laboratory. Pre-determined Cr(VI), Pb(II) and Cd(II) waste water concentrations of 10, 5 and 3 mg/L, respectively, were employed. Control experiments on DFBC and KOHBC were run in deionized water as the solvent. All experiments were performed in triplicate.

2.4 Results and Discussion

2.4.1 Characterization of DFBC and KOHBC

Brunauer-Emmett-Teller (BET) adsorption-desorption isotherms confirmed that chemical activation of DFBC by KOH at 700 ^{0}C significantly increased the surface area from 535 m^2/g in DFBC to 1050 m^2/g in KOHBC. Total pore volume rose from 0.249 to 0.672 cm^3/g and average pore diameters from 18.6 to 25.6 Å (Table 2.1). Activation proceeds by collapsing the carbon network through the transformation of KOH to K_2CO_3. The gaseous CO, CO_2, H_2O and H_2 species generated during activation exit the solid generating enlarged pore diameters, while an *in-situ* generated metallic K diffuses into the internal structure. KOH activation reactions are summarized by eq. 2.1- 2.4 given below.[34] Fig. 2.1. displays the DFBC and KOHBC surface morphologies. Upon activation of DFBC with KOH, the two morphologies showed no obvious changes despite the large mass loss ~60%. DFBC maintained its macroporous morphology, and its increase in pore diameter indicates that most of the mass loss from DFBC occurs from internal carbon loss as new micropores and ultra micropores form and existing pore diameters are enlarged or lengths

extended. The remarkable ~60% drop in overall weight and carbon wt.% and the large increase in ash wt.% confirms carbon loss upon activation (Table 2.1).

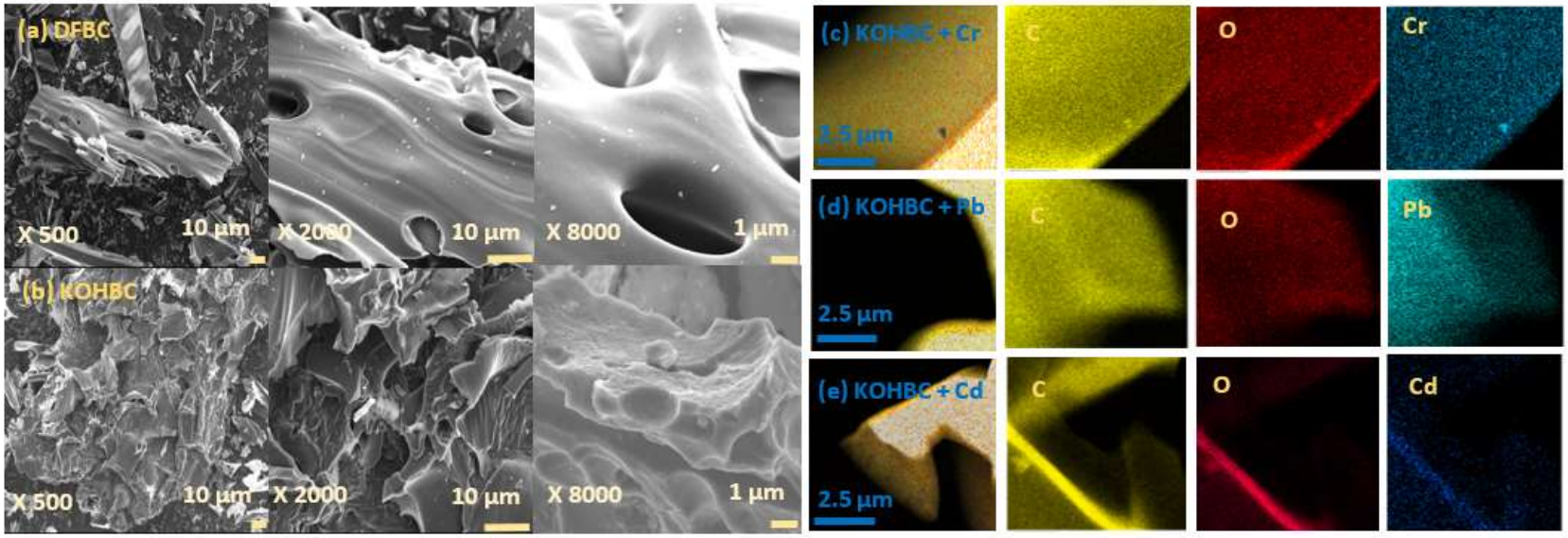

Figure 2.1 SEM images of *(*a) DFBC (b) KOHBC and TEM-EDX elemental mapping images on KOHBC after adsorption of (c) Cr, (d) Pb and (e) Cd

SEM and TEM images were obtained at the Institute of Imaging and Analytical Technologies (I^2AT), Mississippi State University.

The large increase in oxygen wt.% (Table 2.1) verifies that activated KOHBC has more oxygenated functional groups within its carbonaceous regions than DFBC per g, even when the KOHBC ash content also contains more oxygen than in DFBC. The ash content of DFBC comes from the oxides and carbonates of calcium, magnesium and potassium in the biomass.[35] The higher ash content (16.90%) of KOHBC is due to the oxides and carbonates of potassium. Chemical activation using KOH, H_3PO_4 or $ZnCl_2$ separately is more pronounced verses air, steam or CO_2 activation (eq. 2.5-2.7).[21,36] Lower activation temperatures are required for the former and the activation process is faster.[37] The chemical activation employed greatly influences the surface area, pore volume and pore structure of the biochar.

The original 900-1000 °C pyrolysis used to generate DFBC converted the organic substances into a more carbon rich high surface area (535 m^2/g) char feed for the KOH activation process. This pre-carbonization to form DFBC under nitrogen before activating with KOH also modified the pore size distribution. DFBC's morphology allowed KOH to easily contact substantial regions of DFBC before heating to 700 °C in the activation step. This KOH activation decreased the amount of carbon in the char. Potassium ions intercalated into the char during heating at 700 °C, widening existing pores and creating new pores. The 60% wt. loss during DFBC conversion into KOHBC occurs due to the carbon liberation as the micropores expanded into mesopores. The pore volume increase is due to widening of existing micropores into mesopores and generation of new micropores and ultra micropores. KOH chemically etches this dense carbon network to produce mesopores via equations 2.1-2.4. The decomposition rate becomes faster at high temperature, promoting the pore size increase.[38] Mass loss occurs via formation of CO_2, CO,

H_2O, and H_2. K_2CO_3 is also formed and left in the pores. Formation of metallic K and K_2CO_3 during the activation process acts to template macropores.[37,39]

$$C + 2KOH \rightarrow 2K + H_2 + CO_2 \quad (2.1)$$

$$C + 2KOH \rightarrow 2K + H_2O + CO \quad (2.2)$$

$$CO_2 + 2KOH \rightarrow K_2CO_3 + H_2O \quad (2.3)$$

$$K_2CO_3 + 2C \rightarrow 2K + 3CO \quad (2.4)$$

$$C + H_2O \rightarrow CO + H_2 \quad (2.5)$$

$$CO + H_2O \rightarrow CO_2 + H_2 \quad (2.6)$$

$$C + CO_2 \rightarrow 2CO \quad (2.7)$$

Table 2.1 Elemental composition and surface morphology parameters of DFBC and KOHBC[a]

Elemental content/ wt.%									S_{BET}[c]	V_T[c]	S[c]
	C	H	N	O[b]	H/C	O/C	(O+N)/C	Ash	(m^2/g)	(cm^3/g)	(A^0)
DFBC	80.36	2.00	0.97	13.78	0.02	0.17	0.18	2.89	535	0.249	18.6
KOHBC	52.21	2.63	0.28	27.98	0.05	0.53	0.54	16.90	1050	0.672	25.6

[a]C, H and N wt.% were obtained by combustion analysis using an elemental analyzer (EAI CE-440)

[b] The organic oxygen content was calculated by subtracting the wt.% of C, H, N and ash from the total wt.% (100 %) and doesn't include the O present as metal oxides in the ash. [c]S_{BET} stands for BET specific surface area; V_T for total pore volume; S for pore size of biochar prepared.

DFBC elemental analysis exhibits lower H/C and O/C mole ratios and polarity index (O+N)/C (Table 2.1) compared to biochars prepared at lower pyrolysis temperatures.[40,41] DFBC formation occurred at 900-1000 °C consistent with its low H/C ratio, which indicates it has a highly condensed aromatic system. This pyrolysis temperature induces more surface functional group cleavage and more complete destruction of aliphatic carbon regions, reforming the biochar into a more aromatic graphite-like structure. Therefore, the DFBC surface is less hydrophilic and more non-polar than many biochars. Upon KOH activation to generate KOHBC, a three-fold increase in H/C, O/C and polarity index (O+N)/C ratio occurred due to an increase in oxygenated functional group abundance compared to that of DFBC (Table 2.1). This increased surface oxidative functionalization is reflected in the XPS spectra.

2.4.2 Thermogravimetric analysis (TGA) of biochar

TGA of DFBC and KOHBC at 10 °C/min heating rate under air (Fig. 2.2(a).) showed two distinct weight loss regions. Minor weight loss at 40–90 ^{0}C, due to moisture removal. This was followed by a significant weight loss from 470-600 °C, with a maximum weight loss rate at 550 °C. Significant changes in surface functional groups begin to appear at about 400 °C. The highest

rate of weight change at around 550 ^{0}C is due to the oxidative degradation of the carbon skeleton. KOHBC gives a lower mass loss at 600 ºC than DFBC as more thermally stable solid formation occurs. KOHBC had ~30% wt. residue left compared to only ~3% for DFBC. This is due to the high ash content in KOHBC and formation of K_2CO_3 during chemical activation. K_2CO_3 decomposes at about 1300 ºC, well beyond the TGA temperature limit employed. TG analysis under nitrogen was conducted for DFBC and KOHBC (Fig. A.1) DFBC exhibited ~80% wt. loss at 1000 ºC, while KOHBC showed a higher thermal stability with a weight loss of only about 10% at 1000 ºC. A reference sample of K_2CO_3 heated to 1000 ºC exhibited almost no mass loss except a small loss of moisture (Fig. A.1). Thus, the K_2CO_3 formed in KOHBC during KOH activation does not thermally degrade up to 1000 ºC while the carbonaceous portion of KOHBC has about the same stability as that of DFBC. The amount of residue is greater above 650 ºC in KOHBC due to its greater, mostly K_2CO_3, ash content.

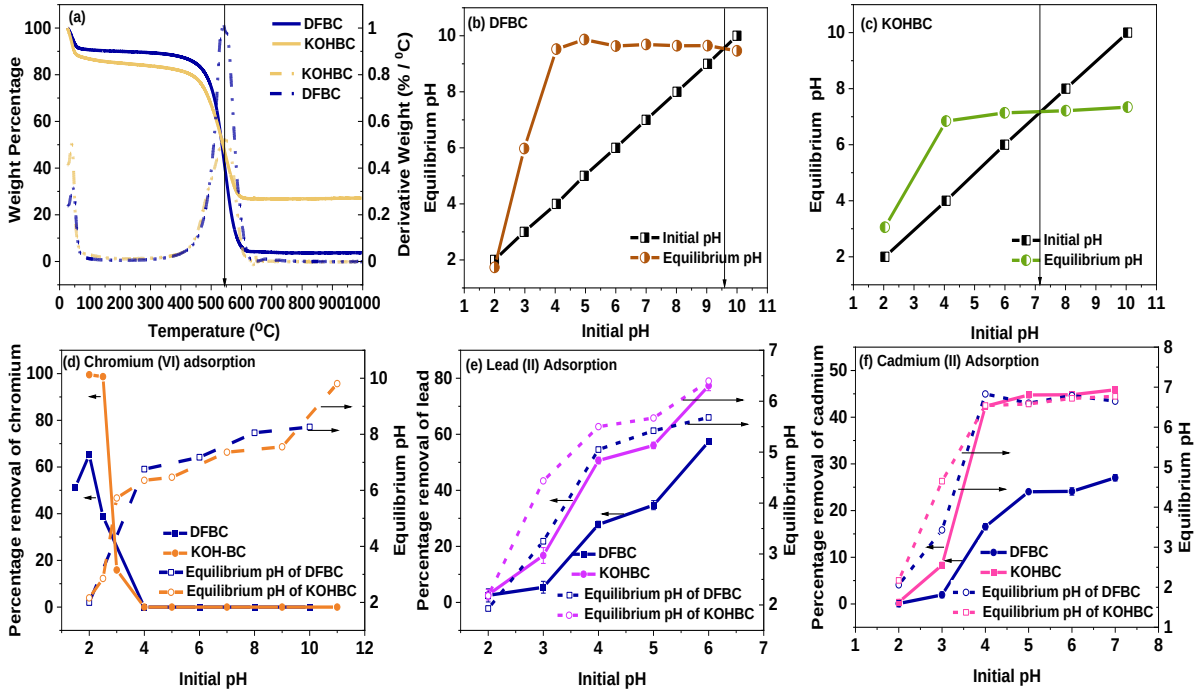

Figure 2.2 TGA and DTG curves for (a) DFBC, (b) KOHBC at a 10 ºC/min heating rate in air, PZC measurement for (c) DFBC, (d) KOHBC, Effect of solution pH on adsorption of Cr(VI), Pb(II) and Cd(II) onto DFBC and KOHBC (d) Cr(VI) 50 mg/L, (e) Pb(II) 300 mg/L and (f) Cd(II) 100 mg/L.

25 mL of aqueous analyte solution at 25 ºC with 25 mg of adsorbent doses used for each.

2.4.3 Point of zero charge measurement

The point of zero charge (PZC) is the solution pH where surface net electrical charge is zero. PZC is 9.6 for DFBC and 7.2 for KOHBC (Fig. 2.2(b),(c)). DFBC's higher PZC indicates that basic groups dominate on its surface and is consistent with its higher pyrolysis temperature leading to a higher PZC. In a solution pH below 9.6 the DFBC surface is net positively charged helping attract anionic sorbents. At a solution pH above 9.6, DFBC's surface has a net negative charge, facilitating metal cation sorption. KOHBC's PZC is 7.2, suggesting both toxic metal anions and cations would not be repelled at slightly acidic or basic pH values.

2.4.4 Effect of solution pH on Cr(VI), Pb(II) and Cd(II) sorption

The adsorption of Cr(VI), Pb(II) and Cd(II) ions was highly pH dependent (Fig. 2.2) as expected. Cr(V1) is present in solution as oxyanions. Hydrogen chromate ($HCrO_4^-$) predominates in a solution at pH 1-6 and chromate (CrO_4^{2-}) at pH > 6. Cr(VI) is only adsorbed on DFBC or KOHBC surfaces at pH < 4 due to negatively charged adsorbent surfaces repelling ($HCrO_4^-$) and (CrO_4^{2-}) anions. Between pH 4 and 11 neither adsorbent removes Cr(VI). Cr(VI) is readily adsorbed on both biochars at pH 1.0-2.5 but uptake falls significantly at pH 3 (Fig. 2.4a). At pH < 1, Cr(V1) is present as chromic acid (H_2CrO_4). At high concentrations (>1 g/L), $HCrO_4^-$ dimerizes to form dichromate ($Cr_2O_7^{2-}$).[42] Batch sorption studies were not performed at pH < 1. The highest Cr(VI) removal capacity (98%) by KOHBC was observed at pH 2.0 and 2.5 compared to 52% and 65% removal from DFBC. Thus, a pH of 2 was selected for all subsequent Cr(V1) adsorption experiments. UV absorption spectra for Cr(VI) remaining in solutions with DFBC and KOHBC shown in (Fig. A.2).

Pb(II) and Cd(II) sorption on both DFBC and KOHBC rose continuously as solution pH increased. This rise occurred at pH 2 to 6 for Pb(II) and 2 to 7 for Cd(II) (Fig. 2(e) and (f)). Pb(II) and Cd(II) exist as free hydrated ions between pH 2-5. Upon a further pH rise, Pb and Cd ions can begin to precipitate as hydroxides. $Pb(OH)_2$ ($Ksp = 5.00\times10^{-16}$ at 298 K) starts precipitation at pH 5.5 and $Cd(OH)_2$ ($Ksp = 4.00\times10^{-15}$ at 298 K) begins to slowly precipitate at pH 6.5. The predominant Pb(II) species in aqueous medium are Pb(II) ions at pH <6, $Pb(OH)^+$ and $Pb(OH)_2$ at pH = 6–12 and $Pb(OH)_2^{-4}$ at pH>12.[43] Thus, Pb(II) and Cd(II) adsorption can't be specifically studied above pH 6 and 7, respectively, without competiting precipitation. In all cases, KOHBC exhibited higher sorption capacities than DFBC. DFBC and KOHBC are both net positively

charged in the pH ranges that sorption was studied (2-6 for Pb(II) and 2-7 for Cd(II)) where electrostatic repulsion exists towards Pb(II) and Cd(II). Thus, Pb(II) and Cd(II) adsorption is due to a complexation mechanism to surface groups. This overcomes the decreasing electrostatic repulsions as solution pH rises. The amount of lead and cadmium removal was substantially greater than that of Cr(VI) above pH 3. At low pH, from 2 to 3, Pb(II) and Cd(II) uptake is very low.

2.4.5 X-ray photoelectron spectroscopy (XPS) characterization

XPS analysis of DFBC, KOHBC and KOHBC with adsorbed Cr(VI), Pb(II) or Cd(II) was carried out to achieve a more surface-specific quantitative analysis of atomic ratios, adsorbent surface functions, and the oxidation states of the adsorbed metal. HR-XPS of DFBC and KOHBC gave surface region atomic percentages of C (92.7, 49.8) and O (7.2, 38.6) (Table A.1, A.2), respectively, illustrating that KOH activation generated far more oxygen-containing surface functions. After Cr(VI), Pb(II) and Cd(II) uptake at solution pH values of 2, 5, and 6 respectively, the metal ion surface atomic percentages for KOHBC determined by HR-XPS were 1.82 % Cr(VI), 0.36 % Pb(II), and 0.24 % Cd(II).

The C1s peak of DFBC before adsorption was deconvoluted into four peaks corresponding to well defined carbon oxidation state binding energies (BE). These appeared at 284.57, 285.60, 286.57 and 288.14 eV due to C-H/C=C, C-O-C/C-OH, C=O and HO-C=O/ C-O-C=O respectively (Fig. 2.3(a)).These peak assignments are in agreement with the literature.[44,45,46] The deconvoluted C 1s peaks for KOHBC had a greater contribution from higher binding energy peaks. This agrees with KOHBC having a greater fraction of oxidized surface region carbons and with the XPS-

determined carbon and oxygen atomic percentages of 92.7 and 7.2 for DFBC vs. 49.8 and 38.6 after KOH activation for KOHBC.

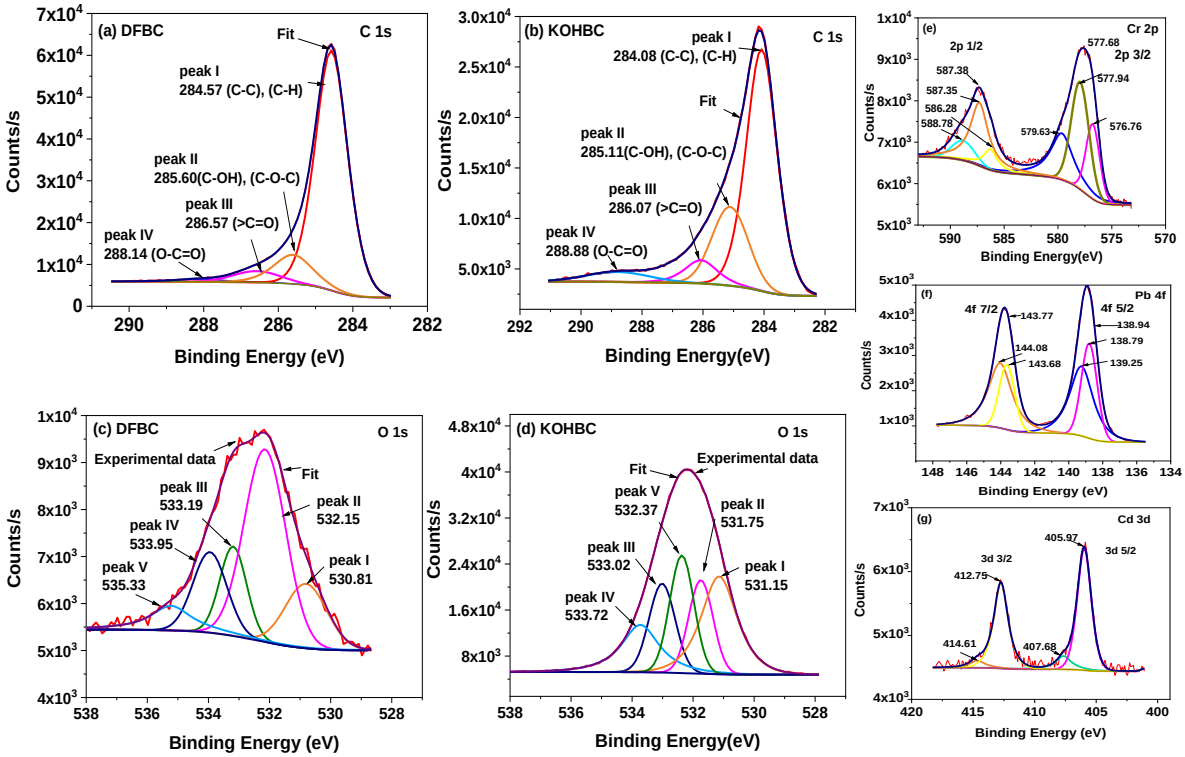

Figure 2.3 Deconvoluted C1s HR-XPS spectra of (a) DFBC and (b) KOHBC, Deconvoluted O1s HR-XPS spectra of (c) DFBC and (d) KOHBC and deconvoluted HR-XPS spectra of (e) Cr(VI), (f) Pb(II) and (g) Cd(II) loaded on KOHBC

Deconvolution of O1s peaks for DFBC and KOHBC resulted five peaks for both adsorbents. DFBC exhibited a dominant peak at 532.15 eV assigned to R_3C-O and other peaks at 530.81 eV, 533.19 eV, 533.95 eV and 535.33 eV (Fig. 2.3). attributed to aromatic C=O, C-OH,

C=O/O- C=O/CO_3^{2-}, and chemisorbed water molecules respectively.[47] These same five peaks were observed for KOHBC at deconvoluted energies of 531.15, 531.75, 532.37, 533.02 and 533.72 eV. The absolute atomic oxygen percentages (given by the counts/s) confirm that every O1s peak in KOHBC is present in greater abundance than that of DFBC. KOH activation greatly enhanced the amount of surface oxygen-containing functions.

2.4.6 Sorption of Cr(VI) onto KOHBC

TEM EDX elemental mapping images obtained for Cr-loaded KOHBC confirm Cr adsorption occurred as well as the presence of C and O (Fig.2.1(c)). TEM-EDX elemental mapping on DFBC and KOHBC before adsorption of Cr, Pb or Cd are shown in supporting information (Fig. A.3) along with the EDX elemental compositions (by wt.%) after Cr, Pb or Cd adsorption (Fig.S4). HR-XPS Cr 2p, Pb 4f and Cd 3d spectra also probed heavy metal adsorption onto the KOHBC (Fig. 2.3(e-g)). Chromium adsorption was confirmed by the Cr 2p doublets observed (Fig. 2.3(e)). The survey spectrum used to identify the elements present on the biochar is shown in supporting information (Fig. A.5).

The high resolution XPS Cr 2p energy level spectrum of KOHBC consists of two broad experimental peaks, one for Cr $2p_{3/2}$ and one for Cr $2p_{1/2}$ at binding energies centered at 577.68 eV and 587.38 eV, respectively (Fig. 3(e)). Deconvolution of the Cr $2p_{3/2}$ peak produced peaks at binding energies of 576.76, 577.94 and 579.63 eV, the first of which is characteristic of Cr(III) and the last for Cr(VI), respectively. Cr(III) is assigned based on the known binding energies of Cr_2O_3 (576.76 eV), $Cr(OH)_3$ (577.94 eV), and sorbed Cr(VI) is assigned based on CrO_3 and $HCrO_4^-$ (579.63 eV), coexisting on the surface. These binding energies are in good agreement with

previous assignments.[48,49,50] The Cr(VI) to Cr(III) ratio on the KOHBC adsorbent surface, based on peak area ratios, was 10/3. Cr(VI) to Cr(III) reduction occurs as Cr(VI) oxidation of organic functional groups occurs during adsorption.[47]

The high resolution C 1s and O 1s peak BEs on KOHBC shifted to higher BEs and atomic percentages after Cr(VI) adsorption. The observation of larger atomic percentages of oxidized carbon and more oxygen establishes that Cr(VI) adsorption occurs with further KOHBC surface oxidation. C 1s peaks of KOHBC at BEs and atomic percentages of (284.08 eV, 32.2%), (C -C, C-H) and (285.11 eV, 11.6%), (C-OH, C-O-C) shifted to (284.79, 43.4%), (285.85 eV, 16.7%), respectively, after Cr(VI) uptake. O 1s BEs and atomic percentages on KOHBC at (532.37 eV, 8.7%), (C-OH) has shifted to (532.53 eV, 4.6%) upon chemisorption of Cr(VI) onto the biochar surface. O1s peak at (533.02 eV, 7.6%), (C=O/O-C=O) has shifted to a higher BE and a higher atomic percentage of (533.41 eV, 9.6%) upon the reduction of Cr(VI) in to Cr(III). The presence of Cr(III) and Cr(VI) as $HCrO_4^-$ on the KOHBC surface was also confirmed by the deconvolution of the Cr $2p_{1/2}$ peak at 587.38 eV. This produced peaks at BEs of 586.28 and 588.78 eV, which matched the reported Cr $2p_{1/2}$ values of Cr(III) in Cr_2O_3 and Cr(VI) in $HCrO_4^-$.[51,52] Cr $2p_{3/2}$ and Cr $2p_{1/2}$ HR-XPS spectra definitively proved that Cr(VI) adsorbed on KOHBC along with some less toxic Cr(III) which was formed by Cr(VI) reduction.[44,53,54] After Cr(VI) uptake, the O 1s peak appearing at 530.96 eV was confirmed as (Cr-O), previously identified as chromium oxide (Cr_2O_3).[55,56]

Cr(VI) adsorption by biochars at pH 2.0 can be interpreted to occur by two main mechanisms.[57] (I) Direct electrostatic attractions occur between positively charged biochar surface sites and negatively charged chromium oxyanions. Surface protonated hydroxyl groups ($-O^+H_2$)

then chemisorb to Cr(VI), displacing water, resulting in surface C-$OCrO_3H^-$ or C-$OCrO_3^{2-}$ functions (eg Cr(VI)). (II) Reduction of Cr(VI) to Cr(III) occurs by oxidation of biochar surface groups at carbon via water-mediated transfer of H^+. These two processes are represented in Scheme 2.1(a) and (b), respectively. Formation of Cr(III) species probably occurs at the surface (not in the solution) during reduction of biochar oxygen-containing functional groups,[53,58]

Spectrophotometric studies were performed on the equilibrated filtrate after adsorption for the detection and quantification of Cr(III) indirectly using 1,5-diphenylcarbazide (DPC) as a complexing and color developing reagent for Cr(VI) formed once Cr(III) has been completely oxidized to Cr(VI) using $KMnO_4$.[59] This confirmed the formation of Cr(III) occurred upon Cr(VI) sorption onto KOHBC (Fig. A.6). The adsorption capacity calculated for 100 mg/L of Cr(VI) solution was 63 mg/g. After oxidizing the filtrate with $KMnO_4$, the calculated capacity was 66 mg/g. According to these results, the amount of Cr(III) oxidized was around 3 mg/g. Thus ~5% of the Cr(VI) adsorbed was converted to Cr(III). Since this reduction probably occurs at the surface, the amount of Cr(III) detected in the filtrate was very low. Furthermore, no Cr(II) was ever detected in solution by UV at 245, 290 nm.[60,61]

At pH 2.0, KOHBC could interact with $HCrO_4^-$ as shown in Scheme 2.1(a) depicting a simple electrostatic interaction of a protonated surface oxygen on KOHBC with $HCrO_4^-$. Protonated KOHBC transfers a proton to $HCrO_4^-$ and then the surface hydroxyl group initiates a nucleophilic attack on Cr(VI) to form a chemisorbed product. This is followed by loss of water from Cr(VI).The reduction of Cr(VI) to Cr(III) shown in (Scheme 2.1(b)) is well known mechanistically in solution and is expected to proceed similarly on biochar surfaces. First Cr(VI) is reduced to Cr(IV) as shown in Scheme 2.1(b). However, the formation of Cr(III) cannot occur

directly from Cr(VI) by a three electron reduction. Most likely this occurs by disproportionation reactions between two Cr(IV) species to Cr(III) and Cr(V) or possibly other reactions between Cr species. It was not possible to probe these possibilities on biochar surfaces. Homogeneous reactions between Cr(VI) and organic substrate hydroxyl groups in acidic media begin with the formation of chromate intermediates.[62] Kinetic analysis and spectroscopy data have found chromate intermediates break apart to give very reactive Cr(IV) and Cr(V) species in different pathways prior reduction to Cr(III) in oxygenated media.[62]

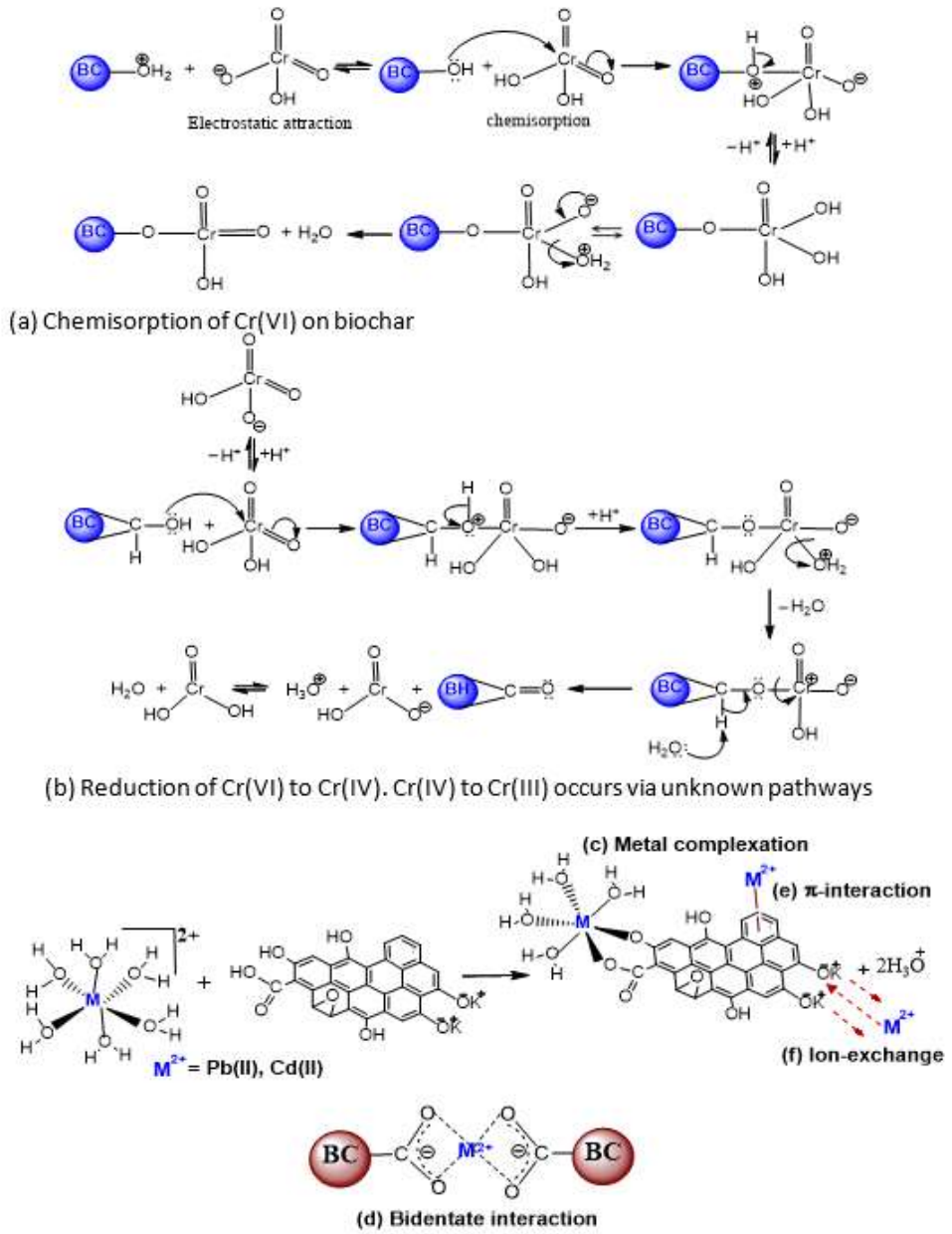

Scheme 2.2 Schematic representation of the reaction mechanism involved in (a) chemisorption of Cr(VI) onto biochar (b) reduction of Cr(VI) into Cr(IV) on model biochar surface and illustration of different types of adsorbed Pb(II) and Cd(II) species which could form on KOHBC during adsorption

Homogeneous reduction of Cr(VI) into Cr(III) is well known, but the mechanism of Cr(VI) reduction on solid char surfaces is not established. Several authors have demonstrated the reduction of Cr(VI) on magnetite and ilmenite through a direct heterogeneous electron exchange between structural Fe atoms and aqueous transition metals at the oxide/solution interface.[63] Reduction studies of Cr(VI) on multiwalled carbon nanotubes (MWCNT)[64] and sulfonated magnetic graphene oxide[65] suggest that $HCrO_4^-$ ions are immobilized first onto -OH, -COOH surface sites on the adsorbent and subsequently reduced to Cr(III) on the surface. Biochar hydroxyl groups and π-electron rich regions on the solid adsorbent can act as electron-donors to the metal center. Model biochar oxygen functionalities can be monodentate or bidentate ligands as in Scheme 2.1.

Biochar surfaces are generally occupied by alcohols, phenols and polyphenol groups which could be oxidized to carbonyl and quinoid moieties by strong oxidizing hexavalent chromium in acidic media. Thermodynamic feasibility of this redox process is mainly determined by the redox potential of biochar functional groups and the redox potential, $E_{(HCrO_4^-/Cr^{3+})}$, of the (Cr^{6+}/Cr^{3+}) system which is determined by the solution pH. For a favorable surface functional group oxidation, the (Cr^{6+}/Cr^{3+}) redox potential should be more positive than that of biochar. The redox potentials of biochar's many functional groups are specifically unknown but the redox potential of $E_{(HCrO_4^-/Cr^{3+})}$ at a given pH is determined using the Nernst equation $E_{(HCrO_4^-/Cr^{3+})} = E^{\theta}_{(HCrO_4^-/Cr^{3+})} + \frac{0.059}{3}\log\frac{[HCrO_4^-]}{[Cr^{3+}]} - 7\frac{0.059}{3}\text{pH}$. At higher (Cr^{6+}/Cr^{3+}) ratios, and lower pH values, the $E_{(HCrO_4^-/Cr^{3+})}$ system has a higher redox potential and a stronger ability to oxidize biochar. Therefore, biochar oxidation is increasingly favored at progressively lower pH. The pH

has the dominant role in determining the $HCrO_4^-/Cr^{3+}$ redox potential for biomass oxidation, not the (Cr^{6+}/Cr^{3+}) ratio.[66,67]

2.4.7 Sorption of Pb(II) and Cd(II) onto KOHBC

The TEM-EDX elemental mapping of KOHBC after Pb(II) adsorption (Fig. A.4) gives the elemental surface abundances by wt.% of C (78.7%), Pb (16.4%) and O (4.8%). The high resolution Pb 4f XPS spectrum (Fig. 2.3(f)) of KOHBC after Pb(II) uptake exhibited a doublet due to the spin orbital splitting of the 4f levels into $4f_{7/2}$ and $4f_{5/2}$ contributions. This resulted in binding energies of 138.94 and 143.77 eV, respectively. Deconvolution resolved the Pb $4f_{7/2}$ energy level at 138.94 eV into peak at 138.79 eV, which matches the Pb(II) eV value for PbO.[68,69] Above pH 5.5, uptake of Pb^{2+} increased because some $Pb(OH)_2$ precipitates. Therefore, the optimum pH for studying Pb(II) sorption of Pb^{2+} was restricted to 5.

TEM-EDX elemental mapping of KOHBC after Cd(II) sorption (Fig. A.4) gives a surface elemental analysis atomic wt.% of C (87.1%), O (8.6%) and Cd (4.2%). Cd adsorption onto KOHBC was analyzed by its high resolution Cd 3d XPS spectrum (Fig. 2.3(g)). A Cd 3d doublet due to spin orbit coupling occurred at 405.97 eV($3d_{5/2}$) and 412.75 eV($3d_{3/2}$) binding energies. These are close to those reported for the Cd(II) oxidation in the model compounds $Cd(OH)_2$[70] and CdO,[71] respectively. The pH values at which the sorption of Pb (5.0) and Cd (6.0) were carried out are both below the PZC of KOHBC (7.2). Thus, sorption occurred despite net electrostatic repulsions of Cd(II) with the KOHBC surface that is net positively charged at pH 6. Surface hydroxyl and keto functions are present (-COOH, -OH, >C=O) which generate complexes with Cd(II). Ash content from combustion analysis (16.9 wt.%) indicates substantial K^+ and Ca^{2+} ions

are present in basic inorganic phases and organic functions which can be exchanged for Pb^{2+} and Cd^{2+}. Therefore, ion exchange plays a role in Cd(II) and Pb(II) removal. Recent literature revealed ion exchange accounts for around 40% of Cd(II), Pb(II), Cu(II) and Ni(II) uptake on biochars, as quantified by the amount of K^+ and Ca^{2+} released.[72,73] The ion exchange onto KOHBC is more pronounced with K^+ ions which is the major metal cation present after KOH activation. K^+ cannot be tightly held by surface oxygen functionalities and is more easily exchanged. Bis-carboxylate chelates, $(RCO_2)_2M$ of Ca(II), Cd(II) and Pb(II) are readily formed with their water solubilities greatly decreasing in this order. Thus Pb(II) is strongly adsorbed by carboxylic acid-rich surfaces via carboxylate complexation. However, most K^+ had already been removed from KOHBC after the activation step during neutralization with HCl followed by washing with water.

KOHBC did not release significant amounts of contaminants into aqueous solution. In preliminary experiments on solutions equilibrated with solid KOHBC, AAS measurements confirmed that no toxic metal ions (Cr(VI), Pb(II), Cd(II)) were detected as leaching from the biochar. Trace amounts of nontoxic organic compounds, and Ca(II), Mg(II), and K(I) ions initially present in the biochar could leach into aqueous solutions over time.

Furthermore, the 700 °C pyrolysis during activation would destroy most -COOH functions. Therefore, exchange of K^+ ions by ion exchange for Pb(II) and Cd(II) sorption is reduced in this study. Positively charged Ca(II) and Mg(II), coordinated to biochar surface functionalities that survived acid washing could contribute to exchange with Pb(II) and Cd(II) ions (Scheme 2.1). The higher polynuclear aromatic character of KOHBC and DFBC that was produced at high temperature has π-electron donors sites, known to sorb heavy metal cations (Scheme 2.1).[74] This is increased when electron-donating phenolic hydroxyl groups or ether oxygens are aromatic ring

substituents in these regions. Depending on the availability of favorable steric conditions, the adjacent carboxylic groups could form stable dicarboxylate complexes with Cd(II) or Pb(II) (complex d in Scheme 1). Pb(II) ions have a lower water hydration free energy (1425 kJ mol^{-1}) than that of Cd(II) (1755 kJ mol^{-1})[75] despite the small difference in their ionic radii (Pb(II) 0.119 nm versus Cd(II) 0.095 nm). This could thermodynamically favor removal of Pb(II) from water by KOHBC versus Cd(II).

2.4.8 Adsorption kinetics

Fast adsorption rates are valuable to permit adsorption columns to operate at high flow rates. Batch removal rates of aqueous Pb(II), Cd(II), and Cr(VI) by KOHBC are depicted in Fig. A.7. Fast adsorption of all three adsorbates occurred on KOHBC and DFBC within 1 h except for Cd(II) adsorption on DFBC which proceeded somewhat more slowly. High adsorption rates in the first 1h suggests easy availability of sufficient surface adsorption sites. Pb and Cd have nearly the same magnitude of electric charge but Pb(II) adsorbed nearly five times faster than Cd(II). The lower Pb(II) enthalpy of hydration enhanced its chemisorption rate verses that of Cd(II). Pb(II)'s larger ionic radius lowers surface charge density, lowering its free energy of hydration to below that of Cd(II). Therefore, Pb(II) ions are released more easily than Cd(II) ions from their hydration spheres for complexation with biochar functional groups. These factors if operating in the transition states for complexation, could contribute to faster Pb(II) adsorption onto KOHBC. The amount of Cr(VI) adsorbed increased with increasing contact time and reached equilibrium after 2h. The Pseudo-second-order kinetic model (eq. 2.8 and 2.9) best fit the experimental data for

Cr(VI), Pb(II) and Cd(II) adsorption, with linear regression coefficients (R^2) closer to unity for both DFBC and KOHBC than those of the pseudo first order kinetic model (Table A.2).

$$\frac{dq_t}{d_t} = k_2(q_e - q_t)^2 \tag{2.8}$$

$$\frac{t}{q_t} = \frac{t}{qe} + \frac{1}{k_2 q_e^2} \tag{2.9}$$

2.4.9 Adsorption isotherm studies

Langmuir[76] and Freundlich[77] isotherm models for Cr(VI), Pb(II), and Cd(II) were fitted using experimental equilibrium data obtained at 298, 308, and 318 K on both KOHBC (Fig. A.8) and DFBC (Fig. A.9 and A.10). Cr(VI) batch sorption studies employed concentrations from 10 to 300 ppm and 120 min equilibration periods, while 10-1000 ppm of Pb(II), Cd(II) were equilibrated for 60 min. The Langmuir model (eq. 2.10) assumes a monolayer formation at a finite number of surface adsorption sites and no interaction among adsorbed entities.[76]

$$\frac{C_e}{Q_e} = \frac{1}{Q_m b} + \frac{C_e}{Q_m} \qquad q_e = \frac{Q^0 b C_e}{1 + b C_e} \tag{2.10}$$

Here C_e (mg L^{-1}) is the equilibrium concentration and Q_e denotes the amount adsorbed (mg g^{-1}) at the equilibrium concentration. Q_m is the maximum amount adsorbed (mg g^{-1}). The Langmuir constant, b, is related to net adsorption enthalpy and the affinity of binding sites. The linear Freundlich model equation (eq. 2.11) assumes the surface has binding sites of varying affinities and multilayer surface coverage can occur, where k_f and n are the adsorption capacity constant and adsorption intensity, respectively.

$$\ln Q_e = \ln k_f + \frac{1}{n}\ln C_e \qquad q_e = K_f C_e^{1/n} \tag{2.11}$$

All isotherm data were fitted to Langmuir and Freundlich models by nonlinear regression using Origin Pro 2019 software. All analytes had a greater adsorption capacity on KOHBC than DFBC due to the higher surface concentration of oxygen containing groups and greater surface area of KOHBC.

Langmuir and Freundlich adsorption isotherm parameters are tabulated in Table 2.3. Cr (VI) exhibits the highest Langmuir adsorption capacities of 127.2 and 33.5 mgg^{-1} at 318 K on KOHBC and DFBC, respectively. Adsorption data for Cr(VI) fitted better using the Freundlich isotherm model on DFBC and KOHBC at 308 and 318K with linear regression coefficients, R^2 greater than 0.99. The Cr(VI) capacity on DFBC and KOHBC increases with temperature, showing adsorption is endothermic. The Langmuir adsorption capacity for Cr (VI) increases with temperature and is significantly higher on KOHBC than on DFBC. Pb(II) and Cd (II) adsorption onto both DFBC and KOHBC fitted well with the Langmuir isotherm with higher capacities and regression coefficients. Both Pb(II) and Cd(II) adsorption capacities are higher on KOHBC than DFBC.

2.4.10 Desorption and recovery studies

Chromium adsorption highly depends on the pH of the medium and Cr(VI) is hard to desorb with acidic reagents. Cr(VI) sorption/desorption results on KOHBC are shown in (Fig. 2. 4(a)) and on DFBC are in (Fig. A.11). When stripped with 0.1M HCl, no desorption was observed. Lack of dilute HCl stripping of Cr(VI) has been reported previously,[58,78,79] so desorption from KOHBC was carried out using 0.1M NaOH (Fig. 2.4(a)). The Cr(VI) adsorption capacity at pH 2

was higher (60 and 25 mg/g) in the first cycle on both KOHBC and DFBC, respectively. Then it dropped in the second cycle after stripping with 0.1M NaOH to 46 mg/g with KOHBC and 17 mg/g with DFBC. Then, in the cycle 3 amount adsorbed remained almost constant 45 mg/g for KOHBC and 15 mg/g for DFBC. Amount of Cr(VI) desorbed with 0.1M NaOH was far less than the amount adsorbed in each cycle but the amount of uptake was almost constant in each successive cycle after the first. Strong chemisorption of Cr(VI) occurs onto the biochar surface. Each Cr(VI) adsorption cycle causes some surface oxidation of the char which is accompanied by some Cr(III) deposition. Overall, poor desorption of the adsorbed chromium occurs in consecutive recycles. As illustrated in Fig. 2.4(a), only 48.5 mg/g of chromium is desorbed over all three cycles verses the total of 151 mg/g that was adsorbed in these three cycles. After three cycles, a total of 102.5 mg/g of chromium remain bound to KOHBC. This suggests certain surface sites were able to release adsorbed Cr(VI) and these sites were not changed so they could readsorb Cr(VI) in the next cycle. Other sites did not release chromium. In each cycle further site oxidation always occurs and some Cr(III) is deposited. Some sites adsorbed Cr(VI) and then never release it. Oxidized sites don't behave the same during adsorption or desorption as they did previously or after Cr(III) had been bound.

After 100 mg/g of Pb(II) had been adsorbed during the first cycle onto KOHBC at pH 5, Pb(II) stripping with 0.1M HCl removed almost all of that lead. However, adsorption during the second and third cycles, then decreased to 52 mg/g and 49 mg/g, respectively. DFBC followed a similar adsorption and desorption pattern for Pb(II) (Fig. A.11). About 51 mg/g of Pb(II) adsorbed on DFBC in first cycle. This amount sharply dropped to (25 and 21 mg/g) in the second and third cycles. The reason for this drop in Pb(II) uptake after the first cycle may be due to some chemical

changes in certain adsorption sites so that they no longer bind Pb(II) after the Pb(II) originally sorbed there had been stripped. Other sites can repeatedly adsorb Pb(II). This cause has not been elucidated. Since stripping of Pb(II) with 0.1M HCl is effective and subsequent adsorption (although at a lower capacity) is easy, KOHBC is a potential candidate for treating Pb(II) contaminated water.

Cd(II) exhibited a similar adsorption pattern to that of Pb(II) during its second and third cycles on KOHBC (Fig. 2.4(c)) and on DFBC (Fig. A.10). Nearly a 50% uptake drop occurred between the first and second cycles and then the adsorbed amount stayed almost the same for the third cycle. However, unlike Pb(II) the amount of Cd(II) desorbed always significantly dropped to far less than the amount adsorbed per cycle in all three subsequent cycles. This pattern was observed on both KOHBC and DFBC. Thus, a large cumulative Cd(II) undesorbed uptake had occurred after the three cycles shown in Fig. 2.4(c) (46 mg/g KOHBC). To see if this cadmium build up on KOHBC would continue to rise, Cd(II) adsorption/desorption on KOHBC at pH 6 was then expanded to six cycles (Fig. A.12 (a)). From cycle 2 through 6 the amount adsorbed trended steadily but slowly lower. However, each desorption cycle never removed as much cadmium as had been adsorbed in that cycle. After cycle 3, the fraction of the cadmium, which had adsorbed in that cycle then desorbed, was increased. After all 6 cycles, the total amount of Cd that remained undesorbed on the KOHBC was 69 mg/g. Obviously, KOHBC can accumulate a lot of cadmium. Acid treatment used in the desorption cycles can reactivate portions of the biochar surface partially but never to the point that the amount of Cd(II) taken up in the first cycle can be approached. [80,81,82] The amount of Cd(II) desorbed using 0.1M HCl dropped in all consecutive cycles on both KOHBC

and DFBC. For some reason, 0.1M HCl cannot strip a significant fraction of the sorbed Cd(II) any of the six cycles, so further studies were initiated.

During adsorption, a portion of the Cd(II) might be reduced to Cd(0), perhaps by oxidation of *p*- and *o*-hydroquinone groups that might occur on the char to their quinone forms.[83] If this Cd(0) was not extracted by HCl it might remain on KOHBC or DFBC. Cd(II) might also be hydrolyzed to $Cd(OH)_2$ during stripping and this dehydrated to CdO on the char. To survive being stripped Cd(0) or CdO would need to be difficult to dissolve in 0.1M HCl and Cd(0) would need to be available by Cd(II) reduction.

Ag(I) was reported to be reduced to Ag(0) on previously electrochemically oxidized carbon fibers where hydroquinone functions had been formed.[83,84] Ag(I) to Ag(0) reduction is thermodynamically favored compared to reduction of Pb(II) and Cd(II) to their zero valent states based on their standard redox potentials. While the E^o (Ag^+(aq)/Ag (s) = +0.80 V, reduction of Pb(II) and Cd(II) to their metallic forms under the same biochar chemical environment is far more difficult to accomplish as their redox potentials are -0.13 V and -0.40 V, respectively. But the reduction of Cr(VI) to Cr(III) is possible when considering standard redox potential of +1.35 V.[85] Furthermore, our XPS study provided no evidence for Pb(0) formation on KOHBC or DFBC (see HR-XPS Pb 3d spectra in Fig. 2.3) Pb(II) and Pb(0), when present on the biochar can easily be distinguished by HR-XPS However, Cd(II) and Cd(0) cannot be distinguished since their Cd 3d peaks appear in the same region (Fig. 2.3).[86] Since Pb(II) was not reduced to Pb(0) on KOHBC or DFBC, the reduction of Cd(II) to Cd(0) is improbable since E^o (Cd^{2+}(aq)/Cd (s) = -0.40 V. Only 22.5 mg/g of the 35 mg/g Cd(II) adsorbed originally was desorbed in the first cycle. Thus 12.5

mg/g of adsorbed cadmium remained on biochar after this attempted 0.1M HCl desorption. By the sixth cycle (Fig. A.12 (a)) the unstripped amount had grown to 69 mg/g on KOHBC.

The formation of CdO is accompanied in large favorable decrease in Gibbs free energy ($\Delta_f G^o$ = -228.4 kJ mol^{-1}) when compared to that of PbO which has a free energy change of ($\Delta_f G^o$ = -187.89 kJ mol^{-1})[87] Therefore, CdO formation at the biochar surface is more favorable than the formation of PbO. So this possibility was probed by trying to strip cadmium using a strong acidic oxidizing agent, aqua regia (12M HCl and 16M HNO_3 in a 3:1 volume ratio) (Fig. A.12 (b)). After 35 mg/g of Cd adsorption in the first cycle on KOHBC, this sample was treated with aqua regia on the premise that it may convert CdO to soluble Cd(II) if the unstripped Cd was present in the form of CdO. The amount of Cd desorbed after digestion (30 mg/g) was greater than stripping with 0.1M HCl (23 mg/g). However, aqua regia still desorbed far less than the amount of (35 mg/g) Cd(II) originally adsorbed. Substantial Cd was still strongly held by the biochar. After one desorption cycle using 0.1M HCl as the solvent, the biochar was again stripped with aqua regia (8 mL, 2 h at 80 °C) to determine if more Cd can be desorbed. The amount of Cd(II) desorbed (3 mg/g) was not equal to the difference between the amount desorbed when using both aqua regia and HCl (7.5 mg/g). Since CdO is readily soluble in a variety of acids,[88] it is unlikely that the undesorbed cadmium could possibly have been CdO.

The low desorption of Cd(II) is known to occur in the presence of chloride ions, where Cd(II) forms complexes such as $CdCl^+$, $CdCl_2$, and $CdCl_3^-$.[89] The formation constants ($\log_{10} K$) for these complexes were reported to be 1.95, 2.50 and 2.35 respectively.[90] A high tendency to form $CdCl_2$ and $CdCl_3^-$ likely exists during the HCl desorption of cadmium adsorbed on KOHBC or DFBC. The readsorption of these complexes onto biochar would then hinder cadmium desorption.

These complexes may not be well desorbed with 0.1M HCl. Therefore, 6M and 12M HCl were employed to strip cadmium after the sixth absorption cycle (Fig. A.12 (a)). The total amount of Cd(II) stripped was only 9 mg/g using 6M HCl (Fig. A.12 (a)-X) versus the total accumulated Cd present (69 mg/g) after sixth cycle. The amount of Cd(II) desorbed further increased up to 10.5 mg/g when doubling the volume of 6M HCl. Finally, a total of 26 mg/g of Cd(II) was desorbed when increasing the concentration of HCl up to 12M (Fig. A.12 (a)-Z). Desorption can be enhanced by using high concentrations of HCl although this desorption is far from complete or practical. This is in agreement with earlier literature.[91] Column adsorption studies may be required before large scale commercial application of KOHBC. Continuous flow column adsorption (not batch) can be used after scale-up optimization and would allow for the low-cost separation of adsorbent from solution.

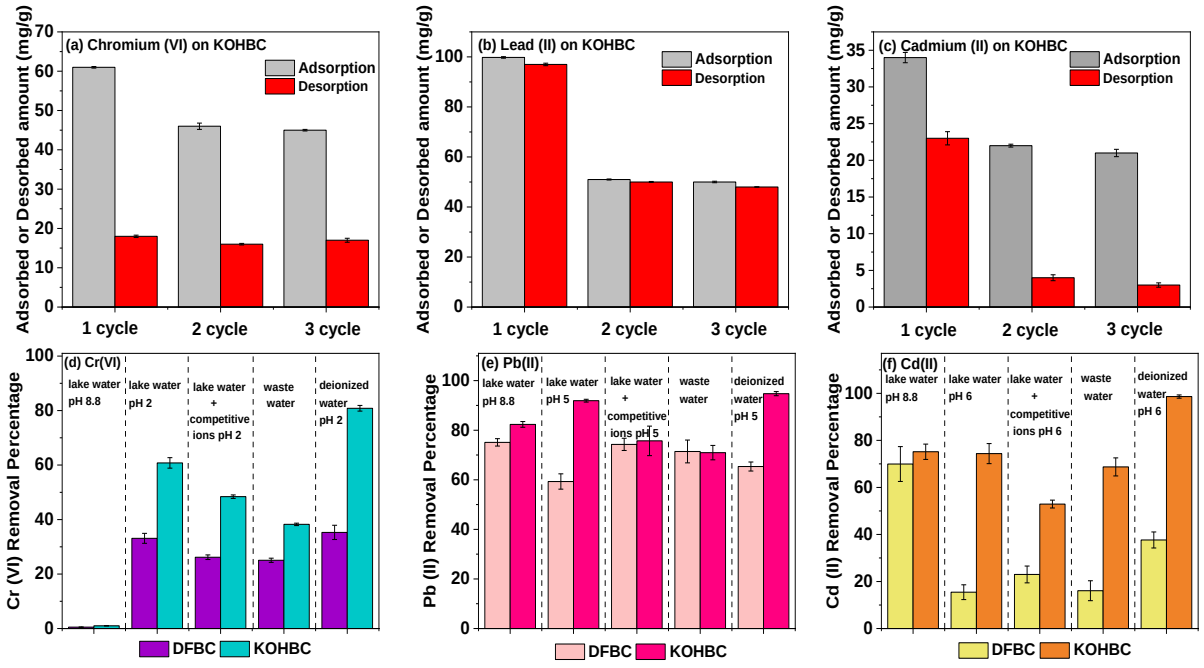

Figure 2.4 Adsorption-desorption cycles on KOHBC for (a) Cr(VI) at pH 2, (b) Pb(II) at pH 5 and (c) Cd(II) at pH 6 and 25 °C.

where 0.200 g of biochar was mixed with 200 mL of adsorbent stirred at 200 rpm. NaOH 0.1M was used to desorb Cr(VI) and 0.1M HCl was used to desorb Pb(II) and Cd(II). (d) Cr(VI), (d) Pb(II) and (f) Cd(II) removal by DFBC and KOHBC. Metal ion removal from natural lake water at pH 8.8, lake water optimized up to pH 2 for Cr(VI), pH 5 for Pb(II) and pH 6 for Cd(II), lake water after the addition of $Cr_2O_7^{2-}$, NO_3^-, PO_4^{3-}, F^-, Cd^{2+}, Pb^{2+} competitive ions, chemical laboratory waste water and control studies in deionized water. 25 mg of DFBC and KOHBC were separately mixed with analyte solution (25 mL) containing 100 mg/g of Cr(VI), 100 mg/g of Pb(II), 20 mg/g of Cd(II) spiked at room temperature for 2 h for Cr(VI) and 1 h for Pb(II) and Cd(II). Error bars are the SD of three replicates.

2.4.11 Sorption analysis for Cr(VI), Pb(II) and Cd(II) spiked into natural and waste water samples

Fig. 4(d-f). depicts the percent Cr(VI), Pb(II) and Cd(II) removal by DFBC and KOHBC from five different aqueous systems: (I) each of the analytes (100 mg/g Cr(VI), 100 mg/g Pb(II) and Cd(II) 20 mg/g) spiked into the lake water sample at its natural pH (8.8), (II) these water samples buffered to generate their optimum pH for each analyte (Cr(VI) pH 2, Pb(II) pH 5 and

Cd(II) pH 6), (III) lake water samples after the addition of competitive ions ($Cr_2O_7^{2-}$, NO_3^-, PO_4^{3-}, F^-, Cd^{2+}, Pb^{2+}), (IV) Cr(VI), Pb(II) and Cd(II) spiked into chemical laboratory waste water and (V) control experiments for Cr(VI), Pb(II) and Cd(II) spiked into deionized water. Cr(VI) removal percentages were insignificant at pH 8.8 on both DFBC and KOHBC. The highest Cr(VI) removal percentage by KOHBC (80%) and DFBC (35%) was obtained for the control samples run in deionized water. The second highest Cr(VI) removal efficiency was achieved by DFBC (33%) and KOHBC (60%) for the lake water samples run at pH 2. The removal efficiencies dropped up to 48 and 38 on KOHBC for the samples treated with competitive ions at the same time and waste water samples. Higher removal percentages of Pb(II) and Cd(II) on DFBC and KOHBC were obtained using the lake water samples at their natural pH 8.8. This is due to precipitation of $Pb(OH)_2$ and $Cd(OH)_2$ above pH 5 and 6, respectively. The removal of Pb(II) and Cd(II) on DFBC and KOHBC dropped in the presence of the competitive ion mixture. These interfering species hinder surface binding of Pb(II) and Cd(II) as was reported previously for Douglas Fir biochar.[31,33,92] The larger amount of oxygen-containing functions after KOH activation contributed to higher Cr(VI), Pb(II) and Cd(II) uptake by KOHBC verses DFBC under all experimental conditions.

Table 2.2 Langmuir and Freundlich isotherm parameters for Cr(VI), Pb(II) and Cd(II)

Adsorbent	Isotherm parameters		Cr (VI)			Cd (II)			Pb (II)		
			Temperature (K)								
			298	308	318	298	308	318	298	308	318
KOHBC	Langmuir	Q° (mg/g)	113.7	120.1	127.2	23.0	27.0	29.0	80.0	105.0	140.0
		b	0.09	0.14	0.23	0.18	0.18	0.18	0.11	0.09	0.04
		R^2	0.99	0.92	0.91	0.99	0.99	0.99	0.99	0.98	0.99
KOHBC	Freundlich	K_f	54.5	63.5	70.1	6.99	7.75	9.75	21.58	20.53	12.39
		n	7.53	8.29	8.73	4.39	4.25	7.27	5.24	4.21	2.87
		R^2	0.99	0.99	0.99	0.97	0.98	0.98	0.98	0.99	0.98
DFBC	Langmuir	Q° (mg/g)	28.1	32.5	33.5	12.6	15.0	18.0	78.2	81.6	84.1
		b	0.48	0.20	0.77	0.15	0.09	0.18	0.20	0.21	0.19
		R^2	0.97	0.99	0.98	0.99	0.99	0.99	0.99	0.99	0.98
DFBC	Freundlich	K_f	12.5	14.4	16.2	4.91	7.83	5.77	18.34	21.68	23.10
		n	5.22	5.83	7.43	5.74	11.95	5.99	3.48	3.88	4.12
		R^2	0.99	0.98	0.99	0.99	0.98	0.99	0.91	0.81	0.84

Qo-monolayer adsorption capacity (mg/g), b - constant related to net enthalpy of adsorption, K_f - constant indicative of the relative adsorption capacity of adsorbent (L/g), n - a constant indicative of the intensity of the adsorption, R^2 - regression coefficient

Table 2.3 Comparison of Cr(VI), Pb(II) and Cd (II) adsorption parameters with those reported in literature

Adsorbent	Analyte	pH	Temp. (K)	Conc. Range (ppm)	Surface area (m^2/g)	Adsorption capacity (mg/g)	Eq. time (h)	Ref.
Hickory wood biochar	Pb II	5	298	2-250	256	11.2	24	[93]
NaOH-treated HMB	Pb II	5	298	2-250	873	53.6	24	[93]
Hickory wood biochar	Cd II	5	298	2-100	256	0.20	24	[93]
NaOH- treated HMB	Cd II	5	298	2-100	873	0.98	24	[93]
KOH activated corn stalk hydrochar	Cd(II)	6	303	0-300	1.83	30.4	24	[94]
KOH-activated biochar	**Cd(II)**	**6**	**318**	**5-1000**	**1050**	**29.0**	**1**	**This study**
	Cd(II)	**6**	**298**	**5-1000**	**1050**	**23.0**	**1**	
KOH-treated corn husk biochar	Pb II	5	298	20-1000	108.58	44.07	6	[22]
Hydrothermal liquefaction of pinewood (P300)	Pb II	5	318	5-40	Not reported	4.25	5	[95]
Maplewood biochar	Pb II	4-7	298	5-550	Not reported	43.3	24	[96]
H_2SO_4 acid treated plum biochar	Pb II	6	295	0-200	146.6	28.29	0.5	[97]
H_2SO_4 acid treated apricot kernel biochar	Pb II	6	295	0-200	85.6	23.89	0.5	[97]
NaOH treated biochar		5.8	303	50-1000	75.92	98.33	0.5	[98]
KOH-activated biochar	**Pb(II)**	**5**	**318**	**5-1000**	**1050**	**140.0**	**1**	**This study**
	Pb(II)	**5**	**298**	**5-1000**	**1050**	**80.0**	**1**	
Oak bark biochar	Cr VI	2	318	1-100	1.88	7.51	48	[99]
Oak wood biochar	Cr VI	2	318	1-100	2.73	4.93	48	[99]
Sugar beet tailing biochar	Cr VI	2	298	50-800	0.2	123	24	[58]
Ramie biochar	Cr VI	2	298	10-500	5.14	82.23	24	[100]
Pd modified silicon rich rice straw biochar-supported nZVI.	Cr VI	3.5	298	20-100	Not reported	110.0	8	[101]
Corncob biochar with polypyrrole (PPy) (MBC/PPy)	Cr VI	5.3	313	20-60	Not reported	27.62	Not reported	[102]
KOH activated sawdust biochar	Cr(VI)	2	298	100	18.69	45.88	8	[103]
KOH activated corn straw biochar	Cr(VI)	2	318	10-200	2183	116.97	2	[104]
KOH-activated biochar	**Cr(VI)**	**2**	**318**	**5-300**	**1050**	**127.2**	**2**	**This study**
	Cr(VI)	**2**	**298**	**5-300**	**1050**	**113.7**	**2**	
H_2SO_4 acid treated plum biochar	Cr(III)	6	295	0-250	146.6	14.02	0.5	[97]
H_2SO_4 acid treated apricot kernel biochar	Cr(III)	6	295	0-250	85.6	12.68	0.5	[97]

2.5 Conclusions

KOH-activated biochar (KOHBC) was much more effective at removing Cr(VI), Pb(II) and Cd(II) from solution than its precursor, unactivated DFBC. KOH activation increased the high original surface area of DFBC from 535 to 1050 m^2/g and average pore diameter from 18.6 to 25.6 Å. This chemical activation of the DFBC contributed fast kinetics (1-2 h) for the sorption of contaminants. KOH activation of DFBC resulted, which decreased the PZC from 9 for DFBC to 7 for KOHBC. Therefore, the KOH activation provided KOHBC with a favorable surface for the removal of negatively and positively charged potentially toxic metal ions, beneficial for environmental remediation. Point of zero charge analysis suggests electrostatic interactions play a key role in the attraction of Cr(VI) oxyanions to the positively charge biochar surface at pH 2 followed by the chemisorption. During the adsorption, portions of Cr(VI) are reduced into less toxic Cr(III) via redox reactions at the surface. Batch sorption studies demonstrated that under a variety of different conditions KOHBC had a much higher adsorption capacity than DFBC for Cr(VI), Pb(II) and Cd(II). Sorption of these metal ions in natural lake water, chemical laboratory waste water and in the presence of various competitive ions were demonstrated. Desorption and recovery studies for Pb(II) on KOHBC and DFBC showed a high regeneration efficiency. The amount of Cr(VI) desorbed by 0.1M NaOH, was less in each consecutive cycle than the amount adsorbed by KOHBC and DFBC. The oxidized biochar surface sites didn't change after the reduction of Cr(VI) into Cr(III) and this Cr(III) was strongly bound on the char which lead to a lower desorption. Cd(II) recovery studies on KOHBC and DFBC revealed that 0.1M HCl is not able to desorb all the amount adsorbed onto the biochar. KOHBC exhibited higher desorption and

recovery than DFBC for Cr(VI), Pb(II) and Cd(II). KOH treatment of DFBC is a promising new route to high surface area adsorbents and may lead to new research avenues in pollution abatement.

2.6 References

1. Cook, J., Environmental pollution by heavy metals. *International Journal of Environmental Studies* **1977,** *10* (4), 253-266.

2. Rai, P. K.; Lee, S. S.; Zhang, M.; Tsang, Y. F.; Kim, K.-H., Heavy metals in food crops: Health risks, fate, mechanisms, and management. *Environment International* **2019,** *125*, 365-385.

3. Jeřábková, J.; Tejnecký, V.; Borůvka, L.; Drábek, O., Chromium in Anthropogenically Polluted and Naturally Enriched Soils: A Review. *Scientia Agriculturae Bohemica* **2018,** *49* (4), 297-312.

4. Cohen, M. D.; Kargacin, B.; Klein, C. B.; Costa, M., Mechanisms of chromium carcinogenicity and toxicity. *Critical Reviews in Toxicology* **1993,** *23* (3), 255-281.

5. WHO, In *Guidelines for Drinking-Water Quality: Fourth Edition Incorporating the First Addendum*, World Health Organization Copyright © World Health Organization 2017.: Geneva, 2017.

6. Uddin, M. K., A review on the adsorption of heavy metals by clay minerals, with special focus on the past decade. *Chemical Engineering Journal* **2017,** *308*, 438-462.

7. Zhang, R.; Wilson, V. L.; Hou, A.; Meng, G., Source of lead pollution, its influence on public health and the countermeasures. *International Journal of Health, Animal Science and Food Safety* **2015,** *2* (1).

8. Liu, J.; Qu, W.; Kadiiska, M. B., Role of oxidative stress in cadmium toxicity and carcinogenesis. *Toxicology and Applied Pharmacology* **2009,** *238* (3), 209-214.

9. Godt, J.; Scheidig, F.; Grosse-Siestrup, C.; Esche, V.; Brandenburg, P.; Reich, A.; Groneberg, D. A., The toxicity of cadmium and resulting hazards for human health. *Journal of Occupational Medicine and Toxicology* **2006,** *1* (1), 22.

10. Heikens, A.; Peijnenburg, W.; Hendriks, A., Bioaccumulation of heavy metals in terrestrial invertebrates. *Environmental Pollution* **2001,** *113* (3), 385-393.

11. Butt, A.; Rehman, K.; Khan, M. X.; Hesselberg, T., Bioaccumulation of cadmium, lead, and zinc in agriculture-based insect food chains. *Environmental Monitoring and Assessment* **2018,** *190* (12), 698.

12. Fu, F.; Wang, Q., Removal of heavy metal ions from wastewaters: a review. *Journal of Environmental Management* **2011,** *92* (3), 407-418.

13. Bolisetty, S.; Peydayesh, M.; Mezzenga, R., Sustainable technologies for water purification from heavy metals: review and analysis. *Chemical Society Reviews* **2019,** *48* (2), 463-487.

14. Lee, S.-J.; Park, J. H.; Ahn, Y.-T.; Chung, J. W., Comparison of heavy metal adsorption by peat moss and peat moss-derived biochar produced under different carbonization conditions. *Water, Air, & Soil Pollution* **2015,** *226* (2), 9.

15. Goharshadi, E.; Moghaddam, M., Adsorption of hexavalent chromium ions from aqueous solution by graphene nanosheets: kinetic and thermodynamic studies. *International Journal of Environmental Science and Technology* **2015,** *12* (7), 2153-2160.

16. Xu, L.; Wang, J., The application of graphene-based materials for the removal of heavy metals and radionuclides from water and wastewater. *Critical Reviews in Environmental Science and Technology* **2017,** *47* (12), 1042-1105.

17. Zhu, H.; Xu, X.; Zhong, X., Adsorption of Co (II) on Graphene Oxides from Aqueous Solution. *Polish Journal of Environmental Studies* **2016,** *25* (6).

18. Moreno-Piraján, J. C.; Giraldo, L., Heavy metal ions adsorption from wastewater using activated carbon from orange peel. *Journal of Chemistry* **2012,** *9* (2), 926-937.

19. Deliyanni, E. A.; Kyzas, G. Z.; Triantafyllidis, K. S.; Matis, K. A., Activated carbons for the removal of heavy metal ions: A systematic review of recent literature focused on lead and arsenic ions. *Open Chemistry* **2015,** *13* (1).

20. Dong, L.; Liu, W.; Jiang, R.; Wang, Z., Study on the adsorption mechanism of activated carbon removing low concentrations of heavy metals. *Desalination and Water Treatment* **2016,** *57* (17), 7812-7822.

21. Liu, W.-J.; Jiang, H.; Yu, H.-Q., Development of biochar-based functional materials: toward a sustainable platform carbon material. *Chemical Reviews* **2015,** *115* (22), 12251-12285.

22. Rwiza, M. J.; Oh, S.-Y.; Kim, K.-W.; Kim, S. D., Comparative sorption isotherms and removal studies for Pb(II) by physical and thermochemical modification of low-cost agro-wastes from Tanzania. *Chemosphere* **2018,** *195*, 135-145.

23. Chen, T.; Zhang, Y.; Wang, H.; Lu, W.; Zhou, Z.; Zhang, Y.; Ren, L., Influence of pyrolysis temperature on characteristics and heavy metal adsorptive performance of biochar derived from municipal sewage sludge. *Bioresource Technology* **2014,** *164*, 47-54.

24. Suliman, W.; Harsh, J. B.; Abu-Lail, N. I.; Fortuna, A.-M.; Dallmeyer, I.; Garcia-Perez, M., Influence of feedstock source and pyrolysis temperature on biochar bulk and surface properties. *Biomass and Bioenergy* **2016,** *84*, 37-48.

25. Suliman, W.; Harsh, J. B.; Abu-Lail, N. I.; Fortuna, A.-M.; Dallmeyer, I.; Garcia-Perez, M., Modification of biochar surface by air oxidation: role of pyrolysis temperature. *Biomass and Bioenergy* **2016,** *85*, 1-11.

26. Aguilar, K. M. M.; Kose, Y.; Amano, Y.; Machida, M.; Imazeki, F., Influence of Oxidation Conditions of Activated Carbon on Adsorption of Pb (II) from Aqueous Solution. *Journal of Environmental Chemistry* **2016,** *26* (3), 109-114.

27. Wepasnick, K. A.; Smith, B. A.; Schrote, K. E.; Wilson, H. K.; Diegelmann, S. R.; Fairbrother, D. H., Surface and structural characterization of multi-walled carbon nanotubes following different oxidative treatments. *Carbon* **2011,** *49* (1), 24-36.

28. Sarkar, A.; Ranjan, A.; Paul, B., Synthesis, characterization and application of surface-modified biochar synthesized from rice husk, an agro-industrial waste for the removal of hexavalent chromium from drinking water at near-neutral pH. *Clean Technologies and Environmental Policy* **2019,** *21* (2), 447-462.

29. Yakout, S. M.; Daifullah, A. E. H. M.; El-Reefy, S. A., Pore structure characterization of chemically modified biochar derived from rice straw. *Environmental Engineering & Management Journal (EEMJ)* **2015,** *14* (2).

30. Luo, Y.; Street, J.; Steele, P.; Entsminger, E.; Guda, V., Activated carbon derived from pyrolyzed pinewood char using elevated temperature, KOH, H_3PO_4, and H_2O_2. *Bio Resources* **2016,** *11* (4), 10433-10447.

31. Dewage, N. B.; Liyanage, A. S.; Pittman Jr, C. U.; Mohan, D.; Mlsna, T., Fast nitrate and fluoride adsorption and magnetic separation from water on α-Fe_2O_3 and Fe_3O_4 dispersed on Douglas fir biochar. *Bioresource Technology* **2018,** *263*, 258-265.

32. Dewage, N. B.; Liyanage, A. S.; Smith, Q.; Pittman Jr, C. U.; Perez, F.; Mohan, D.; Mlsna, T., Fast aniline and nitrobenzene remediation from water on magnetized and nonmagnetized Douglas fir biochar. *Chemosphere* **2019,** *225*, 943-953.

33. Karunanayake, A. G.; Todd, O. A.; Crowley, M.; Ricchetti, L.; Pittman Jr, C. U.; Anderson, R.; Mohan, D.; Mlsna, T., Lead and cadmium remediation using magnetized and nonmagnetized biochar from Douglas fir. *Chemical Engineering Journal* **2018,** *331*, 480-491.

34. Wang, J.; Kaskel, S., KOH activation of carbon-based materials for energy storage. *Journal of Materials Chemistry* **2012,** *22* (45), 23710-23725.

35. Misra, M. K.; Ragland, K. W.; Baker, A. J., Wood ash composition as a function of furnace temperature. *Biomass and Bioenergy* **1993,** *4* (2), 103-116.

36. Cho, D.-W.; Cho, S.-H.; Song, H.; Kwon, E. E., Carbon dioxide assisted sustainability enhancement of pyrolysis of waste biomass: a case study with spent coffee ground. *Bioresource Technology* **2015,** *189*, 1-6.

37. Hui, T. S.; Zaini, M. A. A., Potassium hydroxide activation of activated carbon: a commentary. *Carbon Letters (Carbon Lett.)* **2015,** *16* (4), 275-280.

38. Zhang, X.; Wang, B.; Yu, J.; Wu, X.; Zang, Y.; Gao, H.; Su, P.; Hao, S., Three-dimensional honeycomb-like porous carbon derived from corncob for the removal of heavy metals from water by capacitive deionization. *RSC Advances* **2018,** *8* (3), 1159-1167.

39. Yang, T.; Lua, A. C., Characteristics of activated carbons prepared from pistachio-nut shells by potassium hydroxide activation. *Microporous and Mesoporous Materials* **2003,** *63* (1-3), 113-124.

40. Li, S.; Chen, G., Thermogravimetric, thermochemical, and infrared spectral characterization of feedstocks and biochar derived at different pyrolysis temperatures. *Waste Management* **2018,** *78*, 198-207.

41. Xiao, X.; Chen, Z.; Chen, B., H/C atomic ratio as a smart linkage between pyrolytic temperatures, aromatic clusters and sorption properties of biochars derived from diverse precursory materials. *Scientific Reports* **2016,** *6*, 22644.

42. Mohan, D.; Pittman Jr, C. U., Activated carbons and low cost adsorbents for remediation of tri- and hexavalent chromium from water. *Journal of Hazardous Materials* **2006,** *137* (2), 762-811.

43. Mohan, D.; Singh, P.; Sarswat, A.; Steele, P. H.; Pittman Jr, C. U., Lead sorptive removal using magnetic and nonmagnetic fast pyrolysis energy cane biochars. *Journal of Colloid and Interface Science* **2015,** *448*, 238-250.

44. Zhang, X.; Fu, W.; Yin, Y.; Chen, Z.; Qiu, R.; Simonnot, M.-O.; Wang, X., Adsorption-reduction removal of Cr(VI) by tobacco petiole pyrolytic biochar: Batch experiment, kinetic and mechanism studies. *Bioresource Technology* **2018,** *268*, 149-157.

45. Navarathna, C. M.; Karunanayake, A. G.; Gunatilake, S. R.; Pittman Jr, C. U.; Perez, F.; Mohan, D.; Mlsna, T., Removal of Arsenic (III) from water using magnetite precipitated onto Douglas fir biochar. *Journal of Environmental Management* **2019,** *250*, 109429.

46. Karunanayake, A. G.; Navarathna, C.; Gunatilake, S.; Crowley, M.; Anderson, R.; Mohan, D.; Perez, F.; Pittman Jr, C. U.; Mlsna, T. E., Fe_3O_4 Nanoparticles Dispersed on Douglas Fir Biochar for Phosphate Sorption. *ACS Applied Nano Materials* **2019**.

47. Tian, X.; Wang, W.; Tian, N.; Zhou, C.; Yang, C.; Komarneni, S., Cr (VI) reduction and immobilization by novel carbonaceous modified magnetic Fe_3O_4/halloysite nanohybrid. *Journal of Hazardous Materials* **2016,** *309*, 151-156.

48. Volkov, V.; Zakharova, G.; Kuznetsov, M., Polyvanadochromic acid. *Zhurnal Neorganicheskoj Khimii* **1994,** *39* (6), 877-882.

49. Maurice, V.; Yang, W.; Marcus, P., XPS and STM Investigation of the Passive Film Formed on Cr (110) Single-Crystal Surfaces. *Journal of The Electrochemical Society* **1994,** *141* (11), 3016-3027.

50. Vieira, R. S.; Oliveira, M. L. M.; Guibal, E.; Rodríguez-Castellón, E.; Beppu, M. M., Copper, mercury and chromium adsorption on natural and crosslinked chitosan films: An XPS investigation of mechanism. *Colloids and Surfaces A: Physicochemical and Engineering Aspects* **2011,** *374* (1), 108-114.

51. Desimoni, E.; Malitesta, C.; Zambonin, P.; Riviere, J., An x-ray photoelectron spectroscopic study of some chromium–oxygen systems. *Surface and Interface Analysis* **1988,** *13* (2-3), 173-179.

52. Uekawa, N.; Kaneko, K., Dopant reduction in p-type oxide films upon oxygen absorption. *The Journal of Physical Chemistry* **1996,** *100* (10), 4193-4198.

53. Dupont, L.; Guillon, E., Removal of hexavalent chromium with a lignocellulosic substrate extracted from wheat bran. *Environmental Science & Technology* **2003,** *37* (18), 4235-4241.

54. Sleigh, C.; Pijpers, A. P.; Jaspers, A.; Coussens, B.; Meier, R. J., On the determination of atomic charge via ESCA including application to organometallics. *Journal of Electron Spectroscopy and Related Phenomena* **1996,** *77* (1), 41-57.

55. Frateur, I.; Lecoeur, J.; Zanna, S.; Olsson, C. O. A.; Landolt, D.; Marcus, P., Adsorption of BSA on passivated chromium studied by a flow-cell EQCM and XPS. *Electrochimica Acta* **2007,** *52* (27), 7660-7669.

56. Harju, M.; Järn, M.; Dahlsten, P.; Nikkanen, J.-P.; Rosenholm, J. B.; Mäntylä, T., Influence of long-term aqueous exposure on surface properties of plasma-sprayed oxides Cr_2O_3 and Cr_2O_3–25 wt% TiO_2. *Journal of Colloid and Interface Science* **2008,** *326* (2), 403-410.

57. Miretzky, P.; Cirelli, A. F., Cr (VI) and Cr (III) removal from aqueous solution by raw and modified lignocellulosic materials: a review. *Journal of Hazardous Materials* **2010,** *180* (1-3), 1-19.

58. Dong, X.; Ma, L. Q.; Li, Y., Characteristics and mechanisms of hexavalent chromium removal by biochar from sugar beet tailing. *Journal of Hazardous Materials* **2011,** *190* (1), 909-915.

59. Wiryawan, A.; Retnowati, R.; Burhan, P.; Syekhfani, S., Method of analysis for determination of the chromium (Cr) species in water samples by spectrophotometry with diphenylcarbazide. *Journal of Environmental Engineering and Sustainable Technology* **2018,** *5* (1), 37-46.

60. Bertoni, F. A.; Bellú, S. E.; González, J. C.; Sala, L. F., Reduction of hypervalent chromium in acidic media by alginic acid. *Carbohydrate polymers* **2014,** *114*, 1-11.

61. Pezzin, S. H.; Rivera, J. F. L.; Collins, C. H.; Collins, K. E., Reduction of trace quantities of chromium (VI) by strong acids. *Journal of the Brazilian Chemical Society* **2004,** *15* (1), 58-65.

62. Mangiameli, M. F.; González, J. C.; Bellú, S.; Bertoni, F.; Sala, L. F., Redox and complexation chemistry of the Cr VI/Cr V-d-glucaric acid system. *Dalton Transactions* **2014,** *43* (24), 9242-9254.

63. White, A. F.; Peterson, M. L., Reduction of aqueous transition metal species on the surfaces of Fe (II)-containing oxides. *Geochimica et Cosmochimica Acta* **1996,** *60* (20), 3799-3814.

64. Hu, J.; Wang, S.; Shao, D.; Dong, Y.; Li, J.; Wang, X., Adsorption and reduction of chromium (VI) from aqueous solution by multi-walled carbon nanotubes. *Open Environ. Pollut. Toxicol. J* **2009,** *1*, 66-73.

65. Alizadeh, A.; Abdi, G.; Khodaei, M. M.; Ashokkumar, M.; Amirian, J., Graphene oxide/Fe_3O_4/SO_3H nanohybrid: a new adsorbent for adsorption and reduction of Cr (VI) from aqueous solutions. *RSC Advances* **2017,** *7* (24), 14876-14887.

66. Islam, J. B.; Furukawa, M.; Tateishi, I.; Katsumata, H.; Kaneco, S., Photocatalytic Reduction of Hexavalent Chromium with Nanosized TiO_2 in Presence of Formic Acid. *ChemEngineering* **2019,** *3* (2), 33.

67. Kratochvil, D.; Pimentel, P.; Volesky, B., Removal of trivalent and hexavalent chromium by seaweed biosorbent. *Environmental Science & Technology* **1998,** *32* (18), 2693-2698.

68. Chen, S.; Liu, W.; Yu, L., Study on the structure of PbS nanoparticles coated with dialkyldithiophosphate. *Journal of Materials Research* **1999,** *14* (5), 2147-2151.

69. Wang, T.; Liu, W.; Xiong, L.; Xu, N.; Ni, J., Influence of pH, ionic strength and humic acid on competitive adsorption of Pb(II), Cd(II) and Cr(III) onto titanate nanotubes. *Chemical Engineering Journal* **2013,** *215-216*, 366-374.

70. Hammond, J.; Gaarenstroom, S.; Winograd, N., X-ray photoelectron spectroscopic studies of cadmium-and silver-oxygen surfaces. *Analytical Chemistry* **1975,** *47* (13), 2193-2199.

71. Setty, M.; Sinha, A., Characterization of highly conducting PbO-doped Cd_2SnO_4 thick films. *Thin Solid Films* **1986,** *144* (1), 7-19.

72. Mahdi, Z.; Yu, Q. J.; El Hanandeh, A., Competitive adsorption of heavy metal ions (Pb^{2+}, Cu^{2+}, and Ni^{2+}) onto date seed biochar: batch and fixed bed experiments. *Separation Science and Technology* **2019,** *54* (6), 888-901.

73. Wang, H.; Zhang, M.; Lv, Q., Influence of Pyrolysis Temperature on Cadmium Removal Capacity and Mechanism by Maize Straw and Platanus Leaves Biochars. *International Journal of Environmental Research and Public Health* **2019,** *16* (5), 845.

74. Harvey, O. R.; Herbert, B. E.; Rhue, R. D.; Kuo, L.-J., Metal interactions at the biochar-water interface: energetics and structure-sorption relationships elucidated by flow adsorption microcalorimetry. *Environmental Science & Technology* **2011,** *45* (13), 5550-5556.

75. Yu, C.; Shao, Z.; Hou, H., A functionalized metal–organic framework decorated with O– groups showing excellent performance for lead (II) removal from aqueous solution. *Chemical Science* **2017,** *8* (11), 7611-7619.

76. Langmuir, I., The adsorption of gases on plane surfaces of glass, mica and platinum. *Journal of the American Chemical Society* **1918,** *40* (9), 1361-1403.

77. Freundlich, H., Over the adsorption in solution. *J. Phys. Chem* **1906,** *57* (385471), 1100-1107.

78. Han, Y.; Cao, X.; Ouyang, X.; Sohi, S. P.; Chen, J., Adsorption kinetics of magnetic biochar derived from peanut hull on removal of Cr (VI) from aqueous solution: effects of production conditions and particle size. *Chemosphere* **2016,** *145*, 336-341.

79. Ma, Y.; Liu, W.-J.; Zhang, N.; Li, Y.-S.; Jiang, H.; Sheng, G.-P., Polyethylenimine modified biochar adsorbent for hexavalent chromium removal from the aqueous solution. *Bioresource Technology* **2014,** *169*, 403-408.

80. Tan, I.; Ahmad, A.; Hameed, B., Enhancement of basic dye adsorption uptake from aqueous solutions using chemically modified oil palm shell activated carbon. *Colloids and Surfaces A: Physicochemical and Engineering Aspects* **2008,** *318* (1-3), 88-96.

81. Mahmoud, D. K.; Salleh, M. A. M.; Karim, W. A. W. A.; Idris, A.; Abidin, Z. Z., Batch adsorption of basic dye using acid treated kenaf fibre char: equilibrium, kinetic and thermodynamic studies. *Chemical Engineering Journal* **2012,** *181*, 449-457.

82. Tan, X.-f.; Liu, S.-b.; Liu, Y.-g.; Gu, Y.-l.; Zeng, G.-m.; Hu, X.-j.; Wang, X.; Liu, S.-h.; Jiang, L.-h., Biochar as potential sustainable precursors for activated carbon production: multiple applications in environmental protection and energy storage. *Bioresource Technology* **2017,** *227*, 359-372.

83. Yue, Z.; Jiang, W.; Wang, L.; Toghiani, H.; Gardner, S.; Pittman Jr, C., Adsorption of precious metal ions onto electrochemically oxidized carbon fibers. *Carbon* **1999,** *37* (10), 1607-1618.

84. Pittman Jr, C.; Jiang, W.; Yue, Z.; Gardner, S.; Wang, L.; Toghiani, H.; y Leon, C. L., Surface properties of electrochemically oxidized carbon fibers. *Carbon* **1999,** *37* (11), 1797-1807.

85. Dittert, I. M.; de Lima Brandão, H.; Pina, F.; da Silva, E. A.; de Souza, S. M. G. U.; de Souza, A. A. U.; Botelho, C. M.; Boaventura, R. A.; Vilar, V. J., Integrated reduction/oxidation reactions and sorption processes for Cr (VI) removal from aqueous solutions using Laminaria digitata macro-algae. *Chemical Engineering Journal* **2014,** *237*, 443-454.

86. Parry-Jones, A.; Weightman, P.; Andrews, P., The M4, 5N4, 5N4, 5 Auger spectra of Ag, Cd, In and Sn. *Journal of Physics C: Solid State Physics* **1979,** *12* (8), 1587.

87. Atkin, P. W., Physical Chemistry. Fifth Edition ed.; Oxford University Press, New York, 1994.

88. Wainwright, M.; Supharungsun, S.; Killham, K., Effect of acid rain on the solubility of heavy metal oxides and fluorspar (CaF_2) added to soil. *Science of The Total Environment* **1982,** *24* (1), 85-90.

89. Kipton J. Powell1, Paul L. Brown, Robert H. Byrne, Tamas Gajda,Glenn Hefter, Ann-Kathrin Leuz, Staffan Sjöberg, Hans Wanner, Chemical speciation of environmentally significant metals with inorganic ligands.Part 4: The Cd^{2+}+ OH^{-}, Cl^{-}, CO_3^{2-}, SO_4^{2-}, and PO_4^{3-}systems. In Chem, P. A., Ed. Pure Appl. Chem, IUPAC Analytical Chemistry Division, 2011; Vol. Vol. 83, No. 5, pp pp. 1163–1214

90. Marcus, Y., The anion exchange of metal complexes. III. The cadmium-chloride system. *Journal of Physical Chemistry* **1959,** *63* (6), 1000-1004.

91. Bogusz, A.; Oleszczuk, P.; Dobrowolski, R., Application of laboratory prepared and commercially available biochars to adsorption of cadmium, copper and zinc ions from water. *Bioresource Technology* **2015,** *196*, 540-549.

92. Dewage, N. B.; Fowler, R. E.; Pittman Jr, C. U.; Mohan, D.; Mlsna, T., Lead (Pb^{2+}) Sorptive Removal Using Chitosan-Modified Biochar: Batch and Fixed-Bed Studies. *RSC Adv*. **2018,** *8*, 25368.

93. Ding, Z.; Hu, X.; Wan, Y.; Wang, S.; Gao, B., Removal of lead, copper, cadmium, zinc, and nickel from aqueous solutions by alkali-modified biochar: Batch and column tests. *Journal of Industrial and Engineering Chemistry* **2016,** *33*, 239-245.

94. Sun, K.; Tang, J.; Gong, Y.; Zhang, H., Characterization of potassium hydroxide (KOH) modified hydrochars from different feedstocks for enhanced removal of heavy metals from water. *Environmental Science and Pollution Research* **2015,** *22* (21), 16640-16651.

95. Liu, Z.; Zhang, F.-S., Removal of lead from water using biochars prepared from hydrothermal liquefaction of biomass. *Journal of Hazardous Materials* **2009,** *167* (1), 933-939.

96. Wang, Q.; Wang, B.; Lee, X.; Lehmann, J.; Gao, B., Sorption and desorption of Pb(II) to biochar as affected by oxidation and pH. *Science of The Total Environment* **2018,** *634*, 188-194.

97. Pap, S.; Bezanovic, V.; Radonic, J.; Babic, A.; Saric, S.; Adamovic, D.; Turk Sekulic, M., Synthesis of highly-efficient functionalized biochars from fruit industry waste biomass for the removal of chromium and lead. *Journal of Molecular Liquids* **2018,** *268*, 315-325.

98. Wang, C.; Wang, H.; Cao, Y., Pb (II) sorption by biochar derived from Cinnamomum camphora and its improvement with ultrasound-assisted alkali activation. *Colloids and Surfaces A: Physicochemical and Engineering Aspects* **2018,** *556*, 177-184.

99. Mohan, D.; Rajput, S.; Singh, V. K.; Steele, P. H.; Pittman Jr, C. U., Modeling and evaluation of chromium remediation from water using low cost bio-char, a green adsorbent. *Journal of Hazardous Materials* **2011,** *188* (1), 319-333.

100. Zhou, L.; Liu, Y.; Liu, S.; Yin, Y.; Zeng, G.; Tan, X.; Hu, X.; Hu, X.; Jiang, L.; Ding, Y.; Liu, S.; Huang, X., Investigation of the adsorption-reduction mechanisms of hexavalent chromium by ramie biochars of different pyrolytic temperatures. *Bioresource Technology* **2016,** *218*, 351-359.

101. Qian, L.; Liu, S.; Zhang, W.; Chen, Y.; Ouyang, D.; Han, L.; Yan, J.; Chen, M., Enhanced reduction and adsorption of hexavalent chromium by palladium and silicon rich biochar supported nanoscale zero-valent iron. *Journal of Colloid and Interface Science* **2019,** *533*, 428-436.

102. Yang, Y.; Chen, N.; Feng, C.; Li, M.; Gao, Y., Chromium removal using a magnetic corncob biochar/polypyrrole composite by adsorption combined with reduction: Reaction pathway and contribution degree. *Colloids and Surfaces A: Physicochemical and Engineering Aspects* **2018,** *556*, 201-209.

103. Zhang, X.; Zhang, L.; Li, A., Eucalyptus sawdust derived biochar generated by combining the hydrothermal carbonization and low concentration KOH modification for hexavalent chromium removal. *Journal of Environmental Management* **2018,** *206*, 989-998.

104. Qu, J.; Wang, Y.; Tian, X.; Jiang, Z.; Deng, F.; Tao, Y.; Jiang, Q.; Wang, L.; Zhang, Y., KOH-activated porous biochar with high specific surface area for adsorptive removal of chromium (VI) and naphthalene from water: Affecting factors, mechanisms and reusability exploration. *Journal of Hazardous Materials* **2020,** *401*, 123292.

CHAPTER III

BIOCHAR-SUPPORTED POLYANILINE HYBRID FOR CHROMIUM AND NITRATE AQUEOUS ADSORPTION

(Accepted for publication in *Environmental Management* **2021**)

3.1 Abstract

Biochar adsorbents remove environmental pollutants and the remediation of Cr(VI) and nitrate contaminants are considered here. Cr(VI) is a proven carcinogen causing serious health issues in humans and nitrate induced eutrophication causes negative effect on aquatic systems around the world. Douglas fir biochar (DFBC), synthesized by fast pyrolysis during syn gas production, was treated with aniline. Then, a polyaniline biochar (PANIBC) composite containing 47 wt.% PANI was prepared by precipitating PANI on DFBC surfaces by oxidative chemical polymerization of aniline in 2M HCl. This modified biochar was characterized by obtaining its point of zero charge (PZC), BET (N_2) surface area, thermogravimetric analysis (TGA), scanning electron microscopy (SEM) morphology and surface elements and oxidation states by X-ray photoelectron spectroscopy (XPS). PANIBC exhibited positive surface charge below pH 3, making it an outstanding adsorbent, for Cr(VI) removal. Cr(VI) and nitrate removal mechanism are presented based on XPS analysis. DFBC and PANIBC Cr(VI) and nitrate adsorption data were fitted to Langmuir and Freundlich isotherm models with a maximum Langmuir Cr(VI) and nitrate adsorption capacities of 150 mg/g and 72 mg/g, respectively. Adsorption capacities verses

temperature studies revealed that both Cr(VI) and nitrate adsorption are endothermic and thermodynamically favored. Regeneration studies were conducted on both DFBC and PANIBC using 0.1M NaOH and PANIBC exhibited excellent sorption capacities for Cr(VI) and nitrate in lake water samples and in the presence of competitive ions.

3.2 Introduction

A polyaniline biochar hybrid composite was developed for remediation of water contaminated with chromium and nitrate anions. A low cost and green biochar that provides a high surface area supports for conducting polyaniline resulting higher capacity for adsorbates. Interest in large scale water remediation is growing because with population growth has increased nitrate, fluoride, phosphate, and chromium water pollution.[1,2,3] Polyaniline has been coated on various substrates and used in adsorption studies. Its amine and imine groups can undergo redox reactions and reduce heavy metals with higher valence to lower valency by oxidizing its emeraldine to its pernigraniline form.[4] Polyaniline coated onto ethyl cellulose removed Cr(VI) with a 38.76 mg/g[4] adsorption capacity and a PAN/ferricyanide composite removed 41.62 mg/g Cu(II).[5] However, its behavior as an adsorbent coating on biochar has not been explored. Biochar is used to remove toxic compounds by adsorption onto the surface. In addition, biochar hydroxyl groups can act as electron donors to reduce Cr(VI) into Cr(III). However lower adsorption capacity reduces the application of some untreated biochar for pollution abatement. To improve the Cr(VI) and nitrate removal capacities, we modified Douglas fir biochar with polyaniline.

Chromium is most often found in the environment as hexavalent Cr(VI).[6] The World Health Organization (WHO), recommends a maximum permissible level of chromium in drinking water of 0.05 mg/L.[7] Chrome electroplating, leather tanning, porcelain and ceramics manufacturing, wood preservatives, paints/pigments, and effluents from chemical plants are major

anthropogenic sources of environmental Cr.[6,8] Green, biocompatible, reusable and high surface area nanomaterials, such as biochar, are becoming increasingly popular in the removal of metal cations from contaminated water.[9,10,11] Iron containing nanomaterials including magnetite supported on biochar[10] nano zerovalent iron (nZVI),[12] reduced graphene oxide-nano zero value iron (rGO-nZVI),[13] starch and sodium carboxymethyl cellulose coated Fe and Fe /Ni nanoparticles[14] have good Cr(VI) adsorption properties.

Septic tanks, animal manures, and fertilizers are common non-point sources that release nitrate to surface and ground waters.[1,15] Over 7.5 million tons of nitrogenous fertilizers are used in US agriculture[16] each year and a significant fraction is washed away in stormwater runoff.[17,18] The WHO specified a maximum nitrate contaminant level in drinking water of 11 mg/L(as nitrate-nitrogen)[7] while stormwater runoff can have concentrations as high as 16 mg/L.[19] Excess nitrates leaching to ground and surface water cause eutrophication of aquatic systems due to enrichment of nutrients. This ultimately leads excessive plant and algal bloom which causes deterioration of ecological system.[20,21] Reverse osmosis, electrodialysis, ion-exchange, and biodenitrification methods have been used to remediate nitrate from water, but these techniques are expensive and produce waste.[22,23,24] These limitations have invoked the need of other alternative approaches.

Biochar applications as a soil stabilizer, where it can preserve or add nutrients[25,26] and as an adsorbent for harmful pollutants, is increasing.[17] It is derived by fast or slow pyrolysis of plant biomass in the absence of or in an oxygen deficient atmosphere.[27,28] Over a decade of research has established renewable biochar's ability to remove heavy metals and organic contaminates from water,[29,30,31] sometimes exhibiting comparable or better adsorption capacities than commercially activated carbon.[32] Biochar's high surface area, porosity[33,34] and ability to be further modified[35,36] all contribute to high sorption capacities. Biochar surface area, ash content, pore distribution and

functionalities can all be tailored by activation.[37,38,39] Modification with other supported phases like Fe_3O_4 can provide additional adsorption capacity for metal ion removal from aqueous solutions.[40] Sorption occurs between positively charged metal ions coordinating with delocalized π electrons in electron-rich fused aromatic rings on the carbonaceous biochar surfaces.[41]

Organic polymers comprised of electron-rich nitrogen moieties, such as polyaniline, are capable of binding cationic metal ions while protonated amines can attract negatively charged oxyanions. Therefore, environmentally stable conducting polyaniline (PANI), when coated on high surface area biochar, has the potential to result in an excellent adsorbent composite. Aniline monomers in acidic media undergo *in-situ* oxidative polymerization electrochemically or chemically forming PANI. Different forms of PANI can be prepared by varying the pH or by applying different potentials. Based on the amine/imine ratio and the extent of protonation, PANI can be tuned to its (I) nonconducting, fully reduced leucoemeraldine-base (LB-PANI), (II) fully oxidized pernigraniline-base (PB-PANI), (III) conducting emeraldine-salt (ES-PANI), and (IV) semiconducting partially oxidized, emeraldine-base (EB-PANI).[42,43,44,45] This polymer has many applications due to its conductivity including dye-sensitized solar cells,[46,47] organic light emitting diodes,[48] chemical and biosensors,[49,50] supercapacitors,[51,52] and anticorrosion materials[53,54]. Herein we use an in-situ oxidative polymerization method to form a composite containing biochar and polyaniline (PANIBC). We present composite sorption kinetics, isotherms and possible Cr(VI) and nitrate adsorption mechanisms. This PANIBC was used in regeneration studies and was also tested in different aqueous model systems to remove Cr(VI) and nitrate representative of real world contaminated water samples.

3.3 Materials and Methods

3.3.1 Chemicals and Equipment

All chemicals used (aniline, ammonium persulfate, potassium dichromate, sodium nitrate and auxiliaries) were analytical reagent grade (AR) (Sigma-Aldrich, Fischer) unless otherwise specified. Aqueous stock solutions of chromium and nitrate were prepared in deionized (DI) water (Millipore-Q system). The pH of these solutions was adjusted using 1 M, 0.1 M, and 0.01 M HCl or NaOH and measured using a Hanna HI 2211 pH meter.

Douglas fir biochar (Biochar Supreme Inc., Everson, WA) is a waste byproduct of wood gasification from the timber industry. Green wood chips (~3 inches) were introduced into an air-fed updraft gasifier at 900-1000 °C for a 1-10 s residence time in the absence of air. Biochar particles (~2 cm) were collected, rinsed with water to remove water soluble organic residues, fine surface particles and other impurities. They were dried at room temperature for 24 h, ground, sieved (0.1-0.5 mm) and stored in a closed container until use. Hereafter they are referred as DFBC.

3.3.2 Preparation of polyaniline (PANI) / biochar composite

Polyaniline (PANI) was synthesized by modifying a previously reported method.[55] Briefly, doubly distilled aniline (4.0 mL) dissolved in HCl (2 M, 40.0 mL) was mixed with DFBC (1.00 g) and sonicated for 1h. Ammonium persulfate (APS) (2.50 g) dissolved in HCl (2 M, 40.0 mL) was added dropwise to the aniline/HCl/DFBC mixture. This mixture was continuously mixing in an ice bath (0-5 °C) for 4 h to achieve *in-situ* polymerization. A black-green solid was produced as PANI precipitation occurred onto DFBC surfaces. This dark PANI-DFBC hybrid was rinsed with 2M HCl and separated by vacuum filtration. This solid product was further rinsed several times with distilled water and ethanol and air dried at 50 °C at 1 atm for 24 h in a vacuum oven to give

1.92 g of polyaniline/ biochar composite, referred to hereafter as PANIBC. Based on the weight gain, this PANIBC contained 47% wt.% PANI.

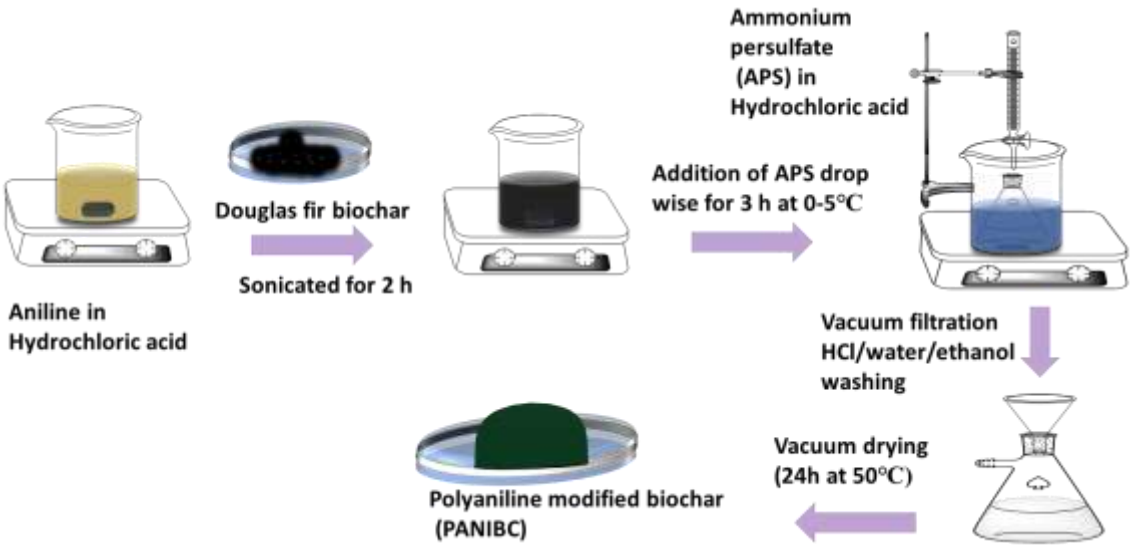

Scheme 3.1 Synthesis of polyaniline modified biochar (PANIBC)

3.3.3 Characterization of DFBC and PANIBC

DFBC and PANIBC surface morphologies were examined by a JEOL JSM-6500F scanning electron microscope (SEM) operated at 5 kV, coupled to an energy dispersive X-ray (EDX) detector. Transmission electron microscopy (TEM) analyses were carried out using a TEM JEOL model 2100 operated at 200 kV, while TEM/EDX analyses were performed using an Oxford X-max-80 detector. XPS analyses were conducted with a Thermo Scientific K-Alpha XPS system. A monochromatic 1486.6 eV (Al Kα line) X-ray source was used with a spot size of 400 μm^2 with a maximum analytical penetration depth of 100 Å. The Brunauer-Emmet-Teller (BET) surface

areas and total pore volumes of both DFBC and PANIBC were determined by N_2 adsorption-desorption isotherms using a Micromeritics Tristar II Plus 3030 surface area analyzer at ~277 K. Thermogravimetric analyses (TGA) were carried out using a Mettler TGA/DSC thermogravimetric analyzer (TGA/DSC 1, STARe System, Mettler Toledo, USA) at a heating rate of 10 ^{0}C/ min from 50 ^{0}C to 1000 ^{0}C under both an air and nitrogen atmosphere. Fourier Transformed Infrared spectroscopic (FTIR) analysis (ATR mode) was employed using a Thermo Scientific iD-5 instrument. C, H and N percentages were obtained using a %CHN analyzer (CHN: ASTM D5291). Ash content of DFBC and PANIBC were found by incinerating 1 g of each sample at 650 °C for 4 h in a muffle furnace and then comparing the initial and final masses. Points of zero charge (PZC) of DFBC and PANIBC surfaces were determined in 0.01M NaCl solutions at pH values from 2 to 10. Biochar (0.05 g) was mixed with 50 mL of these solutions adjusted to each pH with 0.1 M HCl or 0.1M NaOH for 24 h. PZC was determined by a plot of equilibrium pH vs. initial pH.

3.3.4 Batch adsorption and desorption studies

Cr(VI) and nitrate equilibrium adsorption studies of DFBC and PANIBC investigated the effect of solution pH, contact time and adsorbate concentration. The effect of pH on adsorption employed three replicates at each pH from 2 to 10 in 25.0 mL solutions containing 50 mg L^{-1} of analyte. Effect of contact time on adsorption was monitored by varying the equilibrium time for each analyte. Adsorption studies employed 0.025 g of biochar with 25.00 mL of each adsorbate at different concentrations. All sample mixtures were sealed in plastic vials and shaken for 24 h to reach the equilibrium. After equilibration, the solutions were filtered (Whatman filter paper No.1) and the chromium concentrations remaining in each filtrate were determined by atomic absorption spectroscopy (AAS) (Shimadzu AA-7000). The residual nitrate concentration was determined by

liquid chromatography (LC) coupled with a UV-Vis diode array detector at 210 nm. Standard errors were calculated using standard deviations for three replicates. The amount of adsorbate adsorbed per unit mass of biochar at equilibrium, Q_e (mgg^{-1}) was obtained from $Q_e = \frac{(C_i - C_e)V}{W}$ and used for adsorption isotherm analysis. Here C_i and C_e denote the initial and equilibrium concentration of adsorbate in mg L^{-1}, V, is the volume of adsorbate solution in mL, and W is the weight of biochar in g.

Three adsorption/desorption cycles after adsorption of Cr(VI) and nitrate on to both PANIBC and DFBC were carried out. Initial Cr(VI) and nitrate concentrations were 60 mg/L and 100 mg/L at pH 2 and 6, respectively. DFBC and PANIBC (0.20 g of each) were separately added to 200 mL of each adsorbate solution in a plastic bottle at 25 °C. They were shaken until reaching equilibrium. Then, the residual biochar was washed several times with deionized water and oven dried at 50 °C for 8 h. Next, desorption experiments were carried out by stripping nitrate and Cr(VI) in 0.1 M NaOH. Desorbed Cr(VI) and nitrate were analyzed by AAS and LC respectively.

3.3.5 Competitive batch sorption studies and sorption on natural water system

Competitive batch sorption studies on DFBC and PANIBC for both Cr(VI) and nitrate were conducted with fluoride, chloride, and carbonate. Final concentrations (2, 5 and 10 mg/L) of each anion were spiked in to deionized water containing Cr(VI) (50 mg/L, pH 2) or nitrate (50 mg/L, pH 6). DFBC or PANIBC (25 mg) were individually equilibrated with water samples (25 mL) at room temperature in plastic vials (50 mL) at a shaking speed of 200 rpm for Cr(VI) 4h, and nitrate 2 h. Samples were filtered and the residual aqueous adsorbate concentrations were obtained by liquid chromatography (LC) for nitrate and atomic absorption spectroscopy for Cr(VI).

Cr(VI) and nitrate removal capacities from a natural water system was analyzed by spiking Cr(VI) (50 mg/L) or nitrate (50 mg/L) into natural lake water (pH 8.3) (Sanderson lake, Starkville, MS) at room temperature and following the same sorption process. This was repeated for the lake water samples buffered in to pH 2 for Cr(VI) and pH 6 for nitrate.

3.4 Results and Discussion

3.4.1 Surface characterization

Table 3.1 DFBC and PANIBC elemental composition and surface morphology parameters[a]

Elemental content	DFBC (wt.%)	PANI (wt.%)	PANIBC (wt.%)
C	80.42	60.95	71.70
H	2.08	5.13	3.54
N	1.21	11.53	5.59
O[b]	13.51	-	7.77
H/C	0.03	0.08	0.05
O/C	0.17	-	0.11
N/C	0.02	0.19	0.07
(O+N)/C	0.18	-	0.19
Ash	2.78	9.40	11.40
S_{BET}[c](m^2/g)	466	27	8.92
V_T[c](cm^3/g)	0.107	0.006	0.002
S[c](A^0)	18.6	9.64	9.18

[a]C, H and N wt.% were obtained by combustion analysis
[b] The organic oxygen content was calculated by subtracting the wt.% of C, H, N and ash from the total wt.% (100 %) and doesn't include the O present as metal oxides in the ash.
[c]S_{BET} stands for BET specific surface area; V_T for total pore volume; S for average pore size of biochar prepared.

DFBC had a 466 m^2/g Brunauer-Emmett-Teller (BET) surface area which sharply dropped to 8.9 m^2/g upon modification by polyaniline. The DFBC average pore size dropped ~50% from 18.6 to 9.18 Å and pore volume was reduced from 0.107 to 0.002 cm^3/g. These values were compared with polyaniline. PANI exhibited a 0.006 cm^3/g pore volume and 9.64 Å of pore diameter. Polyaniline deposition blocked micropores and ultramicropores at the char surface limiting N_2 access and adsorption, decreasing BET-determined surface area, pore size and pore volume. SEM micrographs of DFBC and PANIBC of different magnifications are shown in Fig. 3.1. DFBC exhibits a porous classical pine morphological char structure verses PANIBC which exhibits a distinctive tangled tubular fibrous structure under different magnification. A curved rod-shaped network-like polyaniline aggregated deposit is observed covering the biochar surface in PANIBC. After nitrate or chromium adsorption onto PANIBC, surface morphology changes were not observed. Fig. 3.1 depicts the TEM elemental mapping images of DFBC, PANIBC and both Cr(VI)- or nitrate-laden PANIBC. TEM-EDX elemental mapping on DFBC and PANIBC (Fig. B.1) after adsorption of these adsorbates confirms the presence of Cr and nitrogen, respectively.

DFBC has a fairly hydrophobic surface since the oxygenated functional group surface density is low after exposure to fast pyrolysis at 900 – 1000 °C. Elemental analysis of DFBC confirms low H/C (0.03), O/C (0.17) and N/C (0.02) wt. ratios as well as a low polarity index (O+N)/C (0.18) (Table 3.1). These values confirm a more hydrophobic and non-polar DFBC nature compared to a variety of other biochar varieties produced at lower pyrolysis temperatures.[56,57] Pure PANI exhibited a higher %N (11.53) than DFBC (1.21%) and PANIBC (5.59%). H/C and N/C values obtained for PANI were 0.08 and 0.19 respectively. PANIBC exhibited H/C (0.05), O/C (0.11) and N/C (0.07) wt. ratios and a (O+N)/C polarity index of (0.19).

PANIBC has substantial increase in the amount of nitrogen (5.59%) verses DFBC (1.21%). This was introduced by precipitation of PANI particulates formed by the oxidative polymerization of aniline in solution. These can be reflected in the FTIR and XPS spectra. The wt.% of PANI on the PANIBC composite calculated was 47% based on the weight gain found in synthesis. %N of PANIBC calculated based on the elemental analysis N wt.% data of PANI was 5.53%. This was in close agreement with the %N (5.53%) obtained for PANIBC from elemental analysis. %C and %H in the PANIBC were also calculated based on the elemental analysis %C and %H data obtained from PANI and DFBC separately. They were found to be C (71.08%) and H (3.54%). These C and H percentages calculated were also very close to C% and H% (71.70, 3.54%) obtained on PANIBC by elemental analysis.

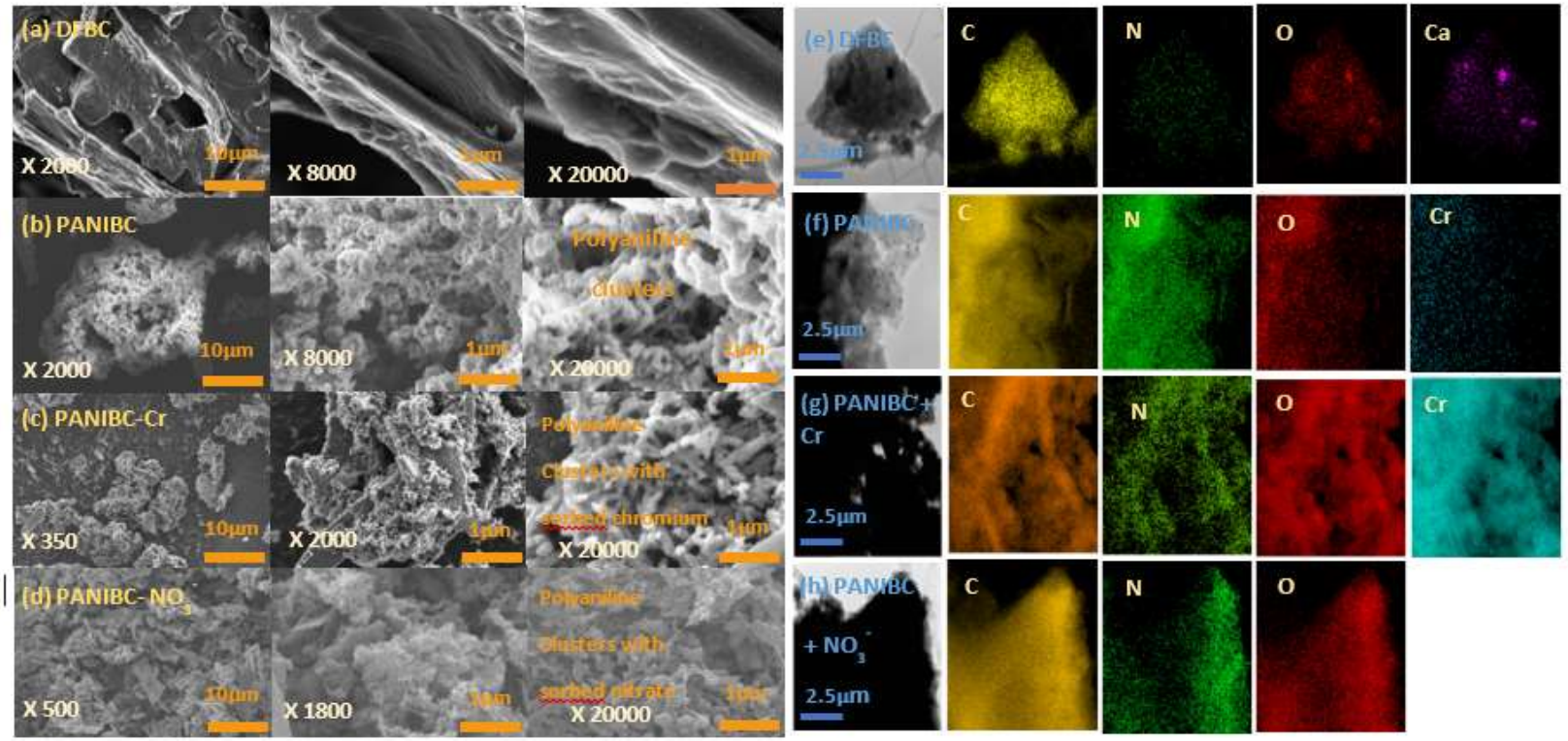

Figure 3.1 SEM micrographs and TEM-EDX elemental mapping images

SEM micrographs of (a) DFBC (b) PANIBC (c) chromium-laden PANIBC and (d) nitrate-loaded PANIBC. Oxidative polymerization of aniline deposits spindle-like aggregated mass of PANI on DFBC. TEM-EDX elemental mapping images of (e) DFBC, (f) PANIBC, (g) chromium-laden PANIBC and (h) nitrate-laden PANIBC. SEM and TEM images were obtained at the Institute of Imaging and Analytical Technologies (I^2AT), Mississippi State University.

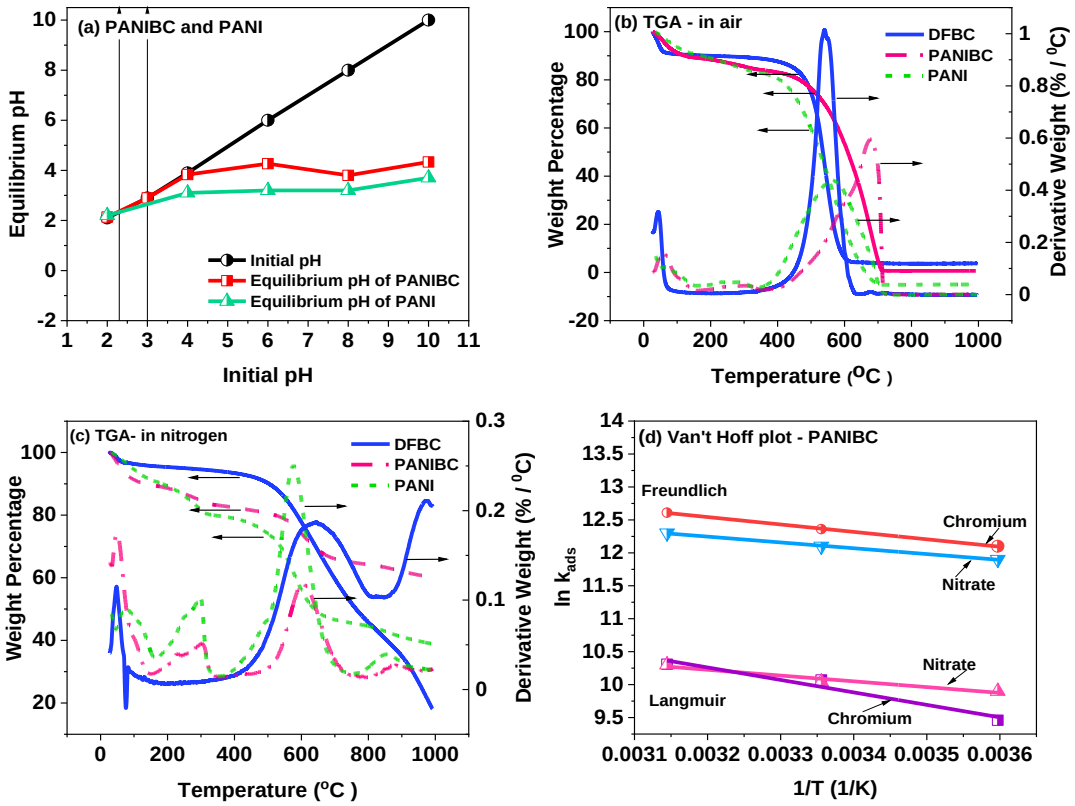

Figure 3.2 Point of zero charge (PZC) measurements for (a) PANIBC and PANI, Thermogravimetric analysis (TGA) for DFBC and PANIBC at a 10 °C/min heating rate in (b) air, (c) nitrogen, (d) Van't Hoff plot for Cr(VI) and nitrate adsorption on PANIBC

The points of zero charge (PZC) were, DFBC (9.2) (Fig. B.2), PANI (2.2) and PANIBC (3.0) (Fig. 3.2(a)) using the pH drift method.[58] The high PZC of DFBC is due to carbonate and oxide formation from Ca, Mg, K and decarboxylation during the 900-1000 °C pyrolysis. PANI has a low PZC value as its synthesized in highly acidic medium hence have surface adsorbed protons.[59] PANIBC's acidic PZC is consistent with other literature reports of materials coated with PANI. Polyaniline/multiwalled carbon nanotube composites exhibited a PZC of 2.12.[60] A polyaniline-

coated lignocellulose PZC of 4.5 was reported from a synthesis in a highly acidic medium, where protons adsorbed on the surface.[59]

Cr(VI) adsorption is highly pH dependent because negatively charged surfaces repel the Cr(VI) oxyanions, $HCrO_4^-$ predominating from pH 1 to 6 and CrO_4^{2-} existing above pH 6.[61] At high Cr(VI) concentrations (>1 g/L), $HCrO_4^-$ dimerizes to form dichromate ($Cr_2O_7^{2-}$). Cr(VI) becomes chromic acid (H_2CrO_4) at pH < 1. Adsorption of Cr(VI) on DFBC was poor from pH 2 to 8 except at pH 2 (Fig. 3.3(a)). Despite being positively charged below pH 9.3, DFBC only adsorbs Cr(VI) reasonably around pH 2, suggesting that $HCrO_4^-$ must experience strong electrostatic attractions to be removed from water. $HCrO_4^-$ and CrO_4^{2-} anions are strongly exothermically solvated by water. Similar results were reported for Cr(VI) adsorption by KOH-activated DFBC.[62] Conversely, PANIBC has a large Cr(VI) adsorption pH window. At pH 2, 90% Cr(VI) removal occurred and this only dropped to 80% at pH 8 (Fig. 3.3). Langmuir adsorption capacity for Cr(VI) adsorption at pH 6 was 86.5 mg/g (Fig. B.3). High Cr(VI) uptake at pH 2 is due to electrostatic attractions between $HCrO_4^-$ and large number of protonated amine groups present on PANI and due to H bonding and ion exchange.

Fig. 3.4(a). illustrates DFBC is a mediocre nitrate sorbent (22% removed at pH 2 to 18% at pH 6) Nitrate uptake by DFBC dropped to ~5% above pH 6. PANIBC is a better nitrate adsorbent. It gave 32% removal at pH 2, which then improved to 65% at pH 4, 60% at pH 6 and 55% at pH 8. This adsorption pattern might result from H bonding and ion exchange on PANIBC surface and pH 6 was selected as the optimum practical pH for further nitrate adsorption studies for both DFBC and PANIBC considering that most natural water stream pH values are closer to neutral.

3.4.1.2 FTIR analysis

The FTIR vibrational bands (Fig. B.2) observed for PANI at 1544 and 1424 cm^{-1} are assignable to the C=C stretching vibration in quinonoid (Q) and benzenoid (B) rings, which are shifted to 1580 and 1440 cm^{-1} in PANIBC, respectively. This corresponds to the extent of oxidation and reduction of PANI on PANIBC.[63] The bands appearing at 1302 and 1275 cm^{-1} in PANI verses 1325 and 1224 cm^{-1} in PANIBC correspond to C-N stretching adjacent to the benzenoid ring and the C-$N^{\bullet+}$ polaron stretching band.[64] The strong absorptions centered at 1144 and 1166 cm^{-1} are attributed to the vibrational mode of the =NH^{+}- structure accompanying the high degree of electron delocalization in Q=NH^{+}-B or B–$NH^{\bullet+}$-B.[63,65] They appeared at 1198 and 1069 cm^{-1} in PANI.[66] Bands appearing from 750-850 cm^{-1} are due to the C–H out-of-plane bending vibrations of 1,4-disubstituted aromatic rings.[64,67] PANIBC antisymmetric stretching vibrations of CH_2 appear at 2944 cm^{-1}.[68]

3.4.1.3 Thermogravimetric analysis (TGA) of biochar

DFBC and PANIBC each underwent two distinct weight losses under air during TGA (Fig. 3.2 (b). Both lose adsorbed water around 100 ℃. A similar weight loss was observed for pure PANI. The major weight loss for DFBC occurring from ~550 to 600 ℃ is due to thermal decompositions including decarboxylation, decarbonylation and carbon skeleton changes during further carbonization. PANIBC begins a slow weight loss at lower temperature (~350 ℃) but transitions into to a major weight loss from 575-700 ℃, indicating a thermally stable char formation develops as the PANI component of PANIBC decomposed. PANI gives a major wt. loss below this temperature, indicating the PANI in PANIBC interacts with the DFBC products to give a more thermally stable intermediate material during decomposition. Under nitrogen, PANI and

PANIBC both decompose at about the same temperature, but this is now lower than the major wt. loss temperature of DFBC from 600-750 °C. However, the presence of nitrogen leads to high residual weights. PANIBC gave a 60% residual wt. verses 20% for DFBC and 40% for PANI at 1000 °C. Under nitrogen, PANIBC gives a small weight loss around 300 °C from elimination of chloride as HCl. Similarly, PANI eliminated adsorbed HCl.[4,69] This is not prominent in the TGA run in the oxygen since other large mass loses are occurring in this region.

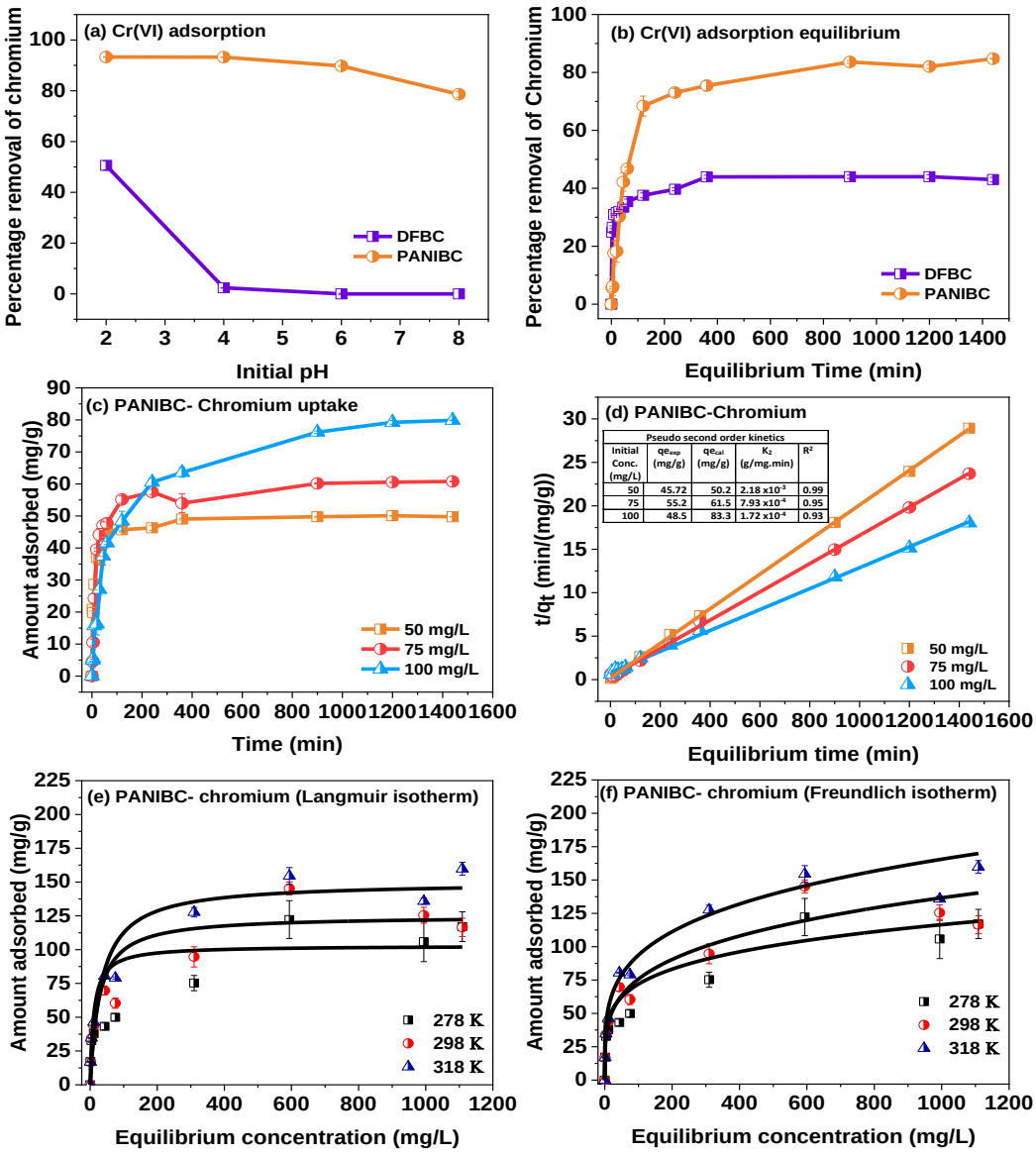

Figure 3.3 Cr(VI) adsorption on PANIBC

(a) Effect of solution pH on chromium adsorption onto DFBC and PANIBC (50 mg/L), (b) percentage of chromium removal verses time by DFBC and PANIBC, 100 mg/L. 25 mL of aqueous chromium at 25 °C with 25 mg adsorbent doses, (c) Chromium uptake on PANIBC (25 mg) verses time at initial concentrations of 50, 75, 100 mg/L at pH 2, (d) Pseudo second order model plot for Cr(VI) adsorption on PANIBC at pH 2 with Cr(VI) concentrations of 50, 75, 100 mg/L, (e) Langmuir and (f) Freundlich isotherm plots for chromium adsorption on PANIBC at 278, 298, and 318 K at pH 2, Error bars represent standard deviation of three replicates for each measurement.

3.4.2 Adsorption kinetics and thermodynamic studies

Cr(VI) (Fig. 3.3) and nitrate (Fig. 3.4) removal on DFBC and PANIBC were plotted verses the equilibrium time. PANIBC removed higher percentages of Cr(VI) and nitrate than that of DFBC. The Cr(VI) and nitrate uptake rates were fast initially because sufficient adsorption sites were available. The rate slowed with time due to increasing saturation of the adsorbent by the adsorbates. Cr(VI) reached the equilibrium after 3 h after a 40% removal on DFBC and a 68% on PANIBC, using 100 mg/L of Cr(VI) at pH 2(Fig. 3(b)). The Cr(VI) uptakes after 3 h at pH 2 (Fig. 3.3(c)) by PANIBC were 46, 56, 60 mg/g, respectively, when the initial Cr(VI) concentrations were increased from 50, 75, and 100 mg/L. Nitrate removal capacity on DFBC was initially very low (~4%) and remained almost constant after > 1500 min using 75 mg/g of adsorbate at pH 6 (Fig. 3.4 (b)). At these conditions, PANIBC removed 48% of the nitrate after 2 h and this remained constant for 24 h. The amount of nitrate adsorbed on PANIBC was measured at concentrations of 25, 50, and 75 mg/L (Fig. 3.4 (c)). The adsorption capacities were 12, 19, 32 mg/g, respectively, after 2 h at pH 6 when nitrate concentrations increased from 25 to 50 to 75 mg/L. Experimental data for Cr(VI) (Fig. 3.3(d)) and nitrate (Fig. 3.4(d)) adsorption on PANIBC fitted well to the pseudo second order kinetic model $t/q_t = t/qe + 1/k_2 q_e^2$, with linear regression coefficients (R^2) close to unity. Here, t is the contact time, q_e denotes the amount adsorbed (mg/g) at the equilibrium time, q_t is the amount adsorbed at time t (mg/g) and k_2 is the second order rate constant (g/mg.min).

The temperature effect on the Cr(VI) and nitrate adsorption capacities of PANIBC was monitored at 5, 25 and 45 °C (Fig. 3.2 (d)). All three capacities increased as temperature rose from 5 to 45 °C. The Van't Hoff equation, $\ln K_{ads} = \Delta H°/R\ (1/T) + \Delta S°/R$ was used to calculate the changes in Gibbs free energy (ΔG), enthalpy (ΔH), and entropy (ΔS) for the adsorption of Cr(VI) or nitrate onto PANIBC (Table 3. 2) and DFBC (Table. B.1). The isotherm constants at 5, 25, 45

°C were converted into dimensionless constants, via multiplying by the liquid phase density (1×10^6 mg/L).[70] The ΔH, and ΔS values for Cr(VI) adsorption based on Langmuir model isotherm constants were 15.75 kJ/mol and 0.14 kJ/mol K and those for the Freundlich model were 9.35 kJ/mol, 0.13 kJ/mol K. The ΔH, and ΔS values for nitrate adsorption on PANIBC, from Langmuir and Freundlich model isotherm constants were (7.28 kJ/mol, 0.11 kJ/mol K) and (7.33 kJ/mol, 0.13 kJ/mol K) respectively. The positive values of ΔH and ΔS indicate that if the adsorption of both oxyanion, Cr(VI) and nitrate on PANIBC are both endothermic (ΔH = +) processes they must occur with an increase in entropy (more randomness) as these solvated ions from solution are adsorbed on the adsorbent surface sites at the solid/liquid interface. Gibbs free energy values, (ΔG) were negative at all three temperatures for both Cr(VI) and nitrate sorption. The magnitude of ΔG increased as the temperature rose, indicating adsorption is thermodynamically spontaneous and driven entropically under experimental conditions.

Table 3.2 Thermodynamic parameters for chromium and nitrate adsorption on PANIBC

		T (K)	R^2	K_{ads}	$\ln K_{ads}$	ΔG^0 (kJ/mol)	ΔH^0 (kJ/mol)	ΔS^0 (kJ/mol K)
Cr	Langmuir	278	0.915	1.28×10^4	9.46	-23.17	15.75	0.14
		298		2.37×10^4	10.07	-25.97		
		318		3.00×10^4	10.31	-28.77		
	Freundlich	278	0.998	1.80×10^5	12.10	-26.79	9.35	0.13
		298		2.34×10^5	12.36	-29.39		
		318		3.00×10^5	12.61	-31.99		
nitrate	Langmuir	278	0.912	2.00×10^4	9.90	-23.3	7.28	0.11
		298		2.30×10^4	10.04	-25.5		
		318		3.00×10^4	10.30	-27.7		
	Freundlich	278	0.998	1.48×10^5	11.90	-28.81	7.33	0.13
		298		1.80×10^5	12.10	-31.41		
		318		2.20×10^5	12.30	-34.01		

3.4.3 Adsorption isotherms

Cr(VI) and nitrate adsorptions on PANIBC Fig. 3.3 and 3.4 and DFBC (Fig. B.4) were conducted at 278, 298, 318 K. Langmuir[71] and Freundlich[72] isotherm model fits were made using Origin Pro 2020 software. Cr(VI) batch equilibrium sorption studies were conducted at Cr(VI) concentrations ranging from 10-1000 mg/L for 3 h at pH 2 on PANIBC and DFBC. Similar nitrate (10-500 mg/L) equilibrations were run for 2 h at pH 6. Both isotherms' parameters were evaluated by nonlinear regression fitting Table. 3.3. Cr(VI) exhibits the higher Langmuir adsorption capacities (150.0 on PANIBC and 49.0 mg/g on DFBC at 318 K) than nitrate. Langmuir adsorption capacities for nitrate at 298 and 318 K are (50.0, 72.0 mg/g) on PANIBC and (6.0, 10.6 mg/g) on DFBC, respectively. Cr(VI) and nitrate adsorption data fitted well to both Langmuir and Freundlich isotherm models have linear regression coefficients (R^2) greater than 0.97 for both Cr(VI) and nitrate sorption. The Freundlich fittings were better overall, but the differences were not sufficient to support mechanistic differences in their derivation on way or the other.

Cr(VI) and nitrate uptakes were then obtained on a biochar-PANI composite prepared under same conditions already described for PANIBC, but the amount of aniline loaded was greatly reduced on to the char (PANIBC-LA). This contained 9% of PANI and exhibited 32.9 m^2/g surface area, 0.009 cm^3/g pore volume and 11.3 Å pore diameter. The adsorption capacity for Cr(VI) solution (150 mg/L, pH 2, 25 °C) on PANIBC was 104.26 mg/g verses 75.31 mg/g for PANIBC-LA (Table B.2). Amount of Cr(VI) adsorbed per square meter of surface for PANIBC was 11.7 mg/m^2 verses 2.3 mg/m^2 for PANIBC-LA. However, the amount of Cr(VI) adsorbed per gram of PANI on these two were 217.6 and 828.5 mg/g respectively. Adsorption capacities obtained for a nitrate solution (50 mg/L, pH 6, 25 °C) on PANIBC and PANIBC-LA were 25.5 and 16.6 mg/g, respectively (Table B.3).

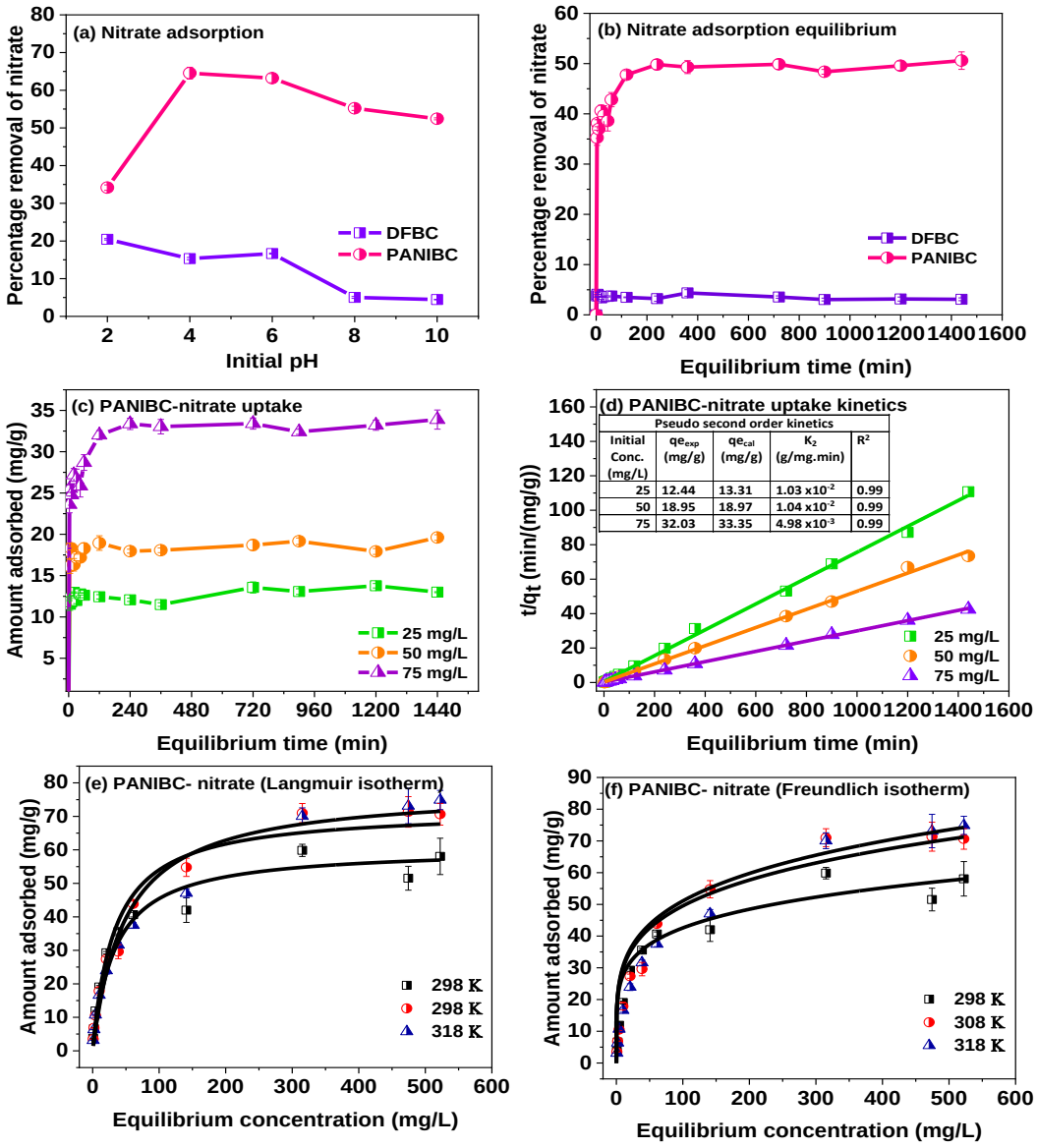

Figure 3.4 Nitrate adsorption onto PANIBC

(a) Effect of solution pH on nitrate adsorption onto PANIBC, (50 mg/L) (b) percent nitrate removal verses time on DFBC and PANIBC, 25 mL of aqueous nitrate (75 mg/L) solution at 25 °C with 25 mg adsorbent doses (c) Amount of nitrate adsorbed on PANIBC verses time from initial 25, 50, 75 mg/L concentrations at pH 6, (d) Pseudo second order model plot for nitrate adsorption on PANIBC at pH 6 from 25, 50, 75 mg/L concentrations, (e) Langmuir and (f) Freundlich isotherm plots for nitrate adsorption on PANIBC at 278, 298, and 318 K at pH 6, Error bars are the standard deviations of three replicates.

Table 3.3 Langmuir and Freundlich isotherm parameters[a] for Cr(VI), and nitrate adsorption on PANIBC and DFBC

Analyte	Adsorbent	Isotherm parameters		Temperature 278 K	298 K	318 K
Cr(VI)	PANIBC	Langmuir	q_o (mg/g)	90.0	114.9	150.0
		$q_e = \frac{q_0 K_L C_e}{(1 + K_L C_e)}$	K_L(L/mg)	0.0128	0.0287	0.0300
			R^2	0.970	0.981	0.985
	DFBC		q_o (mg/g)	40.0	42.43	49.0
			K_L(L/mg)	0.054	0.059	0.060
			R^2	0.990	0.988	0.971
	PANIBC	Freundlich	K_F (L/g)	18.0	23.24	30
		$q_e = K_F C_e^{(1/n)}$	n	3.866	3.9	4.037
			R^2	0.998	0.997	0.998
	DFBC		K_F (L/g)	18.0	18.5	19.36
			n	7.8307	8.0309	8.2
			R^2	0.992	0.995	0.990
nitrate	PANIBC	Langmuir	q_o (mg/g)	50.0	63.0	72.03
		$q_e = \frac{q_0 K_L C_e}{(1 + K_L C_e)}$	K_L(L/mg)	0.02	0.0229	0.03
			R^2	0.975	0.987	0.992
	DFBC		q_o (mg/g)	6.0	8.01	10.57
			K_L(L/mg)	0.022	0.024	0.03
			R^2	0.971	0.988	0.983
	PANIBC	Freundlich	K_F (L/g)	14.73	18	22
		$q_e = K_F C_e^{(1/n)}$	n	3.9	1.56	5.47
			R^2	0.987	0.997	0.995
	DFBC		K_F (L/g)	2.0	2.5	2.9
			n	3.36	3.52	4.13
			R^2	0.991	0995	0.998

Q_0_monolayer adsorption capacity (mg/g), K_L -Langmuir isotherm constant (L/mg),
K_f - Freundlich isotherm constant (L/g), n - a constant indicative of the intensity of the adsorption,
R^2 - regression coefficient

3.4.4 XPS analysis

Surface region specific quantitative analysis of atomic ratios, adsorbent surface functions and oxidation states, including the adsorbed chromium, was conducted by XPS of DFBC, PANIBC and chromium- and nitrate-laden PANIBC. The low resolution survey scan (LR-XPS) of DFBC detected the C and O present on the surface. After performing oxidative aniline polymerization on DFBC (PANIBC) C, O, N, and Cl were detected on the surface, illustrating polymerization has occurred depositing PANI on the char (Fig. B.5). LR-XPS of PANIBC surfaces after chromium or nitrate sorption gives the presence of the elements shown in Fig. B.5. HR-XPS of DFBC and PANIBC gave surface region atomic percentages of C and O (92.8, 7.19) and for PANIBC C, O, N (82.87, 3.45, 13.25 (Table B.4, B.5), respectively, illustrating that oxidative polymerization of aniline deposited far more nitrogen-containing surface functions. Cr(VI) and nitrate atomic percent uptakes on PANIBC at pH 2 and 6 respectively, were 9.33% for Cr(VI), and 13.28% for nitrogen, 7.67% for oxygen on PANIBC. The larger Cr uptake on the surface was obvious. These %N and %O values cannot definitively establish nitrate or nitrite uptake.

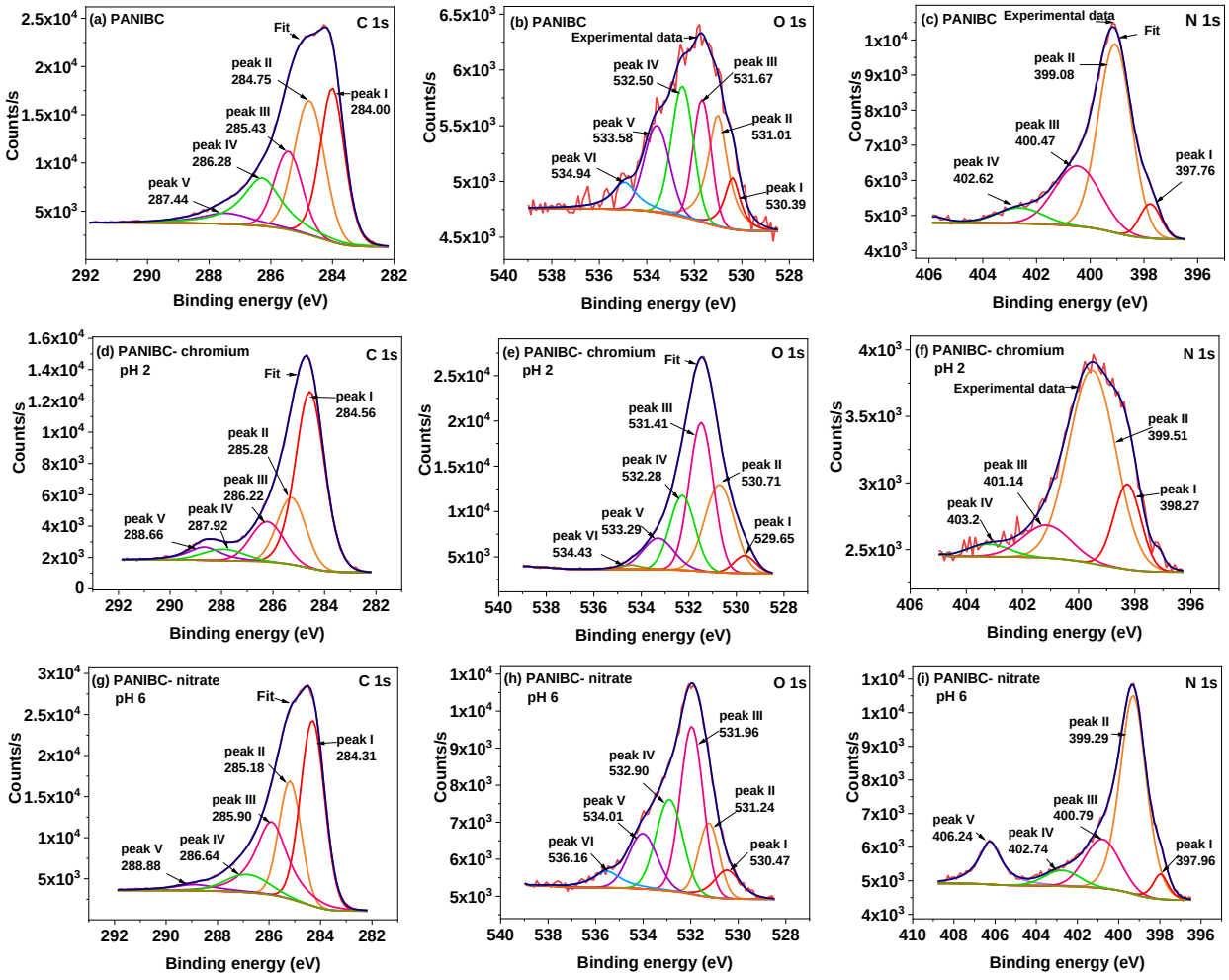

Figure 3.5 HR-XPS for PANIBC, PANIBC-Cr(VI) and PANIBC-nitrate

High resolution XPS of PANIBC's C1s, O1s and N1s (a), (b), and (c), after chromium adsorption on to PANIBC at pH 2 C1s, O1s and N1s (d), (e), and (f), spectra, respectively, and after nitrate adsorption on to PANIBC at pH 6 C1s, O1s and N1s (g), (h), and (i).

The C1s and O 1s peaks of DFBC before chromium adsorption were deconvoluted in to four and five peaks respectively, C 1s peaks are assigned at binding energies (BEs) centered at 284.57 (C-H/C-C), 285.60 (C=C), 286.57 (C-OH) and 288.14 eV (C=O) (Table. B.4) O 1s peaks are assigned at BEs 530.81 (C=O), 532.1 (O-CR3), 533.19 (C-OH), 533.95 (CO_3^{2-}) and 535.33

eV (COOH) for O1s (Fig. B.5). In PANIBC C1s peak was deconvoluted into five peaks with binding energies centered at 284.0 (C-C/C-H), 284.75 (C=C/aromatic C), 285.43 (C-OH/C-N/C=N), 286.28(C=O), and 287.44 eV (COOH(R)) (Table B.4, B.5). These peaks on DFBC and PANIBC are in good agreement with the literature.[73,74] Oxidative polymerization has increased the C atomic percentages of PANIBC up to 25.65 (aromatic C/C=C), 13.83 (C-OH/C-N/C=N), 14.62 (C=O) verses 11.22, 5.04, 1.51 in DFBC. The O1s peak in PANIBC was deconvoluted into five peaks at 530.39, 531.01, 531.67, 532.5, 533.58 and 534.94 eV which are due to the C=O, O- CR_3, C-OH, CO_3^{2-}, COOH and O-N (Fig. 3.5). After Cr(VI) was adsorbed onto PANIBC HR-XPS was analyzed at pH 2, 6 and 8.

Characterization of PANIBC by deconvolution of the HR-XPS's high-resolution N l s core-level reveals the presence of the quinonoid imine (=N- moiety) 397.76, benzenoid amine (-NH- moiety) 399.08, and both the positively charged nitrogen polaron (400.47) and bipolaron (402.62 eV) functions in the PANIBC composite. These peaks with their binding energies are tabulated (Table. B.6). These peak positions and corresponding binding energy values are consistent with the values obtained in the literature.[75,76,77,4] Both FTIR and XPS data analysis for PANIBC confirm that PANI exists on PANIBC in the moderately oxidized emeraldine salt form (greenish color). During acid doping, imine sites are protonated to form diamagnetic bipolaron states Fig. 3.6(I). This bipolaron state can undergo further rearrangement to form paramagnetic radical cations Fig. 3.6(II) and (III). The resulting emeraldine salt, therefore, has a mixture of both bipolaron and polaron states as depicted in Fig. 3.6. Biochar surfaces contain various oxygen functionalities as evidenced from XPS analysis which H-bond with amine and imine moieties of PANI at their interfaces. In addition, delocalized π-electrons of PANI could interact with aromatic moieties of DFBC. These interactions between biochar and polyaniline form a stable complex (Fig.

3.7.). XPS and FTIR analysis confirm that the PANI in the PANIBC is essentially its emeraldine salt consisting of imine and amine moieties with positively charged N centers. This is best described by the three structures in Fig. 3.6.

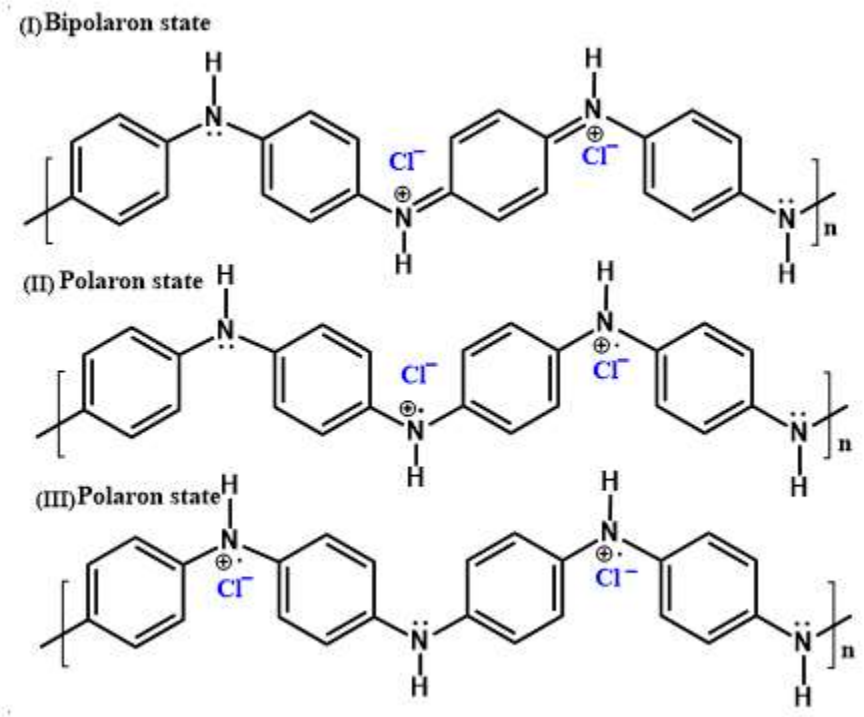

Figure 3.6 Structures of the Cl-doped PANI

Chemical structures of the Cl-doped PANI formed through *in-situ* chemical oxidative polymerization of aniline and precipitated onto DFBC to form PANI. The repeating unit includes bipolaron and polaron states.

Figure 3.7 Illustration of the interaction between PANI and biochar at their interface

3.4.5 Adsorption mechanism of Cr(VI)

HR-XPS of Cr(VI)-laden PANIBC, where adsorption occurred at pH 2, 6 and 8, are provided in (Fig. B.6). From uptake at pH 2, the Cr 2p spectrum exhibits two broad peaks at 577 (Cr $2p_{3/2}$) and 587 eV (Cr $2p_{1/2}$) (Fig. B.6). Their deconvolution gave binding energies for both Cr(III) and Cr(VI). Atomic percentages of Cr(III) and Cr(VI) at pH 2 were 7.2 and 2.18, respectively. Cr(III) species appear at 576.34 eV (Cr_2O_3),[78] 577.38 eV ($CrCl_3$),[79,80] $Cr(OH)_3$,[81] 586.02 eV (Cr_2O_3)[82] and 586.96 eV $Cr(NO_3)_2$[82] while Cr(VI) appears at 579.34 eV (CrO_3).[79] Atomic percentage ratio of Cr(III) to Cr(VI) at pH 2 was 7.2 : 2.2 (Table B.7). In acidic medium Cr(VI) exists as $HCrO_4^-$ and as CrO_4^{2-} at pH >6. Upon protonation of negative oxygens, electron

density around Cr(VI) will drop and results an increasing in Cr 2p binding energy. As pH increased from 2 to 8, Cr 2p BE values were slightly decreased. Peak shifts to lower BE upon deprotonation for phosphate species on biochar P 2p 133.9 eV (pH 1) from 133.5 eV (pH 13) was reported in literature.[10] At pH 2, a 10.2% atomic% of Cr(VI)-O in the O1s peak at 530.71 eV[83] vs. 2.01% and 0.74% at pH 6, and 8, respectively were obtained (Table S5). Also 14.2% (C-OH), 7.4% (O-C=O) atomic percentages were obtained at pH 2 compared to lower atomic percentages for oxygen in these functions at pH 6 and 8 in the HR-XPS O 1s spectra. This correspond to oxygen-containing functional groups on the biochar surface binding to chromium during chemisorption of ($HCrO_4^-$) Fig. 3.8C and D. The N 1s deconvoluted peaks significantly changed at every pH after Cr(VI) adsorption onto PANIBC. The peak at 397.76 eV (quinoid imine -N=) shifted to higher binding energies (eV) and a greater atomic percentage (%), respectively, at pH 2 (398.27, 0.82), pH 6 (398.36, 4.15) and pH 8 (398.42, 5.01). The N1s peak of benzenoid amine (-NH-) in PANIBC (399.08 eV, 8.02%) shifted to higher binding energies (eV) and lower atomic percentages as pH increased (399.51, 3.21, pH 2), (399.43, 2.69, pH 6), and (399.55, 2.58, pH 8). Cr(VI) adsorption caused benzenoid amine (-NH-) atomic percentages to drop while higher oxidation state quinoid imine (-N=) atomic percentages rose due to oxidation of (-NH-) groups by Cr(VI) to quinoid imine as Cr(VI) was reduced to Cr(III) Fig. 3.8-A, B and C. ($HCrO_4^-$) at pH 2 or (CrO_4^{2-}) at pH >6 are electrostatically attracted to the protonated amine surface NH_2^+ sites. H bonding also helps anchor them (Fig. 3.8 D). This interaction is further supported by density functional theory calculations for Cr(VI) adsorption of followed by reduction to Cr(III) on a polyethyleneimine-silica nanocomposite in acidic media.[84] Polaron-and bipolaron-doped N functions share electrons with Cr during Cr(VI) fixation and also with Cr(III) formation and surface chelation. Dissolved Cr(VI) oxyanions can exchange with Cl^- ions in PANI phases. At low pH, $HCrO_4^-$ has a higher affinity to

protonated nitrogen than chloride ions, promoting anion-exchange. Therefore, in addition to reduction to Cr(III) a significant amount of Cr(VI) is removed from solution by adsorption through anion exchange with chloride[85] (Fig. 3.8C). Presence of chloride counter ions was confirmed in both HR-XPS and TEM-EDX of PANIBC.

Cr(VI) reduction to Cr(III) in acidic solution is accompanied by the oxidation of amine and polaron centers of PANI into quinonoid imine moieties (Fig. 3.8). The thermodynamic feasibility of this redox conversion is confirmed by considering the PANI and Cr(VI) redox potentials in acidic media, where PANI undergoes two-electron oxidation at +0.519 V (SHE).[86] This is less positive than Cr(VI)'s redox potential of + 1.35 V.[87] Therefore, PANIBC can reduce Cr(VI) into Cr(III). Less Cr(VI) was removed by unmodified DFBC than by PANIBC under identical experimental conditions.

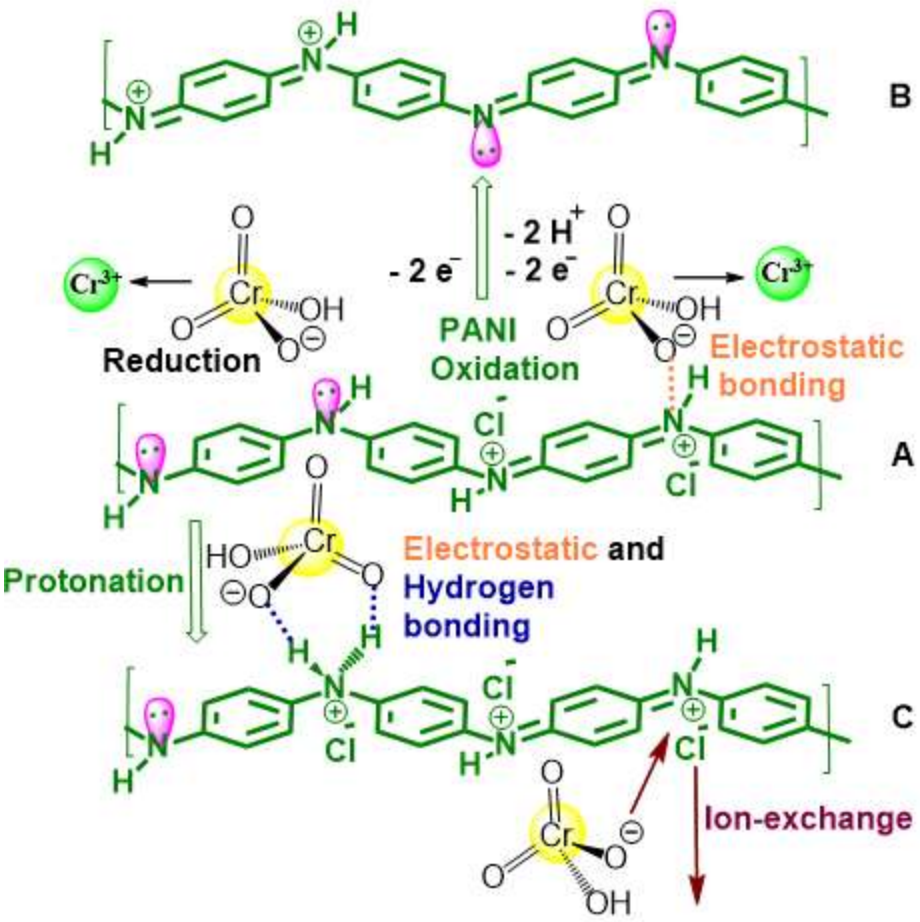

Figure 3.8 Schematic representation of Cr(VI) removal and partial reduction to Cr(III) by PANIBC

3.4.6 Nitrate adsorption mechanism

The peak HR-XPS assignments of PANIBC after nitrate adsorption at pH 2, 6 and 8 are tabulated in Table B.6. The PANIBC surface is more highly positively charged at pH 2 than at higher pH values, but nitrate adsorption is low. Maximum nitrate adsorption on PANIBC occurs at pH 4 to 6. Thus, electrostatic attractions with the positive PANI surface don't dominate. Ion exchange likely occurs, assisted by H-bonding to nitrate oxygens from nitrogen-bound protons

attached to -NH_2- sites which are better H bond donors than -NH- sites. Some electrostatic interactions with protonated PANIBC polaron and bipolaron structures may also contribute (Fig. 3.9). Nitrate-laden PANIBC at pH 6 exhibits N1s peak binding energies at 397.96, 399.29, 400.79, 402.74 and 406.24 eV, all of which have shifted to higher binding energies than those of PANIBC and nitrate-laden PANIBC obtained at pH 2 and 10, respectively. (Fig. B.7). After nitrate adsorption, the atomic percentages of every peak have dropped compared to PANIBC but they were higher than the corresponding values obtained at pH 2 and 10. N 1 s core-level XPS peaks for nitrate and nitrite ions appear at binding energies between 405 - 407 eV.[88] A new peak at ~406 eV appeared after nitrate adsorption on PANIBC. Nitrate at 406 and nitrite at 405 eV can coexist on the biochar surface, but they could not be differentiated by XPS since there peaks occur close to each other and may overlap.[89] This peak appeared PANIBC/ NO_3^- at 406.24 eV at pH 6, indicating either nitrate and/or nitrite adsorption had occurred. Some nitrite formation by nitrate reduction on PANIBC appears possible from nitrate's reduction potential (eq. 3.1 and 3.2) and because a portion of nitrate was converted into ammonia. N1s XPS peak for NH_4Cl appears at a binding energy of 400.79 eV.[90] If nitrite formed, that was not further reduced to ammonia, it would be electrostatically attracted and able to H-bond to PANIBC like nitrate. The reductions of nitrate by PANIBC to ammonium ions or even nitrogen are thermodynamically reasonable from their standard redox potentials (see eq. 3.3 and 3.4).[91] Nitrite might also be further reduced to ammonium ions as its redox potential is close to that of nitrate/ammonium couple (eq. 3.3 and 3.4).

$$NO_3^- + 2\,H^+ + 2\,e^- \rightarrow NO_2^- + H_2O \qquad E = +0.84\ V \qquad (3.1)$$

$$NO_3^- + 10\,H^+ + 8\,e^- \rightarrow NH_4^+ + 3\,H_2O \qquad E = +0.88\ V \qquad (3.2)$$

$$2\,NO_3^- + 12\,H^+ + 10\,e^- \rightarrow N_2 + 6\,H_2O \qquad E = +1.24\ V \qquad (3.3)$$

$$NO_2^- + 8\,H^+ + 6\,e^- \rightarrow NH_4^+ + 2\,H_2O \qquad E = +0.90\ V \qquad (3.4)$$

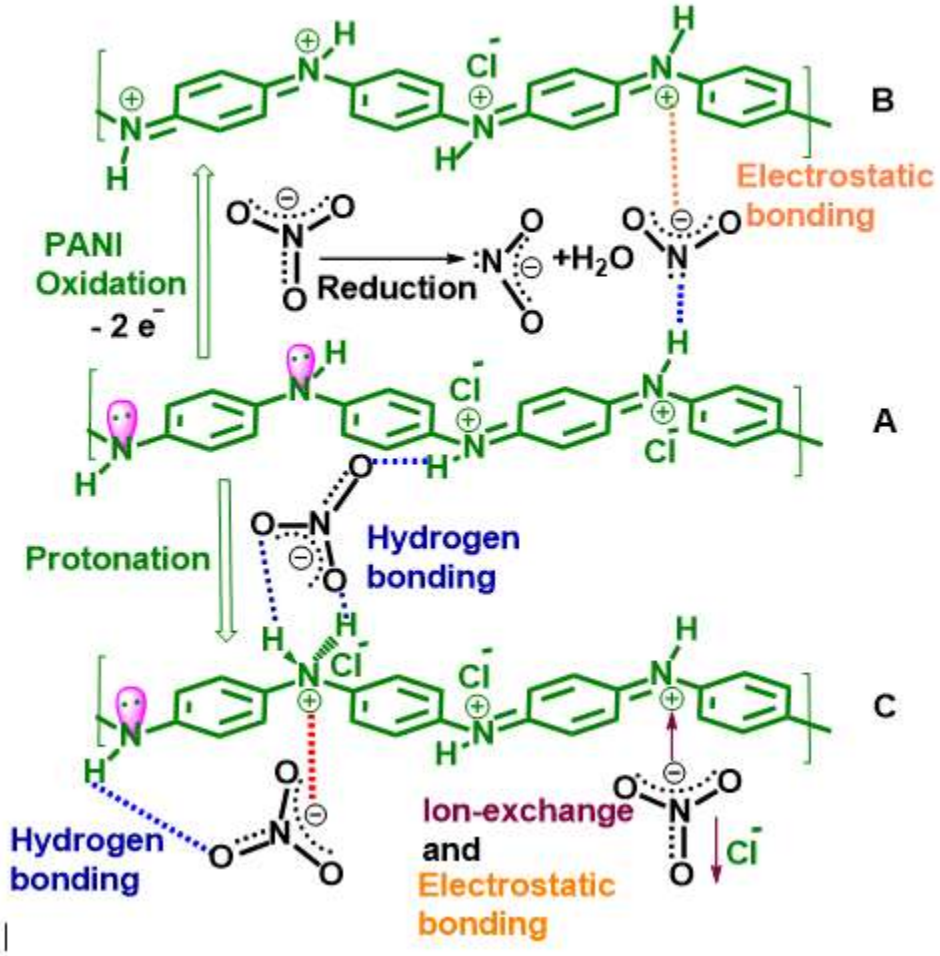

Figure 3.9 Nitrate adsorption and reduction on PANIBC

3.4.7 Adsorption regeneration and competitive studies

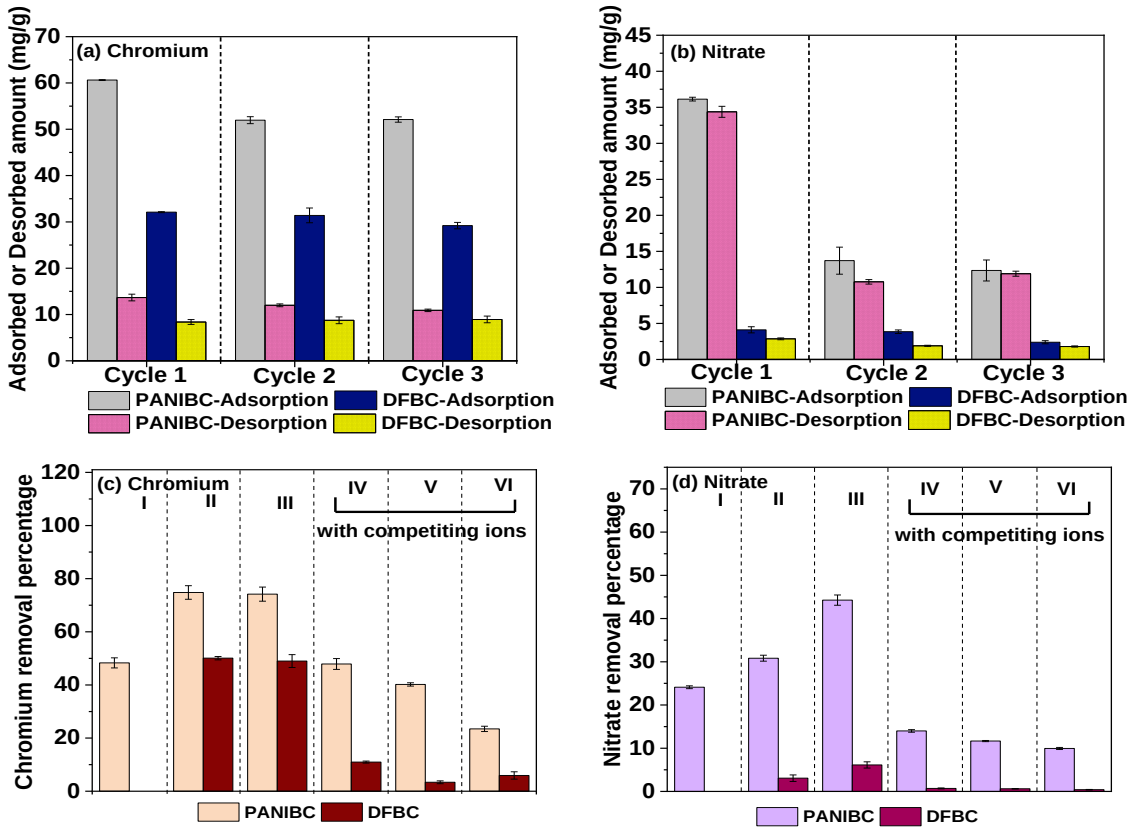

Figure 3.10 Adsorption-desorption cycles and effect of competitive ions on Cr(VI) and nitrate adsorption

Adsorption-desorption cycles at 25 °C on PANIBC and DFBC for (a) Cr(VI) at pH 2, and (b) nitrate at pH 6, where 0.200 g of biochar was mixed with 200 mL of Cr(VI) (60 mg/L) or nitrate (50 mg/L) and stirred at 200 rpm. NaOH 0.1M was used to desorb Cr(VI) and nitrate. Error bars are the SD of three replicates. (c) and (d) chromium and nitrate removal on PANIBC and DFBC from six different aqueous solutions. (I) 50 mg/L, analyte spiked a natural pond water at pH 8.3, (II) 50 mg/L, analyte spiked a natural pond water at pH buffered to 2 for Cr(VI) and 6 for nitrate, (III) 50 mg/L, analyte spiked into deionized water at buffered pH 2 for Cr(VI) and pH 6 for nitrate, (IV) 50 mg/L, analyte spiked in to deionized water at pH 2 for Cr(VI) and pH 6 for nitrate in the presence of fluoride, chloride, carbonate competitive ions, each having a concentration in the mixture of 2 mg/L, (V) 5 mg/L and (VI) 10 mg/L, respectively.

Cr(VI) sorption/desorption results on PANIBC and DFBC are shown in Fig. 3.10(a). Cr(VI) adsorption highly depends on the solution pH. Since most Cr(VI) adsorption studies on biochar are reported in acidic pH, basic stripping is required as previously reported,[92] no desorption was observed with a 0.1M HCl stripper. Thus, 0.1M NaOH was used for chromium desorption from both PANIBC and DFBC. PANIBC adsorbed 61 mg/g of Cr(VI) in the first cycle at pH 2 vs 32 mg/g by DFBC. Stripping by 0.1M NaOH adsorbed Cr(VI) 52 and 51.5 mg/g in the second and third consecutive cycles from PANIBC. Cr(VI) uptake on DFBC in the second and third cycles were 31 and 29 mg/g. The amount of Cr(VI) desorbed by 0.1M NaOH was (14, 12, 11 mg/g) for PANIBC and (8.3, 8.7, 8.9 mg/g) DFBC. The amount of Cr(VI) desorbed from both PANIBC and DFBC was less than the amount adsorbed in each cycle but remained almost constant throughout all three consecutive cycles.

Nitrate adsorption at pH 6 on PANIBC and DFBC is illustrated in Fig. 3.10(b). The amount of nitrate uptake on PANIBC was always far higher than on DFBC. In the first adsorption cycle, 36 mg/g of nitrate was adsorbed by PANIBC vs 4 mg/g by DFBC. The amount of nitrate adsorbed on PANIBC dropped to 13.7 and 12.3 mg/g in the second and third cycles. Nitrate was desorbed from PANIBC (34.4, 10.7 and 11.9 mg/g) each cycle by 0.1M NaOH. The amount of nitrate stripped from DFBC in the three cycles was 2.8, 1.9, 1.8 mg/g verses uptakes of 4.1, 3.8 and 2.4 mg/g. The amount of nitrate desorbed from both PANIBC and DFBC by 0.1M NaOH was higher than the amount of Cr(VI) desorbed in each cycle. The emeraldine salt form of PANIBC is structurally changed into PANI base following treatment with NaOH in desorption studies. The base form of PANI does not have a positive charge on nitrogen or a chloride ion. Therefore, most of the nitrate ions can no longer be retain on the PANI structure leading to greater desorption of nitrate. During the second and third adsorption cycles, nitrate ions cannot be adsorbed through

electrostatic attraction or through ion exchange with doped chloride ions. At this stage PANIBC exists in its base form where adsorption primarily occurs through hydrogen bonding. Therefore, adsorption of nitrate is reduced compared to the first cycle where the emeraldine salt form of PANIBC exhibited greater nitrate adsorption.

Fig. 3.10(c) and (d) illustrate the percent removal of adsorbed Cr(VI) and nitrate using DFBC and PANIBC from six aqueous systems: (I) 50 mg/L Cr(VI) or 50 mg/L nitrate were spiked into lake water at its pH (8.3), (II) identical samples to (I) were buffered to their optimum pH (Cr(VI) pH 2, nitrate pH 6), (III) Cr(VI) and nitrate were spiked into deionized water as controls, (IV) Cr(VI) or nitrate (50 mg/L) in deionized water were combined with five competitive ions ($Cr_2O_7^{2-}$, NO_3^-, CO_3^{2-}, F^-, Cl^-) with individual concentration of 2 mg/L (V) 5 mg/L and (VI) 10 mg/L.

PANIBC removed 48% of Cr(VI) from lake water at pH 8.3, but DFBC removed very little. Lake water's high initial pH causes DFBC's surface to be negatively charged, retarding Cr(VI) uptake. Buffering lake water to pH 2, as expected, increased Cr(VI) removal of 50%. This same result was occurred using deionized water. PANIBC removed ~75% of the Cr(VI) in both lake water and DI water buffered to pH 2 no species interfered in lake water. Competitive ions (NO_3^-, CO_3^{2-}, F^-, Cl^-), lowered Cr(VI) removal on both DFBC and PANIBC as their concentrations rose from 2 to 10 mg/L. These interfering ions hindered Cr(VI) sorption on DFBC in previous work.[93,94,95] DFBC didn't remove nitrate from lake water at pH 8.3, while PANIBC removed 23%. Buffering lake water to pH 6, increased nitrate uptakes slightly. The deionized water gave the highest nitrate removal percentages for both DFBC and PANIBC. The competitive anions $Cr_2O_7^{2-}$, CO_3^{2-}, F^-, Cl^- reduced nitrate removal by PANIBC. Comparison of PANIBC's nitrate and Cr(VI) adsorption capacities verses other adsorbents are shown in Table 4.

Table 3.4 Comparison of PANIBC's nitrate and Cr(VI) adsorption capacities verses other adsorbents

Adsorbent	Adsorbate	pH	Equilibrium time	Temp. (K)	Surface area (m^2/g)	Adsorption capacity (mg/g)	Reference
Magnetic Douglas fir biochar	nitrate	7.0	10 min	298	494	14.84	[93]
				308		15.05	
				318		15.53	
Sugarcane bagasse biochar	nitrate	3	60 min	295	41.67	28.21	[17]
Bamboo biochar	nitrate	6.4	24 h	298	28	4.6	[96]
Bamboo biochar/ montmorillonite	nitrate	6.4	24 h	298	156	8.5	[96]
Corn-straw Biochar-magnetic	nitrate	6.0	24 h	278	115	6.31	[97]
Polyaniline modified activated carbon	nitrate	-	30 min	298	260	48.9	[98]
PANIBC	**nitrate**	**6.0**	**2 h**	**318**	**8.9**	**72.0**	**This study**
				298		**63.0**	**This study**
Ramie biochar	Cr(VI)	2	24 h	298	5.14	82.23	[99]
Eucalyptus globulus bark biochar	Cr(VI)	2	6 h	303	265	21.3	[100]
		2	6 h	313	265	25.4	
		2	6 h	323	265	28.4	
Magnetic biochar	Cr(VI)	2	>24 h	298	59.34	45.45	[101]
Chitosan combined magnetic biochar	Cr(VI)	2	18 h	303	104.91	30.14	[102]
Chitosan doped carbon nanotubes	Cr(VI)	6	2 h	308	-	26.14	[103]
Graphene oxide incorporated chitosan	Cr(VI)	3	3 h	308	-	76.92	[104]
Carbon microfibers supported iron/nickel bisalloy	Cr(VI)	1	60 s	298	435	89.6	[105]
Amine impregnated crab shells	Cr(VI)	2	24 h	-	1.22	41.41	[106]
PANIBC	**Cr(VI)**	**2**	**3 h**	**313**	**8.9**	**150.0**	**This study**
				298		**114.9**	**This study**
PANIBC	**Cr(VI)**	**6**	**3 h**	**298**	**8.9**	**86.5**	**This study**

3.5 Conclusion

Polyaniline/biochar composite (PANIBC) was synthesized using high surface area Douglas fir biochar (DFBC), a low cost adsorbent made from timber gasification to serve as a dispersant. Simple in-situ oxidative polymerization of aqueous aniline DFBC slurries yielded PANIBC for the adsorption of chromium and nitrate. Predominantly emeraldine form of polyaniline particles covered the DFBC, causing a lowering of surface area and pore size but resulting in high uptakes of Cr(VI) and nitrate from the introduction of amine, imine and polaron groups by PANI. Significant Cr(VI) was reduced to less toxic Cr(III) by oxidation of amine to polaron/bipolaron imine groups on PANIBC surface. Nitrate removal occurred by H-bonding, electrostatic interactions and ion exchange. By depositing smaller weight fractions of PANI on biochar, dispersion per unit wt. of PANI improved and higher Cr(VI) and nitrate removal capacities per unit wt. of PANI. This suggests that systematic reduction of the amount of PANI deposited on high surface area biochars or other substrates could raise sorption capacities substantially and enhance reductive adsorption markedly by increasing the PANI surface/weight ratio. Plausible mechanisms of Cr(VI) and nitrate removal by PANIBC were elucidated with the evidence of XPS spectroscopy. Maximum Langmuir adsorption capacity for Cr(VI) and nitrate at 318 K was 150, 72 mg/g, respectively. PANIBC exhibited higher desorption and recovery of these adsorbates using 0.1M NaOH than DFBC. Experiments conducted in real water samples on PANIBC indicate the significance of this composite as an excellent adsorbent for Cr(VI) and nitrate remediation.

3.6 References

1. Jani, J.; Yang, Y.-Y.; Lusk, M. G.; Toor, G. S., Composition of nitrogen in urban residential stormwater runoff: Concentrations, loads, and source characterization of nitrate and organic nitrogen. *PloS one* **2020,** *15* (2), e0229715.

2. Jia, L.; Liu, H.; Kong, Q.; Li, M.; Wu, S.; Wu, H., Interactions of high-rate nitrate reduction and heavy metal mitigation in iron-carbon-based constructed wetlands for purifying contaminated groundwater. *Water Research* **2020,** *169*, 115285.

3. Qiu, Y.; Zhang, Q.; Gao, B.; Li, M.; Fan, Z.; Sang, W.; Hao, H.; Wei, X., Removal mechanisms of Cr (VI) and Cr (III) by biochar supported nanosized zero-valent iron: Synergy of adsorption, reduction and transformation. *Environmental Pollution* **2020,** *265*, 115018.

4. Qiu, B.; Xu, C.; Sun, D.; Yi, H.; Guo, J.; Zhang, X.; Qu, H.; Guerrero, M.; Wang, X.; Noel, N., Polyaniline coated ethyl cellulose with improved hexavalent chromium removal. *ACS Sustainable Chemistry & Engineering* **2014,** *2* (8), 2070-2080.

5. Rafiqi, F. A.; Majid, K., Removal of copper from aqueous solution using polyaniline and polyaniline/ferricyanide composite. *Journal of Environmental Chemical Engineering* **2015,** *3* (4), 2492-2501.

6. Zhitkovich, A., Chromium in drinking water: sources, metabolism, and cancer risks. *Chemical Research inToxicology* **2011,** *24* (10), 1617-1629.

7. WHO, In *Guidelines for Drinking-Water Quality: Fourth Edition Incorporating the First Addendum*, World Health Organization Copyright © World Health Organization 2017.: Geneva, 2017.

8. Barrera-Díaz, C. E.; Lugo-Lugo, V.; Bilyeu, B., A review of chemical, electrochemical and biological methods for aqueous Cr (VI) reduction. *Journal of Hazardous Materials* **2012,** *223*, 1-12.

9. Navarathna, C. M.; Karunanayake, A. G.; Gunatilake, S. R.; Pittman Jr, C. U.; Perez, F.; Mohan, D.; Mlsna, T., Removal of Arsenic (III) from water using magnetite precipitated onto Douglas fir biochar. *Journal of Environmental Management* **2019,** *250*, 109429.

10. Karunanayake, A. G.; Navarathna, C.; Gunatilake, S.; Crowley, M.; Anderson, R.; Mohan, D.; Perez, F.; Pittman, C. U.; Mlsna, T. E., Fe_3O_4 Nanoparticles Dispersed on Douglas Fir Biochar for Phosphate Sorption. *ACS Applied Nano Materials* **2019**.

11. Navarathna, C.; Alchouron, J.; Liyanage, A.; Herath, A.; Wathudura, P.; Nawalage, S.; Rodrigo, P.; Gunatilake, S.; Mohan, D.; Pittman Jr, C., Recent Developments in Aqueous Arsenic (III) Remediation Using Biomass-Based Adsorbents. In *Contaminants in Our Water: Identification and Remediation Methods*, ACS Publications: 2020; pp 197-251.

12. Song, Y.; Wang, L.; Lv, B.; Chang, G.; Jiao, W.; Liu, Y., Removal of trace Cr (VI) from aqueous solution by porous activated carbon balls supported by nanoscale zero-valent iron composites. *Environmental Science and Pollution Research* **2020,** *27* (7), 7015-7024.

13. Ren, L.; Dong, J.; Chi, Z.; Huang, H., Reduced graphene oxide-nano zero value iron (rGO-nZVI) micro-electrolysis accelerating Cr (VI) removal in aquifer. *Journal of Environmental Sciences* **2018,** *73*, 96-106.

14. Wang, J.; Ji, B.; Shu, Y.; Chen, W.; Zhu, L.; Chen, F., Cr (VI) Removal from Aqueous Solution Using Starch and Sodium Carboxymethyl Cellulose-Coated Fe and Fe/Ni Nanoparticles. *Polish Journal of Environmental Studies* **2018,** *27* (6).

15. Liang, Y.; Wei, D.; Hu, J.; Zhang, J.; Liu, Z.; Li, A.; Li, R., Glyphosate and nutrients removal from simulated agricultural runoff in a pilot pyrrhotite constructed wetland. *Water Research* **2020,** *168*, 115154.

16. Hauck, R. D., Slow-release and bioinhibitor-amended nitrogen fertilizers. *Fertilizer technology and use* **1985**, 293-322.

17. Hafshejani, L. D.; Hooshmand, A.; Naseri, A. A.; Mohammadi, A. S.; Abbasi, F.; Bhatnagar, A., Removal of nitrate from aqueous solution by modified sugarcane bagasse biochar. *Ecological Engineering* **2016,** *95*, 101-111.

18. Qi, D.; Wu, Q.; Zhu, J., Nitrogen and phosphorus losses from paddy fields and the yield of rice with different water and nitrogen management practices. *Scientific Reports* **2020,** *10* (1), 1-12.

19. Osman, M.; Wan Yusof, K.; Takaijudin, H.; Goh, H. W.; Abdul Malek, M.; Azizan, N. A.; Abdurrasheed, S. i., A Review of Nitrogen Removal for Urban Stormwater Runoff in Bioretention System. *Sustainability* **2019,** *11* (19), 5415.

20. Romanelli, A.; Soto, D. X.; Matiatos, I.; Martínez, D. E.; Esquius, S., A biological and nitrate isotopic assessment framework to understand eutrophication in aquatic ecosystems. *Science of the Total Environment* **2020,** *715*, 136909.

21. Shen, Y.; Huang, Y.; Hu, J.; Li, P.; Zhang, C.; Li, L.; Xu, P.; Zhang, J.; Chen, X., The nitrogen reduction in eutrophic water column driven by Microcystis blooms. *Journal of Hazardous Materials* **2020,** *385*, 121578.

22. Bohdziewicz, J.; Bodzek, M.; Wąsik, E., The application of reverse osmosis and nanofiltration to the removal of nitrates from groundwater. *Desalination* **1999,** *121* (2), 139-147.

23. Bi, J.; Peng, C.; Xu, H.; Ahmed, A.-S., Removal of nitrate from groundwater using the technology of electrodialysis and electrodeionization. *Desalination and Water Treatment* **2011,** *34* (1-3), 394-401.

24. Shyamala, S.; Manikandan, N. A.; Pakshirajan, K.; Tang, V. T.; Rene, E. R.; Park, H.-S.; Behera, S. K., Phytoremediation of nitrate contaminated water using ornamental plants. *Journal of Water Supply: Research and Technology—AQUA* **2019,** *68* (8), 731-743.

25. Weng, Z. H.; Van Zwieten, L.; Singh, B. P.; Tavakkoli, E.; Joseph, S.; Macdonald, L. M.; Rose, T. J.; Rose, M. T.; Kimber, S. W.; Morris, S., Biochar built soil carbon over a decade by stabilizing rhizodeposits. *Nature Climate Change* **2017,** *7* (5), 371-376.

26. Jien, S.-H.; Wang, C.-S., Effects of biochar on soil properties and erosion potential in a highly weathered soil. *Catena* **2013,** *110*, 225-233.

27. Zhang, M.; Gao, B.; Yao, Y.; Xue, Y.; Inyang, M., Synthesis of porous MgO-biochar nanocomposites for removal of phosphate and nitrate from aqueous solutions. *Chemical Engineering Journal* **2012,** *210*, 26-32.

28. Sohi, S. P., Carbon storage with benefits. *Science* **2012,** *338* (6110), 1034-1035.

29. Mohan, D.; Sarswat, A.; Ok, Y. S.; Pittman Jr, C. U., Organic and inorganic contaminants removal from water with biochar, a renewable, low cost and sustainable adsorbent–a critical review. *Bioresource Technology* **2014,** *160*, 191-202.

30. Peiris, C.; Gunatilake, S. R.; Mlsna, T. E.; Mohan, D.; Vithanage, M., Biochar based removal of antibiotic sulfonamides and tetracyclines in aquatic environments: a critical review. *Bioresource Technology* **2017,** *246*, 150-159.

31. Karakoyun, N.; Kubilay, S.; Aktas, N.; Turhan, O.; Kasimoglu, M.; Yilmaz, S.; Sahiner, N., Hydrogel–Biochar composites for effective organic contaminant removal from aqueous media. *Desalination* **2011,** *280* (1-3), 319-325.

32. Xue, Y.; Gao, B.; Yao, Y.; Inyang, M.; Zhang, M.; Zimmerman, A. R.; Ro, K. S., Hydrogen peroxide modification enhances the ability of biochar (hydrochar) produced from hydrothermal carbonization of peanut hull to remove aqueous heavy metals: batch and column tests. *Chemical Engineering Journal* **2012,** *200*, 673-680.

33. Tan, X.; Liu, Y.; Zeng, G.; Wang, X.; Hu, X.; Gu, Y.; Yang, Z., Application of biochar for the removal of pollutants from aqueous solutions. *Chemosphere* **2015,** *125*, 70-85.

34. Burk, G. A.; Herath, A.; Crisler, G.; Bridges, D.; Patel, S.; Pittman Jr, C. U.; Mlsna, T., Cadmium and copper removal from aqueous solutions using chitosan-coated gasifier biochar. *Frontiers in Environmental Science* **2020,** *8*, 186.

35. Bhatnagar, A.; Sillanpää, M., A review of emerging adsorbents for nitrate removal from water. *Chemical Engineering Journal* **2011,** *168* (2), 493-504.

36. Deng, J.; Liu, Y.; Liu, S.; Zeng, G.; Tan, X.; Huang, B.; Tang, X.; Wang, S.; Hua, Q.; Yan, Z., Competitive adsorption of Pb (II), Cd (II) and Cu (II) onto chitosan-pyromellitic

dianhydride modified biochar. *Journal of Colloid and Interface Science* **2017,** *506*, 355-364.

37. Fletcher, A. J.; Smith, M. A.; Heinemeyer, A.; Lord, R.; Ennis, C. J.; Hodgson, E. M.; Farrar, K., Production factors controlling the physical characteristics of biochar derived from phytoremediation willow for agricultural applications. *BioEnergy Research* **2014,** *7* (1), 371-380.

38. Niu, Q.; Luo, J.; Xia, Y.; Sun, S.; Chen, Q., Surface modification of bio-char by dielectric barrier discharge plasma for Hg(0) removal. *Fuel Processing Technology* **2017,** *156*, 310-316.

39. Sizmur, T.; Fresno, T.; Akgül, G.; Frost, H.; Moreno-Jiménez, E., Biochar modification to enhance sorption of inorganics from water. *Bioresource Technology* **2017,** *246*, 34-47.

40. Trakal, L.; Veselská, V.; Šafařík, I.; Vítková, M.; Číhalová, S.; Komárek, M., Lead and cadmium sorption mechanisms on magnetically modified biochars. *Bioresource Technology* **2016,** *203*, 318-324.

41. Harvey, O. R.; Herbert, B. E.; Rhue, R. D.; Kuo, L.-J., Metal interactions at the biochar-water interface: energetics and structure-sorption relationships elucidated by flow adsorption microcalorimetry. *Environmental science & technology* **2011,** *45* (13), 5550-5556.

42. Kang, E.; Neoh, K.; Tan, K., Polyaniline: a polymer with many interesting intrinsic redox states. *Progress in Polymer Science* **1998,** *23* (2), 277-324.

43. Liu, X.; Zhou, W.; Qian, X.; Shen, J.; An, X., Polyaniline/cellulose fiber composite prepared using persulfate as oxidant for Cr (VI)-detoxification. *Carbohydrate Polymers* **2013,** *92* (1), 659-661.

44. Stejskal, J.; Sapurina, I.; Trchová, M.; Konyushenko, E. N., Oxidation of aniline: polyaniline granules, nanotubes, and oligoaniline microspheres. *Macromolecules* **2008,** *41* (10), 3530-3536.

45. Chiou, N. R.; Epstein, A. J., Polyaniline nanofibers prepared by dilute polymerization. *Advanced Materials* **2005,** *17* (13), 1679-1683.

46. Zheng, H.; Xu, X.; Xu, S.; Liu, G.; Chen, S.; Zhang, X.; Chen, T.; Pan, X., The multiple effects of polyaniline additive to improve the efficiency and stability of perovskite solar cells. *Journal of Materials Chemistry C* **2019,** *7* (15), 4441-4448.

47. Al-Dainy, G. A.; Watanabe, F.; Kannarpady, G. K.; Ghosh, A.; Berry, B.; Biris, A. S.; Bourdo, S. E., Optimizing Lignosulfonic Acid-Grafted Polyaniline as a Hole-Transport Layer for Inverted $CH_3NH_3PbI_3$ Perovskite Solar Cells. *ACS Omega* **2020,** *5* (4), 1887-1901.

48. Jang, J.; Ha, J.; Kim, K., Organic light-emitting diode with polyaniline-poly (styrene sulfonate) as a hole injection layer. *Thin Solid Films* **2008,** *516* (10), 3152-3156.

49. Dhand, C.; Das, M.; Datta, M.; Malhotra, B., Recent advances in polyaniline based biosensors. *Biosensors and Bioelectronics* **2011,** *26* (6), 2811-2821.

50. Zare, E. N.; Makvandi, P.; Ashtari, B.; Rossi, F.; Motahari, A.; Perale, G., Progress in Conductive Polyaniline-Based Nanocomposites for Biomedical Applications: A Review. *Journal of medicinal Chemistry* **2019**.

51. Zheng, W.; Lv, R.; Na, B.; Liu, H.; Jin, T.; Yuan, D., Nanocellulose-mediated hybrid polyaniline electrodes for high performance flexible supercapacitors. *Journal of Materials Chemistry A* **2017,** *5* (25), 12969-12976.

52. Kulkarni, S. B.; Patil, U. M.; Shackery, I.; Sohn, J. S.; Lee, S.; Park, B.; Jun, S., High-performance supercapacitor electrode based on a polyaniline nanofibers/3D graphene framework as an efficient charge transporter. *Journal of Materials Chemistry A* **2014,** *2* (14), 4989-4998.

53. Jlassi, K.; Radwan, A. B.; Sadasivuni, K. K.; Mrlik, M.; Abdullah, A. M.; Chehimi, M. M.; Krupa, I., Anti-corrosive and oil sensitive coatings based on epoxy/polyaniline/magnetite-clay composites through diazonium interfacial chemistry. *Scientific Reports* **2018,** *8* (1), 1-13.

54. Hayatgheib, Y.; Ramezanzadeh, B.; Kardar, P.; Mahdavian, M., A comparative study on fabrication of a highly effective corrosion protective system based on graphene oxide-polyaniline nanofibers/epoxy composite. *Corrosion Science* **2018,** *133*, 358-373.

55. Ibrahim, K. A., Synthesis and characterization of polyaniline and poly (aniline-co-o-nitroaniline) using vibrational spectroscopy. *Arabian Journal of Chemistry* **2017,** *10*, S2668-S2674.

56. Li, S.; Chen, G., Thermogravimetric, thermochemical, and infrared spectral characterization of feedstocks and biochar derived at different pyrolysis temperatures. *Waste Management* **2018,** *78*, 198-207.

57. Xiao, X.; Chen, Z.; Chen, B., H/C atomic ratio as a smart linkage between pyrolytic temperatures, aromatic clusters and sorption properties of biochars derived from diverse precursory materials. *Scientific Reports* **2016,** *6*, 22644.

58. Lopez-Ramon, M. V.; Stoeckli, F.; Moreno-Castilla, C.; Carrasco-Marin, F., On the characterization of acidic and basic surface sites on carbons by various techniques. *Carbon* **1999,** *37* (8), 1215-1221.

59. Debnath, S.; Ballav, N.; Maity, A.; Pillay, K., Single stage batch adsorber design for efficient Eosin yellow removal by polyaniline coated ligno-cellulose. *International journal of biological macromolecules* **2015,** *72*, 732-739.

60. Dutra, F. V. A.; Pires, B. C.; Nascimento, T. A.; Borges, K. B., Functional polyaniline/multiwalled carbon nanotube composite as an efficient adsorbent material for removing pharmaceuticals from aqueous media. *Journal of Environmental Management* **2018,** *221*, 28-37.

61. Mohan, D.; Pittman Jr, C. U., Activated carbons and low cost adsorbents for remediation of tri- and hexavalent chromium from water. *Journal of Hazardous Materials* **2006,** *137* (2), 762-811.

62. Herath, A.; Layne, C. A.; Perez, F.; Hassan, E. B.; Pittman Jr, C. U.; Mlsna, T. E., KOH-activated high surface area Douglas Fir biochar for adsorbing aqueous Cr (VI), Pb (II) and Cd (II). *Chemosphere* **2020**, 128409.

63. Amarnath, C.; Palaniappan, S., Polyaniline doped by a new class of dopants, benzoic acid and substituted benzoic acid: synthesis and characterization. *Polymers for Advanced Technologies* **2005,** *16* (5), 420-424.

64. Trchová, M.; Stejskal, J., Polyaniline: The infrared spectroscopy of conducting polymer nanotubes (IUPAC Technical Report). *Pure and Applied Chemistry* **2011,** *83* (10), 1803-1817.

65. Hatchett, D. W.; Josowicz, M.; Janata, J., Acid doping of polyaniline: spectroscopic and electrochemical studies. *The Journal of Physical Chemistry B* **1999,** *103* (50), 10992-10998.

66. Šeděnková, I.; Trchova, M.; Stejskal, J., Thermal degradation of polyaniline films prepared in solutions of strong and weak acids and in water–FTIR and Raman spectroscopic studies. *Polymer Degradation and Stability* **2008,** *93* (12), 2147-2157.

67. Gemeay, A. H.; Mansour, I. A.; El-Sharkawy, R. G.; Zaki, A. B., Preparation and characterization of polyaniline/manganese dioxide composites via oxidative polymerization: Effect of acids. *European Polymer Journal* **2005,** *41* (11), 2575-2583.

68. Sanches, E.; Soares, J.; Iost, R.; Marangoni, V.; Trovati, G.; Batista, T.; Mafud, A.; Zucolotto, V.; Mascarenhas, Y., Structural characterization of emeraldine-salt polyaniline/gold nanoparticles complexes. *Journal of Nanomaterials* **2011,** *2011*.

69. Palaniappan, S.; Narayana, B., Conducting polyaniline salts: thermogravimetric and differential thermal analysis. *Thermochimica Acta* **1994,** *237* (1), 91-97.

70. Milonjić, S. K., A consideration of the correct calculation of thermodynamic parameters of adsorption. *Journal of the Serbian Chemical Society* **2007,** *72* (12), 1363-1367.

71. Langmuir, I., The adsorption of gases on plane surfaces of glass, mica and platinum. *Journal of the American Chemical Society* **1918,** *40* (9), 1361-1403.

72. Freundlich, H., Over the adsorption in solution. *J. Phys. Chem* **1906,** *57* (385471), 1100-1107.

73. Navarathna, C. M.; Karunanayake, A. G.; Gunatilake, S. R.; Pittman, C. U.; Perez, F.; Mohan, D.; Mlsna, T., Removal of Arsenic(III) from Water Using Magnetite Precipitated onto Douglas Fir Biochar. *J. Environ. Manage.* **2019,** *250*, 109429.

74. Peiris, C.; Nayanathara, O.; Navarathna, C. M.; Jayawardhana, Y.; Nawalage, S.; Burk, G.; Karunanayake, A. G.; Madduri, S. B.; Vithanage, M.; Kaumal, M., The influence of three acid modifications on the physicochemical characteristics of tea-waste biochar pyrolyzed at different temperatures: a comparative study. *RSC Advances* **2019,** *9* (31), 17612-17622.

75. Tantawy, H. R.; Kengne, B.-A. F.; McIlroy, D. N.; Nguyen, T.; Heo, D.; Qiang, Y.; Aston, D. E., X-ray photoelectron spectroscopy analysis for the chemical impact of solvent addition rate on electromagnetic shielding effectiveness of HCl-doped polyaniline nanopowders. *Journal of Applied Physics* **2015,** *118* (17), 175501.

76. Inoue, M. B.; Nebesny, K. W.; Fernando, Q.; Inoue, M., X-Ray photoelectron spectroscopy of new soluble polyaniline perchlorates: evidence for the coexistence of polarons and bipolarons. *Journal of Materials Chemistry* **1991,** *1* (2), 213-216.

77. Mahat, M. M.; Mawad, D.; Nelson, G. W.; Fearn, S.; Palgrave, R. G.; Payne, D. J.; Stevens, M. M., Elucidating the deprotonation of polyaniline films by X-ray photoelectron spectroscopy. *Journal of Materials Chemistry C* **2015,** *3* (27), 7180-7186.

78. Shuttleworth, D., Preparation of metal-polymer dispersions by plasma techniques. An ESCA investigation. *The Journal of Physical Chemistry* **1980,** *84* (12), 1629-1634.

79. Sleigh, C.; Pijpers, A.; Jaspers, A.; Coussens, B.; Meier, R. J., On the determination of atomic charge via ESCA including application to organometallics. *Journal of electron spectroscopy and related phenomena* **1996,** *77* (1), 41-57.

80. Carver, J.; Schweitzer, G.; Carlson, T. A., Use of X-Ray photoelectron spectroscopy to study bonding in Cr, Mn, Fe, and Co compounds. *The Journal of Chemical Physics* **1972,** *57* (2), 973-982.

81. Moffat, T.; Latanision, R.; Ruf, R., An X-ray photoelectron spectroscopy study of chromium-metalloid alloys—III. *Electrochimica Acta* **1995,** *40* (11), 1723-1734.

82. Desimoni, E.; Malitesta, C.; Zambonin, P.; Riviere, J., An x-ray photoelectron spectroscopic study of some chromium–oxygen systems. *Surface and Interface Analysis* **1988,** *13* (2-3), 173-179.

83. Lippitz, A.; Hübert, T., XPS investigations of chromium nitride thin films. *Surface and Coatings Technology* **2005,** *200* (1-4), 250-253.

84. Choi, K.; Lee, S.; Park, J. O.; Park, J.-A.; Cho, S.-H.; Lee, S. Y.; Lee, J. H.; Choi, J.-W., Chromium removal from aqueous solution by a PEI-silica nanocomposite. *Scientific Reports* **2018,** *8* (1), 1-10.

85. Zhu, L.; Liu, Y.; Chen, J., Synthesis of N-methylimidazolium functionalized strongly basic anion exchange resins for adsorption of Cr (VI). *Industrial & Engineering Chemistry Research* **2009,** *48* (7), 3261-3267.

86. Bilal, S.; Akbar, A.; Shah, A.-u.-H. A., Highly Selective and Reproducible Electrochemical Sensing of Ascorbic Acid Through a Conductive Polymer Coated Electrode. *Polymers* **2019,** *11* (8), 1346.

87. Dittert, I. M.; de Lima Brandão, H.; Pina, F.; da Silva, E. A.; de Souza, S. M. G. U.; de Souza, A. A. U.; Botelho, C. M.; Boaventura, R. A.; Vilar, V. J., Integrated reduction/oxidation reactions and sorption processes for Cr (VI) removal from aqueous solutions using Laminaria digitata macro-algae. *Chemical Engineering Journal* **2014,** *237*, 443-454.

88. Shul'ga, Y. M.; Bulatov, A. V.; Gould, R. A.; Konze, W. V.; Pignolet, L. H., X-ray photoelectron spectroscopy of a series of heterometallic gold-platinum phosphine cluster compounds. *Inorganic Chemistry* **1992,** *31* (22), 4704-4706.

89. Yamamoto, Y.; Konno, H., Paramagnetic Cobalt (III) Complexes with Organic Ligands. X. The Preparation and Properties of Radical Diamminebis (5-nitrosalicylideneaminato) cobalt (III) Complex and Biradical Diamminebis (5-nitrosalicylideneaminato) cobalt (II) Complex. *Bulletin of the Chemical Society of Japan* **1987,** *60* (4), 1299-1302.

90. Burger, K.; Tschismarov, F.; Ebel, H., XPS/ESCA applied to quick-frozen solutions I.-A study of nitrogen compounds in aqueous solutions. *Journal of Electron Spectroscopy and Related Phenomena* **1977,** *10* (4), 461-465.

91. Bratsch, S. G., Standard electrode potentials and temperature coefficients in water at 298.15 K. *Journal of Physical and Chemical Reference Data* **1989,** *18* (1), 1-21.

92. Han, Y.; Cao, X.; Ouyang, X.; Sohi, S. P.; Chen, J., Adsorption kinetics of magnetic biochar derived from peanut hull on removal of Cr (VI) from aqueous solution: effects of production conditions and particle size. *Chemosphere* **2016,** *145*, 336-341.

93. Dewage, N. B.; Liyanage, A. S.; Pittman Jr, C. U.; Mohan, D.; Mlsna, T., Fast nitrate and fluoride adsorption and magnetic separation from water on α-Fe_2O_3 and Fe_3O_4 dispersed on Douglas fir biochar. *Bioresource Technology* **2018,** *263*, 258-265.

94. Karunanayake, A. G.; Todd, O. A.; Crowley, M.; Ricchetti, L.; Pittman Jr, C. U.; Anderson, R.; Mohan, D.; Mlsna, T., Lead and cadmium remediation using magnetized and nonmagnetized biochar from Douglas fir. *Chemical Engineering Journal* **2018,** *331*, 480-491.

95. Dewage, N. B.; Fowler, R. E.; Pittman, C. U.; Mohan, D.; Mlsna, T., Lead (Pb2+) Sorptive Removal Using Chitosan-Modified Biochar: Batch and Fixed-Bed Studies. *RSC Adv*. **2018,** *8*, 25368.

96. Viglašová, E.; Galamboš, M.; Danková, Z.; Krivosudský, L.; Lengauer, C. L.; Hood-Nowotny, R.; Soja, G.; Rompel, A.; Matík, M.; Briančin, J., Production, characterization and adsorption studies of bamboo-based biochar/montmorillonite composite for nitrate removal. *Waste Management* **2018,** *79*, 385-394.

97. Tan, G.; Mao, Y.; Wang, H.; Xu, N., A comparative study of arsenic (V), tetracycline and nitrate ions adsorption onto magnetic biochars and activated carbon. *Chemical Engineering Research and Design* **2020**.

98. Hu, Q.; Liu, H.; Zhang, Z.; Xie, Y., Nitrate removal from aqueous solution using polyaniline modified activated carbon: Optimization and characterization. *Journal of Molecular Liquids* **2020**, 113057.

99. Zhou, L.; Liu, Y.; Liu, S.; Yin, Y.; Zeng, G.; Tan, X.; Hu, X.; Hu, X.; Jiang, L.; Ding, Y.; Liu, S.; Huang, X., Investigation of the adsorption-reduction mechanisms of hexavalent chromium by ramie biochars of different pyrolytic temperatures. *Bioresource Technology* **2016,** *218*, 351-359.

100. Choudhary, B.; Paul, D., Isotherms, kinetics and thermodynamics of hexavalent chromium removal using biochar. *Journal of Environmental Chemical Engineering* **2018,** *6* (2), 2335-2343.

101. Shang, J.; Pi, J.; Zong, M.; Wang, Y.; Li, W.; Liao, Q., Chromium removal using magnetic biochar derived from herb-residue. *Journal of the Taiwan Institute of Chemical Engineers* **2016,** *68*, 289-294.

102. Xiao, F.; Cheng, J.; Cao, W.; Yang, C.; Chen, J.; Luo, Z., Removal of heavy metals from aqueous solution using chitosan-combined magnetic biochars. *Journal of Colloid and Interface Science* **2019,** *540*, 579-584.

103. Parlayıcı, Ş.; Pehlivan, E., Removal of Chromium (VI) from Aqueous Solution Using Chitosan Doped with Carbon Nanotubes. *Materials Today: Proceedings* **2019,** *18*, 1978-1985.

104. Anush, S.; Chandan, H.; Vishalakshi, B., Synthesis and metal ion adsorption characteristics of graphene oxide incorporated chitosan Schiff base. *International journal of Biological Macromolecules* **2019,** *126*, 908-916.

105. Cai, J.; Wang, W.; Xie, W.; Wei, X.; Liu, H.; Wei, S.; Gu, H.; Guo, Z., Carbon microfibers with tailored surface functionalities supporting iron/nickel bisalloy for highly efficient hexavalent chromium recovery. *Carbon* **2020,** *168*, 640-649.

106. Jeon, C., Removal of Cr (VI) from aqueous solution using amine-impregnated crab shells in the batch process. *Journal of Industrial and Engineering Chemistry* **2019,** *77*, 111-117.

CHAPTER IV

IRON/TITANIUM OXIDE-BIOCHAR COMPOSITE AS A VERSATILE PHOTOCATALYST FOR REMOVAL OF AQUEOUS CHROMIUM, LEAD, FLUORIDE AND METHYLENE BLUE

(Manuscript under preparation)

4.1 Abstract

Incorporation of Fe/Ti oxides into biochar (BC) improves the surface properties for environmental contaminant remediation. This work is the first report on Fe-Ti oxide/biochar (Fe_2TiO_5/BC) composite for sorptive removal of metal cations, oxy anions, inorganics and organic contaminants from aqueous solutions. Nano Fe-Ti oxide particles were dispersed on a high surface area biochar by a simple chemical co-precipitation method using $FeCl_3$ and $TiO(acac)_2$ salts followed by a base treatment and calcination at 500 °C. Surface structures and properties of the as-synthesized composite were characterized by PZC, BET, SEM, TEM, EDS, XRD, TGA, and XPS analysis. Adsorption of Cr(VI), Pb(II), fluoride and methylene blue (MB) on Fe_2TiO_5/BC was studied as a function of pH, equilibrium time and initial adsorbate concentration and temperature. Adsorption isotherm studies were carried out at 5, 25 and 45 °C and kinetics data of all four adsorbates are best fit to the pseudo second order model. Maximum Langmuir adsorption capacities for Cr(VI), Pb(II), fluoride and MB at 45 °C were 141 (pH 2), 200 (pH 5), 36 (pH 6) and 229 (pH 6) mg/g respectively. MB removal on Fe_2TiO_5/BC by the synergistic combination of adsorption and photocatalytic degradation at pH 3 and 6 under UV light irradiation. The removal

mechanisms of these contaminants on Fe_2TiO_5/BC by various mechanisms are proposed. Cr(VI), Pb(II), fluoride and MB exhibited excellent removal capacities in the presence of eight different competitive ions in simulated water samples.

4.2 Introduction

Water pollution caused by natural or anthropogenic activities has been a global concern. The polluted waters can include toxic metal ions[1] and dissolved organic matter consisting of textile dyes,[2] pesticides, cleaning solvents, polyhalogenated hydrocarbons,[3,4,5] and pharmaceuticals. Biological, chemical and physical methods based on biosorption,[6] microbial degradation, chemical precipitation,[7] adsorption[8] and advanced oxidations including electrochemical[9,10] and photocatalysis[11] are used to treat surface and waste water.

Pollutant adsorption onto solid carbon adsorbents such as activated carbon,[12,13] surface-modified biochar,[14] graphene and carbon nanotubes (CNTs)[15] are often used to remove contaminants from waste water. Simple design, low costs, and strong sorption affinities are advantages of many carbon adsorbents. Adsorbent surface area, surface chemical functionality of the adsorbent and adsorbate, pH influences on the adsorbate/adsorbent interaction, contact time and mass transport are crucial factors that determine the pollutant removal efficiency from water.[13,14]

Removal of aqueous toxic metal ions, inorganic and organic contaminants by oxides of Fe_2TiO_5 composites have been rarely reported in the literature. Herein, we present an investigation of the removal of Cr(VI), Pb(II), fluoride, and methylene blue (MB) from water using a Fe_2TiO_5 binary oxide on biochar (BC) composite. High surface area Douglas-Fir biochar was selected as an excellent support platform containing tunable functional groups for dispersing Fe_2TiO_5. An

attractive feature of this composite is its ability to remove both cationic and anionic inorganic species and organic pollutants via adsorption while also having photocatalytic degradation capabilities.

TiO_2,[16] ZnO,[17] and SnO_2[18] have been widely used semiconductor photocatalysts for three decades since their photocatalytic properties were first described by Fujishima and Honda in 1972.[19] TiO_2 has been an attractive candidate in pollution abatement due to its high chemical stability, nontoxicity, abundance and low cost. The photocatalytic oxidation of organic pollutants by these photocatalysts is attributed to the formation of nonselective hydroxyl radicals ($HO^{\bullet}$), superoxide radical ($O_2^{\bullet -}$) and H_2O_2.[11,16] However, TiO_2's the large band gap (3.2 eV) only adsorbs light at $\lambda < 390$[11] nm making it unable to use most of the solar spectrum, thereby limiting its photocatalyst applications.

UV irradiation on TiO_2 exhibited complete degradation of textile dyes with an average overall TOC removal larger than 94% for a photocatalytic reaction for 6 h.[20] Aqueous dye catalytic mineralization occurred by UV irradiation in the presence of TiO_2 via formation of nitrate, sulfate and gaseous N_2 and CO_2 confirming total mineralization of dyes.[19] Therefore, a catalytic system like TiO_2 that could work by to shifting the absorption wavelength totally into visible region could improve solar photoresponsivity.

Interest in Fe_2O_3 particles is growing as a highly efficient, and cost-effective adsorbent for the removal of aqueous Cr(VI), As(III), Pb(II), Cd(II), Cu(II) and organic pollutants.[21,22,23] It also reduces Cr(VI) to less toxic Cr(III) and oxidizes As(III) to As(V) respectively.[24,25] Fe_2O_3 is a good photocatalyst for the photodegradation of organic pollutants such as MB, Rhodamine B. Biochar's high surface area, enormous porosity, easily tunable functionalities, electrical conductivity and chemical stability can be beneficial when supporting or dispersing photocatalytic nanoparticles.[26]

Biochar has electron shuttling and storage properties due to its conductivity and redox properties present in its hydroquinone/quinone moieties. Black carbon biochar has an electron sink capacity of 0.85 and 0.87 mmol e^-/g in an acetate oxidation and a nitrate reduction respectively.[27] In TiO_2-biochar composite, enhanced photocatalytic efficiency was observed in a TiO_2-biochar composite due to the electron reservoir nature of biochar, which increased the charge-separation of generated e^-/hole pair .[28]

We now report the first biochar incorporated an iron/titanium oxide prepared to deposit Fe_2TiO_5 and this composite exhibited good sorption properties towards Cr(VI), Pb(II), fluoride and MB. Additionally, it demonstrated photocatalytic properties towards MB in water upon exposure to UV light. Enhanced removal efficiency of MB is attributed to the synergistic operation of an adsorption/photodegradation mechanisms by Fe_2TiO_5/BC. This composite exhibits higher photocatalytic effects due to the presence of surface active catalytic sites introduced by iron and titanium oxide phases and the aromatic carbon structure of the biochar phase. Fe_2TiO_5/BC performance as an adsorbent in aqueous system was tested in the presence of eight different model competing ions.

4.3 Materials and methods

All chemicals used here were analytical grade (Sigma- Aldrich, Fischer) unless otherwise specified. Aqueous stock solutions of chromium, lead, fluoride and methylene blue were prepared in deionized water and pH of these solutions were adjusted using 1 M, 0.1 M, and 0.01 M NaOH or HCl and measured using a pH meter (Hanna HI 2211).

4.3.1 Preparation of Fe_2TiO_5/BC

Fe_2TiO_5/BC was synthesized by modifying a previously reported hydrothermal method to prepare Fe_2TiO_5.[29] Briefly, titanium(IV) oxyacetylacetonate ($TiO(acac)_2$) (7.5 mmol, 2.18 g), ferric chloride ($FeCl_3$) (15 mmol, 2.97 g), and urea (NH_2CONH_2) (37.5 mmol, 2.25 g) were dissolved in deionized water (250 mL) and mixed with Douglas fir biochar (20 g). This biochar (BC) is a waste from timber industry wood gasification, produced by gasifying green wood chips at 900-1000 °C in an updraft gasifier for a 1-10 s residence time in a nitrogen atmosphere. This was followed by water rinsing to remove soluble organic residues and drying at room temperature.[30,31] The BC particle size obtained by sieving was in the range of 0.1-0.1 mm. The mixed $TiO(acac)_2$/($FeCl_3$ solution's pH was adjusted to 8 using ammonium hydroxide (NH_4OH) and further stirred at 80 °C for 48 h. Fe_2TiO_5 particles nucleate, grow and deposit on BC. Some nucleation and growth might occur at the BC surface. The BC was vacuum filtered from the mixture and washed three times with deionized water and followed by ethanol. Then the solid powder was dried at 60 °C for 2 h in a vacuum oven at 1atm and finally calcinated at 500 °C in a furnace under nitrogen atmosphere for 2 h. The resulting material is referred to as Fe_2TiO_5/BC and this contained 8.2% wt. of Fe_2TiO_5. Neat Fe_2TiO_5 was synthesized for characterization studies following the above-mentioned procedure except the addition of biochar. ($TiO(acac)_2$) (7.5 mmol, 2.18 g), ($FeCl_3$) (15 mmol, 2.97 g), and urea (NH_2CONH_2) (37.5 mmol, 2.25 g) were dissolved in deionized water (250 mL), and this gave Fe_2TiO_5 with a yield of ~85% wt.

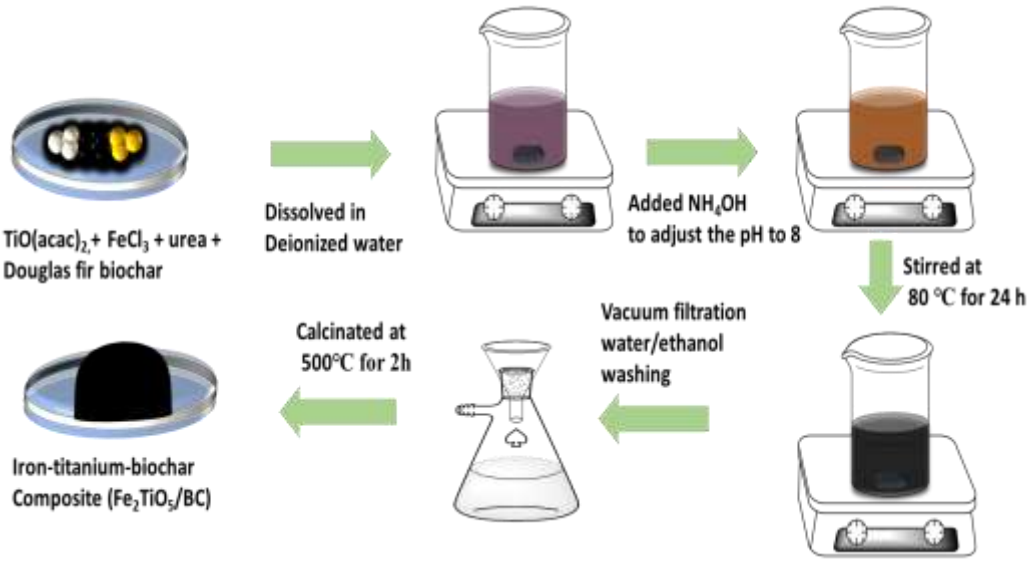

Scheme 4.1 Synthesis of iron-titanium-biochar composite (Fe_2TiO_5/BC)

4.3.2 Characterization of Fe_2TiO_5/BC

Surface morphology of Fe_2TiO_5/BC was examined by scanning electron microscopy (SEM) (JEOL JSM-6500F), at 5 kV coupled to an energy dispersive X-ray (EDX) detector. Transmission electron microscopy images were obtained by a TEM (JEOL model 2100), operated at 200 kV with an Oxford X-max-80 detector for the TEM/EDX analyses. X-ray diffraction analysis was performed using a Rigaku ultima III (Cu-Kα (ƛ = 1.54 Å). Diffuse reflectance UV-Vis spectroscopy was used to acquire the Fe_2TiO_5/BC band gap estimation. Brunauer-Emmet-Teller (BET) surface area, pore volume and pore diameter were determined by N_2 adsorption-desorption isotherms using a Micrometrics Tristar II Plus 3030 surface area analyzer at 277 K. Thermogravimetric analyses (TGA) were carried out at a heating rate of 10 °C/min from 20-1000 °C under nitrogen atmosphere using a Mettler TGA/DSC thermogravimetric analyzer (TGA/DSC STARe system, Mettler Toledo, USA. X-ray photoelectron spectroscopy (XPS) measurements before and after Cr(VI), Pb(II), F and MB adsorption on Fe_2TiO_5/BC were conducted with a

Thermo Scientific K-Alpha system. (1486.6 eV, Al Kα line, 400 μm^2 spot size with a maximum penetration depth of 100 Å). CHN analyzer (CHN: ASTM D5291) was used to get the weight percent C, H, and N in Fe_2TiO_5/BC. Ash content of Fe_2TiO_5/BC was calculated by incinerating 1 g of sample in an open top porcelain crucible in a muffle furnace at 650 °C for 4 h and then comparing the initial and final masses. Fe and Ti wt.% of the material were determined by an acid digestion method. (50 mL of (1:3 v/v 70% HNO_3 : 37% HCl) mixed with composite (0.1 g) at 60 °C for 12 h prior to the analysis). This was followed by inductively coupled plasma mass spectroscopy (ICP-MS). Point of zero charge (PZC) of Fe_2TiO_5/BC was determined by a plot of equilibrium pH vs. initial pH. NaCl (0.01 M) solutions (50 mL) at different pH values were (2 to 10) prepared and mixed with Fe_2TiO_5/BC (0.05 g) for 24 h.

4.3.3 Batch adsorption, effect of competitive ions on adsorption and iron leaching studies

Equilibrium adsorption studies of Cr(VI), Pb(II), fluoride and methylene blue (MB) on Fe_2TiO_5/BC were performed to investigate the effect of solution pH, contact time and adsorbate concentration. The effect of pH on adsorption was examined using three replicates at each pH from 2 to 10 in 25 mL solutions containing 50 mg/L of analyte and (25 mg) Fe_2TiO_5/BC doses. The effect of contact time was monitored by varying the equilibrium time for each analyte. Different adsorbate concentrations were used for batch sorption studies and plastic vials (50 mL) were used to mix all samples (25 mL) with Fe_2TiO_5/BC. Solutions were filtered (Whatman filter paper No. 1) after reaching equilibrium. The remaining concentrations of Cr(VI), Pb(II) were determined by atomic absorption spectroscopy (AAS) (Shimadzu AA-7000). Fluoride was determined using a fluoride ion selective electrode and methylene blue (MB) by double beam UV-Vis spectroscopy at 664 nm. Standard deviations for three replicates were used to calculate error. Adsorption

capacity for each analyte at equilibrium, Q_e (mg/g) was obtained from $Q_e = \frac{(C_i - C_e)V}{W}$. Here, C_i and C_e denote the initial and equilibrium concentration of chromium or nitrate in mg/L, V is the volume of adsorbate in mL, and W is the weight of biochar in g.

Cr(VI), Pb(II), fluoride and MB adsorption onto Fe_2TiO_5/BC in the presence of sulfate, phosphate, nitrate, chloride, carbonate, arsenate, molybdate and Cu(II) competitive ions were investigated since these ions are present in natural and waste water systems in trace or comparatively high amounts. The effect of each competitive ion was monitored at 0.01, 0.1 and 1 mM at room temperature for Cr(VI), 50 mg/L, Pb(II) 100 mg/L, fluoride 50 mg/L and MB 100 mg/L, respectively. Experiments were performed in triplicate. Fe_2TiO_5/BC (25 mg) was mixed with 25 mL of solution containing the competitive ion for 3 h with Cr(VI), Pb(II) 1 h, fluoride 2 h and MB 2 h, respectively. After reaching equilibrium the mixtures were filtered and the adsorbate concentration of each was determined. Also, the remaining competitive ion concentration after adsorption in each mixture was quantified using ICP-MS (for arsenate, phosphate, molybdate and copper), ion selective electrode (for chloride) and liquid chromatography (LC-MS) (for nitrate).

Simultaneous Cr(VI), Pb(II), fluoride and MB removal capability and Fe_2TiO_5BC's performance in complex water matrices were tested by simulating a mixture of 10 mg/L of each species in different matrices (DI water, Chadwick lake water, Noxubee lake water, Atoyac lake water, (Argentina, Latin America)). However, co-existing Pb(II) and Cr(VI) precipitates were removed by filtration prior to the sorption experiments. Removal % was used as a figure of merit for the comparison of sorption performance. Approximately 50.0 mg of Fe_2TiO_5/BC was equilibrated (in triplicate, 2 h) with 25.0 mL of the multi-species pollutant solutions, These suspensions were filtered and filtrate were analyzed for the remaining species concentrations using ICP-MS (Cr(VI), Pb(II)), ISE (F^-) and LC-UV (MB).

Iron leaching experiments were conducted on Fe_2TiO_5/BC (25 mg) after adsorption of Cr(VI), 50 mg/L, Pb(II) 100 mg/L, fluoride 50 mg/L and MB 100 mg/L (25 mL for each solution). These experiments were performed for each analyte at pH 3, 5, 7, and 9 at 25 °C. Iron content in the filtrates after adsorption was measured using atomic absorption spectrophotometer (AAS). All experiments were performed in triplicate and standard deviation was used to calculate the error of each iron measurement.

4.3.4 Photodegradation studies

The photocatalytic activity of the Fe_2TiO_5/BC composite on methylene blue degradation under different experimental conditions was monitored under UV light irradiation. Aqueous MB and Fe_2TiO_5/BC (100 mg/L, 100 mL) containing the composite (100 mg) in a pyrex beaker was placed under a mercury spot lamp (100 W, wavelength 365 nm, UVP P/N 34-0054-01, Upland, USA), This lamp was placed 20 cm above the top level of the solution, which had a depth of 3 cm in the beaker). Photodegradation was conducted at either pH 6 or 3 for all experimental irradiations. Air or nitrogen was continuously bubbled through the aqueous MB solutions. Beakers containing MB and the photocatalyst run in the dark were covered with aluminum foil and stirred (100 rpm) for 2 h to achieve the adsorption equilibrium prior to the photodegradation studies.

4.4 Results and Discussion

4.4.1 Characterization of Fe_2TiO_5/BC

Fe_2TiO_5/BC exhibited a Brunauer-Emmett-Teller (BET) surface area of 576 m^2/g verses an original surface area of 535 m^2/g for the Douglas fir biochar (Table C.1). This area is significantly higher than the as synthesized neat Fe_2TiO_5 (85 m^2/g) when measured alone. The

surface area of the Fe_2TiO_5 deposits on BC are not known because the combined value of 576 m^2/g is composed of both Fe_2TiO_5 and BC phases and Fe_2TiO_5 could be covering entree into a significant amount of BC pore volume. Douglas fir BC's high surface areas (535 m^2/g) results from a porous morphology, large pore volume (0.249 cm^3/g) and pore diameters of 18.6 Å due to mass loss from its internal carbon skeleton, which forms large number of micropores and ultra micropores during wet pyrolysis at 900-1000 °C.[31] The high surface area, pore volume (0.207 cm^3/g) and pore diameter (12.6 Å) obtained for the Fe_2TiO_5/BC composite is a joint contribution of the biochar and Fe_2TiO_5 phases. The elemental Fe and Ti weight percentages obtained using acid digestion method for neat Fe_2TiO_5 and Fe_2TiO_5/BC were (Fe-62.4, Ti-22.7) and (Fe-6.58, Ti-2.4), respectively. The Fe/Ti molar ratio was 2.4 to 1 in Fe_2TiO_5/BC and 2.3 to 1 in Fe_2TiO_5. Fe_2TiO_5 contains a ash content of 96.7% wt. verses 16.3% wt. of ash content for Fe_2TiO_5/BC, where this ash also contains the oxides and carbonates of potassium, magnesium, calcium, silica initially present in the wood feed and the iron and titanium oxides introduced by Fe_2TiO_5/BC.

SEM and TEM characterizations were performed to study the surface morphology. Fig. 4.1 exhibited the well developed porous structure, originally present in the wood precursor of carbon skeleton present in biochar with Fe_2TiO_5 depositions on biochar surface under four different magnification. Fe_2TiO_5 particles can be clearly seen as small octahedral crystalline particle clusters dispersed on the biochar. Approximate atomic percentages obtained by SEM-EDX (Fig. C.1) indicated the composition of each element present on Fe_2TiO_5/BC as C (84.2), O (15.1), Fe (0.5) and Ti (0.3). The atomic ratio of Fe to Ti was closer to 2 but the percent O ratio was higher than 5 in Fe_2TiO_5/BC. This high oxygen percentage may be due to the contribution of both inorganic (SiO_2, $CaCO_3$) and organic oxygen initially present on biochar. SEM-EDX is a surface sensitive technique which analyzes ~2 µm of depth from the material surface. These numbers don't

represent the bulk values. TEM elemental mapping images on Fe_2TiO_5/BC (Fig. C.2) confirms the presence of C, O, Fe and Ti elements on the composite and this is well supported by the weight percentages of C (61.1), O (18.7) Fe (11.1) and Ti (9.0) obtained by TEM-EDX spectra. EDX elemental compositions (by wt.%) after adsorption of Cr(VI), Pb(II), fluoride and MB on to Fe_2TiO_5/BC are presented in the supporting information (Fig. C.3).

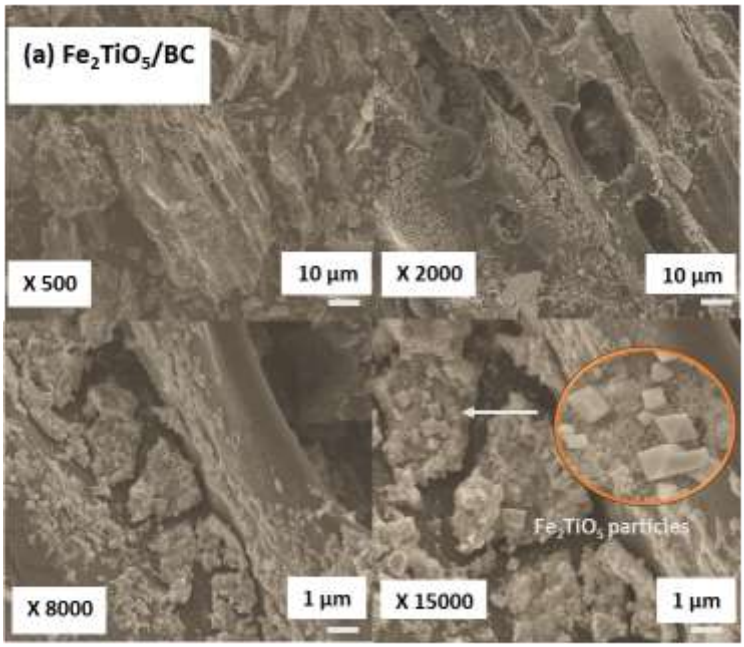

Figure 4.1 SEM images of Fe_2TiO_5/BC under magnifications from 500 x to 15000

SEM images were obtained at the Institute of Imaging and Analytical Technologies (I^2AT), Mississippi State University.

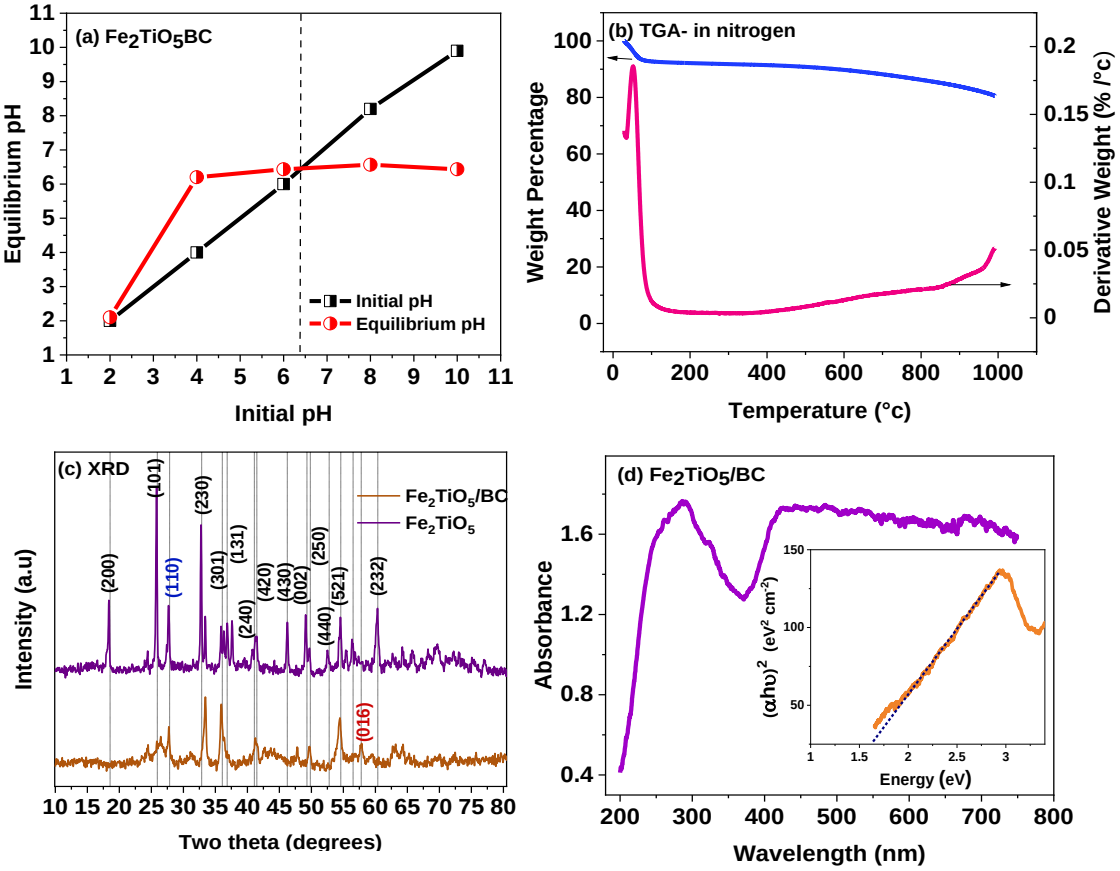

Figure 4.2 Characterization of Fe_2TiO_5/BC

Point of zero charge (PZC=6.4) measurements for (a) Fe_2TiO_5/BC, (b) thermogravimetric analysis (TGA) for Fe_2TiO_5/BC at a 10 °C/min heating rate in nitrogen, (c) XRD and (d) UV-visible diffuse reflectance spectrum of Fe_2TiO_5/BC and its band gap.

The TGA of Fe_2TiO_5/BC at 10 °C/min heating rate under nitrogen exhibited a small weight loss at 40-90 °C due to moisture removal. Then a gradual weight loss of ~18% wt. until 1000 °C was observed and this was due to thermal decomposition of carbon skeleton in the biochar. In this region any significant weight loss at a specific temperature was not observed. Significant weight loss around 565 °C takes place in Douglas fir biochar (Fig. C.4) due to thermal decompositions including decarboxylation, decarbonylation and the thermal destruction of the carbon skeleton.[31]

The XRD patterns of Fe_2TiO_5 and Fe_2TiO_5/BC are presented in Fig. 2(c). The XRD peaks get broad and show low intensities due to the existence of amorphous material and poor particle crystallinity..[29,32,33,34] Neat Fe_2TiO_5 exhibited several strong sharp peaks in the 2θ range of 10 to 80º. The JCPDS file No. 41-1432 for Fe_2TiO_5 matches well with synthesized Fe_2TiO_5's major peaks and their indexed planes at 18.34º (200), 25.54º (101), 32.78º (230), 35.9º (301), 36.82º (131), 46.20º (430), 49.10º (002), and 60.34º (232).[29,35,36] Fe_2TiO_5/BC exhibits majority of the peaks related to Fe_2TiO_5 (Fig. 4.2(c)) confirming the successful formation of Fe_2TiO_5 on biochar surface. The broad peak ~25° in Fe_2TiO_5/BC is due to the biochar originates from the disordered cellulose crystal structure becoming increasing aromatized during high temperature pyrolysis[37] and this peak overlaps with the peak at 25.54º. In addition, the peaks at 27.1° (110) attribute for the presence of trace amounts of TiO_2 (JCPDS file No. 21-1276)[38,39] and α-Fe_2O_3 at 57.62º (016), (JCPDS file No. 33-0664)[40,41] in both the neat Fe_2TiO_5 and Fe_2TiO_5/BC formed in this work.

The bandgap of Fe_2TiO_5/BC was calculated by UV-Visible diffuse reflectance spectra in the wavelength range from 200 to 800 nm (Fig. 4.2 d). The spectra obtained was converted to the Kulbelka-Munk function,[42] which is proportional to the absorption coefficient. The bandgap was estimated using a Tauc plot and extrapolating the linear region of the $(\alpha h\nu)^2$ versus photon energy ($h\nu$) curve given by the following formula. $(\alpha h\nu)^2 = A (h\nu - Eg)$ where α is the absorption coefficient, A is constant, $h\nu$ is the energy of light and n is a constant, which depends on the nature of the electron transition. The band gap was estimated as 1.65 eV. Band gaps of 1.41[43] and 1.95[44] eV have been reported for Fe_2TiO_5 nanopowder. Similar results were obtained for the 1.5 eV band gap for bare biochar and 1.86 eV for a $CuWO_4$-biochar composite.[45]

Fe_2TiO_5/BC exhibited a net point of zero charge (PZC) of 6.4 resulting from the contribution of Fe_2O_3, TiO_2 and biochar phases in the composite. PZC values for Fe_2O_3/TiO_2

ceramic[46] (4.8), Fe_2O_3[47] (6.9) and TiO_2[47] (5.2) were reported previously in the literature. PZC of the BC in Fe_2TiO_5/BC is around 9.20 and this highly depends on the surface functional groups and the ash content.[31] At high pyrolysis temperature, Ca, Mg carbonates and oxides formed lead to a high PZC. PZC of 6.4 of Fe_2TiO_5/BC reflects the contribution of surface Fe-OH, Ti-OH and Fe-O-Ti functional groups.

The pH dependence for adsorption of Cr(VI), Pb(II), fluoride and MB on Fe_2TiO_5/BC are presented in Fig. C.5. In aqueous solutions Cr(VI) is present as oxyanions. Hydrogen chromate ($HCrO_4^-$), predominates at pH 1-6, and chromate (CrO_4^{2-}) dominates at pH > 6.[31] Cr(VI) is present as chromic acid (H_2CrO_4) at pH < 1,[48] but in this work experiments were not conducted below pH 2. The highest Cr(VI) removal of 75% was observed at pH 2 for a 100 mg/L solution. This rapidly decreased to 20% removal at pH 3. Cr(VI) removal was negligible from pH 4-10. Above pH 4 , $HCrO_4^-$ species may be repelled from negatively charged adsorbent surfaces which leads to a poor Cr(VI) removal. Thus pH 2 was selected for all Cr(VI) adsorption studies.

Pb(II) adsorption on Fe_2TiO_5/BC rose continuously as solution pH increased from 2 to 5. 34%. Pb(II) removal occurred at pH 5 was observed for a 100 mg/L solution at 25 °C. Pb(II) exists as free hydrated ions between pH 2-5 and electrostatic repulsions exist in positively charged surface below pH 6.4. Yet high Pb(II) removal from solution at these low pH values can be seen. When pH of the solution rose electrostatic repulsions are decreased but Pb(II) removal experiments were not continued after pH 5 since Pb(II) starts to precipitate as $Pb(OH)_2$ at pH 5.5 (Ksp = 5.0 x 10^{-16} at 298 K). Above pH 6 lead hydroxyl complexes such as $Pb(OH)^+$, $Pb_4(OH)_4^{4+}$, $Pb_3(OH)_4^{2+}$ are formed, so precipitation dominates and adsorption can't be studied above pH 6.[49]

Fluoride adsorption was robust in pH 3 -10 (~22 %). This is mainly due to greater electrostatic attractions with positively charged Fe-O^+H_2, Ti-O^+H_2 surfaces and hydrogen bonding

with protonated Fe_2TiO_5BC surfaces. The removal percentage dropped slightly when increasing pH all the way to 12 (15 % removal). This could be due to the electrostatic repulsion from Fe-O^- and TiO^- as well as negative BC surfaces above pH 9.2 and increasing competition from OH^- ions. MB exhibited a wide pH window from 4 to 10. MB was 50% removed from solution at pH 4 and this remained almost constant from pH 4 to 10. BC's aromatic structure can trigger the MB adsorption via π-π interactions, hydrogen bonding with N centers present in MB. At low pH values positively charged N centers on MB repel the positively charged Fe_2TiO_5/BC surfaces resulting low adsorption. At a pH above the pzc of Fe_2TiO_5 (4.8), negatively charged deprotonated Fe-O^-, Ti-O^- surfaces enhance the MB adsorption via electrostatic attractions.

4.4.2 Adsorption kinetics

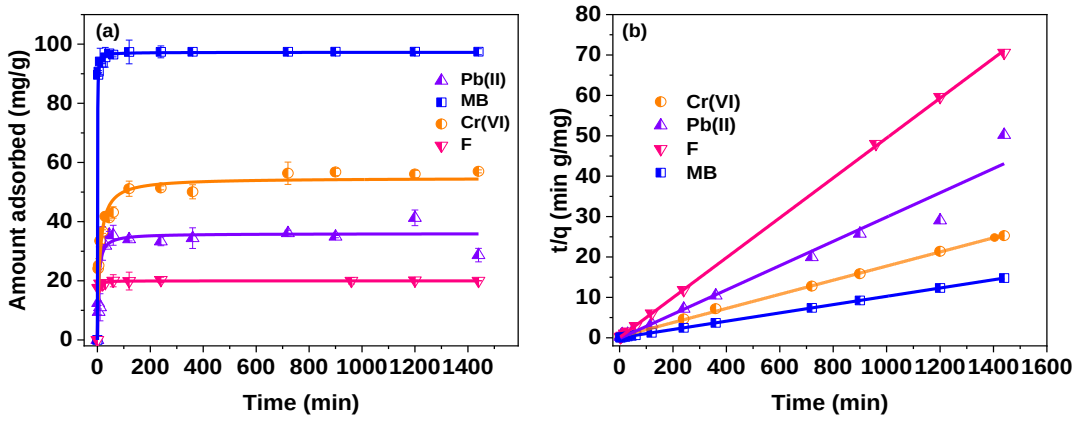

Figure 4.3 Effect of contact time

Effect of contact time on Cr(VI) (100 mg/L, pH 2), Pb(II) (50 mg/L, pH 5), F (50 mg/L, pH 6) and MB (100 mg/L, pH 6) adsorption at 25 °C onto Fe_2TiO_5/BC. (a) amount adsorbed in mg/g (b) linear fit of pseudo second order kinetics. Fe_2TiO_5/BC (25 mg) was mixed with 25 mL of solution containing each of the analyte with a stirring rate of 200 rpm.

Cr(VI), Pb(II), fluoride and MB removal on Fe_2TiO_5/BC were plotted verses the time (Fig. 4.3). All adsorbates reached the equilibrium after 2 h and then remained almost constant for 24 h.

Cr(VI) removal percentage at pH 2 was 52% using 100 mg/L solution. Pb(II) removal at pH 5 and fluoride removal at pH 6 for a 50 mg/L solution were ~60% and ~38%, respectively. MB (pH 6) exhibited 98%, a higher removal percentage than the other analytes on Fe_2TiO_5/BC. Fast uptake rates were observed initially for all analytes due to the availability of sufficient adsorption sites on the composite surface. Uptake gradually slowed down with time due to the increasing surface saturation. Experimental data for Cr(VI), Pb(II), fluoride and MB adsorption on Fe_2TiO_5/BC fitted well to the pseudo second order kinetic model, $t/q_t = t/qe + 1/k_2 q_e^2$ with high correlation coefficients (R^2) closer to unity., Here, t is the contact time, q_e denotes the amount adsorbed (mg/g) at the equilibrium time, q_t is the amount adsorbed (mg/g) at time t and k_2 is the second order rate constant (g/mg.min).

4.4.3 Adsorption isotherms and thermodynamics

Cr(VI), Pb(II), fluoride and MB adsorptions on Fe_2TiO_5/BC were conducted at 278, 298 and 318 K and data was fitted to Langmuir[50] and Freundlich[51] isotherms using Origin Pro 2020 software (Fig. 4.4) and Table 4.1. Batch sorption equilibrium studies were conducted for Cr(VI) and MB (10-1200 mg/L), Pb(II) (10-1000 mg/L) and fluoride (5-600 mg/L). The maximum Langmuir capacities obtained for Cr(VI), Pb(II), fluoride and MB adsorption on Fe_2TiO_5/BC at 318 K were 141, 200, 36, and 130 mg/g and 119, 180, 26, and 210 mg/g at 298 K respectively.

Adsorption capacities increased as temperature increased from 278 to 318 K. The Van't Hoff equation, $\ln K_{ads} = -\Delta H°/R\ (1/T) + \Delta S°/R$, was used to calculate the enthalpy (ΔH), and entropy (ΔS) for Langmuir and Freundlich constants (Fig. C.6). The isotherm constants at each temperature (5, 25, 45 °C) were converted into dimensionless constants. This was performed by multiplying by the density of the liquid phase ($1x10^6$ mg/L).[52] The ΔH, and ΔS values for Langmuir and Freundlich model isotherm constants for Cr(VI), Pb(II), fluoride and MB

adsorptions on Fe_2TiO_5/BC were tabulated in Table 4.2. All values for ΔH and ΔS are positive showing that all four analytes adsorbed on Fe_2TiO_5/BC endothermically with increasing randomness between initial and final states. Gibbs free energy values, (ΔG) were negative for all four sorbates at all three temperatures. The magnitude of (ΔG) increased with increasing the temperature. These adsorptions are thermodynamically feasible, spontaneous processes.

Table 4.1 Langmuir and Freundlich isotherm parameters for Cr(VI), Pb(II), fluoride and MB adsorption on Fe_2TiO_5/BC

Analyte	Isotherm parameters		Temperature		
			278 K	298 K	318 K
Cr(VI)	Langmuir	q_o (mg/g)	83.0	119.9	141.6
	$q_e = \frac{q_0 K_L C_e}{(1 + K_L C_e)}$	K_L(L/mg)	0.024	0.026	0.030
		R^2	0.988	0.987	0.993
	Freundlich	K_F (L/g)	4.0	7.0	10
	$q_e = K_F C_e^{(1/n)}$	n	2.19	2.36	2.49
		R^2	0.990	0.991	0.983
Pb(II)	Langmuir	q_o (mg/g)	150.0	180.0	200.0
	$q_e = \frac{q_0 K_L C_e}{(1 + K_L C_e)}$	K_L(L/mg)	0.015	0.021	0.042
		R^2	0.991	0.996	0.994
	Freundlich	K_F (L/g)	2.3	5.5	10.0
	$q_e = K_F C_e^{(1/n)}$	n	1.48	2.0	2.16
		R^2	0.979	0.993	0.996
F^-	Langmuir	q_o (mg/g)	24.174	26.0	36.0
	$q_e = \frac{q_0 K_L C_e}{(1 + K_L C_e)}$	K_L(L/mg)	0.0152	0.0166	0.0190
		R^2	0.989	0.991	0.973
	Freundlich	K_F (L/g)	2.14	2.46	3.17

Table 4.1 (continued)

	$q_e = K_F C_e^{(1/n)}$	n	2.30	2.31	2.34
		R^2	0.992	0.990	0.991
MB	Langmuir	q_o (mg/g)	175.0	210.6	229.9
	$q_e = \frac{q_0 K_L C_e}{(1 + K_L C_e)}$	K_L(L/mg)	0.013	0.016	0.02
		R^2	0.995	0.998	0.991
	Freundlich	K_F (L/g)	21.1	23.3	26.1
	$q_e = K_F C_e^{(1/n)}$	n	2.84	3.20	3.43
		R^2	0.992	0.998	0.989

q_e - adsorption capacity at equilibrium (mg/g), q_o - monolayer adsorption capacity (mg/g), K_L- Langmuir isotherm constant (L/mg), K_f - Freundlich isotherm constant (L/g), n - a constant indicative of the intensity of the adsorption, R^2 - regression coefficient

Table 4.2 Thermodynamic parameters for Cr(VI), Pb(II), Fluoride and MB adsorption on Fe_2TiO_5/BC

		T (K)	R^2	K_{ads}	ln K_{ads}	ΔG^0 (kJ/mol)	ΔH^0 (kJ/mol)	ΔS^0 (kJ/molK)
Cr	Langmuir	278	0.90	2.43×10^4	10.1	-23.1	3.84	0.09
		298		2.60×10^4	10.2	-25.4		
		318		3.00×10^4	10.3	-27.0		
	Freundlich	278	0.98	4.00×10^3	8.29	-19.3	16.9	0.13
		298		7.00×10^3	8.85	-21.8		
		318		10.0×10^3	9.21	-24.5		
Pb	Langmuir	278	0.93	1.50×10^4	9.62	-22.1	18.8	0.15
		298		2.20×10^4	9.99	-25.0		
		318		4.20×10^4	10.7	-27.9		
	Freundlich	278	0.98	2.30×10^3	7.74	-17.9	27.1	0.16
		298		5.50×10^3	8.62	-21.2		
		318		10.0×10^3	9.21	-24.4		
F	Langmuir	278	0.95	1.52×10^4	9.63	-22.2	4.07	0.09
		298		1.66×10^4	9.72	-24.1		
		318		1.90×10^4	9.85	-26.0		
	Freundlich	278	0.92	2.14×10^3	7.67	-17.6	7.18	0.09
		298		2.46×10^3	7.81	-19.3		
		318		3.17×10^3	8.07	-21.1		
MB	Langmuir	278	0.97	1.30×10^4	9.52	-21.8	7.09	0.10
		298		1.60×10^4	9.68	-23.9		
		318		2.00×10^4	9.90	-25.9		
	Freundlich	278	0.98	2.11×10^4	9.96	-23.0	3.88	0.10
		298		2.33×10^4	10.1	-24.9		
		318		2.61×10^4	10.2	-26.8		

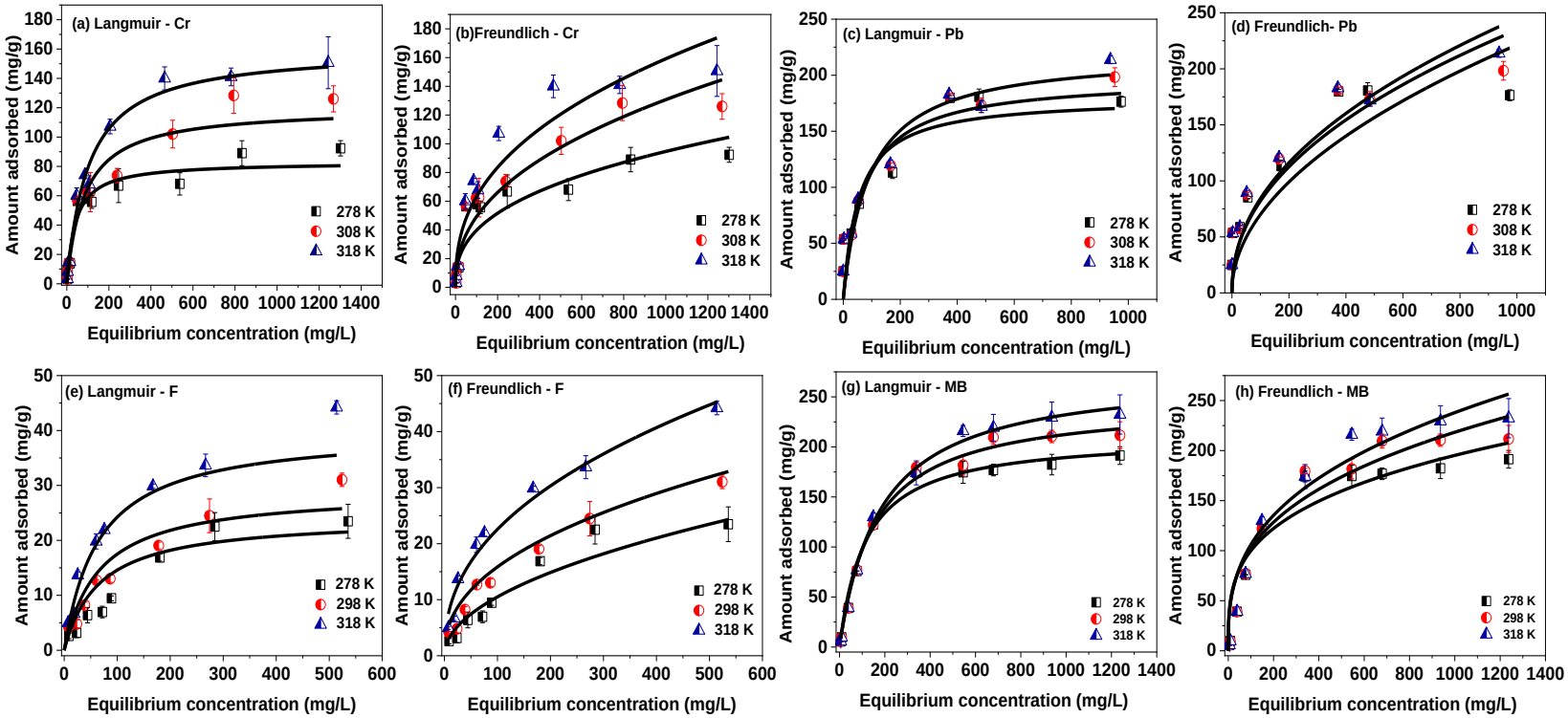

Figure 4.4 Langmuir and Freundlich isotherm plots

Langmuir and Freundlich isotherm plots for Cr(VI), Pb(II), fluoride and MB adsorption on Fe_2TiO_5BC at 278, 298, and 318 K. (a), (b) Cr(VI) at pH 2 for 2 h, (c), (d) Pb(II) at pH 5 for 1 h (e), (f) fluoride at pH 6 for 3 h and (g), (h) MB at pH 6 for 2 h. Fe_2TiO_5/BC (25 mg) was mixed with 25 mL of solution containing each of the analyte with a stirring rate of 200 rpm. Error bars are the standard deviations of three replicates.

4.4.4 Adsorption interaction

4.4.4.1 X-ray photoelectron spectroscopy (XPS) analysis

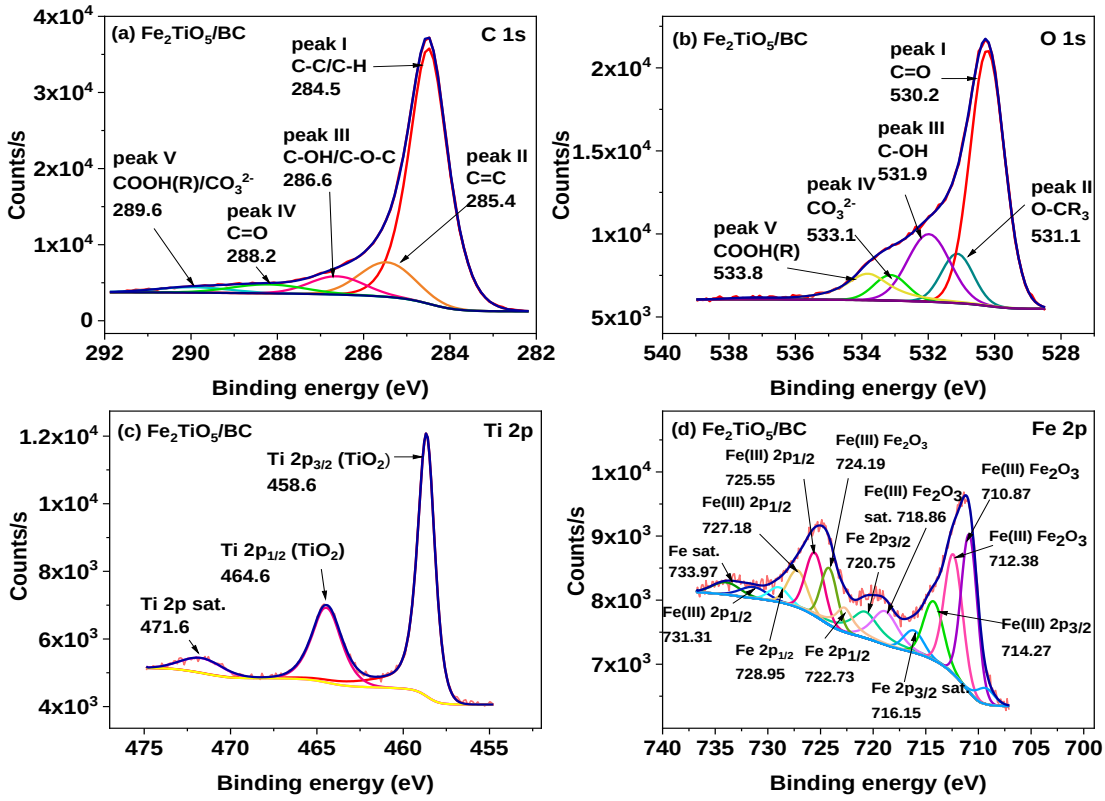

Figure 4.5 HR-XPS deconvoluted spectra of the Fe_2TiO_5/BC's adsorbent surface (a) C1s (b) O1s (c) Ti 2p and (d) Fe 2p

Low resolution survey scan (LR-XPS) of Fe_2TiO_5/BC and the chromium-, lead-, fluoride- and methylene blue-laden Fe_2TiO_5/BC indicate the presence of C, O, Fe, Ti, Cr, Pb, and F elements on the surface regions of the composite (Fig. C.7). This surface specific analysis (maximum penetration 100 Å with increasing sensitivity as the surface layer of atoms is approached) helps define functional groups, atomic ratios and the respective elemental oxidation states by evaluating

the samples' high resolution X-ray photoelectron spectra (HR-XPS). HR-XPS of Fe_2TiO_5/BC exhibited surface region atomic percentages of C (70.4), O (18.5), Fe (6.0) and Ti (4.0) (Table C.2,3). After Cr(VI), Pb(II) and fluoride uptake by Fe_2TiO_5BC at pH 2, 5 and 6 respectively, the ion surface atomic percentages were 2.5% Cr(VI), 1% Pb(II) and 0.3% fluoride, directly confirming adsorption of each.

C1s peak of Fe_2TiO_5/BC was deconvoluted into five peaks at 284.50 eV, 285.46 eV, 286.62 eV, 288.21 eV, and 289.96 eV binding energies corresponding to C-C/C-H, C=C, C-OH/C-O-C, C=O. and CO_3^{2-}/COOH(R) respectively (Fig. 4.5a). Deconvolution of the O1s peak revealed five peaks including a dominant peak at 530.22 eV (C=O) (Fig. 5b). These peaks were at 531.12 eV (O-CR_3), 531.9 eV (C-OH), 533.13 eV (CO_3^{2-}) and 533.82 eV (COOH(R) (Table C.3). Binding energies of the Ti 2p core level are assigned to two characteristic peaks (Fig. 5c) for Ti $2p_{1/2}$ 464.6 eV (TiO_2)[53] and Ti $2p_{3/2}$ 458. 6 eV (TiO_2).[54,] (Fe_2TiO_5)[32,33] A satellite peak at 471.6 eV can be clearly seen for Ti(IV) oxidation state.[55] Fe 2p HR-XPS for Fe_2TiO_5/BC were deconvoluted into multiple peaks, mainly corresponding to the Fe_2O_3 deconvoluted peaks for Fe $2p_{1/2}$ (722.7 eV) and Fe $2p_{3/2}$ (710.8 eV) in Fe_2TiO_5.[32,33] This indicates the Fe(III) oxidation state in the as synthesized material.

Cr(VI) adsorption on the composite surface gave Cr(VI) species and some reduction to Cr(III) (Fig. C.8). This was verified by using the reference Cr $2p_{3/2}$ peaks present for Cr_2O_3 at 576.7 eV[56,57], 577.7 eV[58] for Cr(III). Also a peak at 579.6 eV for Cr(VI) appeared agreeing with the CrO_3.[59,60] The surface atomic percentages of Cr(III) and Cr(VI) after adsorption of Cr(VI) onto Fe_2TiO_5/BC were 2.5 and 1.5. The presence of both Cr(III) and Cr(VI) species on the surface shows a majority of Cr(VI) species has reduced to less toxic Cr(III). The initial O1s peaks (530.22,

10.5), (531.12, 1.87) and (531.98, 3.4) present on Fe_2TiO_5/BC before Cr(VI) uptake have shifted to higher binding energies and larger atomic percentages (530.49, 14.8), (531.40, 5.7) and (532.15, 5.6) after Cr uptake. While greater subresolution of oxygen peaks are impossible, it is clear that the increased binding energies (eV) show that removing 1s electrons from oxygens in these peak regions has become more difficult. Spin orbital splitting of Pb's 4f energy level resulted doublets attributed to $4f_{7/2}$ and $4f_{5/2}$ levels in the HR-XPS of Fe_2TiO_5/BC after Pb(II) uptake (Fig. C.8).Deconvoluted $4f_{7/2}$ peaks at 139.2 eV and 138.73 eV are due to Pb(II) as referred to (PbO).[61,62] HR-XPS for F1s exhibited a fluoride peak at 684.76 eV referred to (NaF).[63,64]

Possible sorption interactions of the Cr(VI), Pb(II), fluoride, MB and competitive contaminants on BC and Fe_2TiO_5 surfaces are briefly summarized in scheme 1. Interactions can occur through electrostatic attractions (CO_3^{2-}), hydrogen bonding (F^-, Cl^-, AsO_4^{3-}, PO_4^{3-}, CO_3^{2-}, NO_3^-, SO_4^{2-} and CrO_4^{2-}), weak chemisorption (AsO_4^{3-}, PO_4^{3-}, CrO_4^{2-}, SO_4^{2-} and CO_3^{2-}), π-π interactions (MB) and coordination (Pb(II) and Cu(II)) on BC phenolics or carboxylates. On the Fe_2TiO_5 surface, chemisorption dominates for AsO_4^{3-}, PO_4^{3-} (inner-sphere), CO_3^{2-} and SO_4^{2-} (outer-sphere). Electrostatic attractions (Pb(II), Cu(II), MB) and hydrogen bonding (NO_3^-, Cl^- and F^-) may also play a role. In addition, the stoichiometric precipitation of Fe(III) compounds of CrO_4^{2-}, PO_4^{3-}, and AsO_4^{3-} oxyanions or F^- and Cl^- anions that are insoluble must be considered at pH values where some ion leaching may occur.

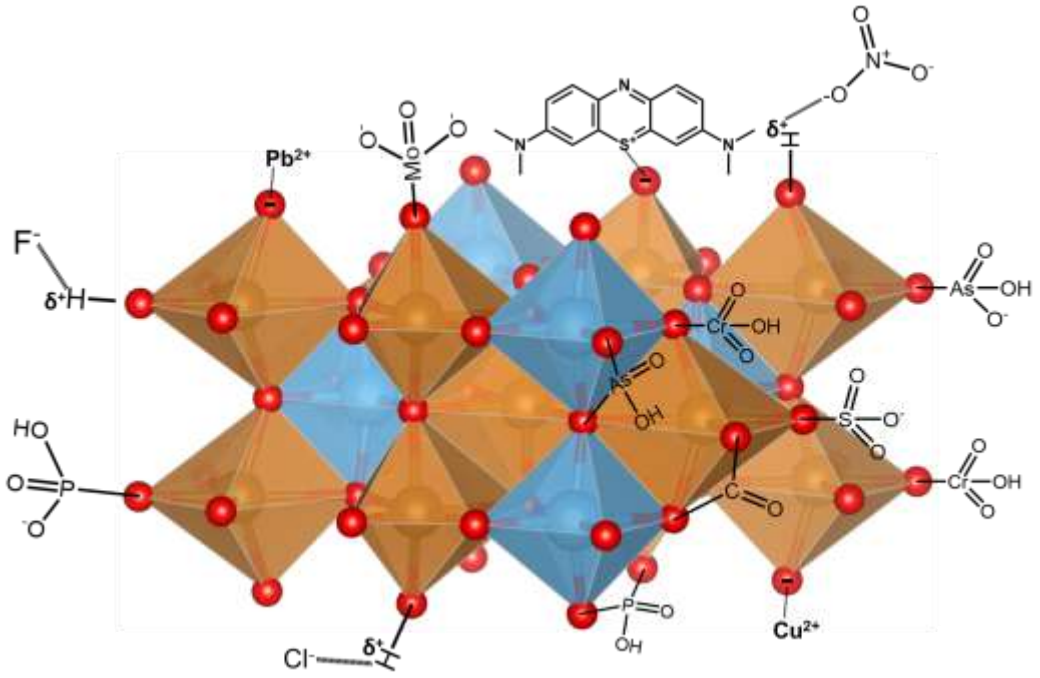

Scheme 4.2 Schematic representation of possible interactions of Cr(VI), Pb(II), fluoride, MB and competitive contaminants ions on Fe_2TiO_5 phase

4.4.5 Effect of competing ions on Cr(VI), Pb(II), F and MB adsorption

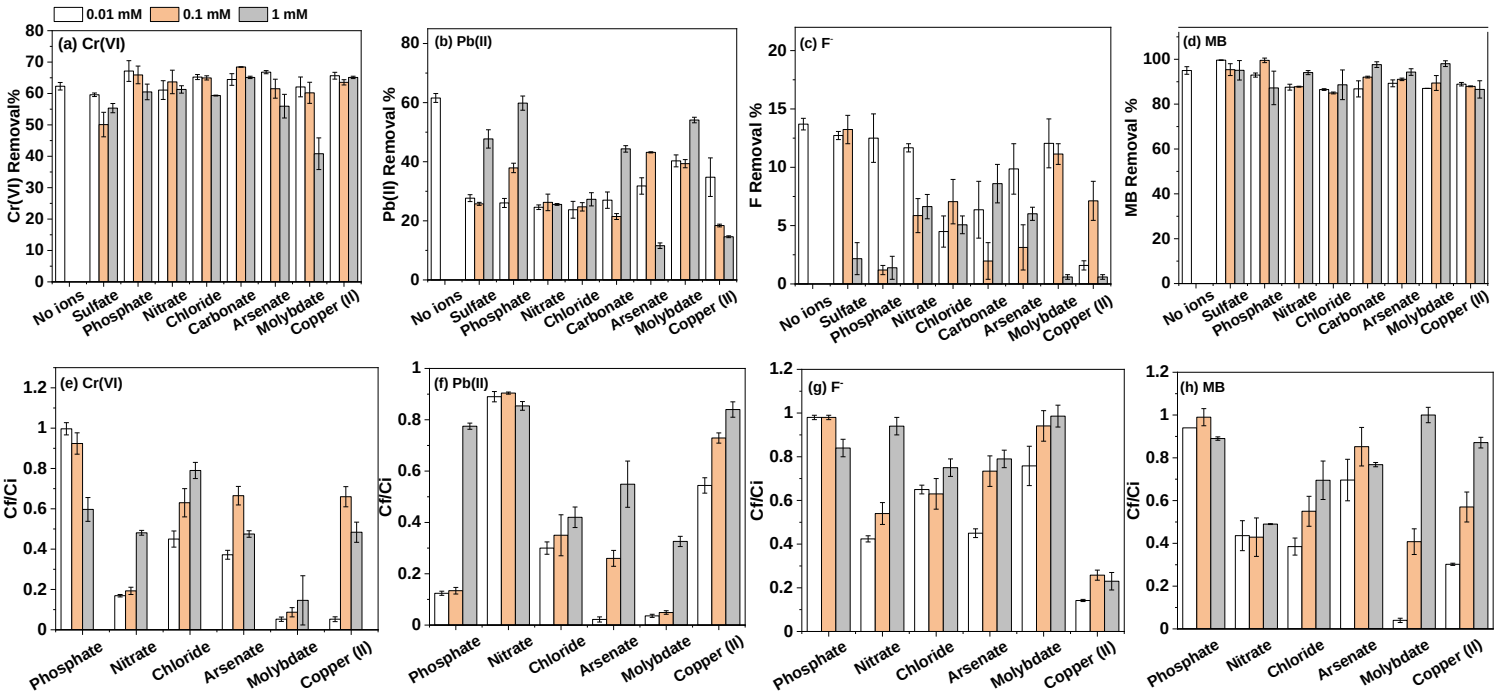

Figure 4.6 Effect of competing ions

Individual effects of competing sulfate, phosphate, nitrate, chloride, carbonate, arsenate, molybdate and Cu(II) (0.01, 0.1 and 1 mM) adsorption on Fe2TiO5/BC (a) Cr(VI) (100 mg/L, pH 2, 2 h), (b) Pb(II) (100 mg/L, pH 5, 1 h), (c) fluoride (50 mg/L, pH 6, 3 h) and (d) MB (100 mg/L, pH 6, 2 h). Quantification of the competing ions individually remaining in the filtrate after adsorption onto (e) Cr(VI), (f) Pb(II), (g) fluoride and (h) MB respectively. Cf/Ci is the ratio of the final and initial aqueous concentrations of competing ions. In all experiments Fe2TiO5/BC (25 mg) was mixed with solutions containing the competing ions (25 mL) at 25 °C.

Cr(VI), Pb(II), fluoride and MB removal by Fe_2TiO_5/BC from aqueous systems depends strongly on the other competing ions present in water bodies because the Fe_2TiO_5 and biochar phases present in Fe_2TiO_5/BC may have a variety of affinities to other ions. Therefore, eight competing ions were used at low, medium and high concentrations (0.01, 0.1, and 1 mM) during the adsorption of Cr(VI), Pb(II), fluoride and MB onto Fe_2TiO_5/BC. Each of these competing ions either enhanced or decreased the adsorption of Cr(VI), Pb(II), fluoride and MB. These competitive ion sorptions (Fig. 4.6) were quantified by analyzing the filtrate after adsorption.

Phosphate, chloride, carbonate, arsenate and Cu(II) enhanced Cr(VI) uptake. Sulfate and molybdate and high concentration arsenate reduced Cr(VI) uptake, but nitrate had no influence. Fe_2TiO_5/BC removed the competing molybdate (~80% for 1 mM) and all other competitive ions as well. Arsenate, phosphate and chromate anions have similar geometries that can compete for the same adsorption sites on the composite, particularly Fe-OH sites.[65] Interestingly, all ions reduced the Pb(II) adsorption onto Fe_2TiO_5/BC. This occurred because Pb(II) makes water-insoluble compounds with most of these anions such as $PbSO_4$, $Pb(H_2PO_4)_2$, $PbCl_2$, $PbCO_3$, $Pb(H_2AsO_4)_2$ and $Pb(MoO_4)$. Arsenate, molybdate, phosphate and chloride used in low concentrations (except 1 mM) were effectively removed either by precipitation or adsorption onto Fe_2TiO_5/BC. Also, these anions can be electrostatically attracted to Fe_2TiO_5/BC, while Pb(II) cations are repelled by the positively charged biochar surfaces. Nitrate, chloride and Cu(II) uptake was low. They may only form weak H-bonds or weak electrostatic interactions with adsorbate surface and Cu(II) has competing effects similar to Pb(II) for the adsorption sites. Fluoride removal dropped in the presence of all the competing anions. The composites net PZC is ~6.5 and these experiments were formed at pH 6. Thus, the char surface phases protonated and have some

electrostatic attractions to fluoride. $CaCO_3$ phases on BC might provide adsorption sites. All the competing anion adsorptions onto Fe_2TiO_5/BC were low except Cu(II). MB adsorption was 95% in the absence of any competing ion. All competing ions slightly reduced MB removal on Fe_2TiO_5/BC except sulfate and phosphate. MB which exhibits a large pH window (pH 4-10) adsorbing to Fe_2TiO_5/BC surface by electrostatic attractions, π-π interactions and chelation. Nitrate, chloride and molybdate (except at high conc.) adsorption on to Fe_2TiO_5/BC was higher than phosphate, arsenate and Cu(II).

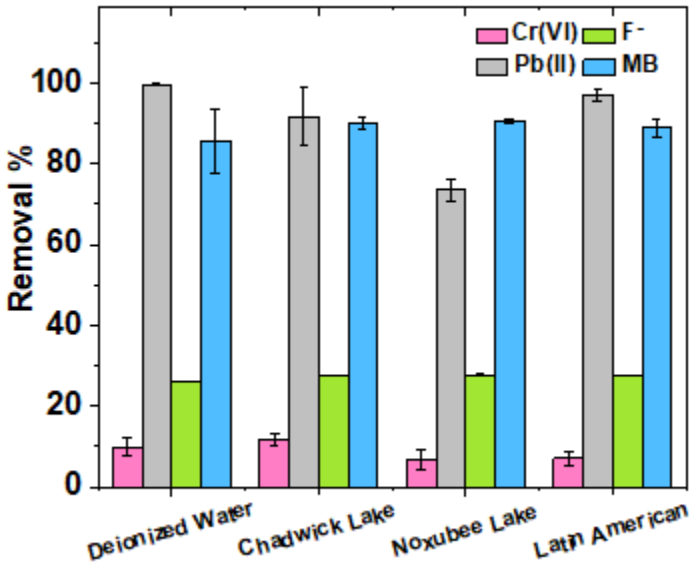

Figure 4.7 Simultaneous removal of Cr(VI), Pb(II), fluoride and MB

Simultaneous removal of Cr(VI), Pb(II), fluoride and MB in DI water, Chadwick lake water, Noxubee lake water and Atoyac lake water from Argentina at pH 6 (50.0 mg of 10 mg/L Fe_2TiO_5/BC was mixed with 25.0 mL of water sample for 2 h at a stirring rate of 200 rpm).

The simultaneous adsorption of all four adsorbents was studied from DI water and three natural water sources. Cr(VI), Pb(II), fluoride and MB removal percentages spanned in (6.6-11.7), (73-92), (27.5-27.8) and (89-90) ranges respectively (Fig. 4.7). These removal percentages did not dramatically differ from that in DI water at pH 6, suggesting that Fe_2TiO_5/BC can perform well in many complex matrices. pH was maintained at 6, close to that of natural water. Thus the maximum sorption performance for each species was not be achieved. These data confirm Fe_2TiO_5/BC can simultaneously remove of heavy metals, oxy anions, dyes, and anions.

Table 4.3 Comparison of Cr(VI), Pb(II), fluoride and MB adsorption with sorbents reported in literature

Adsorbent	Analyte	pH	Temp. (K)	Conc. Range (ppm)	Surface area (m^2/g)	Adsorption capacity (mg/g)	Eq. time (h)	Refs.
Biochar coated TiO_2 nanocomposite	Cr(VI)	3	288	25-150	-	77.52	0.25	[66]
Biochar coated Fe_3O_4@SiO_2-NH_2 particles	Cr(VI)	1	303	500	56.2	27.2	5	[67]
hematite-modified biochar-clay granular composites (HGCs)	Cr(VI)	5	298	0.1-200	61.72	19.51	24	[68]
Fe_2TiO_5/BC composite	**Cr(VI)**	**2**	**318**	**5-1400**	**656**	**141.6**		**This work**
Cellulose acetate/TiO_2	Pb(II)	5.2	308	50	30.2	31.9	5	[69]
TiO_2/lignin composite	Pb(II)	5	293	50	-	37.56	3	[70]
TiO_2 functionalized hydroxide ethyl aniline	Pb(II)	5.5	328	2-100	-	26.05	3	[71]
Fe-Ti oxides nanoparticles	Pb (II)	7.0	298	0.15	208	2.97	0.15	[72]
Fe_2TiO_5/BC composite	**Pb(II)**	**5**	**318**	**5-1000**	**656**	**200.1**		**This work**
Fe-Ti oxides nanoparticles	F	7.0	298	4.5	208	7.2	0.5	[72]
TiO_2-ZrO_2 composite	F	9	298	5	-	13.1	24	[73]
Perennial grass biochar	F	7	298	25	5.57	1.25	1	[74]
Fe_2O_3 and Fe_3O_4 dispersed biochar	F	7	308	1-60	494	9.04	5 min	[40]
Fe_2TiO_5/BC composite	**F**	**6**	**318**	**5-600**	**656**	**36.0**		**This work**
Magnetic biochar	MB	10	298			31.25	2	[75]
Phosphomolybdic acid treated biochar	MB	7	318	5-450	1.18	146.23	72	[76]
Montmorillonite clay modified iron oxide	MB	5.5 - 7.5	333	100-1000	118.1	71.12	4	[77]
Magnetic rectorite/ iron oxide	MB	-	298	1-30	-	31.18	8	[78]
Fe_2TiO_5/BC composite	**MB**	**6**	**318**	**5-1200**	**656**	**229.9**		**This work**

4.4.6 Photodegradation studies of MB

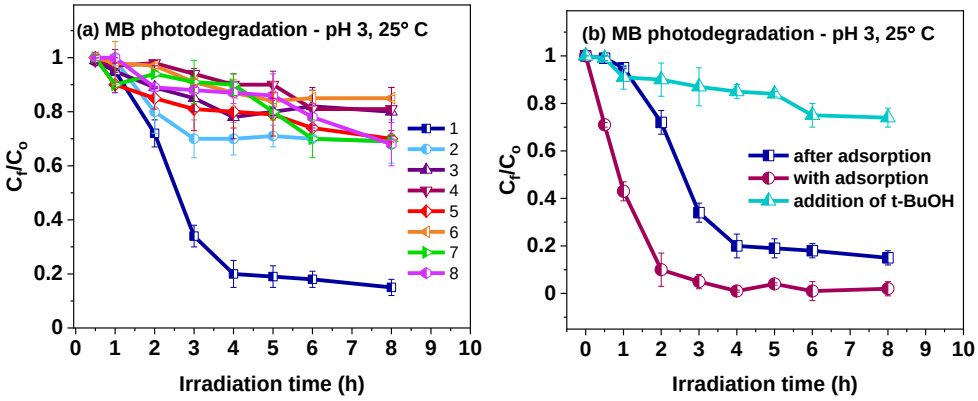

Figure 4.8 MB photodegradation

MB photodegradation (100 mg of Fe_2TiO_5/BC mixed with 100 mL of 100 mg/L MB in a Pyrex beaker (having 95% optical transmittance above 350 nm) with a lamp placed above the open beaker at room temperature, pH 3) (a) 1-4 Fe_2TiO_5/BC in MB solution in the presence of (1) light + air, (2) dark + air, (3) light + N_2 and (4) dark + N_2. 5-8 MB solution without photocatalyst in the presence of (5) light + air, (6) dark + air, (7) light + N_2 and (8) dark + N_2. (b) MB photodegradation on Fe_2TiO_5/BC after a 2 h pre-adsorption period, adsorption and photodegradation together and photodegradation after addition of (t-BuOH). Here, C_f and C_i are the final and initial concentration of MB after and before photodegradation.

In the absence of Fe_2TiO_5/BC, photolysis of MB irradiated under air or nitrogen was negligible at both pH 3(Fig. 4.8) and 6 (Fig. C.9).The degradation of MB under air/dark or under nitrogen/light in the presence of the photocatalyst was also very slow (Fig. 4.8). The MB degradation rate increased in the presence of Fe_2TiO_5 with light and oxygen but, exposing Fe_2TiO_5/BC and MB aqueous to light and air exhibited the highest MB degradation rate at both pH 3 and 6. The photodegradation rate and efficiency of MB were higher when simultaneous adsorption and photodegradation were carried out compared to starting irradiation only after dye adsorption equilibrium was established (Fig. 4.8(b)). This high photodegradation rate was likely

due to initial MB adsorption on the Fe_2TiO_5/BC active sites followed by degradation by the reactive oxygen species (ROSs) result exposure of the active sites again for new MB to adsorb and degrade. Therefore, the chance of every MB absorbed onto Fe_2TiO_5/BC to undergo photodegradation is very high. This enhanced photodegradation rate by the synergistic effect of adsorption and photodegradation at the same time[26] since the ROSs don't have to migrate far from the activation centers

Photodegradation of organic pollutants have been largely addressed and the mechanisms are well-established.[79] Energy of light equal or greater than the semiconductor's band gap is absorbed resulting in a formation of electron-hole pair.[80,81] Such photo oxidative degradations are caused by the formation of reactive oxygen species (ROSs) such as $HO^{\bullet}$, $O_2^{\bullet -}$ and h^+ generated upon illumination of the photocatalyst. The ROSs formed can diffuse over submillimeter distances away from the activation sites and degrade MB in solution or adsorbed to biochar and Fe_2TiO_5 phases that they are able to reach.[82]

Upon light absorption, electron in the ground state HOMO level (0.90 V vs. SHE)[83] of MB reaches to the excited LUMO level (-0.94 V vs. SHE)[83] (eq. 4.1). Since HOMO level of MB is higher in energy than the redox potential of $O_2/O_2^{-\cdot}$ couple (-0.33 V)[83], the excited state of MB injects an electron into ground state oxygen. This results in the oxidation of MB into $MB^{+\bullet}$ (eq. 4.2) and reduction of oxygen into superoxide radical anion $O_2^{-\cdot}$ (eq. 4.3) In this context, excited MB can inject an electron in to the low lying conduction band (-0.83 V vs. SHE)[84] of Fe_2TiO_5 resulting in an electron in the conduction band of the Fe_2TiO_5 and the holes position in the oxidized MB (eq. 4.4) In addition, light absorption by Fe_2TiO_5 can result an electron-hole pair formation in the conduction band and valence band of the Fe_2TiO_5 respectively (eq. 4.5). Hydroxyl radicals

formed in the photoprocess can oxidize H_2O giving hydroxyl radicals (eq. 4.6). Superoxide radical anions, in acidic media can undergo protonation giving H_2O_2, another oxidizing agent (eq. 4.7) All these reactive oxygen species can attack $MB^{+\bullet}$ leading to its degradation (eq. 4.8)

$$MB \xrightarrow{h\nu} MB^* \quad (4.1)$$

$$MB^* \rightarrow MB^{+\bullet} + e^- \quad (4.2)$$

$$e^- + O_2 \rightarrow O_2^{\bullet -} \quad (4.3)$$

$$Fe_2TiO_5MB \xrightarrow{h\nu} Fe_2TiO_5MB^* \rightarrow Fe_2TiO_5(e^-) + MB^+ \quad (4.4)$$

$$Fe_2TiO_5 + h\nu \rightarrow Fe_2TiO_5(h^+_{VB} + e^-_{CB}) \quad (4.5)$$

$$Fe_2TiO_5/MB^{+\bullet}(h^+_{VB}) + H_2O \rightarrow HO^{\cdot} + H^+ \quad (4.6)$$

$$O_2^{\bullet -} + H^+ \rightleftharpoons HO_2^{\bullet} \rightarrow H_2O_2 + O_2 \quad (4.7)$$

$$ROSs + MB \rightarrow \text{degradation products} \quad (4.8)$$

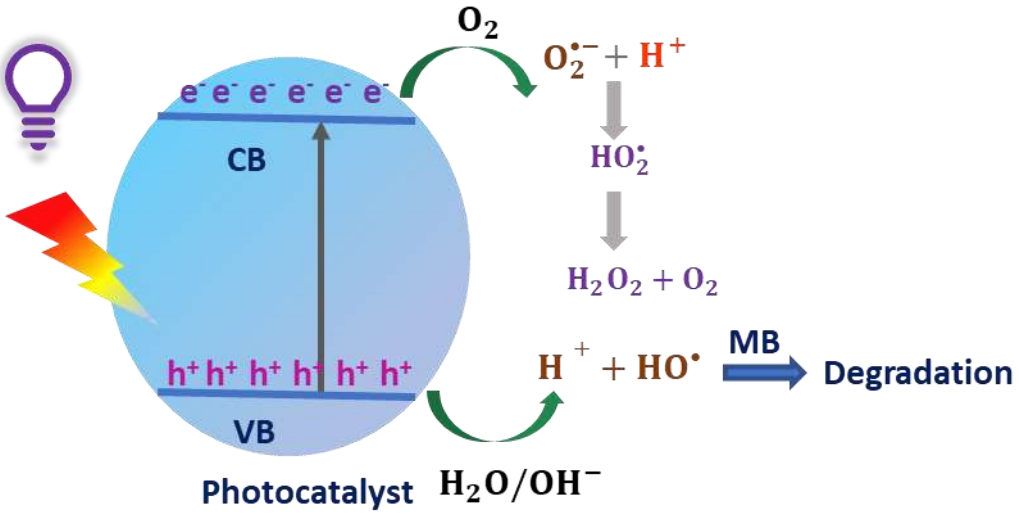

Figure 4.9 Schematic representation of MB degradation under UV light

Biochar surface redox active moieties and its condensed aromatic ring morphology facilitate electron storage and shuttling between different reactants from activation sites to the acceptors.[85] Therefore, biochar is reported to enhance the reactivity of Fe_2TiO_5 present on the biochar surface. Biochar acts as an electron reservoir that conducts electrons away from e/h pairs generated by photoactivation of TiO_2 in TiO_2-biochar composite.[28] This reduces e/h pair recombination and enhance charge separation which, in turn improves photodegradation efficiency.

Addition of 10 ppm of Fe^{2+} into aqueous MB enhanced the ability of UV light to degrade MB via photo-Fenton type production of oxidants. This enhanced the rate of formation of $HO^{\bullet}$ (eq. 4.9). Hydroxyl radicals are strong oxidants in MB degradation. This could explain the higher degradation efficiency of MB observed at pH 3 verses pH 6. Experiments confirmed Fe^{3+} is

leached from the Fe_2TiO_5/BC at ~pH 3 (Fig. C.10) during irradiation and Fe^{3+} ions trigger the photo-Fenton reaction[86,87] which accelerates $HO^{\bullet}$ radical production (eq. 4.10) causing the faster degradation of MB. To ascertain the dominant ROS in this photodegradation, degradation was evaluated in the presence of tertiary butyl alcohol (t-BuOH), a well known $HO^{\bullet}$ scavenger[88]. The degradation of MB significantly decreased upon adding of t-BuOH, confirming that MB degradation is predominantly caused by $HO^{\bullet}$ radicals.

$$Fe^{2+} + H_2O_2 + H^+ \rightarrow Fe^{3+} + H_2O + HO^{\bullet} \quad (4.9)$$

$$Fe^{3+} + H_2O + h\nu \rightarrow Fe^{2+} + HO^{\bullet} + H^+ \quad (4.10)$$

4.5 Conclusion

A cheap commercially available high surface area byproduct biochar from wood gasification was used to support to incorporate Fe_2TiO_5. Fe_2TiO_5 phase in the composite introduced more surface active sites into the biochar surface and facilitated removal of additional contaminants. Aqueous removal of Cr(VI), Pb(II), fluoride and MB on Fe_2TiO_5/BC followed pseudo second order kinetics with maximum Langmuir adsorption capacities of 141, 200, 36 and 229 mg/g at 318 K and 119, 180, 26, 210 mg/g at 298 K respectively. Synergism between adsorption and photocatalytic degradation enhanced the removal of MB under UV light irradiation. At low pH, MB degradation by the Photo-Fenton reaction was accelerated by the leaching of Fe(III) ions to the medium from the synthesized Fe_2TiO_5/BC composite. This increased the formation of hydroxyl radicals, responsible for the destruction of MB. Competitive adsorption

studies reveal this composite can be used to specifically remove Cr(VI), Pb(II), fluoride and MB even in the presence of other common ions present in water bodies.

4.6 References

1. Briffa, J.; Sinagra, E.; Blundell, R., Heavy metal pollution in the environment and their toxicological effects on humans. *Heliyon* **2020,** *6* (9), e04691.

2. Yaseen, D.; Scholz, M., Textile dye wastewater characteristics and constituents of synthetic effluents: a critical review. *International journal of environmental science and technology* **2019,** *16* (2), 1193-1226.

3. Székács, A.; Mörtl, M.; Darvas, B., Monitoring pesticide residues in surface and ground water in Hungary: surveys in 1990–2015. *Journal of Chemistry* **2015,** *2015*.

4. Ruzzin, J., Public health concern behind the exposure to persistent organic pollutants and the risk of metabolic diseases. *BMC Public Health* **2012,** *12* (1), 298.

5. Carpenter, D. O., Health effects of persistent organic pollutants: the challenge for the Pacific Basin and for the world. *Reviews on Environmental Health* **2011,** *26* (1), 61-69.

6. Torres, E., Biosorption: A Review of the Latest Advances. *Processes* **2020,** *8* (12), 1584.

7. Zhang, Y.; Duan, X., Chemical precipitation of heavy metals from wastewater by using the synthetical magnesium hydroxy carbonate. *Water Science and Technology* **2020**.

8. El Qada, E. N.; Allen, S. J.; Walker, G. M., Adsorption of basic dyes from aqueous solution onto activated carbons. *Chemical Engineering Journal* **2008,** *135* (3), 174-184.

9. Yang, Y., Recent advances in the electrochemical oxidation water treatment: Spotlight on byproduct control. *Frontiers of Environmental Science & Engineering* **2020,** *14* (5), 1-12.

10. Nidheesh, P.; Kumar, A.; Babu, D. S.; Scaria, J.; Kumar, M. S., Treatment of mixed industrial wastewater by electrocoagulation and indirect electrochemical oxidation. *Chemosphere* **2020**, 126437.

11. Ahmed, S. N.; Haider, W., Heterogeneous photocatalysis and its potential applications in water and wastewater treatment: a review. *Nanotechnology* **2018,** *29* (34), 342001.

12. Tan, I.; Ahmad, A.; Hameed, B., Enhancement of basic dye adsorption uptake from aqueous solutions using chemically modified oil palm shell activated carbon. *Colloids and Surfaces A: Physicochemical and Engineering Aspects* **2008,** *318* (1-3), 88-96.

13. Bao, Y.; Zhang, G., Study of adsorption characteristics of methylene blue onto activated carbon made by Salix psammophila. *Energy Procedia* **2012,** *16*, 1141-1146.

14. Abd-Elhamid, A.; Emran, M.; El-Sadek, M.; El-Shanshory, A. A.; Soliman, H. M.; Akl, M.; Rashad, M., Enhanced removal of cationic dye by eco-friendly activated biochar derived from rice straw. *Applied Water Science* **2020,** *10* (1), 1-11.

15. Yin, Z.; Cui, C.; Chen, H.; Yu, X.; Qian, W., The Application of Carbon Nanotube/Graphene-Based Nanomaterials in Wastewater Treatment. *Small* **2020,** *16* (15), 1902301.

16. Reza, K. M.; Kurny, A.; Gulshan, F., Parameters affecting the photocatalytic degradation of dyes using TiO 2: a review. *Applied Water Science* **2017,** *7* (4), 1569-1578.

17. Virkki, K.; Tervola, E.; Ince, M.; Torres, T.; Tkachenko, N., Comparison of electron injection and recombination on TiO_2 nanoparticles and ZnO nanorods photosensitized by phthalocyanine. *Royal Society Open Science* **2018,** *5* (7), 180323.

18. Yashas, S.; Shivaraju, H.; Thinley, T.; Pushparaj, K.; Maleki, A.; Shahmoradi, B., Facile synthesis of SnO_2 2D nanoflakes for ultrasound-assisted photodegradation of tetracycline hydrochloride. *International Journal of Environmental Science and Technology* **2020**, 1-12.

19. Fujishima, A.; Honda, K., Electrochemical photolysis of water at a semiconductor electrode. *Nature* **1972,** *238* (5358), 37-38.

20. Khataee, A.; Pons, M.-N.; Zahraa, O., Photocatalytic degradation of three azo dyes using immobilized TiO_2 nanoparticles on glass plates activated by UV light irradiation: Influence of dye molecular structure. *Journal of Hazardous Materials* **2009,** *168* (1), 451-457.

21. Dave, P. N.; Chopda, L. V., Application of iron oxide nanomaterials for the removal of heavy metals. *Journal of Nanotechnology* **2014,** *2014*.

22. Xu, P.; Zeng, G. M.; Huang, D. L.; Feng, C. L.; Hu, S.; Zhao, M. H.; Lai, C.; Wei, Z.; Huang, C.; Xie, G. X., Use of iron oxide nanomaterials in wastewater treatment: a review. *Science of the Total Environment* **2012,** *424*, 1-10.

23. Karunanayake, A. G.; Navarathna, C. M.; Gunatilake, S. R.; Crowley, M.; Anderson, R.; Mohan, D.; Perez, F.; Pittman Jr, C. U.; Mlsna, T., Fe_3O_4 nanoparticles dispersed on Douglas fir biochar for phosphate sorption. *ACS Applied Nano Materials* **2019,** *2* (6), 3467-3479.

24. Ai, Z.; Cheng, Y.; Zhang, L.; Qiu, J., Efficient removal of Cr (VI) from aqueous solution with Fe@ Fe2O3 core− shell nanowires. *Environmental Science & Technology* **2008,** *42* (18), 6955-6960.

25. Predoi, D.; Iconaru, S. L.; Predoi, M. V.; Motelica-Heino, M., Removal and oxidation of As (III) from water using iron oxide coated CTAB as adsorbent. *Polymers* **2020,** *12* (8), 1687.

26. Mian, M. M.; Liu, G., Recent progress in biochar-supported photocatalysts: synthesis, role of biochar, and applications. *RSC advances* **2018,** *8* (26), 14237-14248.

27. Saquing, J. M.; Yu, Y.-H.; Chiu, P. C., Wood-derived black carbon (biochar) as a microbial electron donor and acceptor. *Environmental Science & Technology Letters* **2016,** *3* (2), 62-66.

28. Colmenares, J. C.; Varma, R. S.; Lisowski, P., Sustainable hybrid photocatalysts: titania immobilized on carbon materials derived from renewable and biodegradable resources. *Green Chemistry* **2016,** *18* (21), 5736-5750.

29. Min, K.-M.; Park, K.-S.; Lim, A.-H.; Kim, J.-C.; Kim, D.-W., Synthesis of pseudobrookite-type Fe_2TiO_5 nanoparticles and their Li-ion electroactivity. *Ceramics international* **2012,** *38* (7), 6009-6013.

30. Karunanayake, A. G.; Todd, O. A.; Crowley, M.; Ricchetti, L.; Pittman Jr, C. U.; Anderson, R.; Mohan, D.; Mlsna, T., Lead and cadmium remediation using magnetized and nonmagnetized biochar from Douglas fir. *Chemical Engineering Journal* **2018,** *331*, 480-491.

31. Herath, A.; Layne, C. A.; Perez, F.; Hassan, E. B.; Pittman Jr, C. U.; Mlsna, T. E., KOH-activated high surface area Douglas Fir biochar for adsorbing aqueous Cr (VI), Pb (II) and Cd (II). *Chemosphere* **2020**, 128409.

32. Gao, Q.; Wu, X.; Fan, Y.; Meng, Q., Color performance and near infrared reflectance property of novel yellow pigment based on Fe_2TiO_5 nanorods decorated mica composites. *Dyes and Pigments* **2017,** *146*, 537-542.

33. Gao, Y.; Li, Y.; Yang, G.; Li, S.; Xiao, N.; Xu, B.; Liu, S.; Qiu, P.; Hao, S.; Ge, L., Fe_2TiO_5 as an efficient Co-catalyst to improve the photoelectrochemical water splitting performance of $BiVO_4$. *ACS applied Materials & Interfaces* **2018,** *10* (46), 39713-39722.

34. Cerro, S.; Gargori, C.; Llusar, M.; Monrós, G., Orthorhombic (Fe_2TiO_5)-monoclinic (Cr_2TiO_5) solid solution series: Synthesis by gel routes, coloring and NIR reflectivity evaluation. *Ceramics International* **2018,** *44* (11), 13349-13359.

35. Guo, S.; Wang, S.; Wu, N.; Liu, J.; Ni, Y.; Liu, W., Facile synthesis of porous Fe_2TiO_5 microparticulates serving as anode material with enhanced electrochemical performances. *RSC Advances* **2015,** *5* (126), 103767-103775.

36. Li, J.; Han, M.; Guo, Y.; Wang, F.; Sun, C., Fabrication of $FeVO_4/Fe_2TiO_5$ composite catalyst and photocatalytic removal of norfloxacin. *Chemical Engineering Journal* **2016,** *298*, 300-308.

37. Navarathna, C. M.; Bombuwala Dewage, N.; Keeton, C.; Pennisson, J.; Henderson, R.; Lashley, B.; Zhang, X.; Hassan, E. B.; Perez, F.; Mohan, D., Biochar Adsorbents with Enhanced Hydrophobicity for Oil Spill Removal. *ACS Applied Materials & Interfaces* **2020,** *12* (8), 9248-9260.

38. Karthik, T.; Rathinamoorthy, R.; Murugan, R., Enhancement of wrinkle recovery angle of cotton fabric using citric acid cross-linking agent with nano-TiO_2 as a co-catalyst. *Journal of Industrial Textiles* **2012,** *42* (2), 99-117.

39. Zhu, L.; Lu, Q.; Lv, L.; Wang, Y.; Hu, Y.; Deng, Z.; Lou, Z.; Hou, Y.; Teng, F., Ligand-free rutile and anatase TiO_2 nanocrystals as electron extraction layers for high performance inverted polymer solar cells. *RSC Advances* **2017,** *7* (33), 20084-20092.

40. Dewage, N. B.; Liyanage, A. S.; Pittman Jr, C. U.; Mohan, D.; Mlsna, T., Fast nitrate and fluoride adsorption and magnetic separation from water on α-Fe_2O_3 and Fe_3O_4 dispersed on Douglas fir biochar. *Bioresource Technology* **2018,** *263*, 258-265.

41. Qurashi, A.; Zhong, Z.; Alam, M. W., Synthesis and photocatalytic properties of α-Fe_2O_3 nanoellipsoids. *Solid State Sciences* **2010,** *12* (8), 1516-1519.

42. Kubelka, P.; Munk, F., A contribution to the optics of pigments. *Z. Tech. Phys* **1931,** *12* (593), 193.

43. Lou, Z.; Li, Y.; Song, H.; Ye, Z.; Zhu, L., Fabrication of Fe_2TiO_5/TiO_2 nanoheterostructures with enhanced visible-light photocatalytic activity. *RSC Advances* **2016,** *6* (51), 45343-45348.

44. Enhessari, M.; Razi, M. K.; Etemad, L.; Parviz, A.; Sakhaei, M., Structural, optical and magnetic properties of the Fe_2TiO_5 nanopowders. *Journal of Experimental Nanoscience* **2014,** *9* (2), 167-176.

45. Thiruppathi, M.; Leeladevi, K.; Ramalingan, C.; Chen, K.-C.; Nagarajan, E., Construction of novel biochar supported copper tungstate nanocomposites: A fruitful divergent catalyst for photocatalysis and electrocatalysis. *Materials Science in Semiconductor Processing* **2020,** *106*, 104766.

46. Li, R.; Jia, Y.; Bu, N.; Wu, J.; Zhen, Q., Photocatalytic degradation of methyl blue using Fe_2O_3/TiO_2 composite ceramics. *Journal of Alloys and Compounds* **2015,** *643*, 88-93.

47. Navas-Cárdenas, C.; Benito, N.; Wolf, E. E.; Gracia, F., Effect of Pt-MOx (M= Fe, Co) interaction on the preferential oxidation of CO over Pt/MOx/TiO_2 catalysts prepared by selective electrostatic adsorption. *Applied Catalysis A: General* **2019,** *576*, 11-19.

48. Mohan, D.; Pittman, C. U., Activated carbons and low cost adsorbents for remediation of tri- and hexavalent chromium from water. *Journal of Hazardous Materials* **2006,** *137* (2), 762-811.

49. Li, Z.; Tang, X.; Chen, Y.; Wei, L.; Wang, Y., Activation of Firmiana simplex leaf and the enhanced Pb (II) adsorption performance: equilibrium and kinetic studies. *Journal of Hazardous Materials* **2009,** *169* (1-3), 386-394.

50. Langmuir, I., The adsorption of gases on plane surfaces of glass, mica and platinum. *Journal of the American Chemical Society* **1918,** *40* (9), 1361-1403.

51. Freundlich, H., Over the adsorption in solution. *J. Phys. Chem* **1906,** *57* (385471), 1100-1107.

52. Milonjić, S. K., A consideration of the correct calculation of thermodynamic parameters of adsorption. *Journal of the Serbian Chemical Society* **2007,** *72* (12), 1363-1367.

53. Ong, J.; Lucas, L.; Raikar, G.; Gregory, J., Electrochemical corrosion analyses and characterization of surface-modified titanium. *Applied Surface Science* **1993,** *72* (1), 7-13.

54. Kuznetsov, M.; Zhuravlev, J. F.; Gubanov, V., XPS analysis of adsorption of oxygen molecules on the surface of Ti and TiNx films in vacuum. *Journal of Electron Spectroscopy and Related Phenomena* **1992,** *58* (3), 169-176.

55. Azadmanjiri, J.; Wang, J.; Berndt, C. C.; Kapoor, A.; Zhu, D. M.; Ang, A. S.; Srivastava, V. K., Tantalum-and silver-doped titanium dioxide nanosheets film: Influence on interfacial bonding structure and hardness of the surface system. *Industrial & Engineering Chemistry Research* **2017,** *56* (1), 434-439.

56. Wichterlová, B.; Krajčíková, L.; Tvarůžková, Z.; Beran, S., Chromium ions in zeolites. Part 4.—X-ray photoelectron spectroscopic study of chromium valence states in the surface layers of CrY zeolites. *Journal of the Chemical Society, Faraday Transactions 1: Physical Chemistry in Condensed Phases* **1984,** *80* (10), 2639-2645.

57. Agostinelli, E.; Battistoni, C.; Fiorani, D.; Mattogno, G.; Nogues, M., An XPS study of the electronic structure of the ZnxCd1− xCr2 (X= S, Se) spinel system. *Journal of Physics and Chemistry of Solids* **1989,** *50* (3), 269-272.

58. Paparazzo, E.; Severini, E.; Jimenez-Lopez, A.; Maireles-Torres, P.; Olivera-Pastor, P.; Rodriguez-Castellon, E.; Tomlinson, A. A., Surface chemistry of chromia-pillared tin and zirconium phosphate materials: an X-ray photoelectron spectroscopic study. *Journal of Materials Chemistry* **1992,** *2* (11), 1175-1178.

59. Sleigh, C.; Pijpers, A.; Jaspers, A.; Coussens, B.; Meier, R. J., On the determination of atomic charge via ESCA including application to organometallics. *Journal of Electron Spectroscopy and Related Phenomena* **1996,** *77* (1), 41-57.

60. Rahman, A.; Mohamed, M.; Ahmed, M.; Aitani, A., Characterization of chromia/alumina catalysts by X-ray photoelectron spectroscopy, proton induced X-ray emission and thermogravimetric analysis. *Applied Catalysis A: General* **1995,** *121* (2), 203-216.

61. Bertrand, P.; Fleischauer, P., X-ray photoelectron spectroscopy study of the surface adsorption of lead naphthenate. *Journal of Vacuum Science and Technology* **1980,** *17* (6), 1309-1314.

62. Wang, T.; Liu, W.; Xiong, L.; Xu, N.; Ni, J., Influence of pH, ionic strength and humic acid on competitive adsorption of Pb(II), Cd(II) and Cr(III) onto titanate nanotubes. *Chemical Engineering Journal* **2013,** *215-216*, 366-374.

63. Briggs, D., *Handbook of X-ray and ultraviolet photoelectron spectroscopy*. Heyden: 1977.

64. Morgan, W. E.; Van Wazer, J. R.; Stec, W. J., Inner-orbital photoelectron spectroscopy of the alkali metal halides, perchlorates, phosphates, and pyrophosphates. *Journal of the American Chemical Society* **1973,** *95* (3), 751-755.

65. Alchouron, J.; Navarathna, C.; Rodrigo, P. M.; Snyder, A.; Chludil, H. D.; Vega, A. S.; Bosi, G.; Perez, F.; Mohan, D.; Pittman Jr, C. U., Household arsenic contaminated water treatment employing iron oxide/bamboo biochar composite: An approach to technology transfer. *Journal of Colloid and Interface Science* **2020**.

66. Yousaf, B.; Liu, G.; Abbas, Q.; Wang, R.; Ullah, H.; Mian, M. M.; Rashid, A., Enhanced removal of hexavalent chromium from aqueous media using a highly stable and magnetically separable rosin-biochar-coated TiO 2@ C nanocomposite. *RSC Advances* **2018,** *8* (46), 25983-25996.

67. Shi, S.; Yang, J.; Liang, S.; Li, M.; Gan, Q.; Xiao, K.; Hu, J., Enhanced Cr (VI) removal from acidic solutions using biochar modified by Fe_3O_4@ SiO_2-NH_2 particles. *Science of The Total Environment* **2018,** *628*, 499-508.

68. Zhu, S.; Wang, S.; Yang, X.; Tufail, S.; Chen, C.; Wang, X.; Shang, J., Green sustainable and highly efficient hematite nanoparticles modified biochar-clay granular composite for Cr (VI) removal and related mechanism. *Journal of Cleaner Production* **2020,** *276*, 123009.

69. Gebru, K. A.; Das, C., Removal of Pb (II) and Cu (II) ions from wastewater using composite electrospun cellulose acetate/titanium oxide (TiO_2) adsorbent. *Journal of Water Process Engineering* **2017,** *16*, 1-13.

70. Klapiszewski, Ł.; Siwińska-Stefańska, K.; Kołodyńska, D., Preparation and characterization of novel TiO_2/lignin and TiO_2-SiO_2/lignin hybrids and their use as functional biosorbents for Pb (II). *Chemical Engineering Journal* **2017,** *314*, 169-181.

71. Yousefzadeh, H.; Salarian, A.; Kalal, H. S., Study of Pb (II) adsorption from aqueous solutions by TiO_2 functionalized with hydroxide ethyl aniline (PHEA/n-TiO_2). *Journal of Molecular Liquids* **2018,** *263*, 294-302.

72. Monárrez-Cordero, B.; Sáenz-Trevizo, A.; Bautista-Carrillo, L.; Silva-Vidaurri, L.; Miki-Yoshida, M.; Amézaga-Madrid, P., Simultaneous and fast removal of As^{3+}, As^{5+}, Cd^{2+}, Cu^{2+}, Pb^{2+} and F^- from water with composite Fe-Ti oxides nanoparticles. *Journal of Alloys and Compounds* **2018,** *757*, 150-160.

73. Yu, Y.; Zhou, Z.; Ding, Z.; Zuo, M.; Cheng, J.; Jing, C., Simultaneous arsenic and fluoride removal using {201} TiO_2–ZrO_2: Fabrication, characterization, and mechanism. *Journal of Hazardous Materials* **2019,** *377*, 267-273.

74. Saikia, R.; Goswami, R.; Bordoloi, N.; Senapati, K. K.; Pant, K. K.; Kumar, M.; Kataki, R., Removal of arsenic and fluoride from aqueous solution by biomass based activated biochar: optimization through response surface methodology. *Journal of Environmental Chemical Engineering* **2017,** *5* (6), 5528-5539.

75. Mubarak, N.; Fo, Y.; Al-Salim, H. S.; Sahu, J.; Abdullah, E.; Nizamuddin, S.; Jayakumar, N.; Ganesan, P., Removal of methylene blue and orange-G from waste water using magnetic biochar. *International Journal of Nanoscience* **2015,** *14* (04), 1550009.

76. Liu, S.; Li, J.; Xu, S.; Wang, M.; Zhang, Y.; Xue, X., A modified method for enhancing adsorption capability of banana pseudostem biochar towards methylene blue at low temperature. *Bioresource Technology* **2019,** *282*, 48-55.

77. Cottet, L.; Almeida, C.; Naidek, N.; Viante, M.; Lopes, M.; Debacher, N., Adsorption characteristics of montmorillonite clay modified with iron oxide with respect to methylene blue in aqueous media. *Applied Clay Science* **2014,** *95*, 25-31.

78. Wu, D.; Zheng, P.; Chang, P. R.; Ma, X., Preparation and characterization of magnetic rectorite/iron oxide nanocomposites and its application for the removal of the dyes. *Chemical Engineering Journal* **2011,** *174* (1), 489-494.

79. Liu, H.; Wang, C.; Wang, G., Photocatalytic advanced oxidation processes for water treatment: recent advances and perspective. *Chemistry–An Asian Journal* **2020,** *15* (20), 3239-3253.

80. Pawar, R. C.; Khare, V.; Lee, C. S., Hybrid photocatalysts using graphitic carbon nitride/cadmium sulfide/reduced graphene oxide (gC_3N_4/CdS/RGO) for superior photodegradation of organic pollutants under UV and visible light. *Dalton Transactions* **2014,** *43* (33), 12514-12527.

81. Singh, S.; Mahalingam, H.; Singh, P. K., Polymer-supported titanium dioxide photocatalysts for environmental remediation: A review. *Applied Catalysis A: General* **2013,** *462*, 178-195.

82. Lisowski, P.; Colmenares, J. C.; Mašek, O. e.; Lisowski, W.; Lisovytskiy, D.; Kamińska, A.; Łomot, D., Dual functionality of TiO_2/biochar hybrid materials: photocatalytic phenol degradation in the liquid phase and selective oxidation of methanol in the gas phase. *ACS Sustainable Chemistry & Engineering* **2017,** *5* (7), 6274-6287.

83. Dejpasand, M. T.; Saievar-Iranizad, E.; Bayat, A.; Montaghemi, A.; Ardekani, S. R., Tuning HOMO and LUMO of three region (UV, Vis and IR) photoluminescent nitrogen doped graphene quantum dots for photodegradation of methylene blue. *Materials Research Bulletin* **2020,** *128*, 110886.

84. Vasiljevic, Z. Z.; Dojcinovic, M.; Vujancevic, J.; Jankovic-Castvan, I.; Ognjanovic, M.; Tadic, N.; Stojadinovic, S.; Brankovic, G.; Nikolic, M., Photocatalytic degradation of methylene blue under natural sunlight using iron titanate nanoparticles prepared by a modified sol–gel method. *Royal Society Open Science* **2020,** *7* (9), 200708.

85. Klüpfel, L.; Keiluweit, M.; Kleber, M.; Sander, M., Redox properties of plant biomass-derived black carbon (biochar). *Environmental Science & Technology* **2014,** *48* (10), 5601-5611.

86. Wang, C.; Liu, H.; Sun, Z., Heterogeneous photo-Fenton reaction catalyzed by nanosized iron oxides for water treatment. *International journal of Photoenergy* **2012,** *2012*.

87. Ensing, B.; Buda, F.; Baerends, E. J., Fenton-like chemistry in water: oxidation catalysis by Fe (III) and H_2O_2. *The Journal of Physical Chemistry A* **2003,** *107* (30), 5722-5731.

88. Li, X.; Li, J.; Bai, J.; Dong, Y.; Li, L.; Zhou, B., The inhibition effect of tert-butyl alcohol on the TiO_2 nano assays photoelectrocatalytic degradation of different organics and its mechanism. *Nano-Micro Letters* **2016,** *8* (3), 221-231.

CHAPTER V

FUTURE DIRECTIONS

World-wide water pollution due to anthropogenic activities and natural processes is inevitable and accessible clean water is a major concern in most of the parts in the world. Detrimental health is a consequence of contaminated water that people have already experienced. Therefore, looking for low cost environmentally friendly and simple remediation methods is timely and vital for human and environmental health.

Surface modified biochar has been a promising adsorbate for the removal of most of the organic and inorganic contaminants in drinking and wastewater. The experiments that were performed in this study were mainly focused on batch-mode operation. Although this mode provides useful equilibrium characteristics and adsorption kinetics, the data obtained are not sufficient to provide accurate scale-up data required in the design of adsorption columns. Therefore, studies of continuous flow adsorption will need to be completed before full value of this work can be realized. Columns should be packed with modified biochar and a peristaltic pump can be utilized to drive the heavy metal /organic dye contaminant solution downward through the column at a constant flow rate.

The presence of other pollutant species may compete with target species for adsorption processes. This can lead to a reduced adsorption capacity for the pollutant of interest. Therefore, matrix effects should also be studied to obtain a deeper insight into these adsorption processes. Photocatalytic mineralization of organic pollutants has received much attention. This technique

completely degrades organic pollutant into CO_2, H_2O and simple inorganic compounds and is therefore, environmentally benign. Biochar with its large surface area is a suitable platform for a variety of hybrid photocatalysts. BC, being a good electron acceptor, facilitates electron-hole pair separation upon photoexcitation of the photocatalyst. This enhances the efficiency of photocatalysis towards the mineralization of pollutants. A variety of nanohybrid photocatalysts including iron oxide-BC composites could be prepared and tested towards the degradation of selected organic pollutants. To gain insight into the photodegradation mechanism, photoirradiation experiments should be performed in the presence of oxygen radical quenchers.

APPENDIX A

KOH-ACTIVATED HIGH SURFACE AREA DOUGLAS FIR BIOCHAR FOR ADSORBING AQUEOUS CHROMIUM(VI), LEAD(II) AND CADMIUM(II)-SUPPORTING INFORMATION

A.1 Surface characterization

A.1.1 Surface area measurements

The Brunauer-Emmet-Teller (BET) surface areas and total pore volumes of both DFBC and KOHBC were determined by N_2 adsorption-desorption isotherms using a Micromeritics Tristar 11 Plus surface area analyzer. Biochar samples (100 mg) were degassed at 180 ^{0}C under N_2 for 60 min on a Micrometrics Flow Prep 060 degas system prior to the analysis. The Dubinin-Astakhov equation[105] or pore volume was used to analyze the adsorption data to determine the N_2 adsorption isotherms. This equation is $\log a = \log a_0 - D \log^n (\frac{P_0}{P})$, where a is amount of gas adsorbed per unit mass of adsorbent (mol/g), a_0 is the micropore capacity (mol/g), D is a constant, P and P_0 are the equilibrium and saturation vapor pressure of adsorbate at temperature T (K). Micropore volume was calculated by density functional theory (DFT), $W_0 = a_0 \frac{44 \times 10^3}{\rho}$, where W_0 is the limiting micropore volume (cm^3/g), a_0 is the micropore capacity (mol/g) and ρ is the density of adsorbed gas (g/cm^3).[105]

A.1.2 Scanning electron microscopy analysis (SEM)

DFBC and KOHBC surface morphologies were examined using a JEOL JSM-6500FFE-SEM operated at 5 kV. Sample were coated on a carbon stub attached to carbon tape and mounted into a sample holder for SEM analysis.

A.1.3 Transmission electron microscopy (TEM) and energy dispersive x-ray spectroscopy (EDS)

DFBC and KOHBC samples were examined by TEM (JEOL model 2100) at 200kV. Each sample (10 mg) was mixed with 0.5mL distilled water and vortexed for one minute. A drop of

each suspension was carefully deposited on a carbon film in a 300-mesh copper grid and allowed to vacuum dry for 4 to 5h prior to analysis. EDS was carried out using an Oxford X- max-80 detector.

A.1.4 Elemental analysis (EA)

Carbon, hydrogen, nitrogen content of DFBC and KOHBC were determined using a CE-440 Elemental Analyzer (Exeter Analytical, North Chelmsford, MA). Biochar (~2-3 mg) was placed into a tin capsule and weighed using an ultra-microbalance (Sartorius, Data Weighing Systems, Inc., Elk Grove, IL). The tin capsule was sealed immediately with an Exeter Analytical Capsule Sealer and placed inside a nickel sleeve for sample injection. Static combustion was conducted at 900 °C in pure oxygen. Helium was used to carry the combustion products through the analytical system and for purging the instrument. A calibration verification standard was injected after every ten sample runs to ensure quality control.

A.1.5 Thermogravimetric analysis (TGA)

Thermogravimetric analysis of DFBC and KOHBC were carried out using a Mettler TGA/DSC thermogravimetric analyzer (TGA/DSC 1, STARe System, Mettler Toledo, USA) at a heating rate of 10 ^{0}C/ min from 50 ^{0}C to 1000 ^{0}C under an atmosphere of air (50 mL/ min).

A.1.6 X-ray photoelectron spectroscopy (XPS)

Surface analysis of KOHBC and Cd-, Pb-, Cr-laden samples were carried out using a Thermo Scientific K-Alpha XPS system. A monochromatic1486.6 eV (Al Kα line) X-ray source was used with a spot size of 400 µm^2 with a maximum analytical penetration depth of 100 Å. Low resolution survey scans provided the surface elemental distribution. High resolution spectra of

each element present in the biochar surface were deconvoluted by a Gaussian method using Origin Pro 2019 software.

A.1.7 Point of zero charge (PZC) determination

The point of zero charge of DFBC and KOHBC were determined in 0.01M NaCl solutions in pH intervals of 1 at pH values from 2 to 11. The pH was adjusted using 0.1 M HCl and 0.1M NaOH. DFBC and KOHBC samples (0.05g) were immersed in 50mL plastic vials (three replicates) at each pH value, sealed, and stirred for 24h in an Orbital shaker to reach equilibrium. These solutions were filtered, and the pH of the supernatant was recorded using a HI 2211, pH/ORP meter. The PZC was determined by a plot of equilibrium pH vs. initial pH.

Table A.1 O 1s High resolution (HR) XPS peak assignment for Cr(VI), Pb(II), Cd(II) laden biochar

Peak/ chemical species		DFBC	KOH-BC	KOHBC-Cr	KOHBC-Cd	KOHBC-Pb
Aromatic C=O, Cr-O	Binding energy (eV)	530.81	531.15	530.46	531.02	530.87
	Atomic Percentage (%)	1.1	11.75	2.2	1.6	2.3
	FWHM (eV)	1.6	1.4	1.5	1.5	1.5
O-CR_3	Binding energy (eV)	532.15	531.75	531.62	532.05	531.99
	Atomic Percentage (%)	3.4	6.9	8.4	4.3	4.5
	FWHM (eV)	1.6	0.9	1.4	1.6	1.6
C-OH	Binding energy (eV)	533.19	532.37	532.53	533.62	533.32
	Atomic Percentage (%)	1.0	8.7	4.6	14.7	8.9
	FWHM (eV)	1.0	1.0	1.3	1.6	1.5
CO_3^{2-}, C=O, O-C=O	Binding energy (eV)	533.95	533.02	533.41	534.48	534.42

Table A.1 (Continued)

	Atomic Percentage (%)	1.2	7.6	9.6	3.4	4.5
	FWHM (eV)	1.3	1.2	1.5	1.8	1.6
Chemisorbed water molecules	Binding energy (eV)	535.33	533.72	534.59	535.32	535.88
	Atomic Percentage (%)	0.5	6.8	2.8	4.7	1.2
	FWHM (eV)	1.6	1.6	1.5	1.6	1.6

*The BE values were estimated with a maximum error of ±0.05 eV in curve fitting

Table A.2 C1s High resolution (HR) XPS peak assignments for Cr(VI), Pb(II), Cd(II) laden biochar

Peak/ chemical species		DFBC	KOH-BC	KOHBC-Cr	KOHBC-Cd	KOHBC-Pb
aromatic C, C-H, C-C, (protonated and alkylated aromatic C)	Binding energy (eV)	284.57	284.08	284.79	284.84	284.53
	Atomic Percentage (%)	75.0	32.2	43.4	56.1	58.9
	FWHM (eV)	1.0	1.2	1.4	1.0	1.0
O-C-O, C-OH	Binding energy (eV)	285.60	285.11	285.85	286.14	285.89
	Atomic Percentage (%)	11.2	11.6	16.7	8.4	12.5
	FWHM (eV)	1.2	1.4	1.5	1.4	1.5
C-OH, (phenolic C), C=O (ketonic C)	Binding energy (eV)	286.57	286.07	287.11	287.09	287.22
	Atomic Percentage (%)	5.0	3.4	4.8	3.9	3.5
	FWHM (eV)	1.5	1.3	1.5	1.5	1.5
COOH (carboxylic C), CO_3^{2-}	Binding energy (eV)	288.14	288.88	288.86	288.83	288.75
	Atomic Percentage (%)	1.5	2.6	3.6	1.2	2.3
	FWHM (eV)	1.5	2.4	1.5	1.5	1.5

*The BE values were estimated with a maximum error of ±0.05 eV in curve fitting

Table A.3 Adsorption kinetic parameters

				Pseudo first order kinetic model parameters			Pseudo second order kinetic model parameters		
Adsorbate	Adsorbent	Initial conc. (mg/L)	q_e, exp. (mg/g)	q_e, calc. (mg/g)	K_1 (min^{-1})	R^2	q_e, calc. (mg/g)	k_2 ($gmg^1mi n^{-1}$) $x10^{-3}$	R^2
Cr(VI)	DFBC	100	37.1	24.3	0.063	0.891	37.5	7.6	0.998
	KOHBC	75	66.1	37.3	0.065	0.905	67.1	5.4	0.999
		100	88.1	31.5	0.02	0.674	90.1	2.6	0.997
		150	101.8	40.9	0.047	0.945	103.1	2.5	0.998
Pb(II)	DFBC	100	83.8	14.9	0.074	0.615	84.7	10.4	0.999
	KOHBC	100	103.5	2.9	0.072	0.757	103.1	67.0	0.999
Cd(II)	DFBC	25	15.1	8.1	0.045	0.960	15.5	12.8	0.995
	KOHBC	25	21.6	0.9	0.031	0.822	21.6	156.4	0.999

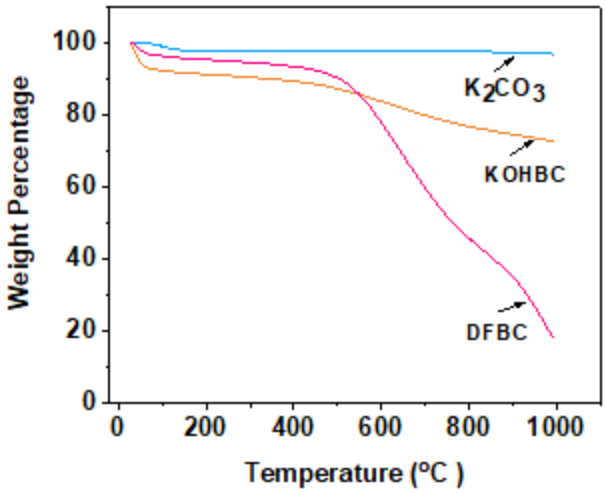

Figure A.1 TGA curves for DFBC and KOHBC in nitrogen

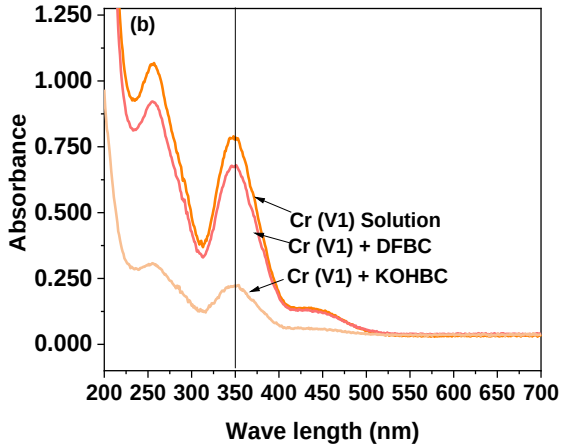

Figure A.2 UV absorption spectra shown for Cr(VI) remaining in solutions with DFBC and KOHBC

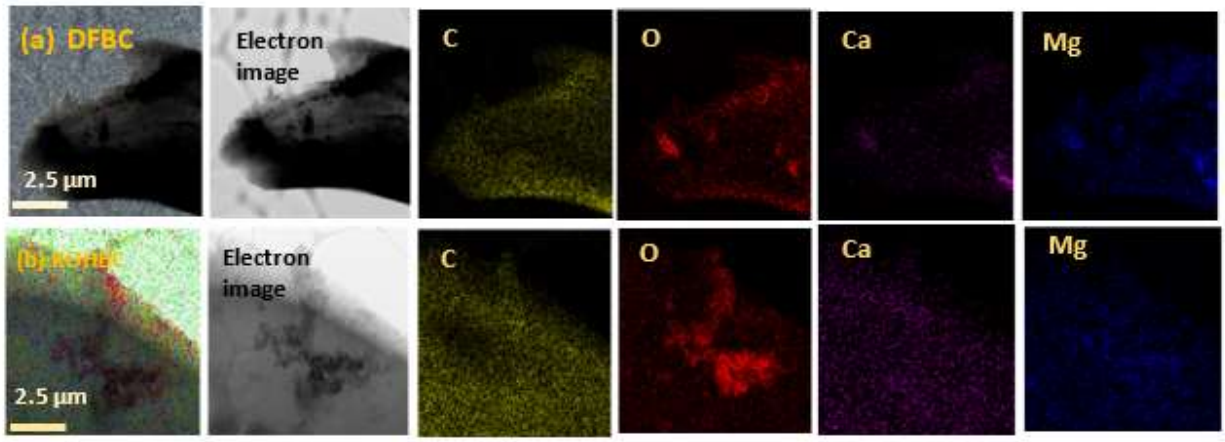

Figure A.3 (a)TEM-EDX elemental mapping images for different elements on (a) DFBC (b) KOHBC before adsorption of Cr, Pb and Cd

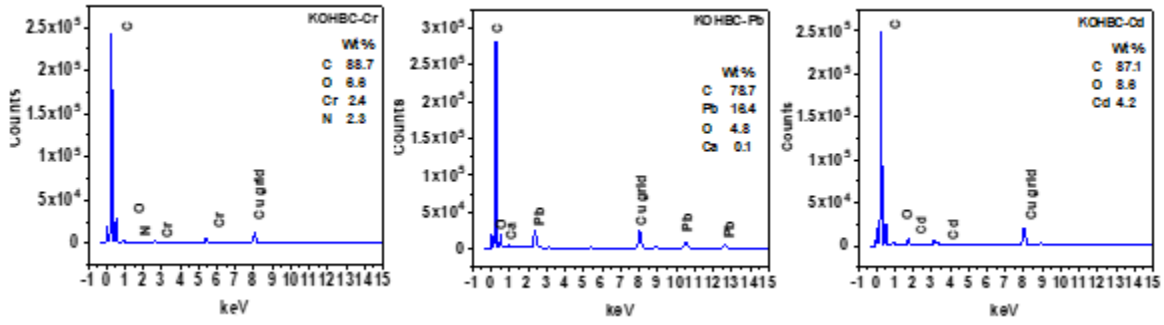

Figure A.4 TEM-EDX spectrum for Cr(VI), Pb(II) and Cd(II) atomic wt.% adsorbed by KOHBC

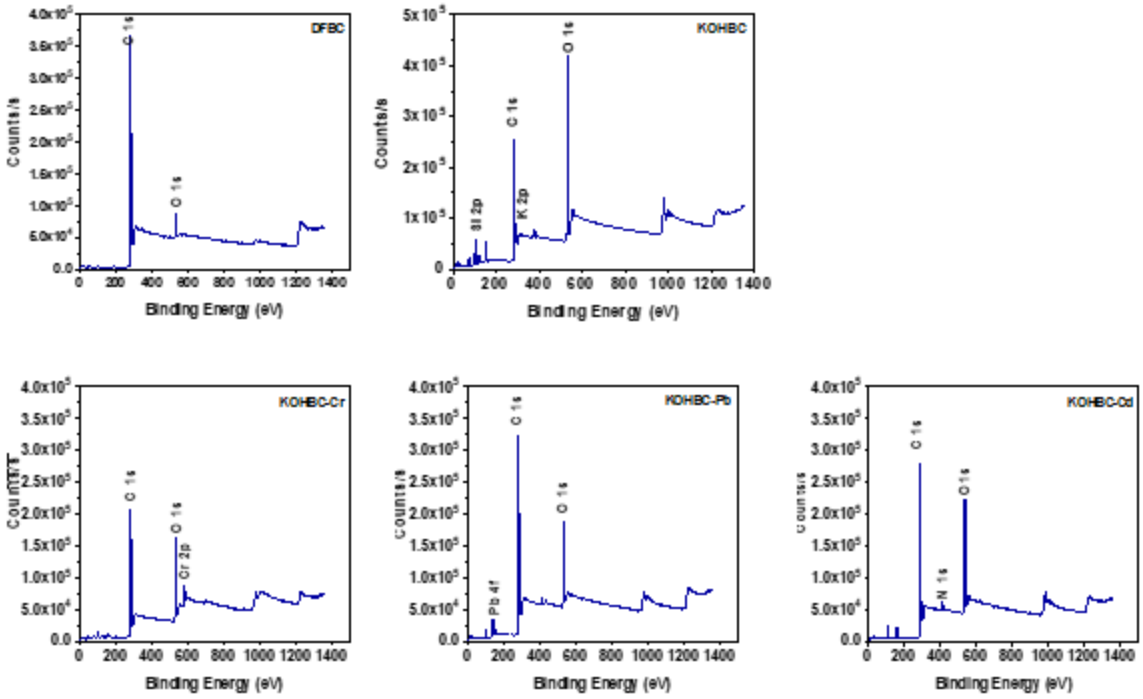

Figure A.5 LR-XPS spectra of DFBC, KOHBC, Cr(VI), Pb(II) and Cd(II) laden biochar

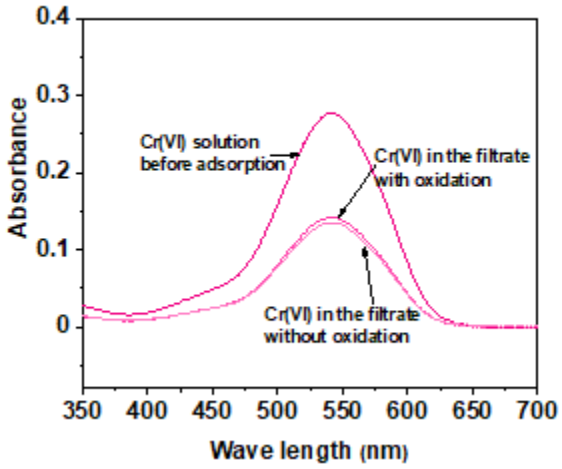

Figure A.6 UV absorption spectra shown for Cr(VI) remaining in solutions with KOHBC

Adsorption of Cr(VI) 100 mg/L at pH 2. 25 mL of Cr(VI) was mixed with 25 mg of KOHBC with a stirring rate of 200 rpm.

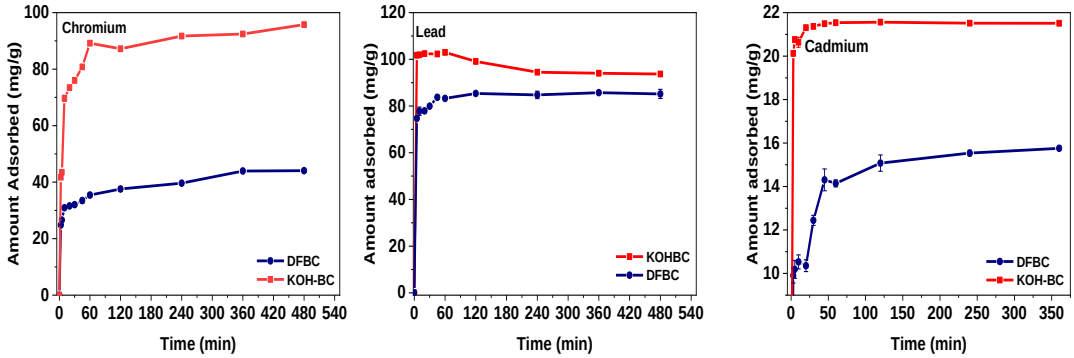

Figure A.7 Adsorption of Cr(VI) at pH 2, Pb(II) at pH 5 and Cd(II) at pH 6 versus time.

Analyte concentration for Cr (VI) and Pb(II) was 100 mg/L and Cd(II) 25 mg/L. 25 mL of the analyte was mixed with 25 mg of each type of biochar with a stirring rate of 200rpm. Three replicates were performed to obtain each data point.

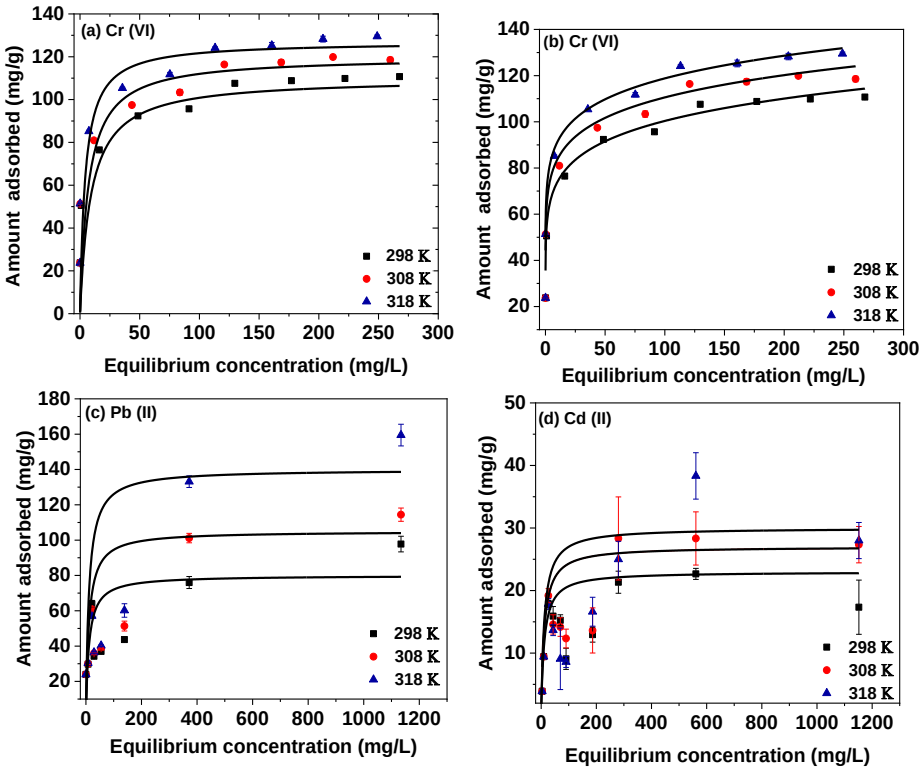

Figure A.8 (a) Langmuir and (b) Freundlich adsorption isotherms at pH 2.0 for Cr (VI) on KOHBC

25mL of Cr(VI) mixed with 25 mg of KOHBC for 120 min at a stirring rate of 200 rpm. Langmuir adsorption isotherms for (c) Pb(II) at pH 5 (d) Cd(II) at pH 6 on KOHBC where 25 mL of analyte was mixed with 25 mg of KOHBC for 60 min at a stirring rate of 200 rpm.

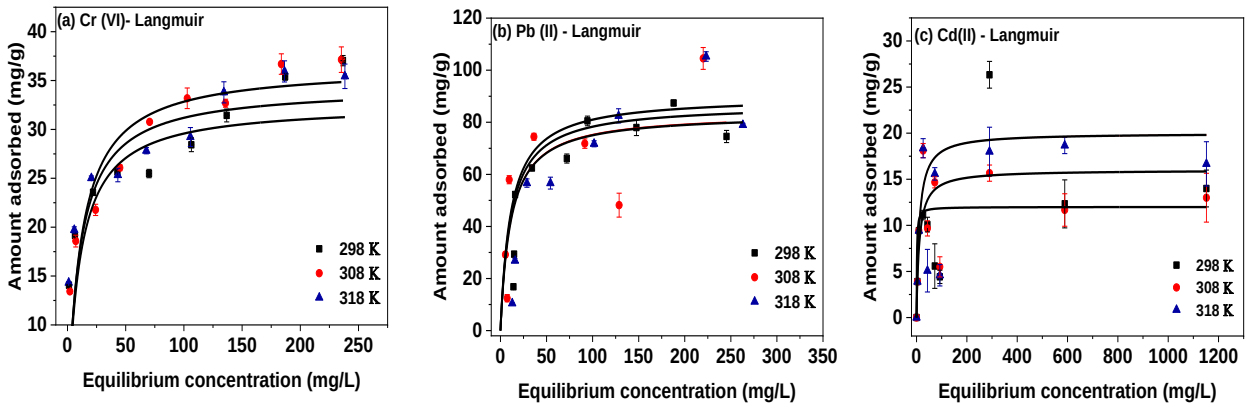

Figure A.9 Langmuir adsorption isotherms on DFBC

(a) at pH 2 for Cr(VI), (b) at pH 5 Pb(II), and (c) at pH 6 Cd(II) using 25mL of analyte was mixed with 25 mg of DFBC for 60 min and stirred at 200 rpm.

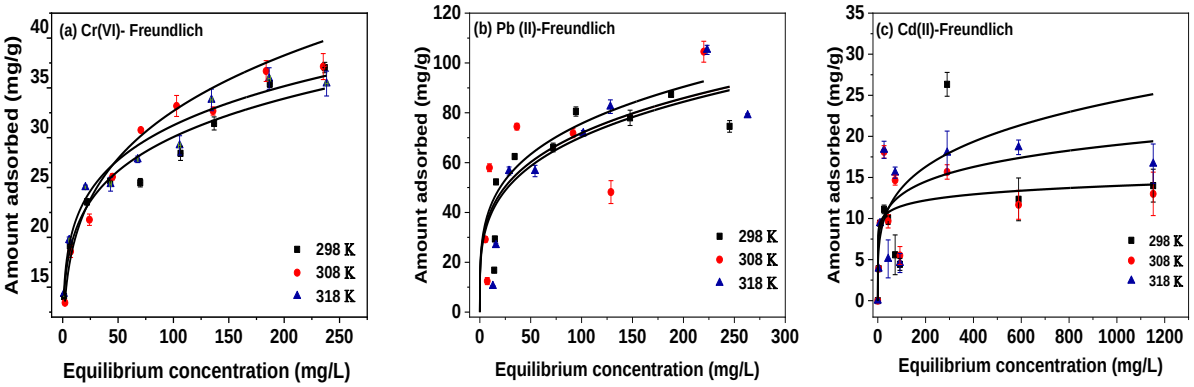

Figure A.10 Freundlich adsorption isotherms on DFBC

(a) at pH 2 for Cr(VI), (b) at pH 5 Pb(II), and (c) at pH 6 Cd(II) using 25mL of analyte was mixed with 25 mg of DFBC for 60 min and stirred at 200 rpm.

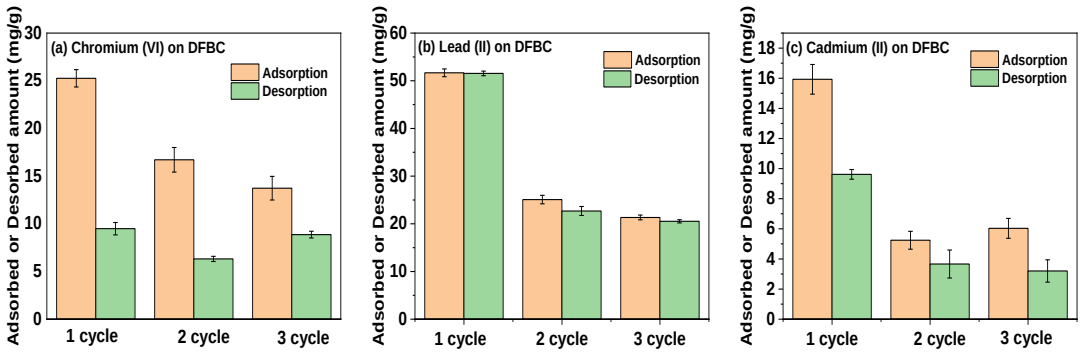

Figure A.11 Adsorption-desorption cycles on DFBC

(a) Cr(VI) at pH 2, (b) Pb(II) at pH 5 and (c) Cd(II) at pH 6 on DFBC at 25°C. 0.200g of biochar was mixed with 200mL of adsorbent at stirring rate of 200 rpm. Error bars are the SD of three replicates.

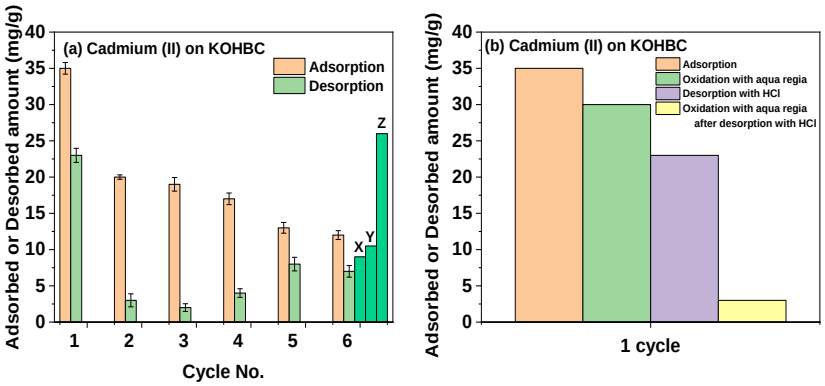

Figure A.12 Adsorption-desorption cycles on KOHBC for Cd(II) at pH 6 and 25 °C

0.200 g of biochar was mixed with 200 mL of adsorbate stirred at 200 rpm. (a) 0.1M HCl was used for the desorption of Cd(II) during cycles 1-6. Then 6M and 12M HCl was used to desorb 25 mg of KOHBC after the sixth cycle's 0.1M HCl desorption. X (6M HCl, 25 mL), Y (6M HCl, 50 mL) and Z (12M, 25 mL). (b) 0.1M HCl was used for the desorption of Cd(II) and aqua regia (HCl to HNO_3) in 3:1 ratio was used as oxidizing agent after the adsorption. Error bars are the SD of three replicates.

APPENDIX B

BIOCHAR-SUPPORTED POLYANILINE HYBRID FOR CHROMIUM AND NITRATE AQUEOUS ADSORPTION-SUPPORTING INFORMATION

Table B.1 Thermodynamic parameters for chromium and nitrate adsorption on DFBC

		T (K)	R^2	K_{ads}	ln K_{ads}	ΔG^0 (kJ/mol)	ΔH^0 (kJ/mol)	ΔS^0 (kJ/mol K)
Cr	Langmuir	278	0.81	5.40×10^4	10.8	-25.8	2.01	0.10
		298		5.90×10^4	10.9	-27.8		
		318		6.00×10^4	11.0	-29.8		
	Freundlich	278	0.97	1.80×10^5	12.1	-29.3	1.27	0.11
		298		1.85×10^5	12.2	-31.5		
		318		1.93×10^5	12.3	-33.7		
nitrate	Langmuir	278	0.84	2.20×10^4	9.9	-22.0	5.81	0.10
		298		2.40×10^4	10.1	-24.0		
		318		3.00×10^4	10.3	-26.0		
	Freundlich	278	0.99	2.00×10^6	14.5	-32.1	6.80	0.14
		298		2.50×10^6	14.7	-35.0		
		318		2.90×10^6	14.9	-37.7		

Table B.2 Comparison of adsorption for Cr(VI) on PANIBC-LA and PANIBC

	N_2 BET surface area (m^2/g)	Pore volume (cm^3/g)	Pore diameter (Å)	Adsorption capacity (mg/g)	Adsorption density (mg/m^2)	Adsorption (mg/g PANI)
PANIBC-LA (PANI wt. 9%)	32.9	0.009	11.3	75.3	2.3	828.5
PANIBC (PANI wt. 47%)	8.92	0.002	9.2	104.3	11.7	217.6

Cr(VI) removal on PANIBC-LA and PANIBC. 25 mL of aqueous Cr(VI) (150 mg/L, pH 2) solution was mixed with 25 mg adsorbent for 3 h at 25 °C. The average value from three replicates for each measurement is reported.

Table B.3 Comparison of adsorption for nitrate on PANIBC-LA and PANIBC

	N_2 BET surface area (m^2/g)	Pore volume (cm^3/g)	Pore diameter (Å)	Adsorption capacity (mg/g)	Adsorption density (mg/m^2)	Adsorption (mg/g PANI)
PANIBC-LA (PANI wt. 9%)	32.9	0.009	11.3	16.6	0.5	182.3
PANIBC (PANI wt. 47%)	8.92	0.002	9.2	25.5	2.9	53.2

Nitrate removal on PANIBC-LA and PANIBC. 25 mL of aqueous nitrate (50 mg/L, pH 6) solution was mixed with 25 mg adsorbent for 3 h at 25 °C. Average value from three replicates for each measurement is reported.

Table B.4 C1s High resolution (HR) XPS peak assignments for DFBC, PANIBC, Cr(VI) (pH 2, 6, 8)- laden PANIBC and nitrate (pH 2,6,10)-laden PANIBC

Peak/ Chemical species				PANIBC-Cr			PANIBC-Nitrate		
		DFBC	PANIBC	pH 2	pH 6	pH 8	pH 2	pH 6	pH 10
C-C, C-H									
	Binding Energy (eV)	284.55	284	284.56	284.36	284.45	284.23	284.31	284.08
	FWHM (eV)	1.02	0.94	1.32	1.04	1.06	0.98	1.09	0.96
	Atomic %	75.0	24.6	26.8	20.4	28.1	22.8	32.0	20.1
C=C, Aromatic C	Binding Energy (eV)	285.6	284.75	285.28	284.87	285.12	285.13	285.18	284.94
	FWHM (eV)	1.23	1.15	1.31	1.3	1.4	1.18	1.01	1.42
	Atomic %	11.2	25.7	9.7	30.6	31.4	24.0	18.8	33.7
C-OH, C-N, C=N	Binding Energy (eV)	286.57	285.43	286.22	285.94	286	286.05	285.9	286.12
	FWHM (eV)	1.5	1.06	1.5	1.5	1.5	1.48	1.48	1.5
	Atomic %	5.0	13.8	6.8	3.5	10.6	17.7	20.2	4.6
C=O	Binding Energy (eV)	288.1	286.3	287.9	287.5	287.4	287.1	286.9	287.5

Table B.4 (Continued)

	FWHM (eV)	1.48	1.49	1.89	1.5	1.5	1.5	2	1.5
	Atomic %	1.5	14.6	2.4	2.1	3.6	4.1	5.7	4.6
COOH(R)	Binding Energy (eV)		287.44	288.66	288.82	288.89	288.64	288.88	288.75
	FWHM (eV)		1.97	1.51	1.5	1.5	1.5	1.99	1.5
	Atomic %		4.1	2.6	2.1	2.0	3.0	2.3	2.4
CO_3^{2-}	Binding Energy (eV)				291.89	292	291.83		291.74
	FWHM (eV)				1.48	1.5	1.5		1.5
	Atomic %				1.9	1.4	3.4		2.1

*The BE values were estimated with a maximum error of ±0.05 eV in curve fitting

Table B.5 O1s High resolution (HR) XPS peak assignments for DFBC, PANIBC, Cr(VI) (pH 2, 6, 8)-laden PANIBC and nitrate (pH 2,6,10)-laden PANIBC

Peak/ Chemical species				PANIBC-Cr			PANIBC-Nitrate		
		DFBC	PANIBC	pH 2	pH 6	pH 8	pH 2	pH 6	pH 10
C=O, Cr(VI)-O	Binding Energy (eV)	530.81	530.39	530.71	530.2	529.89	530.71	530.47	530.3
	FWHM (eV)	1.6	0.79	1.46	1.54	1.22	1.51	1.29	1.18
	Atomic %	1.1	0.3	10.2	2.0	0.7	0.8	0.6	0.7
O-CR_3	Binding Energy (eV)	532.15	531.01	529.65	531.28	530.97	531.57	531.24	531.16
	FWHM (eV)	1.6	0.98	1.06	1.34	1.36	1.35	1.02	1.17
	Atomic %	3.36	0.76	1.5	4.6	2.5	3.3	1.1	1.9
C-OH	Binding Energy (eV)	533.19	531.67	531.48	532.07	531.71	532.2	531.96	531.86
	FWHM (eV)	1.0	0.9	1.2	1.5	1.3	1.2	1.1	1.2

Table B.5 (Continued)

	Atomic %	1.0	0.7	14.2	3.6	3.2	2.1	2.7	3.4
CO_3^{2-}	Binding Energy (eV)	533.95	532.5	532.28	533.11	532.65	532.99	532.9	532.71
	FWHM (eV)	1.3	1.08	1.25	1.49	1.49	1.33	1.32	1.2
	Atomic %	1.1	0.8	7.4	1.5	1.9	1.4	1.7	1.4
COOH(R),	Binding Energy (eV)		533.58	533.29	533.97	533.76	533.88	534.01	533.65
	FWHM (eV)		1.23	1.54	1.42	1.57	1.56	1.42	1.59
	Atomic %		0.9	4.2	0.8	1.4	1.5	1.5	1.8
Chemisorbed water, O-N	Binding Energy (eV)	535.23	534.94	534.43				536.16	
	FWHM (eV)	1.63	1.27	1.02				1.52	
	Atomic %	0.5	0.3	0.5				0.3	

*The BE values were estimated with a maximum error of ±0.05 eV in curve fitting

Table B.6 N1s High resolution (HR) XPS peak assignments for PANIBC, Cr(VI) (pH 2, 6, 8)-laden PANIBC and nitrate (pH 2,6,10)-laden PANIBC

Peak/ Chemical species			PANIBC-Cr			PANIBC-Nitrate		
		PANIBC	pH 2	pH 6	pH 8	pH 2	pH 6	pH 10
Imine =N-	Binding Energy (eV)	397.76	398.27	398.36	398.42	397.89	397.96	397.93
	FWHM (eV)	0.93	1.14	1.14	1.27	1.05	0.86	1.14
	Atomic %	0.5	0.8	4.2	5.0	0.5	0.6	0.9
Amine N-H	Binding Energy (eV)	399.08	399.51	399.43	399.55	399.35	399.29	399.19
	FWHM (eV)	1.45	1.96	1.11	1.05	1.4	1.5	1.39
	Atomic %	8.02	3.2	2.7	2.6	6.9	7.7	6.9
N with radical cation $-NH^{\bullet+}-$ (polaron)	Binding Energy (eV)	400.47	401.14	400.26	400.39	400.69	400.79	400.26
	FWHM (eV)	2	2	1.5	1.5	1.5	2	1.5
	Atomic %	3.5	0.6	2.3	1.9	2.1	2.4	1.7
Protonated imine $=NH^{+}-$ (bipolaron)	Binding Energy (eV)	402.62	403.2	402.42	402.52	402.07	402.74	401.43
	FWHM (eV)	2	1.75	2	2	0.5	2	1.5
	Atomic %	0.9	0.2	0.5	0.6	0.8	0.7	1.1
NO_3^-	Binding Energy (eV)			405.41	405.75	406.29	406.24	406.16
	FWHM (eV)			1.51	1.5	1.26	1.34	1.31
	Atomic %			0.3	0.3	1.5	1.8	0.9

*The BE values were estimated with a maximum error of ±0.05 eV in curve fitting

Table B.7 Cr 2p High resolution (HR) XPS peak assignments for Cr(VI) laden PANIBC at pH 2, 6, 8.

Peak/ Chemical species		PANIBC-Cr		
		pH 2	pH 6	pH 8
Cr(III)	Binding Energy (eV)	576.34	576.49	576.39
	FWHM (eV)	1.06	1.35	1.49
	Atomic %	1.1	0.5	0.3
Cr(III)				
	Binding Energy (eV)	577.38	577.61	577.45
	FWHM (eV)	2.17	1.93	2
	Atomic %	6.1	0.6	0.7
Cr(VI)	Binding Energy (eV)	579.34	579.28	579.19
	FWHM (eV)	2.44	1.92	2
	Atomic %	2.2	0.6	0.6

*The BE values were estimated with a maximum error of ±0.05 eV in curve fitting

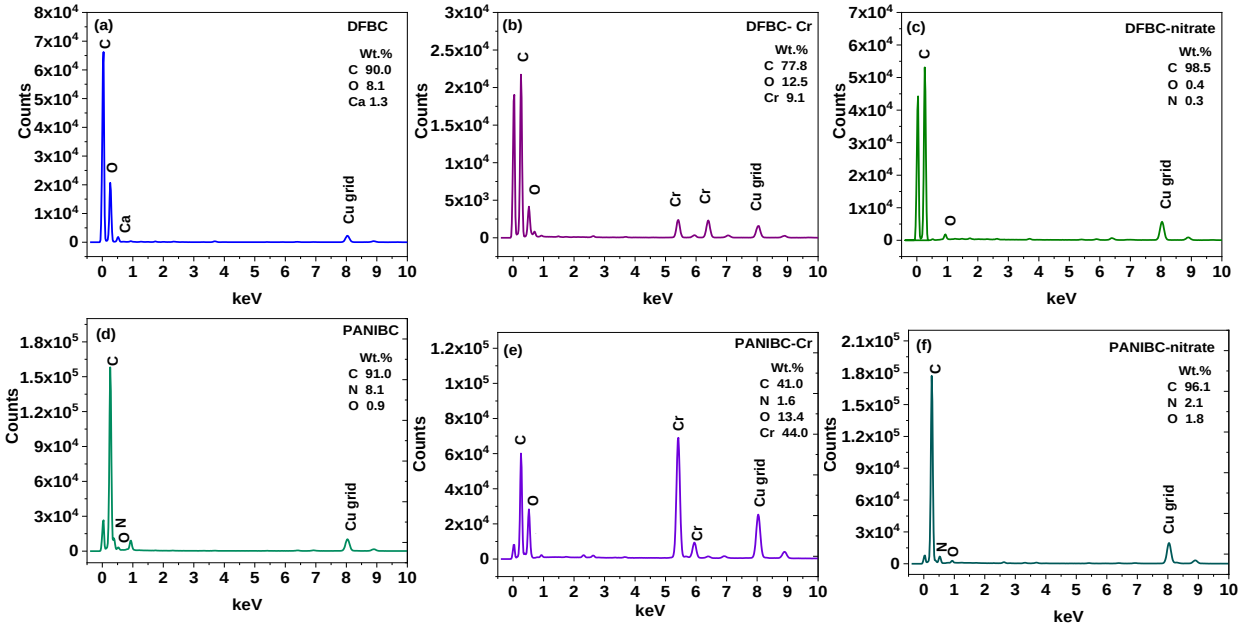

Figure B.1 TEM-EDX spectra for (a) DFBC, (b) DFBC-Cr, (c) DFBC-nitrate, (d) PANIBC, (e) PANIBC-Cr and (f) PANIBC-nitrate

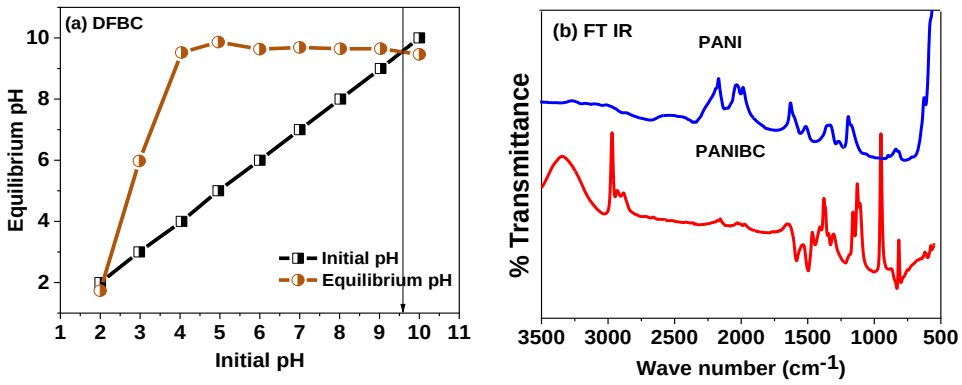

Figure B.2 Point of zero charge (PZC) measurements for (a) DFBC, (b) FTIR spectrum for DFBC and PANIBC

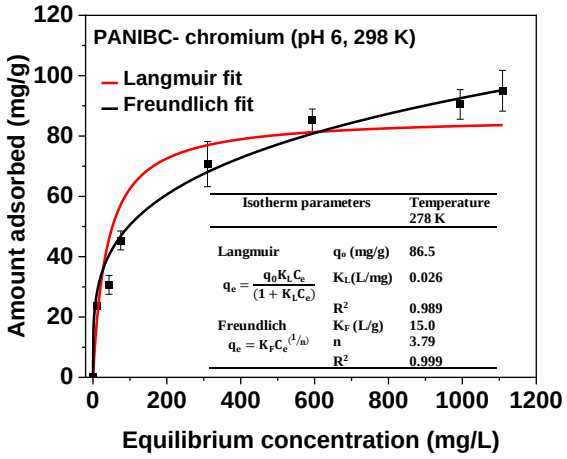

Figure B.3 Langmuir and Freundlich isotherm plots for Cr(VI) adsorption on PANIBC

25 mg of PANIBC was mixed with 25 mL of Cr(VI) for 3 h at 298 K and pH 6 at 200 rpm. Error bars are the standard deviations of three replicates.

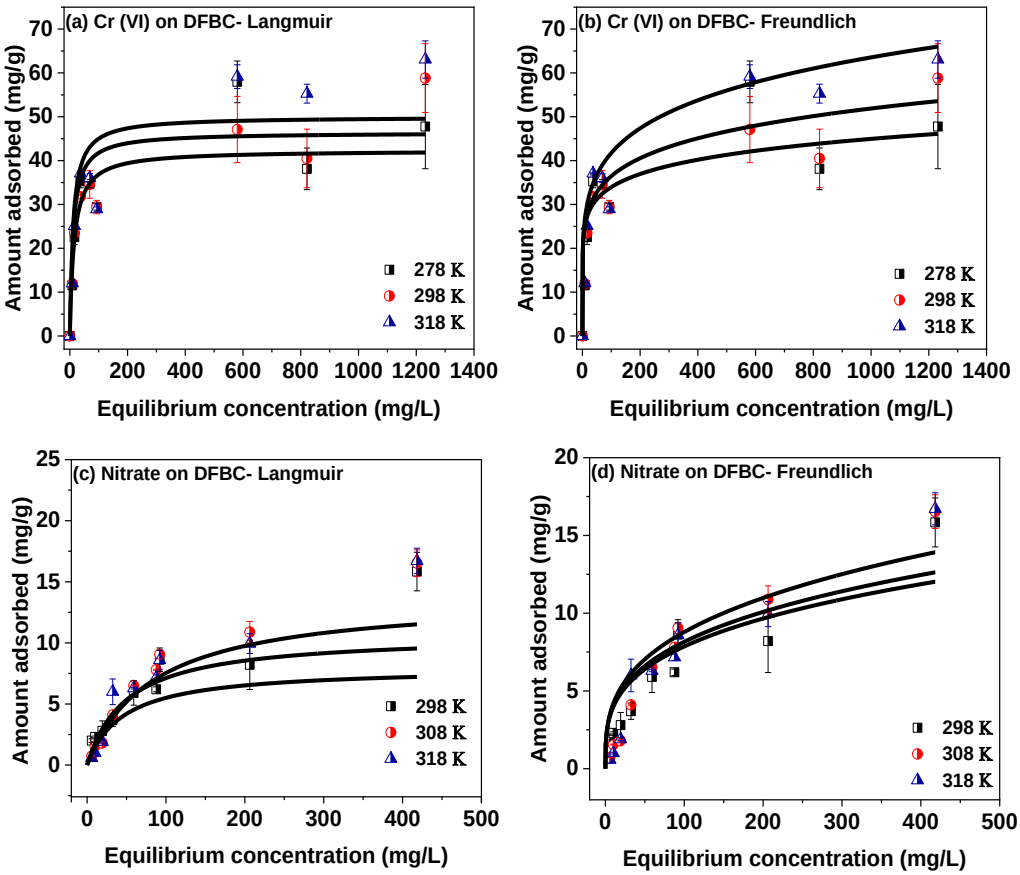

Figure B.4 Langmuir and Freundlich adsorption isotherm for Cr(VI) and nitrate on DFBC

(a) Langmuir, and (b) Freundlich adsorption isotherm for Cr(VI) at pH 2 on DFBC at 298, 308, 318 K. (c) Langmuir, and (d) Freundlich adsorption isotherm for nitrate at pH 6 on DFBC at 298, 308, 318 K. Error bars are the standard deviations of three replicates.

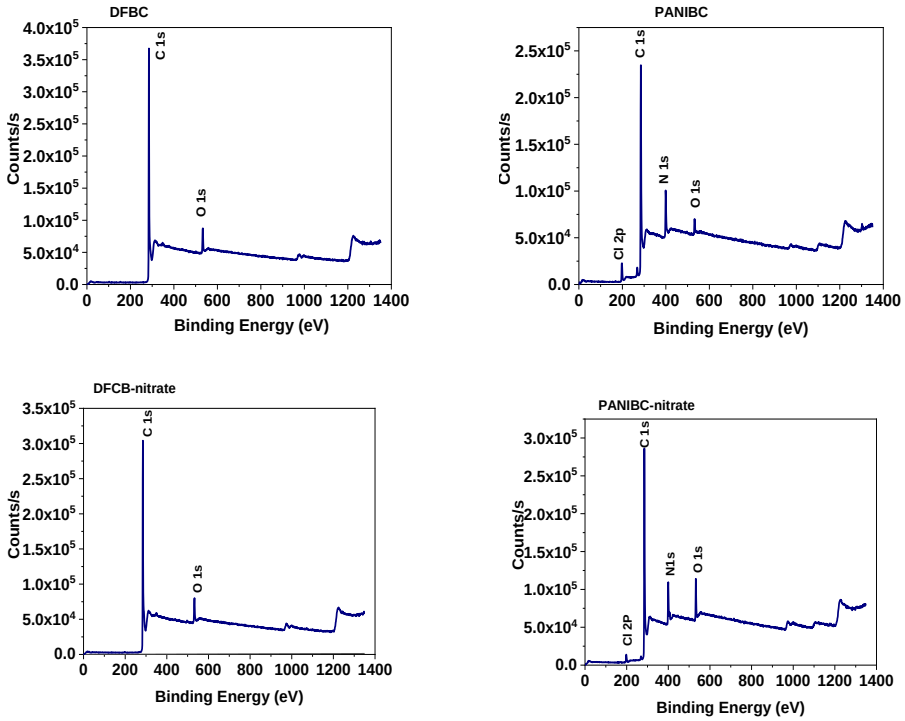

Figure B.5 LS-XPS spectra for DFBC, PANIBC, DFBC-nitrate and PANIBC-nitrate

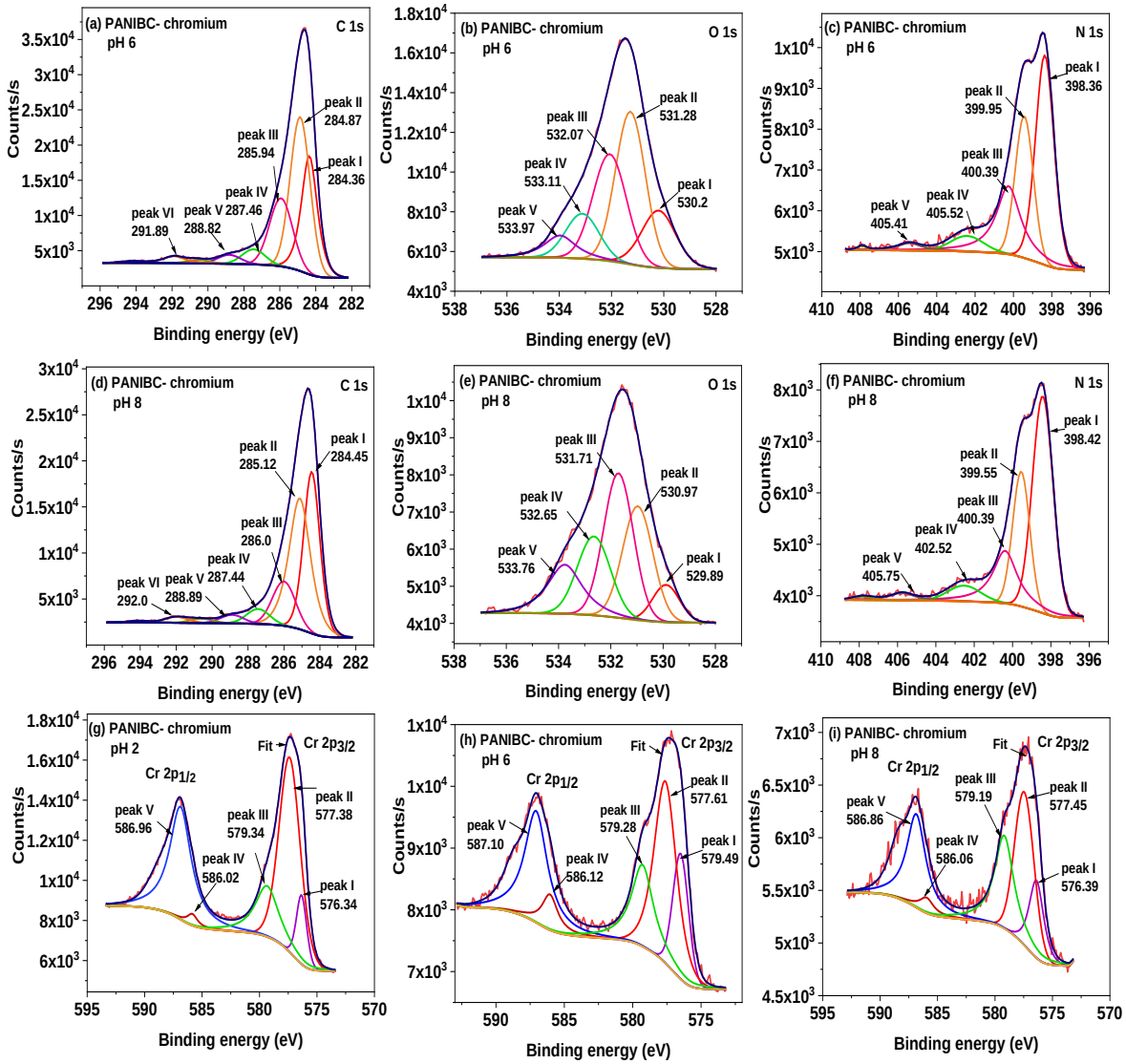

Figure B.6 High resolution XPS spectra after chromium adsorption on to PANIBC

PANIBC's C1s, O1s and N1s, at pH 6 (a), (b), (c) and at pH 8 (d), (e), (f). HR-XPS spectra on PANIBC of Cr $2p_{1/2}$ and Cr $2p_{3/2}$ at pH 2, 6, 8 (g), (h), (i), respectively.

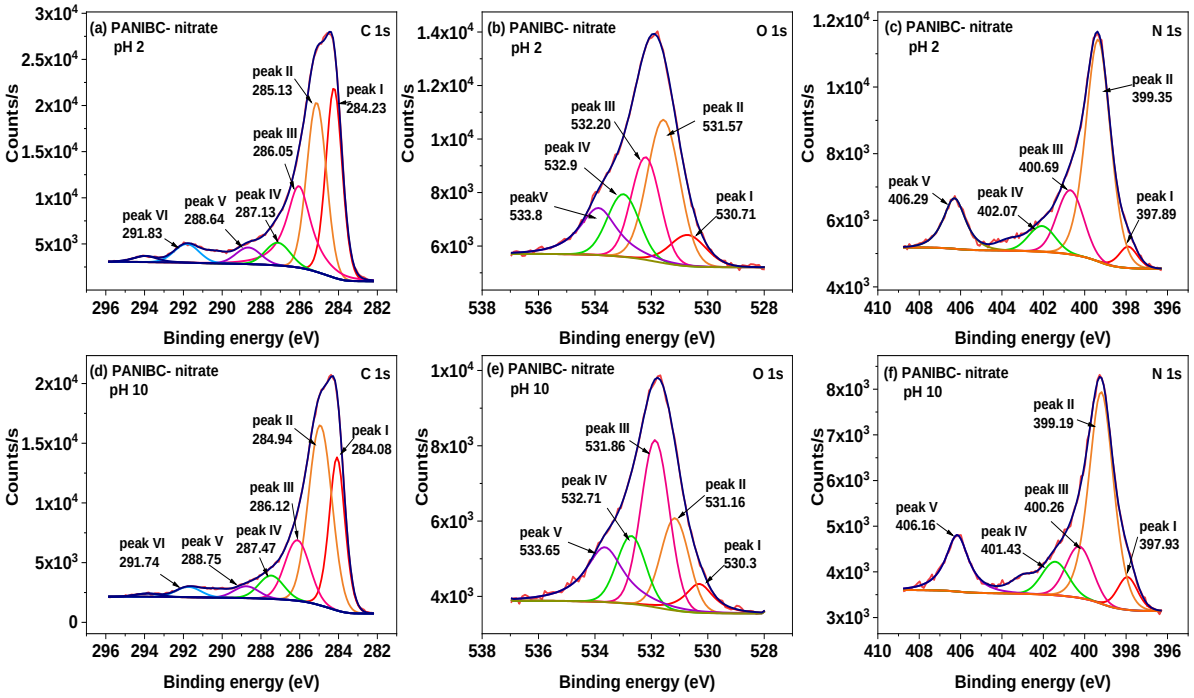

Figure B.7 High resolution XPS spectra after nitrate adsorption on to PANIBC PANIBC's C1s, O1s and N1s, at pH 2 (a), (b), (c), and at pH 10 (d), (e), and (f) respectively.

APPENDIX C

IRON/TITANIUM OXIDE-BIOCHAR COMPOSITE AS A VERSATILE PHOTOCATALYST FOR REMOVAL OF AQUEOUS CHROMIUM, LEAD, FLUORIDE AND METHYLENE BLUE - SUPPORTING INFORMATION

Table C.1 Elemental composition and surface morphology parameters of Fe_2TiO_5/BC

Elemental content/ wt.%											S_{BET}[c]	V_T[c]	S[c]
	C	H	N	O[b]	H/C	O/C	(O+N)/C	Ash	Fe	Ti	(m^2/g)	(cm^3/g)	(A^0)
DFBC[d]	80.36	2.00	0.97	13.78	0.02	0.17	0.18	2.89	0.68		535	0.249	18.6
Fe_2TiO_5/BC	38.85	6.08	1.71	17.56	0.16	0.45	0.49	16.3	6.58	2.3	576	0.207	12.6
Fe_2TiO_5								96.9	32.4	16.7	85	0.023	10.8

[a]C, H and N wt.% were obtained by combustion analysis using an elemental analyzer (EAI CE-440)

[b] The organic oxygen content was calculated by subtracting the wt.% of C, H, N, and ash from the total wt.% (100 %) and doesn't include the O present as metal oxides in the ash. [c]S_{BET} stands for BET specific surface area; V_T for total pore volume; S for pore size of biochar prepared.

[d]Douglas fir biochar

Table C.2 C1s High resolution (HR) XPS peak assignments for Fe_2TiO_5, Fe_2TiO_5/BC, Cr(VI)-laden Fe_2TiO_5/BC, Pb(II)-laden Fe_2TiO_5/BC, fluoride-laden Fe_2TiO_5/BC, and MB-laden Fe_2TiO_5/BC

		Peak/ Chemical species					
	Characteristic (units)	Fe_2TiO_5	Fe_2TiO_5/BC	Cr	Pb	F	MB
C-C, C-H							
	Binding Energy (eV)	284.8	284.5	284.77	284.5	284.66	284.67
	FWHM (eV)	1.33	1.06	1.06	1.07	1.03	1.08
	Atomic %	13.57	51.27	36.89	52.27	63.02	48.89
C=C, Aromatic C	Binding Energy (eV)	285.46	285.46	285.38	285.52	285.56	285.86
	FWHM (eV)	0.86	1.5	1.5	1.5	1.5	1.5
	Atomic %	1.01	9.18	7.47	9.08	8.77	11.82
C-OH,	Binding Energy (eV)	286.41	286.62	286.63	286.56	286.42	287.04
	FWHM (eV)	1.34	1.5	1.5	1.5	1.5	1.5
	Atomic %	1.8	4.85	5.26	4.76	8.9	3.65
C=O	Binding Energy (eV)	288.86	288.21	288.5	288.09	287.91	288.57
	FWHM (eV)	1.29	2	2	2	2	2
	Atomic %	1.25	3.16	3.34	3.25	5.01	3.15
COOH(R)	Binding Energy (eV)	289.51	289.96	290.49	290.04	290.06	290.36
	FWHM (eV)	0.95	2	1.71	2	2	1.72
	Atomic %	0.21	1.92	0.74	1.82	2.77	1.21

Table C.3 O1s High resolution (HR) XPS peak assignments for Fe_2TiO_5, Fe_2TiO_5/BC, Cr(VI)-laden Fe_2TiO_5/BC, Pb(II)-laden Fe_2TiO_5/BC, fluoride-laden Fe_2TiO_5/BC, and MB-laden Fe_2TiO_5/BC

		Peak/ Chemical species					
	Characteristic (units)	Fe_2TiO_5	Fe_2TiO_5/BC	Cr	Pb	F	MB
C=O, Cr(VI)-O	Binding Energy (eV)	530.31	530.22	530.49	530.27	530.32	530.38
	FWHM (eV)	1.25	1.22	1.32	1.26	1.16	1.23
	Atomic %	37.12	10.5	14.8	10.63	2.5	10.03
O-CR_3	Binding Energy (eV)	531.21	531.12	531.4	531.17	531.25	531.47
	FWHM (eV)	1.39	1.13	1.12	1.02	1.39	1.54
	Atomic %	4.28	1.87	5.72	1.76	1.01	5.29
C-OH	Binding Energy (eV)	532.07	531.98	532.15	531.96	532.08	532.48
	FWHM (eV)	1.35	1.5	1.2	1.43	1.43	1.15
	Atomic %	3.58	3.41	5.85	3.23	1.47	1.87
CO_3^{2-}	Binding Energy (eV)	533.04	533.13	533	533.12	533.35	533.35
	FWHM (eV)	0.75	1.18	0.93	1.21	1.59	1
	Atomic %	0.34	1.01	1.57	0.92	2.23	0.84
COOH(R),	Binding Energy (eV)	533.69	533.82	533.64	533.82	534.28	533.96
	FWHM (eV)	0.79	1.6	0.89	1.56	1.61	1.55
	Atomic %	0.23	1.75	1.2	0.93	1.19	1.35
Chemisorbed water,	Binding Energy (eV)	536.67		534.23	535.48	535.42	536.54
	FWHM (eV)	1.48		1.29	1.52	1.5	1.47
	Atomic %	0.28		1.72	0.29	0.54	0.15

Table C.4 Ti2p High resolution (HR) XPS peak assignments for Fe_2TiO_5, Fe_2TiO_5/BC, Cr(VI)-laden Fe_2TiO_5/BC, Pb(II)-laden Fe_2TiO_5/BC, fluoride-laden Fe_2TiO_5/BC, and MB-laden Fe_2TiO_5/BC

	Peak/ Chemical species						
	Characteristic (units)	Fe_2TiO_5	Fe_2TiO_5/BC	Cr	Pb	F	MB
Ti $2p_{1/2}$ TiO_2, Fe_2TiO_5	Binding Energy (eV)	458.77	458.65	458.9	458.65	458.86	458.83
	FWHM (eV)	1.2	1.17	1.25	1.22	1.14	1.19
	Atomic %	15.05	3.74	4.14	3.71	0.91	3.67
Ti 2p satellite							
	Binding Energy (eV)	471.79	471.65	471.84	471.86		471.62
	FWHM (eV)	2.56	2.82	2.81	2.83		1.7
	Atomic %	1.04	0.29	0.3	0.29		0.12

Table C.5 Fe2p High resolution (HR) XPS peak assignments for Fe_2TiO_5, Fe_2TiO_5/BC, Cr(VI)-laden Fe_2TiO_5/BC, Pb(II)-laden Fe_2TiO_5/BC, fluoride-laden Fe_2TiO_5/BC, and MB-laden Fe_2TiO_5/BC

		Peak/ Chemical species					
	Characteristic (units)	Fe_2TiO_5	Fe_2TiO_5/BC	Cr	Pb	F	MB
Fe(III) $2p_{3/2}$ Fe_2O_3							
	Binding Energy (eV)	708.94	710.87	711.06	710.77	711.74	710.9
	FWHM (eV)	1.23	1.8	1.91	1.76	1.91	1.82
	Atomic %	0.3	0.83	0.98	0.78	0.16	0.76
Fe(III) $2p_{3/2}$ Fe_2O_3	Binding Energy (eV)	710.85	712.38	712.38	711.94	713.53	712.01
	FWHM (eV)	1.88	2.04	1.92	2	2.2	1.99
	Atomic %	3.04	0.72	0.67	0.62	0.13	0.62
Fe(III)	Binding Energy (eV)	712.27	714.27	714	713.62	724.87	713.59
	FWHM (eV)	1.98	2.2	2.2	2.2	1.91	2.13
	Atomic %	2.15	0.38	0.52	0.45	0.32	0.41
Fe $2p_{3/2}$ satellite	Binding Energy (eV)	713.81	716.15	716.06	715.43	726.44	715.06
	FWHM (eV)	2.2	2.2	2.2	2.119	2.2	1.86
	Atomic %	1.35	0.14	0.23	0.24	0.15	0.19
Fe(III) $2p_{3/2}$ Maghemite satellite	Binding Energy (eV)	715.69	718.86	717.98	716.52	728.26	716.74
	FWHM (eV)	2.2	2.87	1.54	2.19	1.54	2.2
	Atomic %	0.61	0.3	0.21	0.14	0.13	0.14
Fe $2p_{3/2}$	Binding Energy (eV)	718.23	720.75	719.69	719.14		719.35
	FWHM (eV)	3	3.12	2.31	3		2.87
	Atomic %	0.76	0.32	0.31	0.33		0.29

Table C.5 (Continued)

Fe $2p_{1/2}$	Binding Energy (eV)	720.59	722.73	721.75	721.59		721.58
	FWHM (eV)	3.26	2	2.58	3.2		3.29
	Atomic %	1.21	0.45	0.28	0.28		0.34
Fe(III) $2p_{1/2}$ maghemite	Binding Energy (eV)	722.34	724.19	723.86	723.57		723.7
	FWHM (eV)	1.28	1.81	2	1.8		1.86
	Atomic %	0.44	0.7	0.67	0.38		0.36
Fe $2p_{1/2}$	Binding Energy (eV)	723.99	725.55	725.18	724.82		725
	FWHM (eV)	1.91	2.05	2	1.98		1.98
	Atomic %	2.82	0.88	1.06	0.89		0.78
Fe $2p_{1/2}$	Binding Energy (eV)	725.51	727.18	726.8	726.42		726.4
	FWHM (eV)	2.06	2.2	2.16	2.2		2.07
	Atomic %	3.21	0.55	0.94	0.8		0.73
Fe $2p_{1/2}$	Binding Energy (eV)	727.21	728.95	728.86	728.23		727.86
	FWHM (eV)	2.2	2.2	2.2	2.17		1.83
	Atomic %	1.72	0.38	0.48	0.46		0.37
Fe(III) $2p_{1/2}$	Binding Energy (eV)	729.02	731.36	732.19	732.31		729.54
	FWHM (eV)	2.17	3	2.4	2.9		2.18
	Atomic %	0.92	0.23	0.26	0.23		0.17
Fe(III) satellite	Binding Energy (eV)	730.8	733.97	734.25	734.09		732
	FWHM (eV)	2.91	3.12	2.54	3.26		2.9
	Atomic %	0.19	0.26	0.25	0.22		0.12

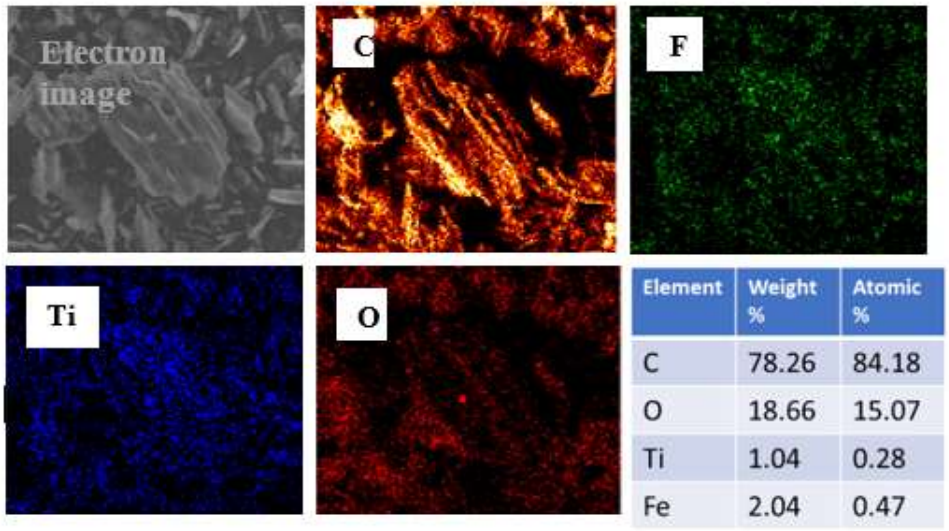

Element	Weight %	Atomic %
C	78.26	84.18
O	18.66	15.07
Ti	1.04	0.28
Fe	2.04	0.47

Figure C.1 SEM-EDX elemental mapping for Fe_2TiO_5/BC

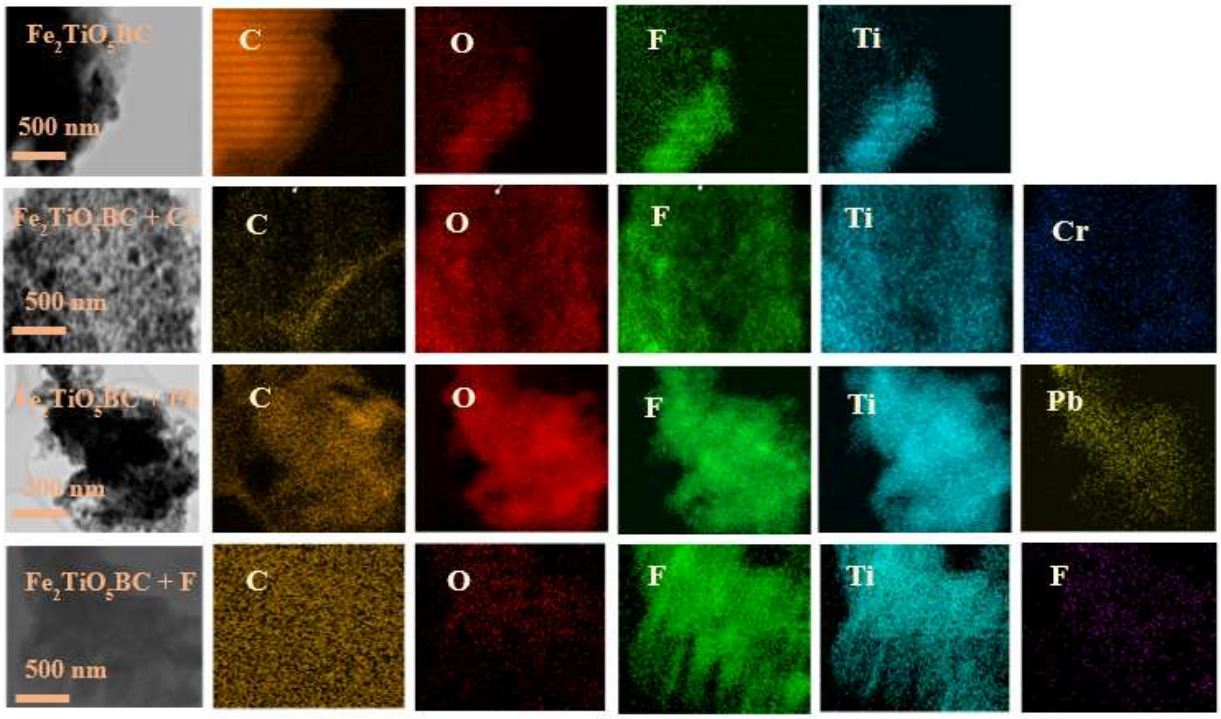

Figure C.2 TEM-EDX images with elemental mapping of Fe_2TiO_5/BC, Cr-laden-Fe_2TiO_5/BC, Pb-laden- Fe_2TiO_5/BC, F-laden- Fe_2TiO_5/BC, and MB-laden-Fe_2TiO_5/BC

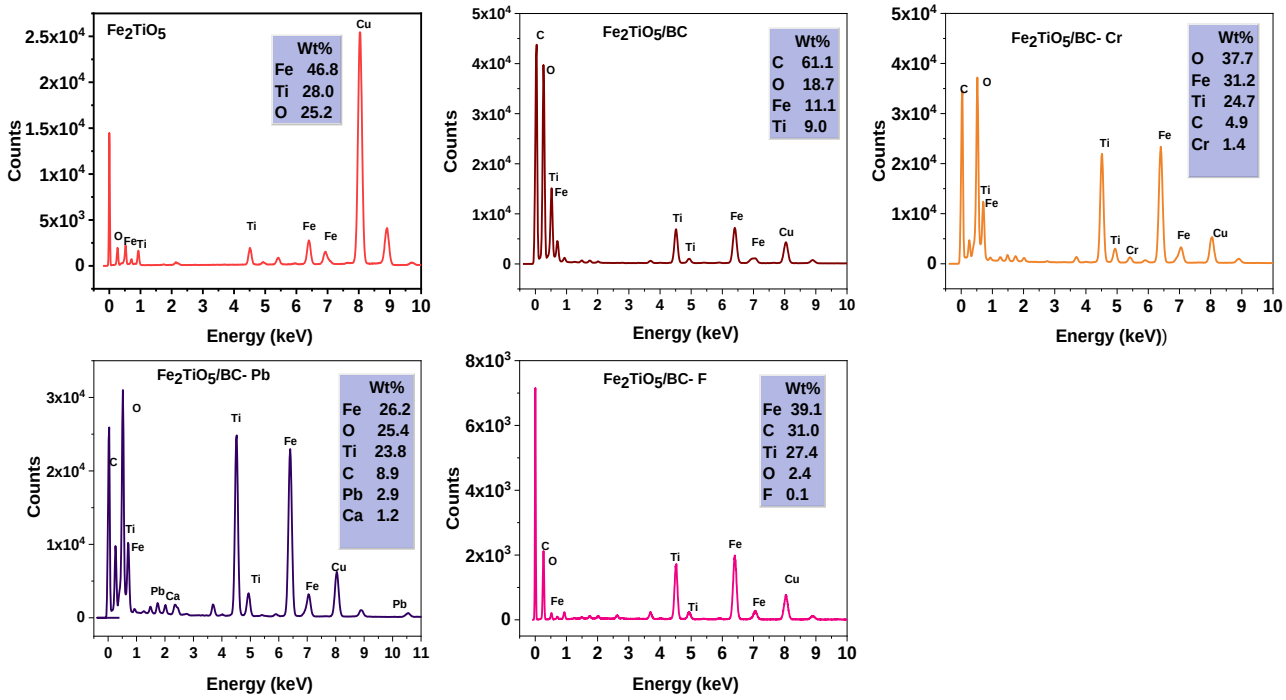

Figure C.3 TEM-EDX spectra for Fe_2TiO_5, Fe_2TiO_5/BC, Cr-laden- Fe_2TiO_5/BC, Pb-laden- Fe_2TiO_5/BC, and F-laden- Fe_2TiO_5/BC

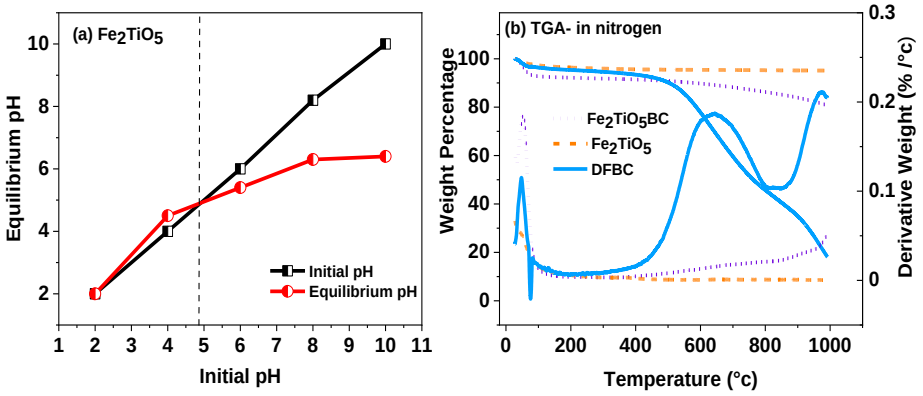

Figure C.4 (a) Point of zero charge (PZC) for Fe_2TiO_5, (b) thermogravimetric analysis (TGA) for DFBC and Fe_2TiO_5

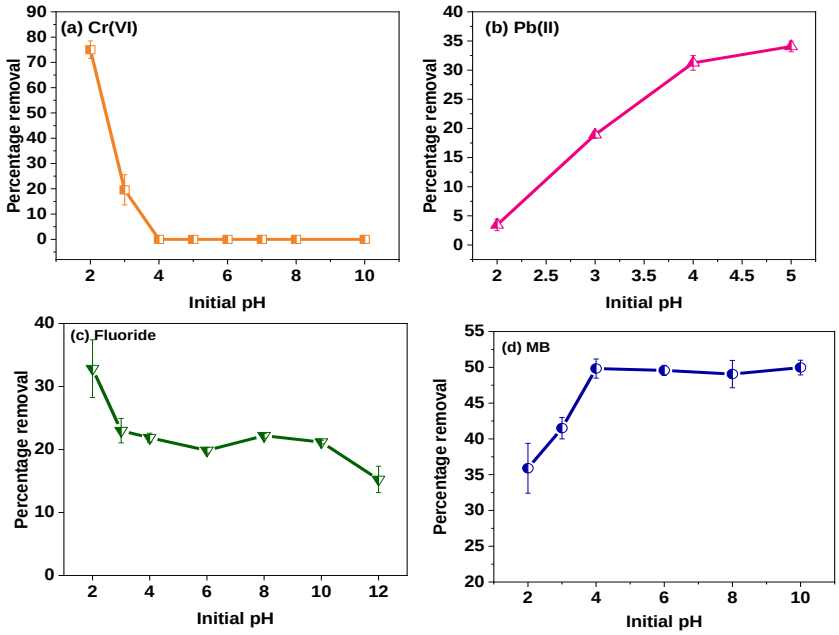

Figure C.5 pH dependance for removal by Fe2TiO5/BC

pH dependance for removal by Fe_2TiO_5/BC of (a) Cr(VI) 50 mg/L, (b) Pb(II) 100 mg/L, (c) fluoride 50 mg/L and (d) MB 200 mg/L. Fe_2TiO_5/BC (25 mg) was mixed with 25 mL of solution at room temperature for 24 h.

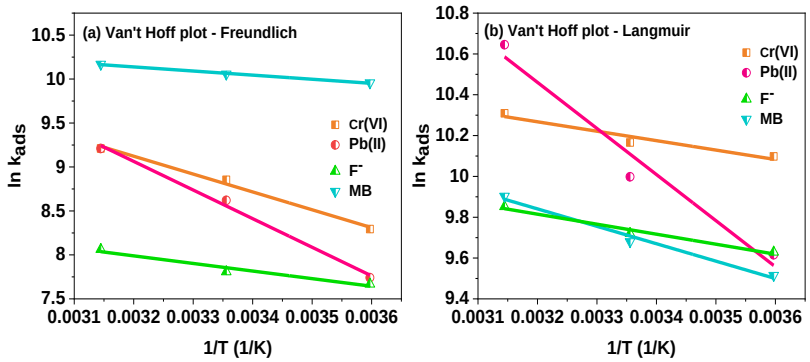

Figure C.6 Van't Hoff plot for (a) Freundlich and (b) Langmuir adsorption models of Cr(VI), Pb(II), fluoride and MB on Fe_2TiO_5/BC

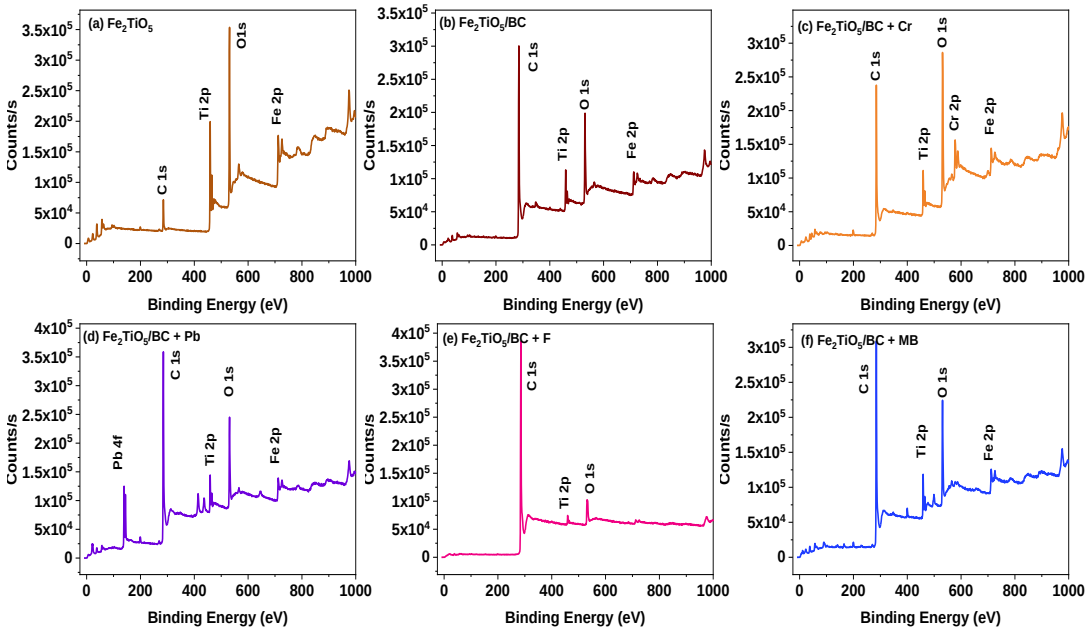

Figure C.7 Low resolution XPS spectra for (a) Fe_2TiO_5, (b) Fe_2TiO_5/BC, (c) Cr-laden-Fe_2TiO_5/BC, (d) Pb-laden-Fe_2TiO_5/BC, (e) F^--laden-Fe_2TiO_5/BC, (f) MB-laden-Fe_2TiO_5/BC

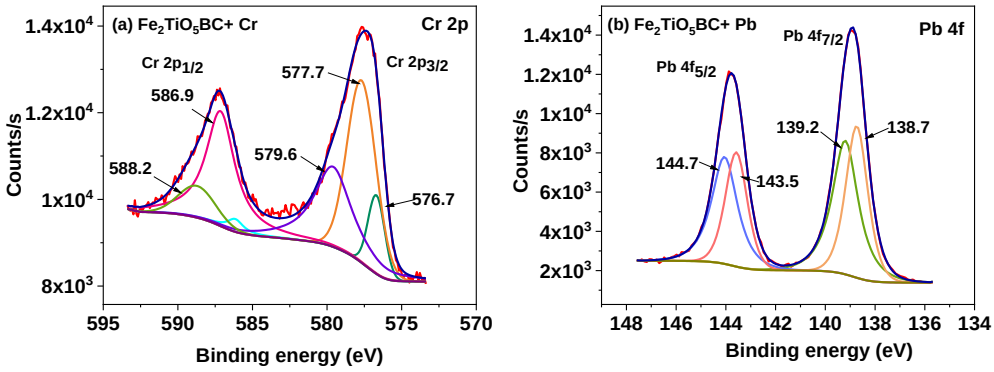

Figure C.8 HR-XPS deconvoluted spectra of (a) Cr-laden- Fe_2TiO_5/BC and (b) Pb-laden- Fe_2TiO_5/BC

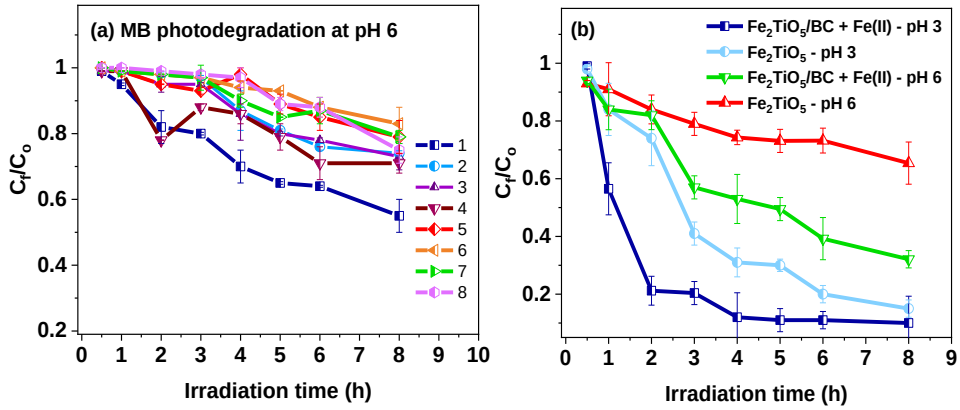

Figure C.9 MB photodegradation

MB photodegradation (100 mg of Fe_2TiO_5/BC mixed with 100 mL of 100 mg/L MB in a Pyrex beaker (having 95% optical transmittance above 350 nm) at room temperature, pH 6) (a) 1-4 Fe_2TiO_5/BC in MB solution in the presence of (1) light + air, (2) dark + air, (3) light + N_2 and (4) dark + N_2. 5-8 MB solution without photocatalyst in the presence of (5) light + air, (6) dark + air, (7) light + N_2 and (8) dark + N_2. (b) MB photodegradation in the presence of Fe_2TiO_5/BC + 10 mg/L Fe(II) and Fe_2TiO_5 at pH 6 or 3. Here, C_f and C_i are the final and initial concentration of MB after and before photodegradation

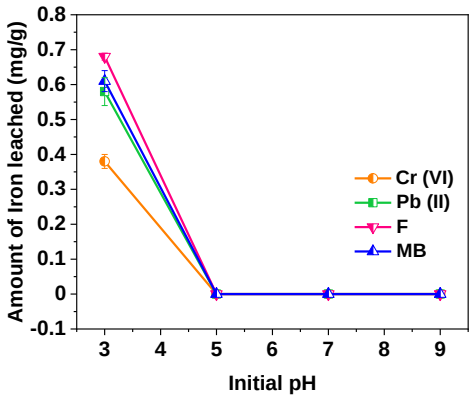

Figure C.10 Amount of iron leached after adsorption

Amount of iron leached after completing the adsorption of Cr(VI), Pb(II), fluoride and MB on Fe_2TiO_5/BC. 25 mg of Fe_2TiO_5/BC was mixed with 25 mL of analyte each containing 50 mg/L at 298 K.